INFORMATION TO USERS

This manuscript has been reproduced from the microfilm master. UMI films the text directly from the original or copy submitted. Thus, some thesis and dissertation copies are in typewriter face, while others may be from any type of computer printer.

The quality of this reproduction is dependent upon the quality of the copy submitted. Broken or indistinct print, colored or poor quality illustrations and photographs, print bleedthrough, substandard margins, and improper alignment can adversely affect reproduction.

In the unlikely event that the author did not send UMI a complete manuscript and there are missing pages, these will be noted. Also, if unauthorized copyright material had to be removed, a note will indicate the deletion.

Oversize materials (e.g., maps, drawings, charts) are reproduced by sectioning the original, beginning at the upper left-hand corner and continuing from left to right in equal sections with small overlaps.

Photographs included in the original manuscript have been reproduced xerographically in this copy. Higher quality 6" x 9" black and white photographic prints are available for any photographs or illustrations appearing in this copy for an additional charge. Contact UMI directly to order.

Bell & Howell Information and Learning
300 North Zeeb Road, Ann Arbor, MI 48106-1346 USA
800-521-0600

MODELING OF SURGES CAUSED BY THE RELEASE OF BREAKUP ICE JAMS

Raafat G. Saadé

A Thesis
in
The Department
of
Civil Engineering

Presented in Partial Fulfilment of the Requirements
for the Degree of Doctor of Philosophy at
Concordia University
Montreal, Quebec, Canada

January 1995

ABSTRACT

MODELING OF SURGES CAUSED BY THE RELEASE OF BREAKUP ICE JAMS

Raafat G. Saade, Ph.D.
Concordia University, 1995

In late winter and early spring, ice covers become weak in strength and break-up. The passage of the resulting ice floes may be arrested at a downstream location and create an ice jam. The increase in ice and water pressures may eventually cause the break-up of the blockage. The sudden release of the jam can result in violent ice runs and surges. Ice jam related floods can cause substantial damage to property, erode river beds, endanger hydraulic structures and affect safety at river crossings. The current understanding of the breakup ice jam phenomena is insufficient and therefore the state-of-the-art is not well advanced. There is an urgent need to improve it.

The primary objective of this study is to identify and determine through laboratory as well as numerical modeling, the processes involved during the collapse of an ice jam and the formation, development and propagation of the resulting surges and ice run. The research work was carried out in three parts, namely the investigation of the phreatic water levels along an ice jam, the transport of accumulation ice covers, and the characteristics of surges and ice runs caused by the jam release.

From this study, five different types of release mechanisms related to the break-up of ice jams were identified. It was evident that the surge characteristics

depend primarily on the type of release mechanism and the prevailing initial hydrodynamic conditions prevailing immediately before release. Observations showed that during the collapse of the jam, its thickness profile at the toe of the ice jam undergoes redistribution for a short period of time and subsequently the ice mass moves downstream in a relatively single layer scenario.

A two-dimensional two-layer model is formulated for the simulation of an ice jam release event. The model is capable of simulating the phreatic water surface profile along an ice jam, the formation, development and propagation of the surge and ice run after the release and the redistribution of ice jam thickness after release.

The numerical model was validated by the experimental data of the present and past studies.

In the name of 'Allah'; The most merciful; The most compassionate

When we consider the infinite power and wisdom of the maker, we have reason to thank that it is suitable to the magnificent harmony of the universe, and the great design and infinite goodness of the Architect, that the species of creatures should also, by gentle degrees, ascend upward from us toward his infinite perfection, as wee see they gradually descend from us downwards.
(Dante)

DEDICATION

This thesis is dedicated to my family:
my wife Christina; my Daughter Elana; and my Son George

ACKNOWLEDGEMENT

I take this opportunity to thank my supervisors, Dr. Ramamurthy and Dr. Troitsky for their critical review of my work. I also am grateful for their efforts to ensure my continuous progress, especially during my last year of residency. Their help is greatly appreciated.

I would also like to show my sincere gratitude to my wife and children for their patience, and continuous encouragement. Their strong support was very important to me. Thank you.

I also deeple appreciate and value the rest of my family for their unconditional love and care: My Mom and Dad, Eleonore and George Saade, my sister Tina, George and Anastasia Amanatidis, and Soumela.

Last but not least, I thank very much Dr. Spyridon Beltaos (NWRI, Burlington, Ontario) for his valuable feedback and comments during the undertaking of my research work, and Mr. Graham Holder (Lasalle Consulting Group) for the laboratory equipment and material that he made available for me in order to carry out my research. Without them, this research work probably would have not been possible.

Table of Contents

page

page

LIST OF FIGURES

Page

Page

Page

LIST OF TABLES

LIST OF PHOTOS

Page

CHAPTER 1.0

INTRODUCTION

Ice jams in general are the cause of many problems occurring in Northern rivers and lakes. The damages that ice jams may inflict on property and river works and sometimes on human lives render their study to be essential to improve the understanding of their behavior and hopefully limit the damages they incur.

In this chapter, (a) The processes associated with the formation and release of breakup ice jams are described, (b) the scope and objectives are identified, and (c) the outline of this study is presented.

1.1 Background

In Northern Countries, during the winter season, rivers and lakes are subject to significant heat loss from their surface. Eventually the water temperature in the river drops close to a critical freezing point. Cooling beyond that critical point will lead to ice formation.

In slow-flowing areas of the river, the turbulence intensity is not strong enough to completely mix the cold water over the depth. In this case, stationary ice cover extending over the river width, border ice (photo 1a), or moving skim ice can develop. In zones where the flow is characterized by high velocities, the cold water will be well mixed over the flow depth give rise to frazil ice crystals. These crystals grow in size and develop fully into flocs and float on the river surface to form surface ice (or ice pans, photo 1b).

If the surface ice concentration increases continuously, ice pans can grow in size and strengthen with persisting subfreezing temperatures. These ice pans can either join with larger ice floes if they travel over long distances or break into fragments, if they pass through zones with high flow velocity. In any case, ice pans result in the reduction of open water surface area and hence in the net ice production, as a result of the insulating effect of the floating ice sheets. The transport of surface ice may cease at artificial obstacles or at congested river sections, thereby initiating an ice cover.

After the initiation of a stationary ice cover, progression of the leading edge may occur. The progression of the leading edge of ice depends on the rate of incoming surface ice and the thickness of the new ice cover. When the flow velocity is relatively low, incoming surface ice will accumulate in the form of juxtaposition. When the velocity is high, ice floes can underturn and submerge to

form an ice cover by hydraulic thickening (narrow jam). If the strength of the ice cover together with the bank shear cannot support external forces, then mechanical thickening or shoving will occur until the cover reaches a thickness capable of withstanding the external forces (wide jam). The latter discussion is associated with the formation of ice covers during freeze-up.

Similar processes occur in late winter and early spring when a large quantity of surface ice pieces is released due to the breakup of ice covers. In this case, the leading edge of the intact downstream ice cover often acts as the obstacle that initiates the formation of breakup ice jams.

In general, a breakup ice jam is initiated when the downstream passage of floating ice in a stream is arrested. An obstacle to the passage of ice floes arriving from the upstream side is produced and the stage is set for the development of an ice jam. The stability of the arriving ice floes at the upstream edge (leading edge) of the obstacle depends on the flow conditions and ice floe geometry. The ice floes swept under the ice cover which may be viewed as an obstacle will experience one of the following possibilities: a) come to rest near the upstream end of the ice cover and eventually form a "hanging dam"; b) get transported and deposited further downstream; or c) get flushed past the obstruction and continue downstream (figure 1.1).

The above processes are quoted widely in literature and have been studied in the laboratory where it is implicitly assumed that the ice discharge and transport comprises a single layer of ice floes ad the initiating jam is unbreakable. The latter assumption is acceptable and generally realistic when the phenomena of freeze-up ice jams are considered. During breakup ice jams, however, the accumulation and transport of ice floes involve many other processes such as thickening, erosion and deposition of the ice jam during both formation and release.

Clearly, neither of the two assumptions are valid in this case. Once initiated, ice jams propagate upstream. As the incoming floes accumulate near the leading edge of the obstacle or ice cover, internal stresses increase due to flow shear and the jam's own weight component acting along the water surface slope. Such stresses are moderated by bank friction and cohesion at the sides of the jam. If the internal compressive strength of an ice jam is exceeded, the ice jam will collapse locally (or "shove") and assume a new thickness capable of resisting the applied forces. Ice jams that are formed by submergence and deposition of ice floes alone are called "narrow channel" jams or narrow jams while those formed by shoving are referred to as "wide channel" jams or wide jams (Pariset et al. 1966). The thickness characteristics of "wide channel" ice jams depend on the shear stress at the water-ice interface, channel width and slope, hydraulic gradient and the internal strength of the ice jam. "Wide channel" ice jams often attain considerable thicknesses which may extend several meters as often evidenced by the high shear walls left on the river banks following the release of a jam and subsequent drop of the water level.

With increasing water and ice pressures, most breakup ice jams eventually get released. Ice jams lasting from a few minutes to several days have been reported. A sudden ice jam release results in the development and propagation of downstream and upstream surges as well as in violent ice runs. During release, the stage rises very rapidly at the downstream locations and water velocities may exceed even those attained during extreme open water floods.

During the period of 1963 to 1973 the United States reported the annual average loss due to ice jams to be of the order of $16,600,000. The actual annual loss was estimated at $80, 000, 000 (Carey et al. 1973). In Canada, the annual cost due to ice jams alone has been estimated to be approximately $37, 000, 000.

Almost $4, 000, 000 is spent annually for the repair and maintenance of bridges damaged by ice, and about $6, 000, 000 per year for protection against flooding caused by river ice jams. It should be pointed out that although these figures are annually average, equally high costs can accrue from a single event. For example, an ice jam on the St. John river in 1936 resulted in damages totaling approximately $36, 000, 000 and the total damage due to a 1:100 year ice jam flood at Fort McMurray, Alberta was calculated to cost over $500, 000, 000. (Beltaos et al. 1990)

Little is known about the processes associated with the release event of ice jams. This lack of information results in a serious handicap for engineers planning hydropower dams, and bridges on rivers where severe jams are known to occur (photo 2). The processes occurring during an ice jam release event involve many parameters that are not only very difficult to measure but to isolate on site or in laboratory experiments. As a result of the scarcity of field and laboratory data make the process very difficult for one to understand. The investigation of the processes by which an ice jam collapses and the resulting surges and ice run which is the primary concern in this study constitutes an important step towards providing engineers and planners with a better understanding of the phenomena.

The primary objective of the present research work is the modeling of an ice jam release event in an attempt to better understand and quantify the processes involved. This has been met by carrying out laboratory experiments and through the formulation of a numerical model which is capable of simulating the release of ice jams.

1.2 Objectives and scope

The major objectives of the present study are: (a) to investigate the processes occurring during the sudden collapse of breakup ice jams; (b) to identify and evaluate the key parameters affecting the resulting surge formation; and (c) to study the development and propagation of the surges after the release. Numerical as well as physical methods are developed to attain these objectives.

A two-dimensional finite difference numerical model is developed. Separate mass conservation laws are introduced for each of the water and ice layers. The ice layer is described by an integral conservation law for water and the ice mass and for the bottom layer the classical continuity equation was adopted. The depth-averaged mass conservation equations are coupled in order to ensure proper overall conservation of water and ice masses over the study reach. In addition, ice transport equations and proper constitutive relations are included.

The laboratory experiments aim at: providing a better understanding of the processes involved; identifying the parameters pertinent to the problem at hand; and quantifying measurements and data by correlation of the main variables.

Laboratory experiments have been designed and carried out in order to isolate and better understand the processes involved during the release of ice jams. Parameters playing significant roles in the problem at hand are identified and quantified. The additional understanding acquired from the laboratory experiments were integrated into the numerical model. Selected experimental test runs and corresponding measurements are used to verify the final model's computational results.

1.3 Description of research work

In order to model the release of breakup ice jams, it was found necessary to investigate the possibility of formation of a breakup ice jam in the laboratory, and one which gives a significant drop in the water level across its leading and trailing edges. It is imperative to obtain a significant drop in the water level, in order to model the release of the ice jam and consequently the development and propagation of the surge and ice run. The necessity of carrying out laboratory studies is due to the lack of such data.

With the possible formation of a breakup ice jam in the laboratory, water levels and velocities throughout the entire flume could be measured. Analysis of the measurements could then be carried out. Consequently, empirical relations can be formulated and finally conclusions could be drawn. This part of the research work is of extreme importance to the modeling of surges caused by the release of breakup ice jams. This is because water levels, velocities, and the ice jam thickness profile constitute the initial conditions for the release event. The findings from this part of the experiments could be used to understand processes occurring during the release event as well as be incorporated in the numerical model.

Before proceeding to the modeling of the surges caused by the release of an ice jam, the empirical relations obtained from the first part of the laboratory should first be integrated into the numerical model and then tested. Therefore, a set of simulation runs with the numerical model were carried out to investigate the ice jam resistance to the main channel flow. For the verification of this component of the numerical model, six experiments were used, three of which were carried out at NWRI by wong et al. 1985 and three others that were performed in this study.

Having the initial conditions for ice jam release investigated experimentally and numerically, one last major aspect of ice jam release is needed to be studied before going on to the modeling of surges due to ice jam release. This part of the research work includes the modeling of the transport of ice floes which occurs after release. This study was performed again through experimental and numerical simulations. The primary objective of this part of the research work is to obtain insight into the dominant parameters affecting the transport of ice as well as to attempt to quantify these parameters.

Finally, the processes under which an ice jam collapses and the resulting surges and ice run was carried out. Experiments followed by some numerical simulations were performed to that effect. The conditions leading to the collapse of an ice jam and the formation development and propagation of the resulting surges and ice run are studied.

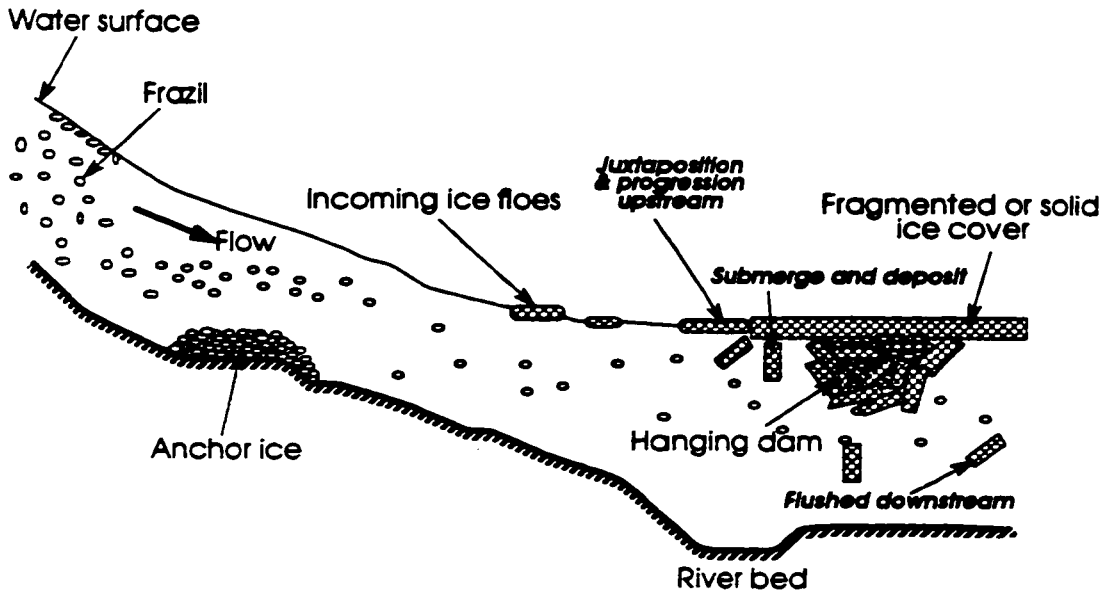

Figure 1.1: Schematic of the conceptual river ice formation processes

a) border ice formation

b) Frazil accumulation - ice pans

Photo 1.1: River ice processes

a) Flooding of towns

b) Obstruction of Highway

c) Jam at railway bridge

d) Bridge collapsing

Photo 1.2: Damages due to ice jams

CHAPTER 2.0

LITERATURE REVIEW

Most theoretical as well as experimental studies of river ice jams have focused essentially on the mechanical stability of the passive type of static ice jamming which bears little resemblance to the dynamic and phenomenal spring ice jamming (Pariset et al., 1966; Michel, 1971; Uzuner and Kennedy, 1976; Tatinclaux, 1977).

A study related to the propagation of surge caused by the release of an ice jam was presented by Henderson and Gerard (1981). This study presents a preliminary theoretical study of the sudden changes in depth and velocity that can be caused by the sudden formation, failure and re-formation of ice jams. This problem is essentially taken as the classic dam break. They stressed that ice jams formed in rivers at the time of spring break-up of river ice can cause a substantial blockage of the river flow, and a substantial rise in water level behind the jam. For higher return periods of 100 and 1000 years, water levels reached at spring breakup can be four or five meters higher than those of summer floods (Gerard, 1979).

From the observation of a temporary release of ice jam in the Athabasca River at McMurray, Alberta in 1977, and from analysis of the one-dimensional momentum equation, assuming negligible bed slope and resistance, Henderson and Gerard (1981) concluded that the immediate effect of ice jam release results in a rapid increase in velocity within the jam, while it has no effect on the flow depth. Consequently, a theoretical formulation of the development of a flood wave was derived. Analysis of the surge continuity and the momentum equation shows that the surge moving downstream caused by the sudden failure of an ice jam cannot have a height greater than one half of the difference in water level across the original jam.

Henderson and Gerard (1981) further indicated the surge resulting from the collapse of an ice-jam might be carrying a large mass of ice-blocks riding on its surface, which in turn may result in yet another jam downstream of the original jam-release site. Re-formation of a jam may cause positive surge moving upstream and a negative wave moving downstream. The concept of relative permeability between the original jam and the new jam, proportional to a ratio of the drop in water level across the jam to the square of the discharge through the jam, was proposed to access the upstream and downstream momentum. They concluded that the subsequent re-formation of the jam may produce a reflected positive surge behind the new jam, the water levels of which may exceed the original surge level by up to six times the height of the surge. It was also shown that the reflection of negative waves from the backwater curve behind the original jam can produce a significant surge attenuation, and increases in direct proportion to the slope of the river.

The above formulation of Henderson and Gerard (1981) is an ideal presentation of ice jam release. The results provide engineers the basic

understanding of the physical phenomena of the release of ice jam and the subsequent consequence. However, there are not enough records or data to support the theoretical formulation and conclusions given in this study. Zero slope and zero resistance assumptions in the formulation of release of ice jam especially are restrictive. The concept of relative jam permeability is very abstract, and is not proven and investigated at all. Besides, the ice movement effects on flow are not taken into account in this formulation.

Beltaos and Krishnappan (1982) presented a case study of surge from ice jam release. The equations of the ice-water flow that occurs after the release of an ice jam were formulated. In their model a one-dimensional wide, rectangular channel with constant porosity of ice cover, hydrostatic pressure assumption, and negligible thermal effects were taken into account. A concept of two-layer flow, including ice fragment flow assuming constant porosity on the top layer and water flow in the lower layer, was proposed. A uniform velocity distribution was assumed through the top layer, while a nonuniform velocity distribution with no slip condition at bed and identical ice fragment velocity at ice-water interface on lower layer was suggested. They integrated the hydrodynamic equations through the lower water layer and proposed a momentum equation for a moving ice element for which the convective momentum was balanced by the gravity force and boundary shear forces. They further indicated that once the initially stationary cover accelerates to the full water speed, ice velocity can be approximated by depth-averaged flow velocity. Consequently, this problem may be approximately treated as a one-dimensional, unsteady, water-only flow of total depth identical to that of ice-water flow.

Data reported in Doyle and Andres (1979) in the Fort McMurray case study were used to verify the results obtained from the application of their model. Cross

sections were approximated by a trapezoid. This trapezoid was then approximated by a rectangle of the same depth and of width equal to the average width of trapezoid. The initial conditions used were the water surface, bed profile, and flow discharge along the study reach. The flow through the voids in the jammed reach is assumed negligible. Boundary conditions in terms of the depth or flow rate were taken at the upstream and downstream boundaries. The boundary conditions were selected sufficiently far upstream and downstream of the jam to ensure that surge effects do not reach these locations during the computation period. The friction factor was expressed using the Chezy resistance coefficient. The friction factor was selected by trial and error so as to give the optimum agreement between predicted and observed downstream stages. The effects of jam length were considered by assuming longer jams of the same maximum water depth.

In the study of Beltaos and Krishnappan (1982), the formulation of the one-dimensional model for the ice jam release is simple and easy to apply. However, there are some limitations to its application. The assumption of constant void ratio of ice is restrictive. Because after the ice jam releases, due to the redistribution of ice, the void ratio of ice is likely to change with time and space. The assumption of identical ice velocity and current velocity may cause arguments. The friction factor for flow with an ice cover was taken as constant. This may be too simplistic for simulation in a natural river with irregular geometric cross section. Further, the initial ice condition and interaction among ice elements were not considered in this study. Hence, simulation may underestimate the water stage in absence of ice.

Wong et al. (1985) conducted laboratory tests to investigate the unsteady-flow condition after the release of an ice jam. The propagation of the surges

resulting from the release of ice jams was studied in a 1 m wide rectangular flume by feeding polyethylene blocks. It revealed that the presence of the moving polyethylene blocks (ice) has no discernible effect on the characteristics of the surge that follows the release of the jam and that the model of Beltaos and Krishnappon (1982) gives good predictions of the water levels and fair predictions of the water speeds. However, this conclusion is only valid for one-dimensional flow approximation, and fully developed conditions for the speed of the ice block. As such, no internal interaction among ice floes is considered.

Beltaos and Wong (1986) proposed the granular mass theory of river ice jams for their downstream transition as a means of improving understanding of conditions at the jam toe. It is recognized that the downstream transition plays an important role in many applications. These include conditions for grounding of ice jams and the design of measures to prevent or remove destructive jams. The theory is coupled with the equations of motion under, and seepage through, the jam. The resulting differential equations are solved numerically. This model applies to wide rectangular channels under steady flow conditions. Although the model involves several coefficients whose precise values in nature are unknown, the results may provide an understanding of ice breakup and help one to denote the appropriate boundary conditions for release of ice jam. Example calculations have been performed to illustrate the sensitivity of the model to various coefficients, and the preliminary applications to two case studies have resulted implausible findings with regard to grounding of ice jam.

Parkinson and Holder (1988) studied ice jam development, release and surge wave propagation. They collected observations of the record high level of ice jam on the Mackenzie River at Norman wells during the 1982 spring breakup. Reliable surveys of the water levels at Norman Wells were taken during the rise

and fall corresponding to the jam development and release. The location of the key of the ice jam was also observed. Less complete information was gathered at the downstream of Norman Wells. Although the field information was not as complete as would be desired, it was adequate to support the analysis of both the ice jam characteristics and the propagation of the surge wave downstream following the destruction of the jam.

Using a one-dimensional ice model, Glace III, Parkinson and Holder 1988 adopted steady state calculations to define the jam characteristics at the jam peak. The output was then used as the input to a dam-break model, developed by US National Weather Service, to calculate the surge wave propagation downstream and the inflow and outflow hydrographies at the jam site. Release of the ice jam was taken as a dam break problem, and the simulated results were in good agreement with the prototype behaviour by assuming complete breach of the dam break in five hours. In this study, the ice effects on the transient flow during the release of ice jam were not considered in the dam break model. Although, encouraging simulated results have been reached, there are arguments regarding the assumption of the breached mode of dam-break. Again, the method proposed here is applicable for the case of low ice concentration, because the interaction among ice floes and resistance between ice and bank are not involved.

The studies described above have neither addressed the question of the simulation of the dynamic interactions between the moving ice blocks and the water flow during ice jam formation and release, nor the question of the timing of ice jam formation and release. Recently, Shen et al. (1990) proposed a theoretical model for the dynamic transport of river ice. They acknowledged that the formation of an ice bridge is related to the ice transport capacity and the

rate of ice discharge from the upstream. Also, the ice transport capacity is a function of flow velocity, channel width, surface slope, size, concentration, and rheological characteristics of ice particles.

The transport of surface ice can be formulated by considering the movement of individual ice particles and their interactions. However, this is impractical due to the large number of surface ice particles varying in size and shape. Therefore, the continuum concept of granular surface ice mass in the river (Pariset and Hausser, 1961; Pariset et al., 1966; Uzuner and Kennedy, 1976; and Tsai et al., 1988) was the basis for the formulation of their ice transport equations. Three equations are involved in the ice transport equations. First, the equation of motion for surface ice is derived from the momentum balance of an element (Tsai et al., 1988). In the one-dimensional case, the convective force of ice mass is balanced by the internal stress due to particles interaction, bank resistance, wind drag, water drag, and pressure force. Secondly, the conservation of ice mass equation is presented considering external sources or sinks. However, the diffusion term of ice mass transport is neglected. Lastly, the conservation of ice area equation is also presented considering melting/freezing and the mechanical redistribution of ice area change. Similarly, the diffusion term of ice area transport is neglected.

Two constitutive equations for expression of internal shear and bank shear are also proposed to solve the equation of motion for surface ice. The constitutive relationships for rapid flow (low concentration) and slow flow (high concentration) regimes are adopted from the studies of Shen et al. (1987) of single-layer ice movement, and Pariset and Hausser (1961, 1966) of multi-layer ice movement, respectively. During the transition from rapid flow regime to slow flow regime, multi-layer rapid flow and single-layer slow flow conditions may occur. In

these situations, the above constitutive equations should not apply. However they were still taken for approximation in their study. Provided the constitutive relationships for internal stress and bank shear are given and the water flow condition is established, to obtain the unknown ice velocity, ice concentration, and ice thickness.

A Lagrangian-Eulerian algorithm, was used to solve the ice transport equations. In this method, trajectories of ice elements situated at fixed Eulerian grids along the river at the beginning of each time step are traced on the time-space domains. Ice velocity, ice concentration, and ice thickness of each moving ice element during the time step are determined by solving each respective ice transport equation in the Lagrangian form. In their examples of ice transport in a uniform current, the effects of internal ice resistance and bank shear on transport of ice were calculated by assuming constant current velocity, absence of wind, horizontal water surface slope, and negligible ice effects on water current. The ice production along the channel was considered constant unless the ice concentration reached the maximum possible ice concentration. Initial ice concentration and ice thickness were given as constant along the channel studied, while the initial ice velocity was determined from the ice transport momentum equation under steady uniform condition. The boundary conditions at the upstream end were constant ice concentration and ice velocity. At the downstream boundary, zero ice concentration and zero ice velocity gradients were assumed. The simulated results for ice transport at the early winter ice cover formation show that : (a) The internal resistance and bank shear increase with ice mass concentration, and in the case of rapid flow, the ice velocity. (b) Current drag increases with ice area concentration and the difference between ice velocity and current velocity. (c) Due to ice production,

ice concentration increases along the channel with time. (d) The location of ice bridging can be found where ice velocity is zero. After the formation of the ice bridge, the cover is extended upstream. Downstream of the bridge, some ice bleeding occurs due to the current drag. This bleeding later ceases with the increase in ice mass concentration through production. (e) Since the initial ice particle thickness is greater than the equilibrium ice jam thickness, the ice jam is a single-layer ice jam, i.e. formed in the juxtaposition mode.

To solve the one-dimensional coupled ice transport and channel flow problem, Shen et al. (1990) presented continuity and momentum equations of water with consideration of surface ice. The effect of phase change on the conservation of water mass was neglected, and the effect of ice thickness and ice velocity on water continuity were not taken into account. The solution was obtained first based on known ice conditions at the previous time level. The hydraulic condition was then used to determine the ice condition at the present time step. The flow condition was determined using a four-point implicit finite difference method with Newton-Raphson scheme. Again, ice transport was simulated numerically using the Lagrangian-Eulerian scheme. Steady state ice and flow coupled conditions were used as initial conditions. The error of this approximation disappeared after an initial period equal to the travel time of ice in the reach studied.

To illustrate the effects of channel geometry and border ice on ice transport, four examples were presented. In these examples of coupled ice transport and channel flow, constant flow discharge and ice velocity were imposed at the upstream boundary; zero ice flux (uniform ice concentration and thickness) was imposed at the downstream boundary; the stage at the downstream end was a function of discharge (rating curve). The rating curve was

obtained from momentum equation for water by imposing the steady uniform condition (equivalent to Manning's or Chezy relations). The initial value of ice concentration and ice thickness were constant along the channel. Simulated results showed that: (a) Case 1: for constant channel width, ice concentration increases along the channel with time, ice velocity decreases along the channel with time, and the discharge (velocity) decreases along with an increase in water level with time. These changes in discharge and water level are accompanied by a reduction of velocity, which causes faster ice jam initiation. (b) Case 2: for contraction of channel width, the current velocity increases (width decreases) compared to the first case, therefore, the shear stress (or water drag) at the ice-water interface increases accordingly. The increase of water drag on ice is compensated by internal ice stress and the bank shear due to the increase in ice concentration. The jam is initiated at about the same location and the same time as in the first example. (c) Case 3: for the case of constant channel width, but with border ice existing on both sides of the channel with their width increasing linearly from upstream to downstream, the ice concentration increases faster towards downstream due to the convergence of the surface width, and jamming condition occurs earlier than that in the first example. (d) Case 4: for a trench located between part of channel, due to the sudden decrease in channel velocity when entering the trench, the ice concentration increases rapidly. An ice bridge forms at the upstream end of the trench. Near the downstream end of the trench, ice concentration decreases with time. This is due to increases in flow and ice velocities at the exit of the trench.

The study of Shen et al. (1990) discussed above was aimed at exploring the ice transport at the early winter of ice cover formation and was not foucused on the release of ice jams. The examples show that the location and time of the ice

jam initiation is affected significantly by channel geometry and flow conditions. Both affect the ice transport. Ice jams are usually initiated at locations where convergence of ice mass, i.e. ice velocity decelerates. This is because the convergence of ice mass leads to a rapid increase in ice concentration. As a result, both ice resistance and bank shear increase to decelerate the ice mass.

Some observations can be made about the study of Shen et al. (1990). First of all, the constitutive relationships for internal ice stresses and bank shear are formulated based on the limited current state of knowledge. The constitutive relationships were originally developed based on uniform flow and static ice jams, however, they are used in the dynamic transport of ice jam. Some parameters like particle diameter, maximum-packing ice concentration are not easy to estimate. These may cause discrepancy while dealing with two-dimensional flow and irregular channel geometry. All of these facts need to be further improved through a combination of theoretical and laboratory studies together with field calibration. Secondly, several mechanisms, which may be important in field situations, are not included. These mechanisms include the hydrodynamic stability of ice floes at the leading edge, the formation of solid ice crust in the surface ice accumulation, and undercover erosion. Natural rivers are irregular in geometry. It is required to extend current model to a two-dimensional model for practical application. This is also useful for calibrating model parameters against field data, and to simulate dynamic border ice formation in irregular channel geometry. The ice production rate, ice area reduction rate due to mechanical redistribution, and rate of increase of ice area due to external sources as presented in this study are abstract and are not easy to be quantified. The ice flow regimes are classified as rapid and slow flow regimes. The former applies to the single-layer ice jam and the latter, to the multi-layer ice jam. This may be not

practical while considering a two-dimensional model with irregular channel geometry. In this situation, both flow conditions may happen alternatively along the channel. It also assumes that the faster single-layer and slow multi-layer flow do not exist. However, these two situations may arise in the transition zone from rapid flow regime to slow flow regime.

Shen et al. (1991) proposed a two-dimensional surface drift model which is developed for river ice with low ice discharge condition. The model assumes free drift of surface ice except in the vicinity of a stationary boundary. The model is applied to the Grass Island Pool area of the Niagara River and compared with field observations. They emphasize generalized river ice model should consider dynamics of ice transport and ice jam evolution. The study by Shen et al. (1990) proposed a formulation for dynamic ice transport in rivers and developed a one dimensional numerical model for simulation of the processes of surface ice transport, jam initiation, and jam progression. Since jam initiation, is the key to ice cover formation, is a two-dimensional phenomenon. They presented this two-dimensional surface ice drift model as an extension of an earlier model (Shen et al. 1990).

In their formulation, governing equations for a dynamic ice transport model include hydrodynamic equations and the ice dynamic equations. Basically, these equations are similar to those of Shen et al. (1990), except that the momentum equations of water and ice are two dimensional. The surface ice layer is considered as a continuum, and the equations of motion for the surface ice layer are derived from the momentum balance of an element area in Lagrangian form. For surface ice elements in contact with a solid boundary, boundary stresses were also considered.

They also stated that the internal ice resistance can vary over a wide range depending on concentration, kinematic variables and ice properties, and suggested that at low concentrations, the interaction between ice particles is negligible, and that ice particles will drift with the flow. They quoted from a theoretical analysis (Babic et al., 1990), and indicated that the interaction is negligible when the ice surface concentration is lower than a transitional value of 0.7. When the ice concentration is low and the size of ice floes is small, the surface ice element can be considered to drift with the water current. Under this condition, they proposed, that the ice velocity can be assumed to be the same as the surface current velocity. This will simplify the ice transport equations. Only in the close proximity to rigid boundaries, such as shoreline, border ice, and ice island, the free-drift assumption is no longer valid, and the force acting on the ice element needs to be considered. The movement of surface ice is simulated using a Lagrangian discrete-parcel algorithm. The surface ice is represented by discrete parcels of known mass. At each time level, a parcel has associated with it a spatial coordinates obtained by numerical integrating ice transport equation assuming the ice velocity equals to the current velocity. Based on the distribution of parcels, ice mass and concentration distribution can be determined.

In the vicinity of a stationary boundary, ice velocities are calculated from the momentum equation taking into account the boundary friction. The boundary friction is formulated according to a dynamic Coulomb yield criterion. The thickness of ice accumulation is calculated based on the hydraulic thickening formula of Pariset and Hausser (1961). This is valid only in the absence of the mechanical thickening phenomenon.

This model is applicable to low ice discharge conditions. Extension of the model to include the complete ice dynamics for simulating events with higher ice

concentration is needed to describe the formation and evolution of ice jams. For ice surface concentration less than 0.7, the internal interaction among ice elements is neglected. The ice elements drift with current. The assumption that ice surface velocity equals current velocity greatly simplifies the solution algorithm, but may cause arguments about the limitations of this assumption. The momentum equation of ice transport is integrated along the movement of ice parcel based on this assumption, and the ice mass of the new time step is obtained.

Because of the above assumptions, the mechanical interaction among ice elements is not considered. Some difficulties may be encountered when considering the mechanical process in the two-dimensional model. This is because most parameters contained in constitutive equations were derived based on one-dimensional analysis, experiments, and field observations and static conditions. Further observation or assumptions for constitutive equations of ice should be made in order to extend application for the two-dimensional dynamic transport of ice problem.

Shen and Chen (1992) developed a coupled two-dimensional numerical model for river ice dynamics and hydrodynamics for the purpose of studying the characteristics of ice movement, stoppage, and jamming in river reaches with complex geometries and flow patterns. For the hydrodynamics simulation, an Eulerian finite element technique is used due to its ability in treating irregular geometry of a river domain using triangle elements. A lumping scheme, which can save the computer memory storage and reduce the complexity of matrix calculation, is adopted. A Lagaragian discrete parcel scheme is used to simulate the transport of the movement of surface ice under the influence of dynamic forces. The discrete parcel method is chosen because of its flexibility in simulating

the complex ice processes which may not be completely described by a single set of governing equations. A graphics based method is applied to define the river boundary and detect where the parcel reaches the boundary.

To simulate the ice dynamics properly, they modified the two-dimensional constitutive laws of the internal ice stresses based on a nonlinear isotropic viscous model proposed by Hibler (1979, 1986), which was originally applied for sea ice movement. The model of Shen and Chen (1992) is applied to the Grass Island Pool of the upper Niagara River. Simulations of ice distribution inside Grass Island Pool with a prelocated ice island are compared with the aerial photos. Sensitivity analysis is presented to examine effects of various ice and flow parameters on ice conditions in the pool. Although the model is developed for the simulation of Grass Island Pool, the authors suggest it be used to analyze similar ice problems in other shallow water bodies.

The release and downriver movement of an ice jam often results in a phenomenon known as the "breaking front" which can be described as a moving sharp transition between relatively intact sheet ice cover and ice rubble. While there is an obvious association between jam releases and breaking fronts, the detailed mechanics of the phenomenon is not understood. Ferrick and co-workers (1985, 1989, and 1991) have studied the problem related to the interaction between a surge and the intact ice cover. This work is based on field observations performed during controlled flow releases from river dams, so as to break and clear the ice cover before the spring runoff arrives. They have used numerical modeling for unsteady flow conditions to interpret and assess the ice breaking potential of a surge.

The numerical works previously published have not addressed the

following aspects of the present problem: (1) the dynamic interactions between the moving ice blocks and the water flow during an ice jam release; (2) the transient variation of the surge immediately after the ice jam release; (3) the hydrodynamic conditions associated with ice jams at an equilibrium steady state conditions; (4) the dynamic interaction between moving ice floes at high concentrations; and (5) the variation in ice thickness due to mechanical, erosion and deposition processes.

It is evident from the foregoing that verification of the available jam release models involves only limited experimental results and case studies. Whichever the case may be, previous laboratory investigations and field studies include very little quantitative data such as water level profiles across the ice jams leading and trailing prior to release, post release stage hydrographs at various locations and surface velocity measurements after release.

CHAPTER 3.0

MATHEMATICAL FORMULATION

The mathematical basis of the numerical model used in this study is presented. The model has the capability of evaluating the quasi-steady hydrodynamic conditions of the flow before the release of the ice jam, the transient hydrodynamic and ice dynamic behaviour after release, and the dominant character of the upstream and downstream surge propagation and corresponding ice run.

3.1 Governing equations

The movement of surface ice depends on the flow regime, wind drag, gravity, interaction between the ice floes and their interaction with the boundaries. Conservation of mass and momentum for the top ice body and the bottom water body are integrated together in order to ensure overall conservation. In addition, conservation of ice mass, ice surface area, ice transport, constitutive, and ice strength-thickness equations comprise the mathematical basis of the model. A series of relations obtained from experimental studies defining unknown processes occuring before and after release are also incorported.

3.1.1 Governing hydrodynamic equations for water flow

The hydrodynamic equations for gradually varied flow have been well established. In the present study, a two-dimensional depth-integrated formulation is used such that the two-dimensional equations for free surface flows are generalized to include the effect of surface ice (Shen et al. 1992(.The two-dimensional unsteady, depth-averaged continuity and momentum equations that govern the flow regime and take into account ice jam effects are given as follows:

Continuity

$$\frac{\partial h}{\partial t} + \frac{\partial}{\partial x}(uh' + u_i C_i \pi_1 \theta) + \frac{\partial}{\partial y}(vh' + v_i C_i \pi_1 \theta) = 0 \qquad (3.1)$$

Momentum: x-direction

$$\frac{\partial}{\partial t}uh' + \frac{\partial}{\partial x}u^2h' + \frac{\partial}{\partial y}uvh' = (1 - C_i)\frac{\tau_{(wa)x}}{\rho} - C_i\frac{\tau_{(wi)x}}{\rho} + P_x \qquad (3.2)$$

Momentum: y-direction

$$\frac{\partial}{\partial t}vh' + \frac{\partial}{\partial x}uvh' + \frac{\partial}{\partial y}v^2h' = (1 - C_i)\frac{\tau_{(wa)y}}{\rho} - C_i\frac{\tau_{(wi)y}}{\rho} + P_y \qquad (3.3)$$

where

$$h' = h - \pi_1 C_i \theta \qquad (3.4)$$

where x is the longitudinal direction along the main channel flow; y is the transversal direction along the width of the channel; h is the depth of water up to the phreatic water surface; t is the time; u and v are the velocities in the x and y directions respectively; θ is the ice cover thickness; C_i is the surface area ice concentration; $\tau_{wi,x}$ and $\tau_{wi,y}$ are the shear stresses at the water-ice interface in the x and y directions respectively; $\tau_{wa,x}$ and $\tau_{wa,y}$ are the shear stresses at the water-air interface in the x and y directions repectively; π_1 is an empirical constant identifying the location of the water surface within the ice cover thickness; ρ is the density of water; and P_x and P_y are the water plus ice pressure force components resolved in the x and y directions.

The value of π_1 depends on whether the ice jam is stationary or in motion. If the jam is stationary, the value of π_1 is a function of its position from the leading edge of the ice jam. If the jam is in motion then the value of π_1 is taken as 0.92. At the water-air interface which is defined by the area where the water is exposed to the atmosphere (1 - C_i), the shear stress due to wind drag is expressed as follows, in the x and y directions respectively:

$$\tau_{(wa)x} = \rho_a C_d^{aw} U_{wind}^2 \cos\alpha_w \tag{3.5}$$

$$\tau_{(wa)x} = \rho_a C_d^{aw} U_{wind}^2 \sin\alpha_w \tag{3.6}$$

where, ρ_a is the air density, C_d^{aw} is the wind stress coefficient at the air-water interface, U_{wind} is the wind velocity at 10m above the water surface and α_w is the angle between the wind direction and the x-axis. The shear stress at the water-ice interface is given by the following expression in the x and y directions respectively:

$$\tau_{(wi)x} = \rho C_d^{wi} \sqrt{(u-u_i)^2 + (v-v_i)^2}\,(u-u_i) \tag{3.7}$$

$$\tau_{(wi)y} = \rho C_d^{wi} \sqrt{(u-u_i)^2 + (v-v_i)^2}\,(v-v_i) \tag{3.8}$$

where, C_d^{wi} is the water drag coefficient on the ice underside.

3.1.2 Development of ice pressure terms

The ice pressure force components acting on the main flow can be determined by considering the illustration presented in figure 3.1. Three zones can be identified from figure 3.1, where the water undergoes major changes in its flow regime. Upstream of the leading edge of the ice jam the water flows under free surface conditions. Towards the leading edge, the effect of the ice jam increases gradually. At the leading edge region, the water undergoes a transition from an unconfined to a confined flow regime. Underneath the ice jam, the water flow is subjected to additional resistance coming from the underside of the ice jam. Now, the flow conditions namely, the flow depth and velocity varies

towards the trailing edge proportionally to the change in the ice jam thickness. At the trailing edge, the water again undergoes a transition from a confined to an unconfined flow regime, and the resistance of the ice jam thickness which was at a maximum at the trailing edge is suddenly lifted. Therefore, the flow is expected to sharply increase in depth and decrease in velocity.

The transition of the flow regime as it passes across an ice jam should be adequately described in the governing flow equations. Therefore, it is necessary to formulate the influence of the ice jam conditions on the channel flow. The ice and pressure force including the water up to point π_1 in the ice jam can be obtained as follows by considering figure 3.2:

$$F_A = \rho_w \pi_1 g \theta_4 h'_4 \tag{3.9}$$

$$F_B = \frac{1}{2} \rho_w \pi_1 g h'^2_4 \tag{3.10}$$

$$F_C = \rho_w \pi_1 g \theta_5 h'_5 \tag{3.11}$$

$$F_D = \frac{1}{2} \rho_w \pi_1 g h'^2_5 \tag{3.12}$$

The horizontal component of the gravity force and that of the resisting force due to the channel bed slope and that of the underside of the ice cover respectively can be expressed as follows:

$$F_{bot} = \rho_w g \, (h' + \pi_1 \theta)_{ave} (z_4 - z_5) \tag{3.13}$$

$$F_w = \rho_w g \pi_1 \theta_{ave} [\, (z_4 + h'_4) - (z_5 + h'_5) \,] \tag{3.14}$$

where z_i is the elevation of river bottom from datum at section i; F_A is the

hydrostatic force represented by rectangle bcde; F_B is the hydrostatic force represented by triangle def; F_C is the hydrostatic force represented by rectangle b'c'd'e'; F_D is the hydrostatic force represented by triangle d'e'f'; F_{bot} is the pressure force due to gravity acting on the element of water; and F_w is the pressure force due to the slope of the ice cover underside acting on the element of water.

By considering these forces, the gradient of the following components describing the conditions dominating the change in the flow regime across an ice jam element should be included in the governing water flow equations:

in the x-direction

$$P_x = g\frac{\partial}{\partial x}(\frac{1}{2}h'^2 + \pi_1\theta h') - g\,(h' + \pi_1\theta)_{ave}S_{fx} + g\pi_1\theta_{ave}\frac{\partial}{\partial x}(z + h') \qquad (3.15)$$

in the y-direction

$$P_y = g\frac{\partial}{\partial y}(\frac{1}{2}h'^2 + \pi_1\theta h') - g\,(h' + \pi_1\theta)_{ave}S_{fy} + g\pi_1\theta_{ave}\frac{\partial}{\partial y}(z + h') \qquad (3.16)$$

$$S_{fx} = \frac{n_b^2 u\sqrt{u^2 + v^2}}{R^{4/3}} \qquad (3.17)$$

$$S_{fy} = \frac{n_b^2 v\sqrt{u^2 + v^2}}{R^{4/3}} \qquad (3.18)$$

and n_b is the Manning coefficient of the river bed.

3.1.3 *Governing dynamic ice transport equations*

Considering the granular surface ice mass in the river as a contimuum, governing equations for ice transport, namely conservation of momentum, mass, and surface area concentration, can be obtained. For two dimensional analysis, the equations of motion for the surface ice can be derived from the force balance of an elemental area in the x and y directions as follows (Tsai et al. 1988, Shen and Chen 1992):

Momentum x-direction

$$M_i \frac{Du_i}{Dt} = R_x + F_{hx} + F_{ax} + F_{wx} \qquad (3.19)$$

Momentum y-direction

$$M_i \frac{Dv_i}{Dt} = R_y + F_{hy} + F_{ay} + F_{wy} \qquad (3.20)$$

where F_{ax} and F_{ay} are the wind drag forces in the x and y directions respectively; F_{wx} and F_{wy} are the water drag forces in the x and y directions given by equations 3.7 and 3.8 respectively; F_{hx} and F_{hy} are the components of the hydrostatic pressure forces acting on a parcel of ice in the x and y directions respectively; u_i and v_i are the ice velocities in the x and y directions respectively; and M_i is the ice mass per unit area equal to $\rho_i C_i \theta$;

$$\frac{D}{Dt} = \frac{\partial}{\partial t} + u_i \frac{\partial}{\partial x} + v_i \frac{\partial}{\partial y} \qquad (3.21)$$

and the internal ice resistance force in the x and y directions respectively are:

$$R_x = \frac{\partial}{\partial x}(\sigma_{xx} C_i \theta) + \frac{\partial}{\partial y}(\sigma_{yx} C_i \theta) \qquad (3.22)$$

$$R_y = \frac{\partial}{\partial x}(\sigma_{xy} C_i \theta) + \frac{\partial}{\partial y}(\sigma_{yy} C_i \theta) \qquad (3.23)$$

where, σ_{xx} , σ_{yy} are the normal stress components; and σ_{yx} , σ_{xy} are the shear stress components.

A proper constitutive law should be selected in order to detemine these stresses. The magnitude of the internal stress in the ice jam accumulation is sensitive to the ice concentration, and ice properties. Theoretical analysis carried out by Babic et al. 1990 revealed that the internal resistance is negligible for ice concentrations less than 0.7. Hibler 1986 observed similar tendencies during his sea ice studies. The hydrostatic pressure due to the water surface slope and the varying ice jam thickness is expressed as follows in the x and y directions respectively:

$$F_{hx} = M_i g \frac{\partial}{\partial x}(h + z_b) \qquad (3.24)$$

$$F_{hy} = M_i g \frac{\partial}{\partial y}(h + z_b) \qquad (3.25)$$

The wind drag acting on the top surface of the ice jam accumulation can be described by the following relation:

$$F_{ax} = C_i \rho_a C_d^{ai} |U_{wind}| U_{wx} \qquad (3.26)$$

$$F_{ay} = C_i \rho_a C_d^{ai} |U_{wind}| U_{wy} \qquad (3.27)$$

where ρ_a is the density of air; c_d^{ai} is the drag coefficient at the air-ice interface; U_{wx} and U_{wy} are the components of the wind velocity in the x and y directions respectively; and is the wind velocity 10 m above the water surfaceis:

$$|U_{wind}| = \sqrt{U_{wx}^2 + U_{wy}^2} \qquad (3.28)$$

Conservation of Ice Mass

The conservation of ice mass equation which describes the net ice mass transport into and out of a specified elemental area is expressed as:

$$\frac{\partial M_i}{\partial t} + \frac{\partial}{\partial x} u_i M_i + \frac{\partial}{\partial y} v_i M_i = 0 \qquad (3.29)$$

Considering that the surface area ice concentration should be constrained to a maximum value yet conserve the total ice mass, then added values of computed ice area concentration greater than a maximum specified should be converted to equivalent increases in the local ice thickness.

Conservation of Surface Area Ice Concentration

The conservation of ice mass per unit area is evaluated using the ice surface area concentration. Therefore, another equation describing the conservation of surface area ice concentration is introduced and expressed as follows:

$$\frac{\partial C_i}{\partial t} + \frac{\partial}{\partial x} u_i C_i + \frac{\partial}{\partial y} v_i C_i = 0 \qquad (3.30)$$

The ice concentration is limited by a maximum value C_{imax}. When this limit is reached, the ice thickness is no longer equal to the single layer thickness and begins to increase due to mechanical thickening. Therefore if $C_i > C_{imax}$, the ice mass and corresponding accumulated ice thickness are calulated as follows:

$$C_i = C_{imax} \qquad (3.31)$$

$$\theta = \frac{M_i}{\rho_i C_{imax}} \qquad (3.32)$$

The equation of motion of ice described above is obviously not enough to describe the actual physical phenomena that occurs during ice jam formation and release. This is because the stress state of an ice element namely σ_{xx}, σ_{xy}, and σ_{yy}, are not specified. Additional constitutive equations are required.

Constitutive Relations

The interaction between ice particles at low ice concentration is not significant. Shen et al. 1991, suggested that when ice concentration is less than 70% of the maximum packing of ice concentration, the internal resistance among the ice particles is negligible, and the ice floes can be considered as drifting freely with the flow of water. Immediately after the release of an ice jam, the surface ice concentration is at its maximum and interaction between the ice floes does occur. Therefore, the internal resistance due to interaction of the ice pieces are to be accounted for in the ice transport equations.

Pariset and Hausser 1966, proposed constitutive relationships for static ice jams. Shen et al. 1990 modified these constitutive relationships by introducing a ratio between ice concentration and maximum packing ice concentration. Shen and Chen 1992, used a viscous-plastic model based on the formulation proposed by Hibler 1978 used for the simulation of sea ice interaction. The present study adopts the same model for river ice transport, however it is applied to the release of ice jams.

For modeling the interaction between the ice floes, the ice pack is considered to follow a non-linear viscous compressible behaviour, obeying the following constitutive law (Hibler 1978):

$$\sigma_{xx} = 2\eta\frac{\partial u_i}{\partial x} + (\zeta - \eta)\left(\frac{\partial u_i}{\partial x} + \frac{\partial v_i}{\partial y}\right) - \frac{P}{2} \qquad (3.33)$$

$$\sigma_{yy} = 2\eta\frac{\partial v_i}{\partial y} + (\zeta - \eta)\left(\frac{\partial u_i}{\partial x} + \frac{\partial v_i}{\partial y}\right) - \frac{P}{2} \qquad (3.34)$$

$$\sigma_{xy} = \sigma_{yx} = \eta\left(\frac{\partial v_i}{\partial x} + \frac{\partial u_i}{\partial y}\right) \qquad (3.35)$$

where σ_{xx} and σ_{yy} are the normal stresses in the x and y directions respectively; σ_{xy} and σ_{yx} are the shear stresses; P/2 is the pressure term; and ζ and η are non-linear bulk and shear viscosities given by:

$$\zeta = \frac{P}{2\Delta} \qquad (3.36)$$

$$\eta = \frac{\zeta}{e^2} \qquad (3.37)$$

$$\Delta = \sqrt{\left(\frac{\partial u_i}{\partial x} + \frac{\partial v_i}{\partial y}\right)^2 + \frac{\left(\frac{\partial u_i}{\partial x} + \frac{\partial v_i}{\partial y}\right)^2 + \left(\frac{\partial v_i}{\partial x} + \frac{\partial u_i}{\partial y}\right)^2}{2e}} \qquad (3.38)$$

where e = ratio of principle axes of the ellipse taken as 2.

For very small or zero velocity gradients, the viscosities will become very large. For computational efficiency, it is necessary to limit the viscosity to a certain maximum value ζ_{max}. In the present study ζ_{max} is set ot be 10^8 kg/s.

Ice Strength-Thickness Relations

Coupling of the ice dynamics equations with the ice thickness characteristics is necessary in order to account for the dynamic ice interaction effects as the ice becomes thicker and/or contains a lower concentration of ice pieces. The ice pressure term P is evaluated by the following expression:

$$P = Tan^2\left(\frac{\pi}{4} \pm \frac{\phi}{2}\right)\left(1 - \frac{\rho_i}{\rho_w}\right)\frac{\rho_i g \theta}{2}\left(\frac{C_i}{C_{imax}}\right)^j \qquad (3.39)$$

where ϕ is the angle of internal friction of surface ice; and j is an empirical constant. The "+" and "-" signs in the equation are for passive and active states of ice flow respectively.

The transport characteristics of an ice accumulation are determined by the balance of the external forces and the internal ice resistance. Therefore, the strength of the ice accumulation plays an important role when the ice concentration is relatively large. Shen and Chen 1992 carried out a sensitivity

analysis of the parameters affecting the strength of ice. These parameters are the internal angle of friction, the ice concentration and the power j found in equation 3.39.

3.2 Numerical Modeling

The numerical solution of hydrodynamic equations and ice transport equations is obtained by using an explicit finite difference method based on the MacCormack time splitting scheme (MacCormack 1969) if proper initial and boundary conditions are applied. Fennema and Chaudhry 1986, and Garcia and Kahawita 1986 have applied this scheme to unsteady flow simulations and obtained satisfactory results. The MacCormack scheme is an explicit, two-step predictor corrector scheme which is second-order accurate in space and time and is capable of capturing the shock waves without isolating them.

3.2.1 The Modified MacCormack scheme

In this study a modified version of the explicit MacCormack finite difference scheme is used (Baldwin et al. 1975). The scheme employs a fractional time step method involving the division of a two-dimensional finite difference operator into a sequence of one-dimensional operators in the x and y directions. Each operator is further split into a predictor-corrector sequence which allows for second order accuracy in space and time. Forward finite-differences are used for approximating the spatial partial differential terms in the predictor part and backward finite-differences using the predicted variables are used in the corrector part.

The modified version of the MacCormack scheme uses a symmetric sequence of predictor-corrector operators grouped as (L_x L_y L'_y L'_x) where no preferred alignment in the flow direction of the scheme is necessary (Garcia 1985). The two dimensional finite difference operator L(Δt) is split into a sequence of one-dimensional operators as follows:

$$L(\Delta t) = L_{x1}(\Delta t_{x1})\, L_{x2}(\Delta t_{x2})\, L'_{x2}(\Delta t_{x2})\, L'_{x1}(\Delta t_{x1}) \qquad (3.40)$$

In this study, an orthogonal finite difference grid is overlain on the channel geometry. Figure 3.3 shows the grid configuration. Subscripts of i indicate points in the x-direction and subscripts of j indicate points inthe y direction. The usual finite difference notation of superscript n to denote present time step and n+1 to denote next time step is employed. Referring to the finite-difference grid shown in figure 3.3, the finite difference approximations are:

Predictor Step:

$$\frac{\partial \phi}{\partial t} = \frac{\phi^p_{i,j} - \phi^n_{i,j}}{\Delta t} \qquad (3.41)$$

$$\frac{\partial \phi}{\partial x} = \frac{\phi^n_{i+1,j} - \phi^n_{i,j}}{\Delta x} \qquad (3.42)$$

$$\frac{\partial \phi}{\partial y} = \frac{\phi^n_{i,j+1} - \phi^n_{i,j}}{\Delta y} \qquad (3.43)$$

Corrector Step:

$$\frac{\partial \phi}{\partial t} = \frac{\phi^c_{i,j} - \phi^p_{i,j}}{\Delta t} \qquad (3.44)$$

$$\frac{\partial \phi}{\partial x} = \frac{\phi^p_{i,j} - \phi^p_{i-1,j}}{\Delta x} \qquad (3.45)$$

$$\frac{\partial \phi}{\partial y} = \frac{\phi^p_{i,j} - \phi^p_{i,j-1}}{\Delta y} \qquad (3.46)$$

where ϕ represents any variable of which the partial differential is approximated by the finite difference; and superscripts p and c refer to the predicted value and the value of the variable after the corrector step respectively. The value of ϕ at the unknown time level 'n+1' is given by:

$$\phi^{n+1}_{i,j} = \frac{1}{2}(\phi^n_{i,j} + \phi^c_{i,j}) \qquad (3.47)$$

It is possible to use backward finite-differences in the predictor part and forward finite-differences in the corrector part. Also, the direction of differencing may be alternated from one time step to the next. All three alternatives gave similar results for the steady state solution considered in the study carried out by Bhallamudi and Chaudhry 1992. (Details to the discretized governing equations using the MacCormack scheme are given in Appendix A)

3.2.2 The Upwind scheme

Simulation of single layer ice floes transport was carried out using the modified MacCormack scheme without difficulties. However, when an attempt was made to simulate the release of ice jams, the use of the modified MacCormack scheme rendered unreasonable results and in many cases was unstable. All the difficulties were around the leading and trailing edges of the ice jam. Imposing boundary conditions at the leading and trailing edges for variables

other that the normal and shear stresses is practically impossible due to the dynamic behaviour of the ice mass in those regions. The large water surface and velocity gradients at the trailing edge of the jam as well as the negative surge developing immediately after release accentuates the computational problem. These computational difficulties rise from the forward and backward differencing used in the MacCormack scheme, which are not appropriate for the leading and trailing edges of the ice jam. From a computational point of view, the conservation of ice mass and surface area concentration need not be solved using the MacCormack scheme since four iterations are required to advance one time step.

Based on the latter discussion, the upwind scheme was used for the conservation of ice mass and ice concentration equations. The upwind scheme falls under the classification of central difference schemes. In cases where convection dominates, the use of the MacCormack scheme may result in unstable solutions. The upwind scheme is an explicit forward time method which takes into account the direction of the convection velocity. The discretization of the two-dimensional ice mass or ice concentration conservation equations is given by:

$$\psi_{i,j}^{n+1} = \psi_{i,j}^{n} - \Delta t \left(\frac{\partial}{\partial x} u_i \psi + \frac{\partial}{\partial y} v_i \psi\right) \qquad (3.48)$$

where y is either the ice mass or surface area ice concentration, and Δt in the simulation time increment. This equation is solved using a one-step approach for x and y derivatives. Backward and forward differences are used when the velocities are positive and negative respectively. Thus the difference is always on the "upwind" or "upstream" side of the point at which $\frac{\partial \psi}{\partial t}$ is evaluated. The convection terms are calculated using the following formulas:

for u_i (i+(1/2),j) > 0

$$\frac{\partial}{\partial x}u_i\psi = \frac{u_i(i+\frac{1}{2},j)\,\psi(i,j) - u_i(i-\frac{1}{2},j)\,\psi(i-1,j)}{\Delta x} \qquad (3.49)$$

for u_i (i+(1/2),j) < 0

$$\frac{\partial}{\partial x}u_i\psi = \frac{u_i(i+\frac{1}{2},j)\,\psi(i+1,j) - u_i(i-\frac{1}{2},j)\,\psi(i,j)}{\Delta x} \qquad (3.50)$$

$$u_i(i+\frac{1}{2},j) = \frac{u_i(i,j) + u_i(i+1,j)}{2} \qquad (3.51)$$

$$u_i(i-\frac{1}{2},j) = \frac{u_i(i-1,j) + u_i(i,j)}{2} \qquad (3.52)$$

In the case of velocity reversal or converging velocities within a cell, a combination of the formulas is used (Roach 1976). A similar derivation is employed for derivatives in the y-direction.

3.2.3 Initial and boundary conditions

To start the unsteady computations, the values of seven primary variables, u, v, h, u_i, v_i, θ and C_i at time t=0 need to be specified at all the grid points. The specification of their approximate values is sufficient in cases where computations are continued till the solution converges to a steady state. If the information is not available, the model needs to begin with assumed initial conditions. For the stresses in the constitutive relations, it is assumed that an ice jam accumulation has already been initiated, and that upstream and downstream of the ice cover are open water. Initially, the thickness and concentration of the ice jam are

known or assumed. The velocity of the ice jam is taken as zero before release. Initially the normal and shear stresses in the x and y directions are assumed to be equal everywhere.

Inclusion of boundaries is an important aspect of the numerical models for hyperbolic systems since errors introduced at a boundary propagate throughout the computational domain and may lead to instabilities (Anderson et al. 1984). The following types of boundaries need to be included: (i) inflows, (ii) outflows, (iii) solid surfaces.

Inflow and outflow boundaries are open boundaries where flow can enter or leave the computational domain. The specification of boundary conditions depends on whether the flow is subcritical or supercritical (Stoker 1957 and Verbroom et al. 1982). For two-dimensional supercritical flows, three boundary conditions have to be specified at the inflow boundary and none at the outflow boundary. For two-dimensional subcritical flow, however two conditions are specified at the inflow boundary and one at the outflow boundary.

Since the governing equations do not consider shear stresses other than the bottom stress, slip condition is the proper boundary condition at a solid surface. Roach 1972 and Anderson et al. 1984 discussed several wall boundary techniques in gas-dynamics applications. Jimenez 1987 tested several techniques for the case of steady supercritical flow. The reflection procedure seems to be more suitable than the other techniques for the envelope of the present research work.

This procedure for the solid side walls is only approximate and is not exact. Referring to figure 3.4, the estimation of the boundary conditions at solid surfaces such as the river banks using the method of reflection requires the specification of

fictitious points outside the computational grid system. The normal gradient of the velocity parallel to the solid wall is set to zero, such that the velocity normal to the wall is set equal to the magnitude of the velocity of the inside cell, but opposite in direction as shown in figure 3.5.

Ice conditions on solid surfaces such as the river banks need to be treated. They are specified in the same fashion as those of the hydrodynamic conditions. The normal velocity component of imaginary ice is assumed to have the same magnitude but in the opposite direction. The tangential component of imaginary ice velocity is the same as the real one, since slip conditions have been considered in this study. Similarly, the value of the water level, bottom elevation, and hydraulic radius, ice mass, surface area ice concentration, and ice thickness at the imaginary nodes are taken equal to the value of the corresponding variable at the interior node. The compressive internal stresses of ice are treated in a similar fashion.

As an ice elements is moving along a solid surface the boundary friction needs to be included in the force balance describing the ice dynamics. The frictional force term should be added to the equation of motion. A dynamic Mohr-Coulomb yield criterion (Hanes and Inman 1985, Shen and Chen 1992) can be applied as follows:

$$F_f = F_c + F_N \tan\phi_b \qquad (3.53)$$

where F_f is the friction force between ice and solid boundary in tangential direction along the boundary; F_c is the ice cohesive force which taken as zero in this study; F_N is the normal component of the summation of internal resistance stress, water drag force and gravitational/pressure force, ΣF_{act}; $\tan\phi_b$ is the dynamic friction coefficient; and ϕ_b is the dynamic internal friction angle.

For ice moving along the solid boundary, the force acting on the ice can be decomposed into tangential and normal forces ΣF_{actT} and ΣF_{actN}, respectively. The movement of ice is actually the balance of tangential action and friction force calculated from the normal force, $F_N = \Sigma F_{actN}$. The direction of the friction force is opposite to the tangential velocity of the ice. The friction exist only when the normal action force pushes parcels against the boundary.

In the case where the jam leading and trailing edges are well defined, the normal stresses at the upstream and downstream edges of the ice cover are set equal to zero.

3.2.4 Stability criterion

A stability analysis was carried out for the system of equations considered in the present study). The Neumann analysis was used to evaluate the stability for a single equation as well as for a system of equations. Also, the analysis was performed for two cases: coupled and uncoupled hydrodynamics and ice dynamics equations (Raafat et al. 1994).

Coupled water and ice flow equations

For the coupled hydrodynamic and ice dynamic equations, the maximum Courant number that could be used is:

$$Cr_j \leq \frac{1}{1 + \kappa Fr_j + \sqrt{\frac{C_i S_i \theta}{h}}} \qquad (3.54)$$

$$Cr_j = u\frac{\Delta t}{\Delta x_j} \qquad (3.55)$$

$$\kappa = max(1; \frac{|u_i|}{u}) \tag{3.56}$$

$$Fr_j = \frac{u_j}{\sqrt{gh}} \tag{3.57}$$

where j = 1, and 2 indicates x and y directions respectively.

Equation 3.58 showns that the courant number is a function of three primary variables namely, the ice concentration, the ice accumulation thickness to flow depth ratio, and the Froude number. An increase of any of these three primary variables results in a lower courant number to ensure stability. Note that the stability analysis does not include the effect of boundary conditions. Also, the friction terms are neglected.

Uncoupled water and ice flow equations

In some application the hydrodynamic and ice dynamic equations are not coupled (e.g. Bjedov 1991), then the stability criterion for the hydrodynamic equations are:

$$Cr_j \leq \frac{1}{1 + \kappa Fr_j} \tag{3.58}$$

and the stability criterion for ice equations is:

$$Cri_j \leq 1 \tag{3.59}$$

$$Cri_j = ui_j \frac{\Delta t}{\Delta x} \tag{3.60}$$

(Details to the stability analysis are presented in Appendix B)

3.2 Advantages and disadvantages

The numerical model presented in this chapter is capable of simulating many processes involved during an ice jam release event. The advantages of the numerical model are as follows: (1) The model can predict the influence of a stationary ice jam on the water levels upstream and downstream of the ice jam and along its length; (2) The model can predict the transport characteristics of ice floes moving downstream with the main channel water flow; (3) The model can simulate the formation of surges immediately after release; (4) The model can simulate the development and propagation of surges immediately after release, (5) The model can simulate the transient ice run characteristics after release; (6) The model can simulate the redistribution of ice jam trailing edge thickness immediately after release; (7) The governing water and ice dynamic equations are fully coupled; (8) The model is stable and robust; (9) The model is a two layer model where two sets of governing equations are solved, namely the ice dynamics and hydrodynamic equations, such that not only the characteristics of water but that of the ice on top are calculated; and (10) The model can simulate stationary ice covers as well as moving ice floes.

The disadvantages of the model are: (1) It can only simulate one ice jam at a time; (2) The model is not tested and formulated to simulated reflected waves; (3) The model cannot simulate an ice jam release event with a stationary ice cover downstream; and (4) The model is not optimized from a computational point of view.

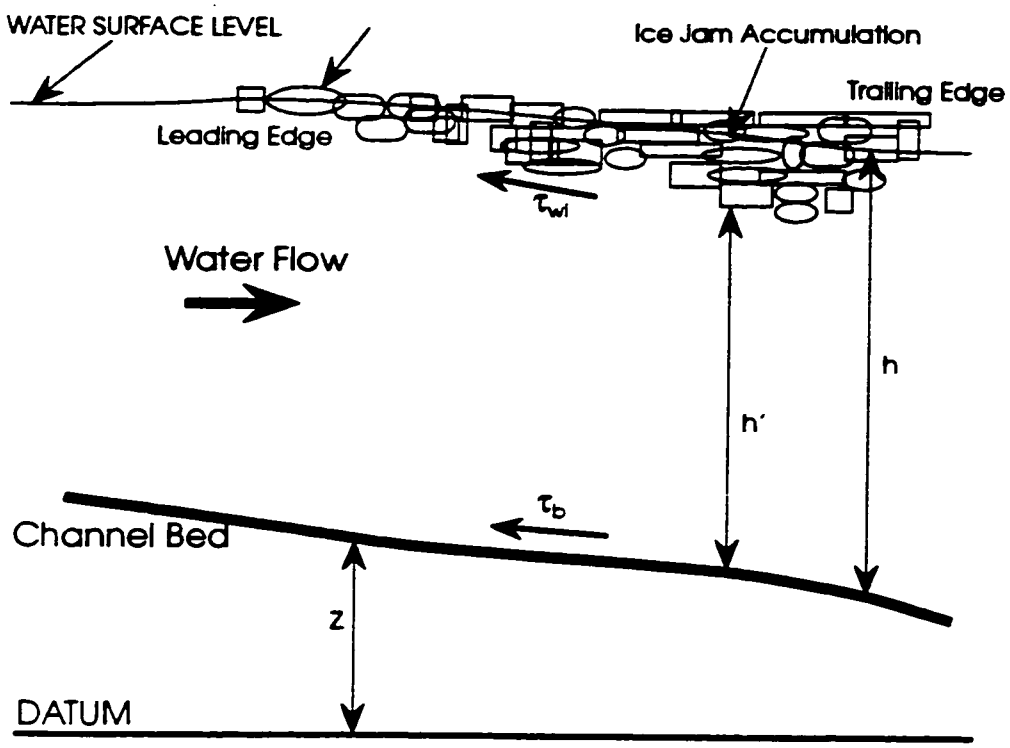

Figure 3.1: Definition sketch for water and ice flow.

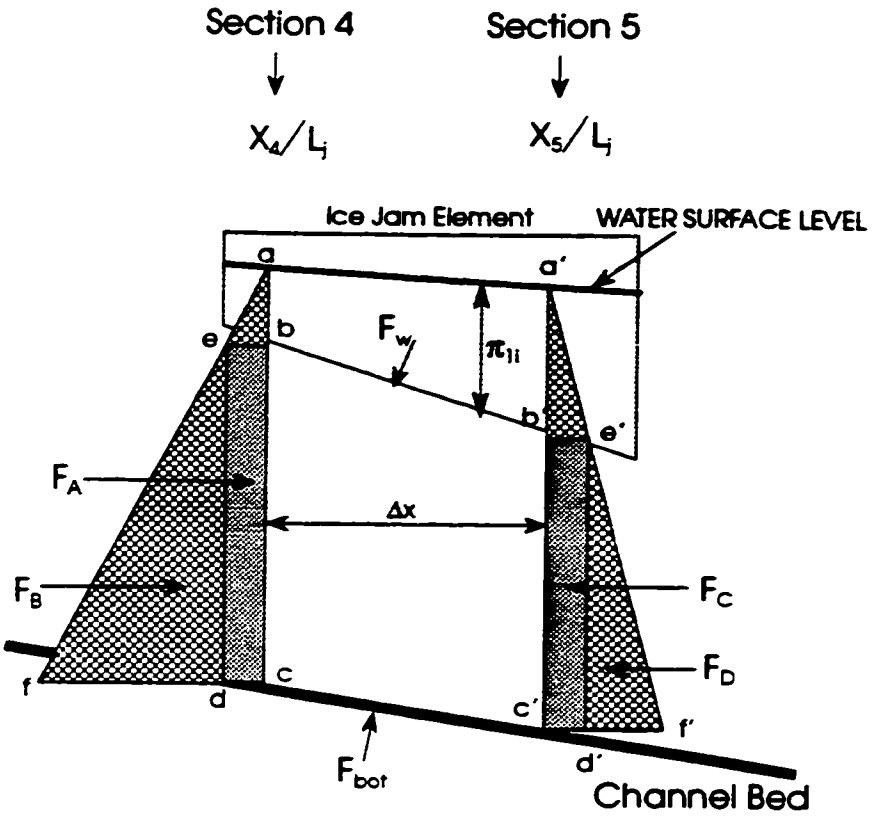

Figure 3.2: Forces acting on an element of water and ice.

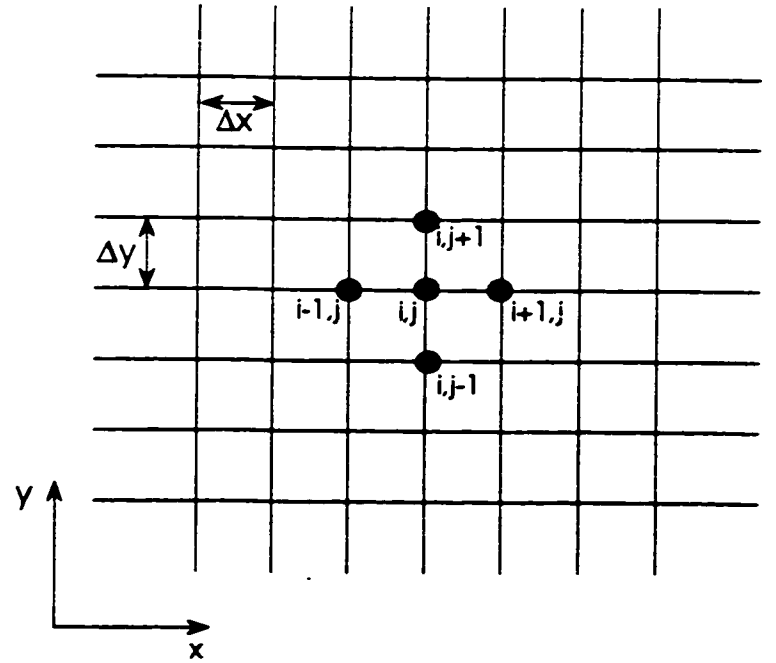

Figure 3.3: Finite difference grid.

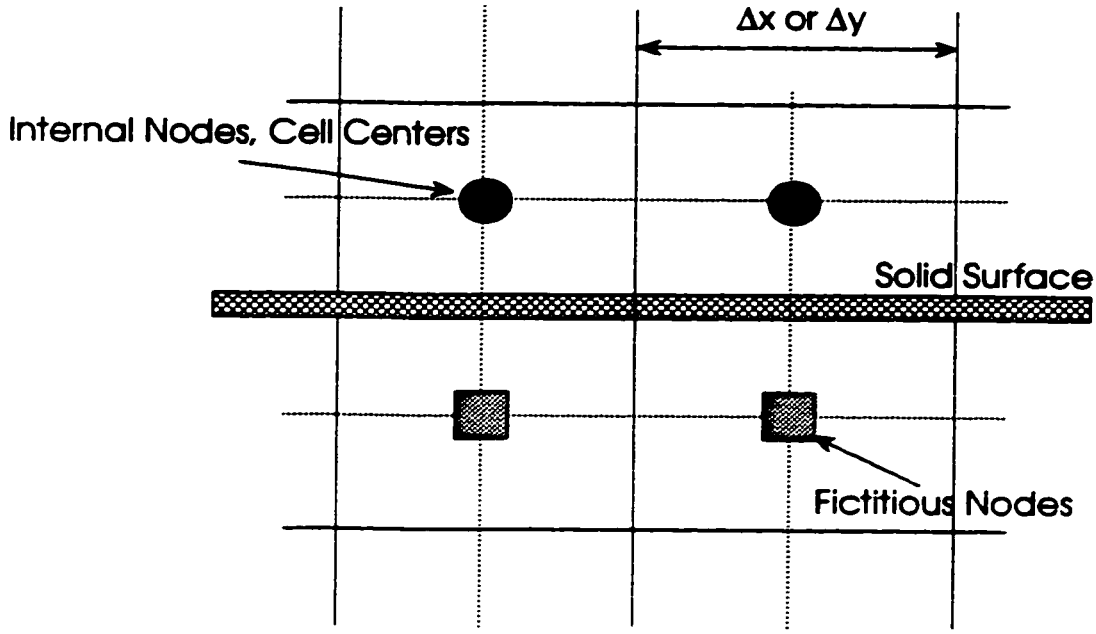

Figure 3.4: Method of reflection at solid surface.

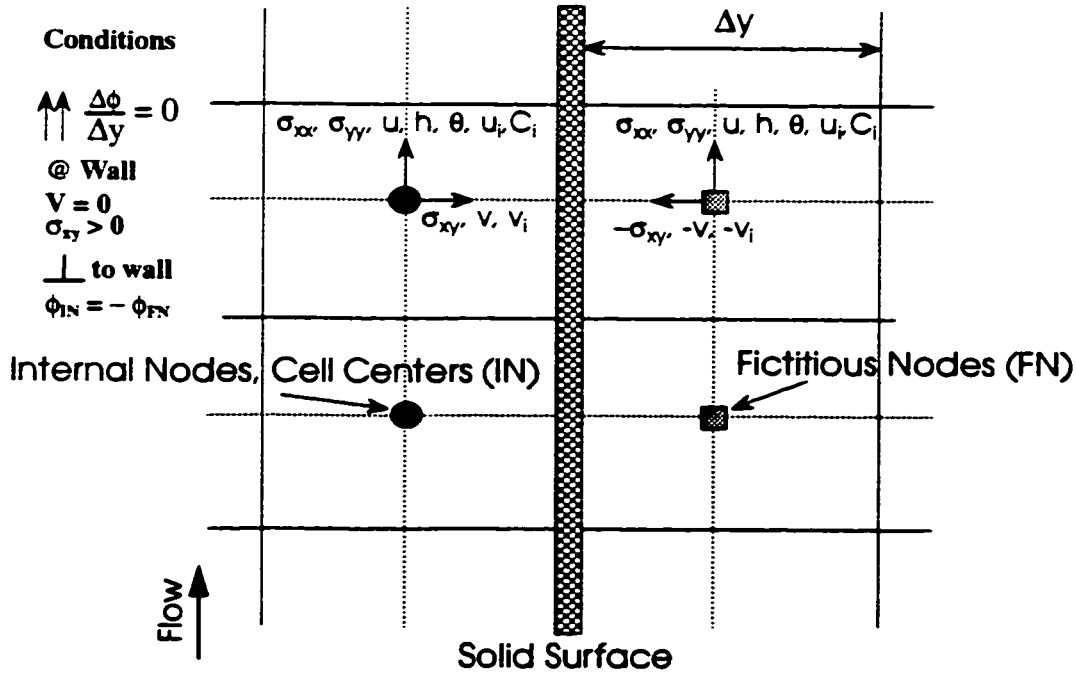

Figure 3.5: Solid wall boundary conditions.

CHAPTER 4.0

EXPERIMENTAL INVESTIGATIONS

The experimental investigation of breakup ice jams immediately before release is crucial for the understanding of the ice jam behavior and the hydrodynamic characteristics after the release. This is true because the conditions prevailing at the instant before the release event constitute the initial conditions for the release of the ice jam which dictate the dominant character of the development and propagation of the resulting surges and corresponding ice runs.

Therefore, an experimental study has been carried out to investigate the water surface levels throughout a rectangular channel just before the release of an ice jam.

The breakup ice jam considered in this research work is that which gives a significant drop in the water level across its leading and trailing edges. This type of ice jam differs from others such as a hanging dam in the sense that it presents more severe conditions before and even after its release. As previously mentioned, only two laboratory experiments were carried out (Henderson and Gerard 1981 and Wong et al. 1985) in earlier studies for the investigation of conditions caused by the release of such breakup ice jams.

The experimental program consisted of two major phases where the first phase is what is usually referred to as "dirty experimentation". In this phase the major objective of the experiments was to explore the possibilities of developing an ice jam which gives a significant drop in the water level across its leading and trailing edges. The second phase entailed the use of the knowledge obtained from the first phase in order to form various ice jams and consequently carry out the experiments for the investigation of the processes occuring during an ice jam release event.

A total of twenty five experiments were carried out. Twelve of these experiments were retained for analysis. The others were rejected because of the sudden failure of the ice jam.

The weakness in the state-of-the-art of ice jams and the scarcity of data make experimental investigation all the more necessary. An preliminary experimental program has been conceptualized with the following objectives in mind: a) Identify the conditions by which an ice jam would give a significant drop in water surface elevation, b) Develop a procedure that would ensure the required ice jam, c) Improve the understanding of ice jams before and after their release and of ice mass flow in general, d) Carry out experiments that accompany the development of a numerical model such that individual

processes are isolated and tested in the laboratory, and e) Perform experiments whose measurements would be used for comparison with the numerical models computations.

4.1 Setup

The experiments were carried out in a rectangular flume 30cm in width and 750cm in length with a horizontal slope, as shown in figure 5.1 and photos 4.1 and 4.2. They illustrate the plan and cross section views of the flume respectively. The experiments were conducted using three different sizes of polyethylene pieces and four different sizes of wood pieces as presented in table 4.1 and shown in photos 4.3 and 4.4. The polyethylene pieces have a specific gravity of approximately 0.92 while the specific gravity of the wood pieces were measured to vary as follows: Painted Pine 0.4-0.59; Pine (not painted) 0.41-0.72; Plywood 0.51-0.75; and Hardwood 0.64-0.87.

Table 4.1: Characteristics of different materials to simulate ice floes.

Type	Length (cm)	Width (cm)	Thickness (cm)	Specific Gravity
Polyethylene Pellets (Cylindrical in shape)	0.45 (Diameter)	-	0.35	0.918
Polyethylene	1.6	1.6	0.2	0.918
Polyethylene	2.0	2.0	0.6	0.918
Triangular Wood (small)	2.0-3.5	2.0-3.5	1.5-2.0	-
Triangular Wood (medium)	4.5-6.0	4.0-6.0	1.5-2.3	-
Triangular Wood (large)	3.5-5.5	2.5-5.0	2.5-4.0	-
Rectangular Wood	2.8-5.0	2.2-3.8	0.6-2.5	-

Polyethylene and wood pieces to simulate ice floes of various sizes were

stored in a trapezoidal container which was mounted on a shaft. These polyethylene pieces were introduced on the water surface at the upstream end of the model. The ice feeding system offers enough flexibility to vary the discharge in time. Polyethylene pieces were recovered in a wire basket and recirculated to the upstream end of the model.

The ice feeder specifically designed to feed the ice pieces from the upstream end of the flume consisted of a hopper trapezoidal in cross section and rectangular in plan (figure 4.2 and photos 4.5 and 4.6). The length of the hopper was 90cm with a top width of 25cm and bottom width of 8.5cm. A shaft was placed at the bottom along the length of the container such that when turned, the ice pieces were pushed by the shaft blades towards the end of the container where the container outlet was located.

Having an internal diameter of approximately 2.7cm and an external diameter of approximately 8.5cm, a complete shaft revolution discharged approximately 500 cm^3. This value is the average between computed and measured ice discharge. The shaft could be driven either manually or by a variable speed motor producing the ice discharge required. Ice pieces were loaded manually into the container and when discharged fell onto an inclined wooden plate which was installed to avoid splashing and significantly disturb the flow by letting free-falling pieces hit the water surface.

To insure the formation of an ice cover in the flume, a polyethylene plate was installed a certain distance downstream of the inlet, such that it was restrained from moving in the horizontal direction along with the flow while at the same time allowed to move in the vertical direction with the variation in the water surface, thanks to the use of guides.

4.2 Test Procedure

Polyethylene or wood pieces to simulate ice floes of various sizes were introduced on the water surface at the upstream end of the flume. As stated earlier, polyethylene pieces were recovered in a wire basket and recirculated to the upstream end of the flume during an experimental test run whenever found necessary.

In order to ensure the formation of an ice jam lodged in place and giving a significant drop in the water level across the leading and trailing edges, the following procedure was developed and given as follows:

1. Impose a certain water discharge in the flume.

2. Adjust the downstream gate to obtain the required initial water depth and velocities in the flume. Velocities should be sufficiently low in order to allow the upstream progression of the ice cover through juxtaposition.

3. place a polyethylene plate in its guides and let local conditions stabilize.

4. Begin the feeding of ice pieces (polyethylene or wooden blocks of various dimensions and/or polyethylene beads) at the upstream region (inlet of the flume).

   At this point, the ice pieces drift downstream with the flow. Their passage is arrested by the polyethylene plate which is located a short distance downstream of the inlet. This polyethylene plate represents a stationary ice cover. The plate is allowed to move freely along the depth and restrained from moving in the x or y directions. Keeping a constant rate of ice inflow, the ice cover is then allowed to progress upstream through the process of juxtaposition,

5. If the leading edge of the ice cover stops from progressing upstream, then stability conditions at the leading edge of the ice cover would have been surpassed and any incoming ice floes will be submerged and deposited

downstream underneath the ice jam. This requires raising of the gate in order to increase the depth in the flume and reduce velocities. Raising the gate slightly will allow the continuing of the leading edge upstream progression. When the ice cover leading edge reaches the inlet of the channel, then feeding of ice floes should be stopped.

6. Allow for steady conditions to be attained.

7. After steady conditions are attained, the downstream gate is slightly lowered in small increments such that conditions are allowed to reach steady state between each increment.

8. By lowering the downstream gate gradually, local velocities are increased and downstream depths are dropped, thereby allowing the ice jam to form through the processes of erosion, shoving and telescoping.

9. Due to the thickening of the ice cover and the formation of the ice jam, the leading edge which was located at the inlet of the channel moves in the downstream direction. In order to allow for more realistic ice jam formation, more ice pieces are fed from the upstream end thereby increasing the volume of ice in the channel.

   Once the required ice jam profile is obtained, measurements of water surface and ice jam profiles and velocities are taken.

10. The latter measurements constitute the initial conditions influencing the character of the surges and ice transport after release. Having the video cameras recording, the ice jam release event is simulated by removing the polyethylene plate by hand as fast as possible.

4.3 Measurements

Typical measurements that were taken during the experimental test runs consist of: discharge measurements from a 30° V-notch weir; water surface level measurements by direct readings from the glass flume walls; velocity

measurements by low flow velocity meter; and complete set of observations by using video cameras. The velocity measurements were done through the use of a velocity meter (Streamflo Velocity Meter, SVM) shown in photo 4.7 and 4.8. The SVM is used to measure the velocity of very low flow rates of water. The SVM instrument has a miniature head which can be inserted across the ice jam without interrupting the ice jam thickness profile, and measured velocities as low as 2.5 cm/s.

The miniature measuring head comprises a five bladed PVC rotor mounted on a hard stainless steel spindle. An insulated gold wire contained within the tube terminates 0.1mm from the rotor blade tips. When the rotor is revolved by the movement of water, the passage of the rotor blades past the gold wire tip slightly varies the measurable impedance between the tip and the tube. This variation is used to modulate a 15 KHz carrier signal, generated within the indicating instrument which in turn is applied to the electronic detector circuits.

PLAN VIEW

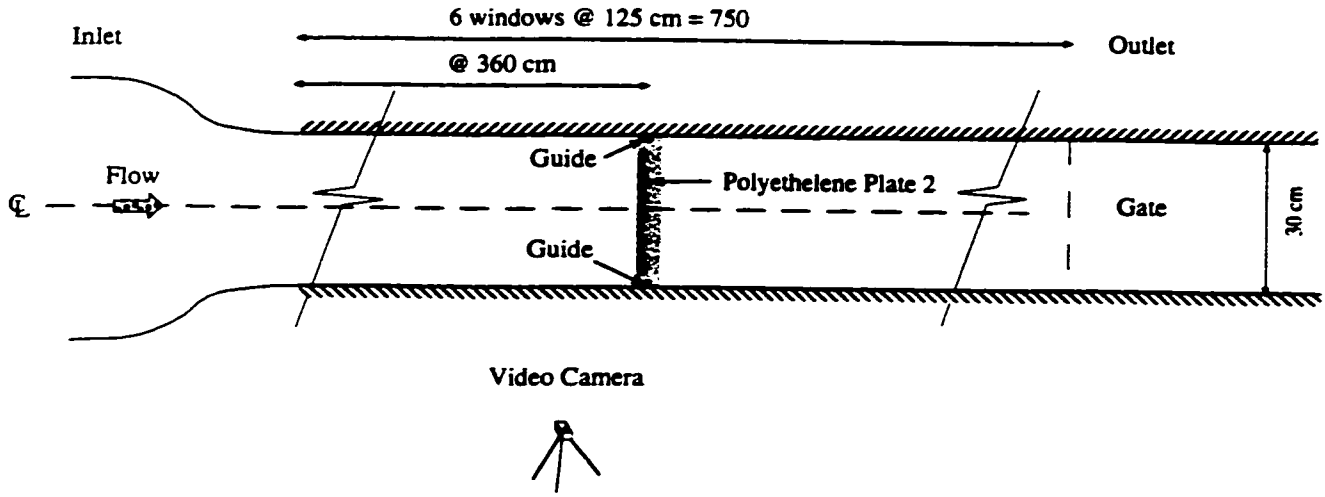

LONGITUDINAL CROSS SECTION VIEW

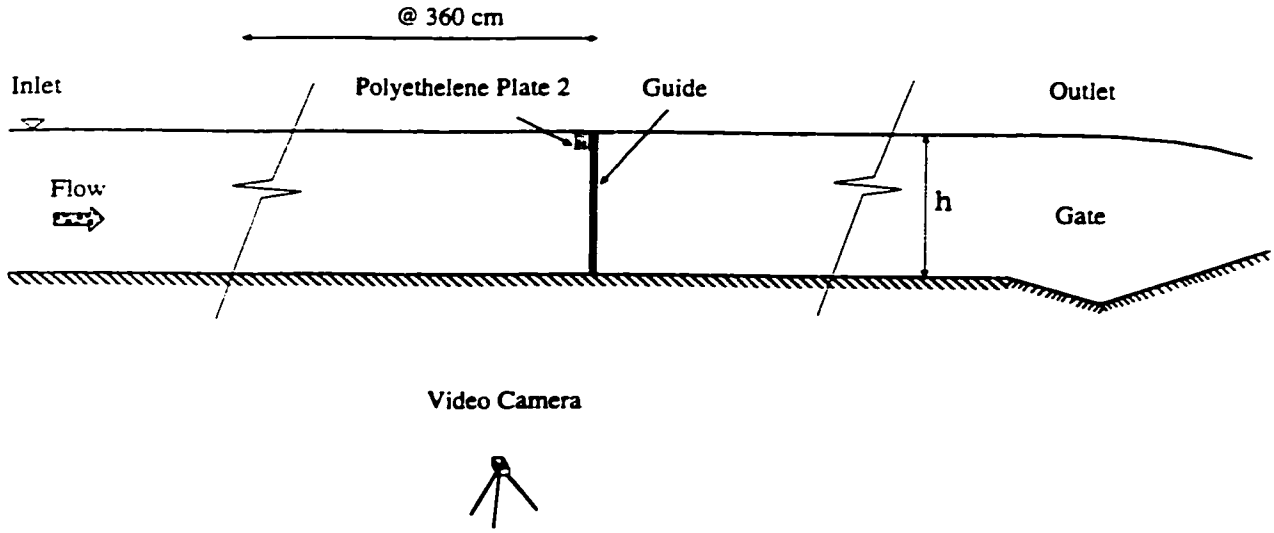

Figure 4.1: Illustration of flume set-up

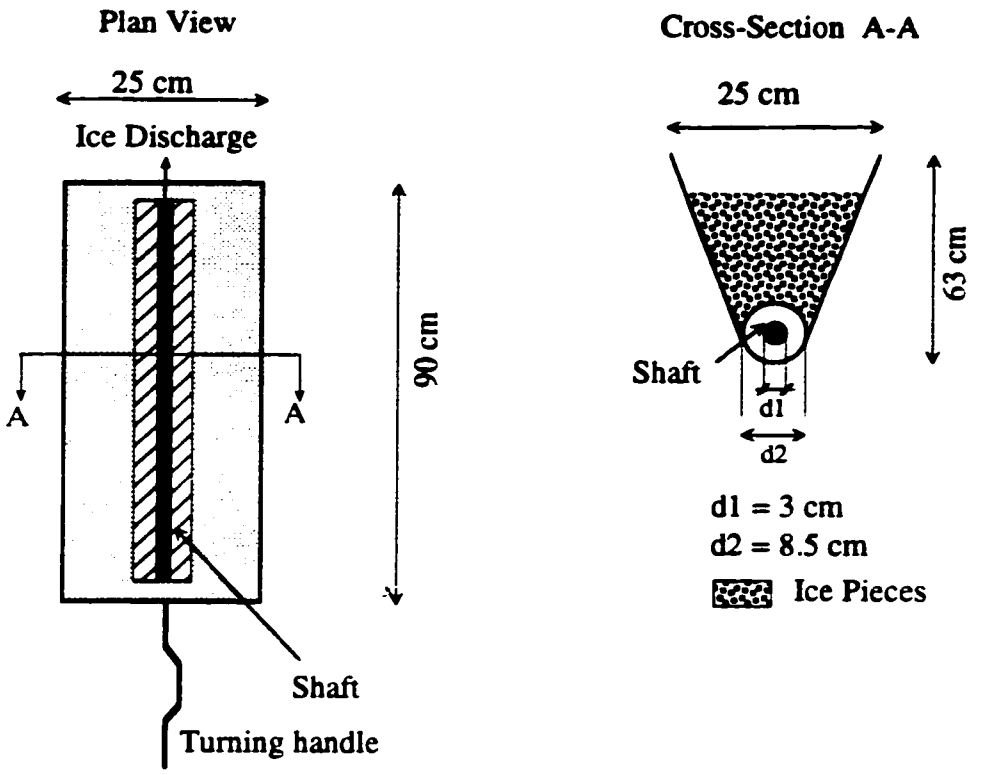

Figure 4.2: Ice feeding apparatus

Photo 4.1: Top view of experimental flume

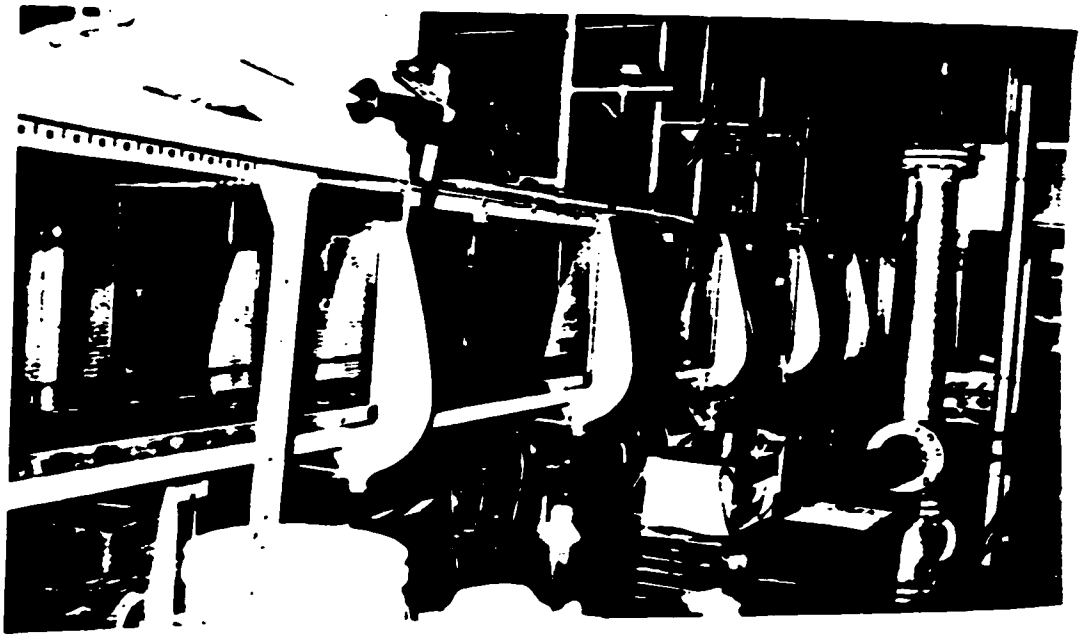

Photo 4.2: Side view of experimental flume

Photo 4.3: Polyethylene ice pieces used in experiments

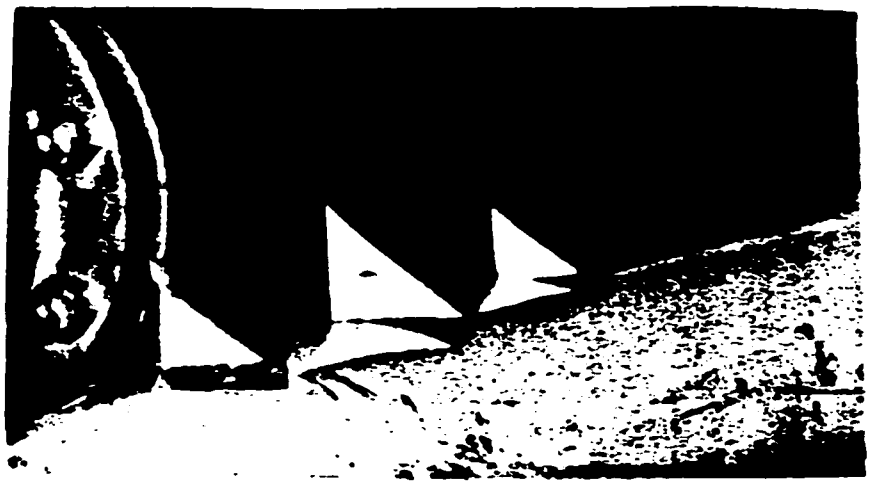

Photo 4.4: Wood pieces used in experiments

Photo 4.5: Side view of ice feeding apparatus

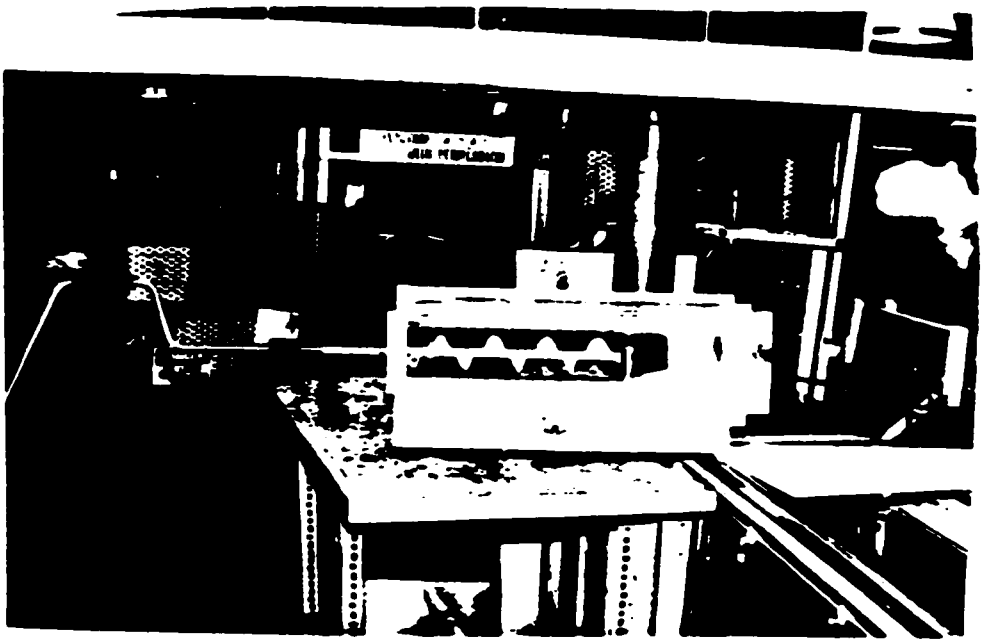

Photo 4.6: Top view of ice feeding apparatus

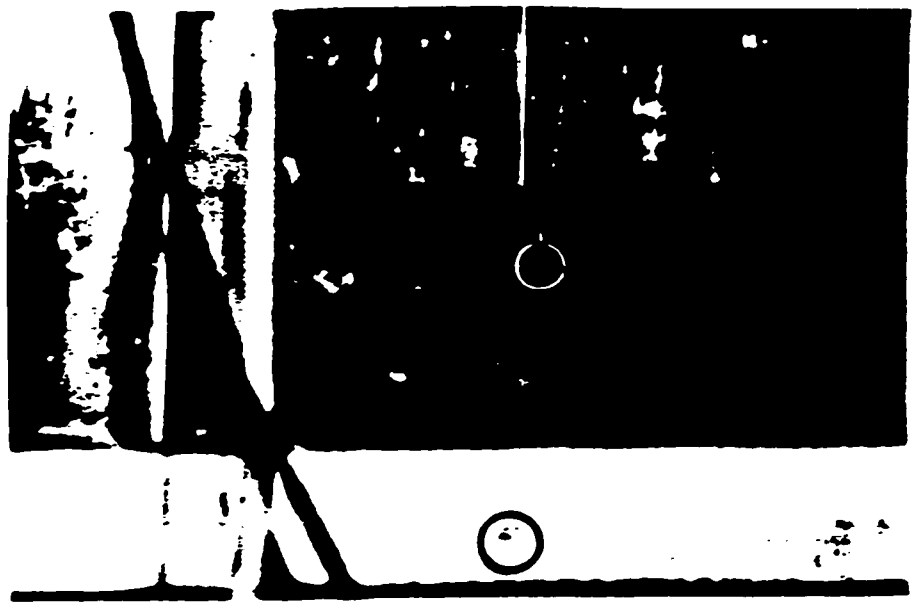

Photo 4.7: View 1 of velocimeter

Photo 4.8: View 2 of velocimeter

CHAPTER 5.0
ICE TRANSPORT IN CHANNELS

In this chapter, results of laboratory experiments aimed at investigating the transport of ice floes in a channel in a release scenario are presented and analyzed. The results were then used to verify some components of the present numerical model developed in the present study.

The results of laboratory and numerical studies for the investigation of the physical parameters of ice floe transport after release are presented and analyzed. First, a single-layer ice cover was formed and then released. The characteristics of the surface area ice concentration were observed to change in the downstream direction. The velocity of the ice floes for a certain duration of time after the release, was observed to vary non-linearly. Also, the transport characteristics of the ice floes was estimated to vary according to the ice floes mixtures, sizes and distribution. Secondly, the numerical reproduction of the laboratory experiments was performed. Through the combination of both numerical and experimental work, various parameters such as drag between the water ice pieces, angle of internal friction of ice, and ice floes size and distribution were found to affect the downstream transport characteristics of ice floes.

5.1 Experimental studies

For experiments in ice hydraulics, certain properties of the model ice material such as the friction between the pieces and the density of each piece are important. The use of polyethylene pieces for such experiments is a common practice since they have a specific gravity close to that of ice (S.G. = 0.918) and the cohesion between the pieces can be considered negligible.

As shown in table 5.1, in this set of experiments, two different sizes of rectangular polyethylene pieces (test runs 1 and 2) and cylindrical pellets (test run 3) were used. Four experimental test runs were conducted. In addition to investigating different sizes of polyethylene pieces, one more test series was carried out using a mix of the three sizes available at a ratio of one third each (test run 3).

Table 5.1: Sizes of polyethylene used in experiments

Test Run	Size Length	Width	Thickness
1	2.0	2.0	0.6
2	1.6	1.6	0.2
3	0.45 (Diameter)		0.35
4	Mixed	Mixed	Mixed

The procedure followed was similar for all the test runs, and was designed such that throughout the ice transport experiments, the hydrodynamic conditions would at least be in quasi-steady state, if not close to steady state conditions. The water flow rate in the channel was kept at 0.0024 m^3/s. The tail gate was set such that the flow depth throughout most of the channel was approximately 0.1m. The channel bed was kept horizontal. An average velocity of 0.08 m/s was estimated. With the latter hydrodynamic conditions prevailing in the channel, no overlap of the polyethylene pieces or pellets would occur and a single layer flow is ensured.

To properly observe and record the transport of ice floes in the channel, two 8mm video cameras were installed on top of the flume as shown in figure 5.1. The first camera was positioned approximately 1.1 m from the upstream entrance of the flume while the second was placed about 6.0 m downstream of the inlet of the channel. Both video cameras were connected to TV monitors, placed beside the channel in order to ensure proper positioning of the video cameras. Two strings, 12.5 cm apart were installed just across the top of the flume in the same locations where the cameras were installed (figure 5.1a and 5.1b). The objective of using such a string setup was place reference points for the analysis of ice transport characteristics while reviewing the video tapes.

Each experiment began with running the flume at the specified discharge and tail gate position. A polyethylene plate was placed in the flume around 1.1 m from the inlet in order to arrest the flow of the ice pieces. This setup imitated the phenomena of ice cover or ice jam initiation as it occurs in nature. Ice pieces were then placed gently at the upstream end of the channel and allowed to flow freely until they were stopped at the polyethylene plate. The feeding of the ice floes from the upstream end was stopped when a single layer ice cover had been formed and extended to the inlet of the flume. The experiment was continued with the flow of water and a stationary ice cover until close to steady state conditions were ensured. The start of the ice transport experiments was marked by the time at which the polyethylene plate was lifted thereby allowing the ice floes to move with the flow.

Using the video cameras did not provide direct measurements of ice floe transport characteristics. Analysis of the video tapes was required to obtain the surface area ice concentration and ice floe velocities. The video cameras captured 30 frames per second. In this case, while reviewing the recorded video tapes, the surface area ice concentration was defined as the total number of polyethylene pieces within the two strings (N) multiplied by the area of each piece (A) thereby giving the area covered by ice floes, and divided by the total surface area BL bounded by the two strings. Here, B is width of the flume and L is the distance between the two strings. The surface area ice concentration (SAIC) was therefore given by the following relation:

$$SAIC(time) = \frac{A(time)\,N(time)}{BL} \qquad (5.1)$$

Velocity measurements of the ice floes were taken by considering the movement of a single ice piece at a time as it floated downstream within the

limits of the two strings. A stop watch capable of measuring to the tenth of a second was used to evaluate the time of travel of an ice floe through the measurement area and the velocity was calculated from the following relation:

$$V_i(time) = \frac{L_{reach}}{T_{travel}(time)} \qquad (5.2)$$

where, L_{reach} is the length of the reach used for analyses, T_{travel} is the travel time of an ice piece through the reach and V_i is the velocity of the ice piece.

5.2 Numerical simulations

To understand the response of the model to the various coefficients used and to evaluate the model's performance, a sensitivity analysis was carried out. Specifically, it is of interest to evaluate the physical parameters that affect the acceleration, speed, and peak surface area ice concentration of ice floes during their downstream movement and the means by which this occurs. In order to accomplish that, similar initial, boundary and hydrodynamic conditions were used for the simulation test cases. A fictitious boundary condition of ice flux, surface area ice concentration, and ice thickness was imposed at the inlet of the flume as shown in figure 5.2. The peak of ice concentration at the upstream (Ci_u) and downstream (Ci_d) locations occur at times ti_u and ti_d respectively. Two ratios are used for the analysis, given by the following relations:

$$d_i = \frac{Ci_d}{Ci_u} \qquad (5.3)$$

and

$$L_{rel} = \frac{ti_d - ti_u}{ti_u} \qquad (5.4)$$

where, d_i represents the dispersion or decay of surface area concentration of ice and L_{rel} denotes the relative lag time for ice transport.

The last two equations can be used to identify two important characteristics for the transport of ice floes. Equation 5.3 is the ratio of the surface area ice concentration at the downstream end to that at the upstream location. This ratio can be viewed as the actual surface area ice concentration at the observations point as a percentage of that measured at the upstream end of the flume. This ratio can represent the dispersion or decay of ice in time. Equation 5.4 describes the relative lag time for ice transport from the upstream to the downstream locations. The relative lag time provides an estimate of time duration between the occurence of the upstream and downstream surface area concentrations as a function of the upstream surface area ice concentration peak time. The last two parameters would provide a time duration between the occurrence of two surface area ice concentration and the corresponding decay of that peak.

Initially, the surface area concentration of ice before release was taken as 0.8. After release, the ice accelerates from 0 m/s to 0.08 m/s in 20 seconds. For the remainder part of the simulations, the ice velocity remained relatively constant. The drag coefficient at the water-ice interface, internal angle of friction of ice and the thickness of the ice pieces were used to carry out the sensitivity analysis. The shear stress τ_{wi} between the water and ice floes and the drag coefficient C_d which is a function of surface area concentration of ice and ice floe geometry, are related through the following expression (Bjedov 1991):

$$\tau_{wi} = \rho C_d |u - V_i| (u - V_i) \qquad (5.5)$$

where, ρ is the density of water, and u is the average water velocity.

Figures 5.3 to 5.6 present the results of the sensitivity analysis. Figure 5.3 and 5.4 illustrate the variation of the upstream to downstream peak of surface area ice concentration and the relative lag time with increasing drag coefficient, respectively. These figures show that drag coefficients inferior to 0.01 are sensitive to the surface area concentration dispersion ratio, d_i and the corresponding relative lag time for ice transport, L_{rel}. Both d_i and L_{rel} decrease as the drag coefficient is decreased. The influence of the drag coefficient beyond the value 0.01 becomes negligible. Additional simulations reveal that the internal angle of the friction of ice pieces is not sensitive to d_i and L_{rel}.

Figures 5.5 and 5.6 present the sensitivity of d_i and L_{rel} on the ice floes thickness and indicate that increasing the thickness of the ice floes leads to a slight increase in d_i and L_{rel}. Doubling and tripling the ice floe thickness results in a 3% and 9% increase of d_i respectively. This indicates that by increasing the thickness of the ice floe, the dispersion of the accumulation ice cover decreases. The variation of L_{rel} with increasing ice floe thickness follows the same pattern and again is indicative of less dispersion and decay as the ice floes move downstream with the flow.

5.3 Analysis and discussion of results

The experimental test runs have shown that the surface area concentration of polyethylene pieces and pellets decreased in the downstream

direction. Due to the fact that the glass flume walls are very smooth, ice floes near the walls did not decelerate. The temporal distribution of the surface area concentration of ice and corresponding ice floe velocities at the two observation posts for the four test runs are presented in figures 5.7 to 5.10. The variation of the surface area ice concentration as a function of time followed a similar pattern for all the test runs. After the release, the surface area ice concentration at the upstream end, reached a peak value in a short period of time and then dropped to zero at approximately the same rate. thereby indicating the fast release of the accumulation ice cover. At the downstream end, the computed peak of the surface area ice concentration was less than that calculated for the upstream end. This decrease is due to the dispersion of the ice cover accumulation in general and was estimated approximately 35%, 20% and 10%, as shown in figures 5.7, 5.8 and 5.9 for test runs 1, 2, and 3 (defined in table 5.1) respectively. In the case where mixed polyethylene pieces were used, the decrease in the maximum surface area ice concentration was estimated to be 40% (figure 5.10).

It is evident that the smaller the sizes of polyethylene ice pieces lesser will be the dispersion of the ice floes as they get transported downstream with the flow. Figures 5.11 and 5.12 show the relationship between the average ice floe velocities, maximum surface area ice concentration, and sizes of ice floes and time of travel of the entire released ice cover respectively as they traverse across the downstream observations post. Considering a uniform ice field consisting of broken pieces of ice, figures 5.11 and 5.12 reveal that an increase in the size of the ice floes results in higher ice floe velocities, higher peaks of surface area ice concentration and consequently lower dispersion. The smaller the ice floes, the faster will they drift with the flow and their transport occurs with less dispersion. The exception occurs when the flow is mixed. In this case, the downstream transport

of the ice floes is the slowest and dispersion effects are the smallest.

Figure 5.12 shows that in all the test runs, the front edge of the ice cover arrived at the downstream observation post at approximately the same time (65 seconds after the start of the experiments). However, the four tests differ in the time duration by which all the ice floes pass across the observations post. In test run 4 where the polyethylene mix was used, the ice floes were passing the observation post forabout 105 seconds. In test run 3 where polyethylene pellets were used, all the ice floes passed the observation post in 80 seconds. This behavior is reflected in figure 5.11 as well. In test run 4, the velocity of the mixed ice floes was the least of all the test runs while in test run 3, the speed of the polyethylene pellets was the most, with a corresponding peak of surface area ice concentration Of 0.45 and 0.75 respectively.

The increase in the dispersion with increasing ice floe sizes can be attributed to the increase in the shear stress at the water ice interface. As the ice floe thickness increases, so does the depth at which the ice floe is submerged. Thus, larger area from the upstream face of the ice floes is subjected to the main flow, and contributes to the dispersion process. Once the surface area concentration becomes less than 0.7, the internal angle of friction between the ice floes becomes negligible and the primary influence on the transport of ice floes becomes the drag force at the water-ice interface.

A mathematical model was used to numerically reproduce the laboratory experiments and to verify the model computation results. The test channel geometry was fitted into an orthogonal grid system with cell sizes 0.25m and 0.1m in the longitudinal and transversal directions respectively. A time step of 0.05 seconds was selected for the simulations based on the Courant Levy Criteria. The

Manning n value for the channel bottom was chosen to be 0.030. A discharge of 0.0024 m^3/s with a uniform flow depth of 0.1m in the far downstream side was imposed in every experiment. An initial surface area ice concentration of 0.8 was used for the experiments. For all the simulation test cases, the internal angle of friction was set at 45°. Since the flume walls are made of glass, the friction angle between the ice floes and the channel walls was considered to be negligible.

Each laboratory test run was numerically reproduced for different drag coefficients as presented in table 5.2. The first column in the table refers to the test case number that was performed using the numerical model. Columns 2, 3, and 4 identify the drag coefficients used in each numerical test case, and for each type of polyethylene sizes used (test run numbers 1, 2 and 3 in reference to table 5.1).

Table 5.2: Drag coefficients used in the numerical simulations

Num. Test Case	Test Run 1	Test Run 2	Test Run 3
NUM1	0.002	0.001	0.010
NUM2	0.005	0.005	0.005
NUM3	0.010	0.003	0.002
NUM4	-	-	0.0015

Measured and computed surface area ice concentration and ice floe velocities as a function of time at the downstream observations location are presented in figures 5.13, 5.14 and 5.15 for the three different sizes of polyethylene ice pieces used. These figures indicate that the appropriate drag coefficient for the three test cases range between 0.002 and 0.005, 0.001 and 0.003, and 0.0015 and 0.005 for test runs 1, 2, and 3 respectively.

In general, the predicted pattern of the temporal variation of surface area ice concentration compares well with the measured values. The time of arrival of the ice cover trailing edge, the time duration at which all the ice floes pass across the observation post and the ice floe velocities as they drift with the flow are reasonably well computed for all the simulation test runs. The predicted temporal dispersion characteristics when expressed as a function of the size of polyethylene ice pieces show similar tendencies to that observed, in terms of dispersion of surface area ice concentration, peak of the surface area ice concentration and velocities. Overall, the numerical model performance is reasonable and computes the transport of ice floes very well. Computed surface area ice concentrations and corresponding velocities of ice floes as a function of time also compare well with measurements.

The results from this study shed light on the steps that should be taken in order to advance the state-of-the-art. They also isolate many important processes which occur during the transport of ice floes in rivers and shows their general tendencies and patterns. For example, the drag coefficient at the water-ice interface varies in time and space and it would be only appropriate to develop relations for it as a function of ice and water flow characteristics, similar to that of flow past spheres where the drag coefficient is a function of the Reynolds number.

PLAN VIEW

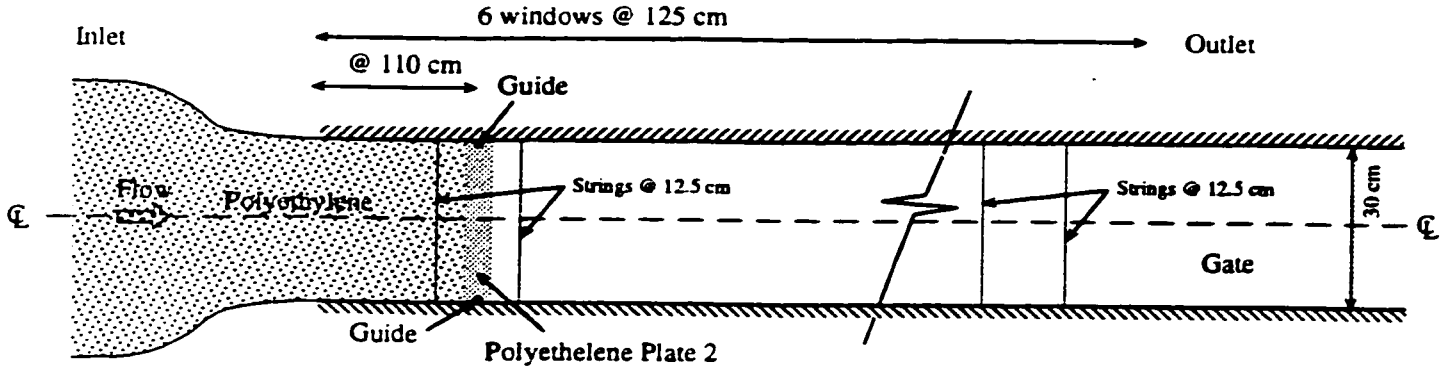

LONGITUDINAL CROSS SECTION

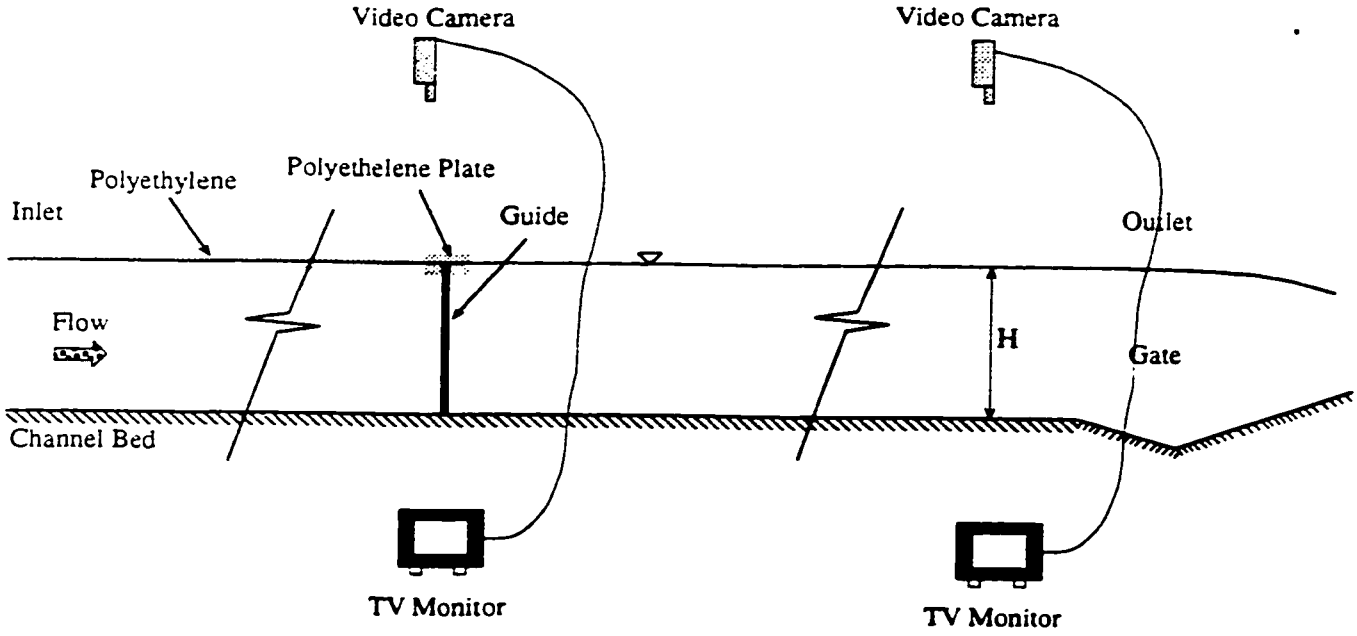

Figure 5.1: Set-up for ice transport experiments.

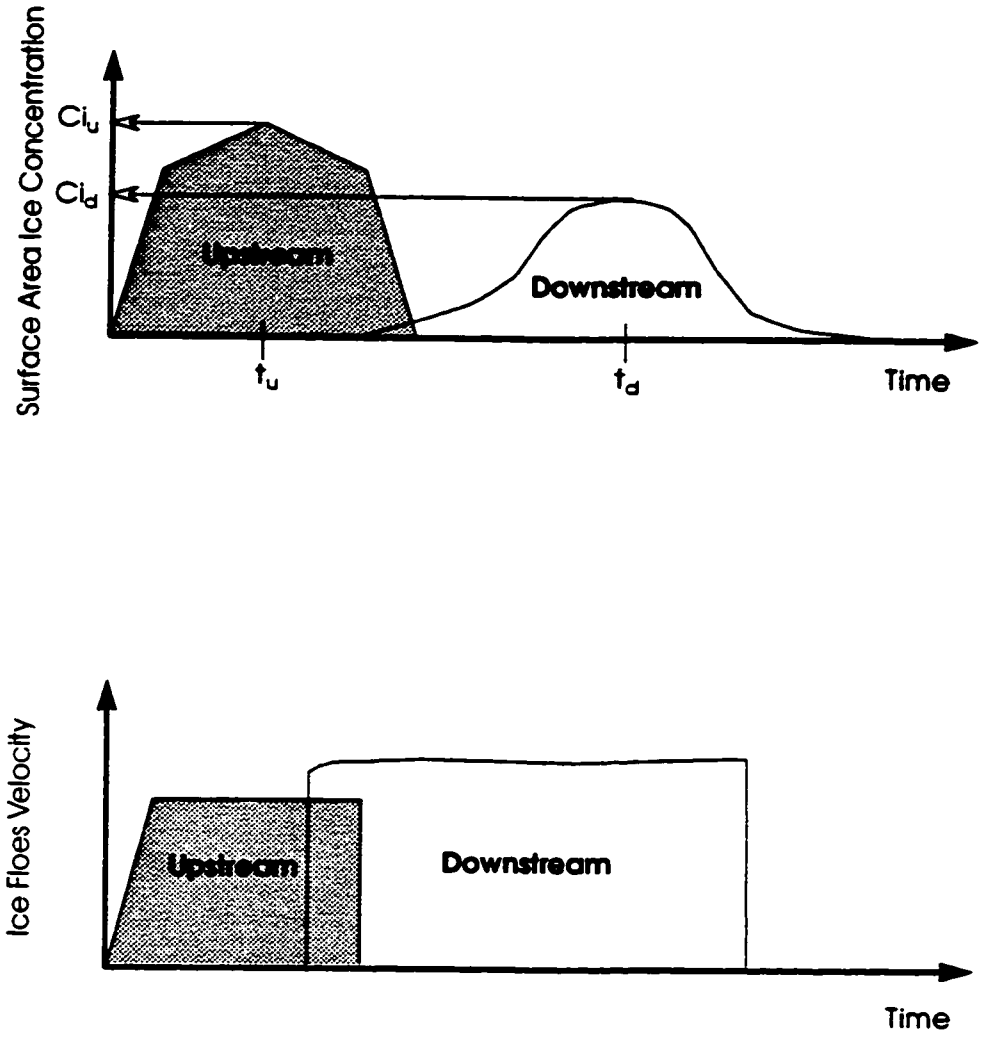

Figure 5.2: Schematic input and output of surface area ice concentration and ice floes velocities.

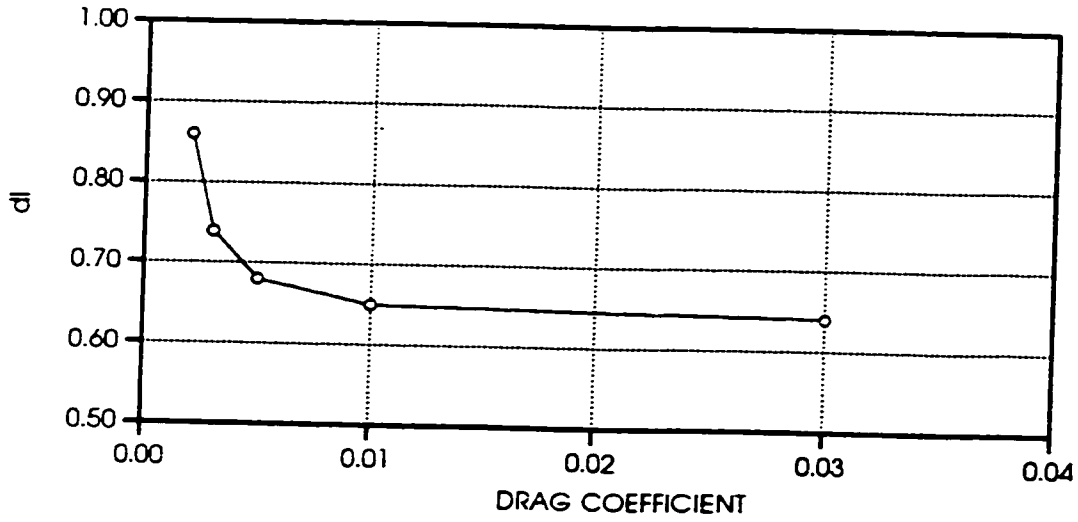

Figure 5.3: Sensitivity analysis (di v.s. drag coefficient).

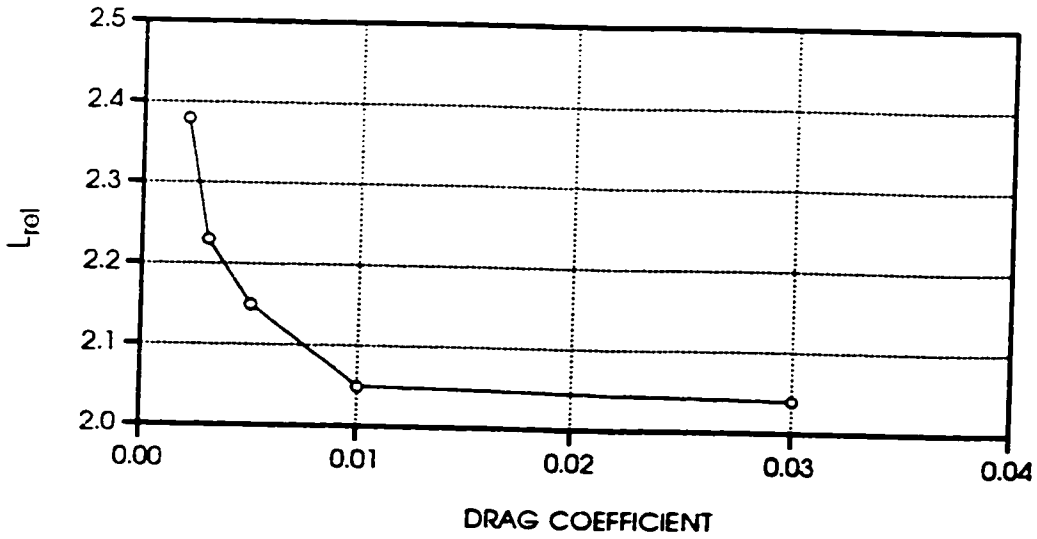

Figure 5.4: Sensitivity analysis (Lrel v.s. drag coefficient).

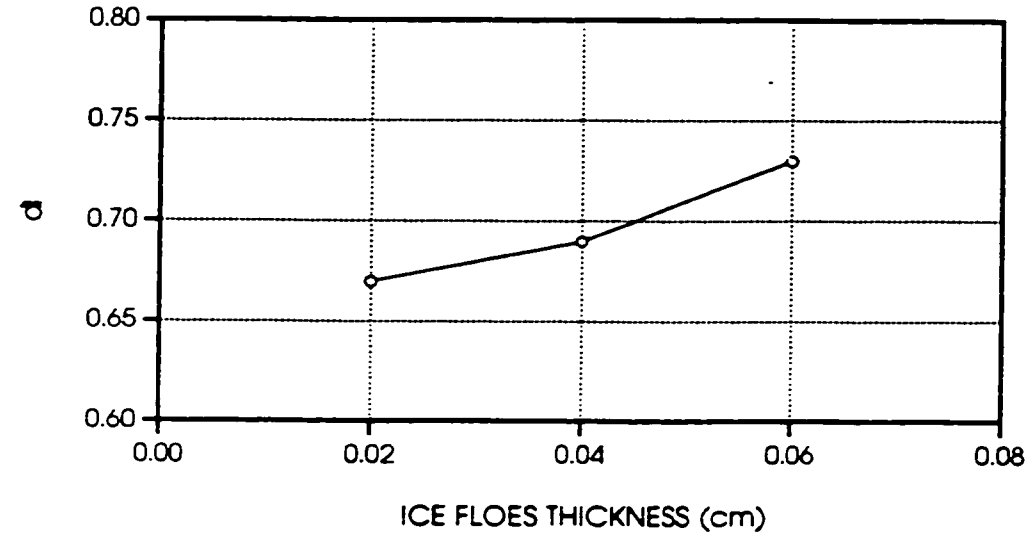

Figure 5.5: Sensitivity of di on increasing ice floes thickness.

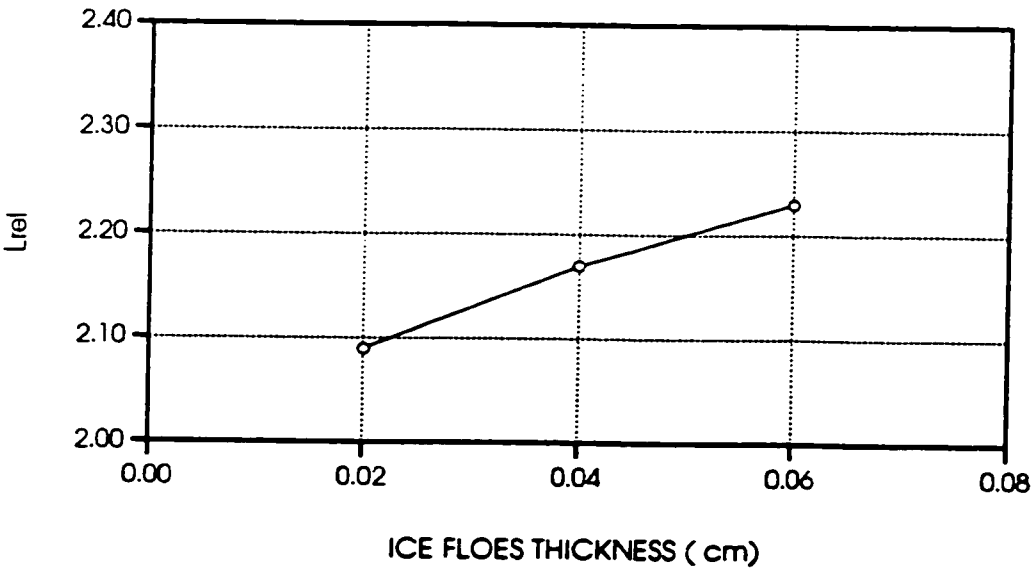

Figure 5.6: Sensitivity of Lrel on increasing ice floes thickness.

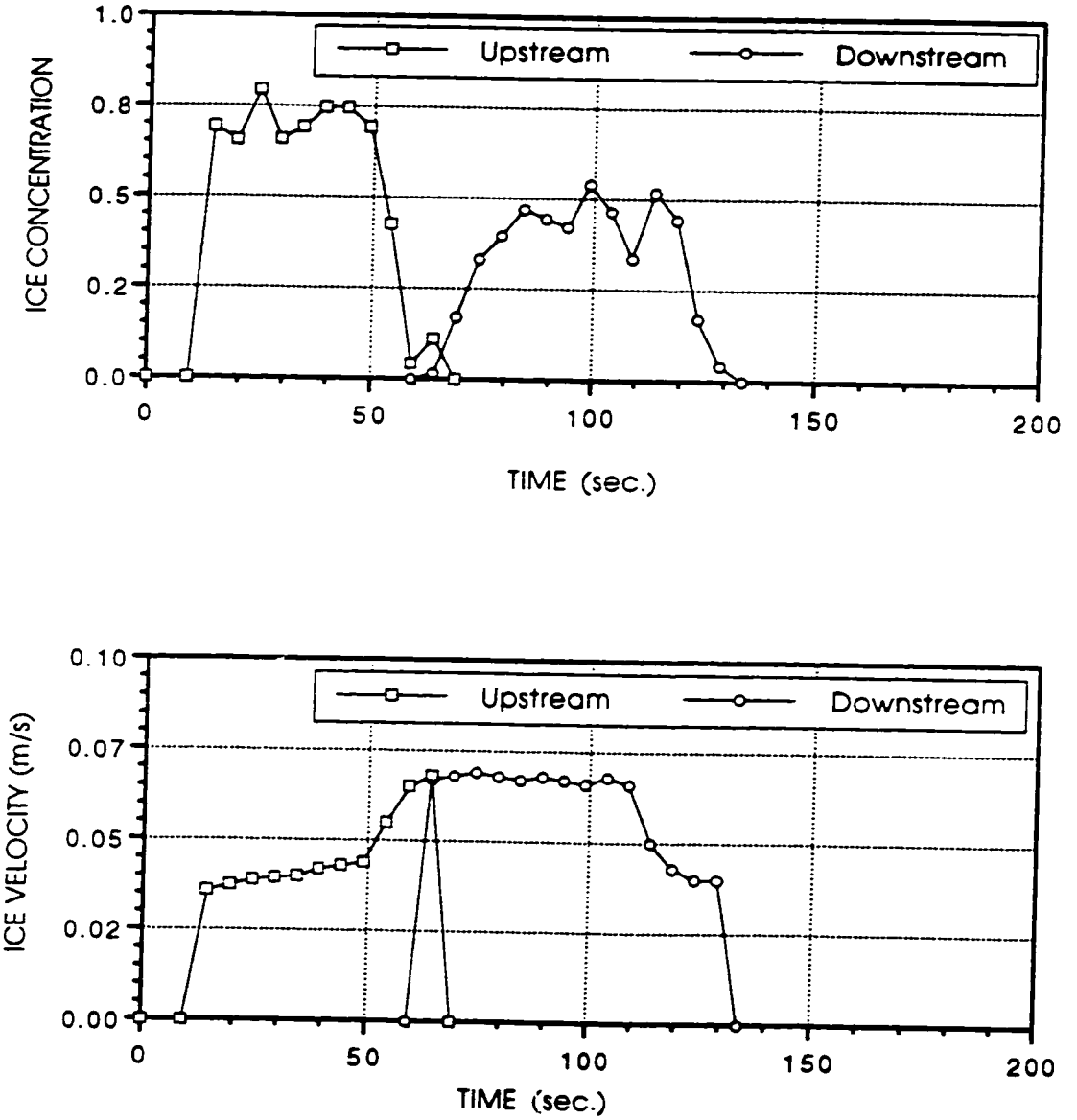

Figure 5.7: Observations of ice transport characteristics for test run 1.

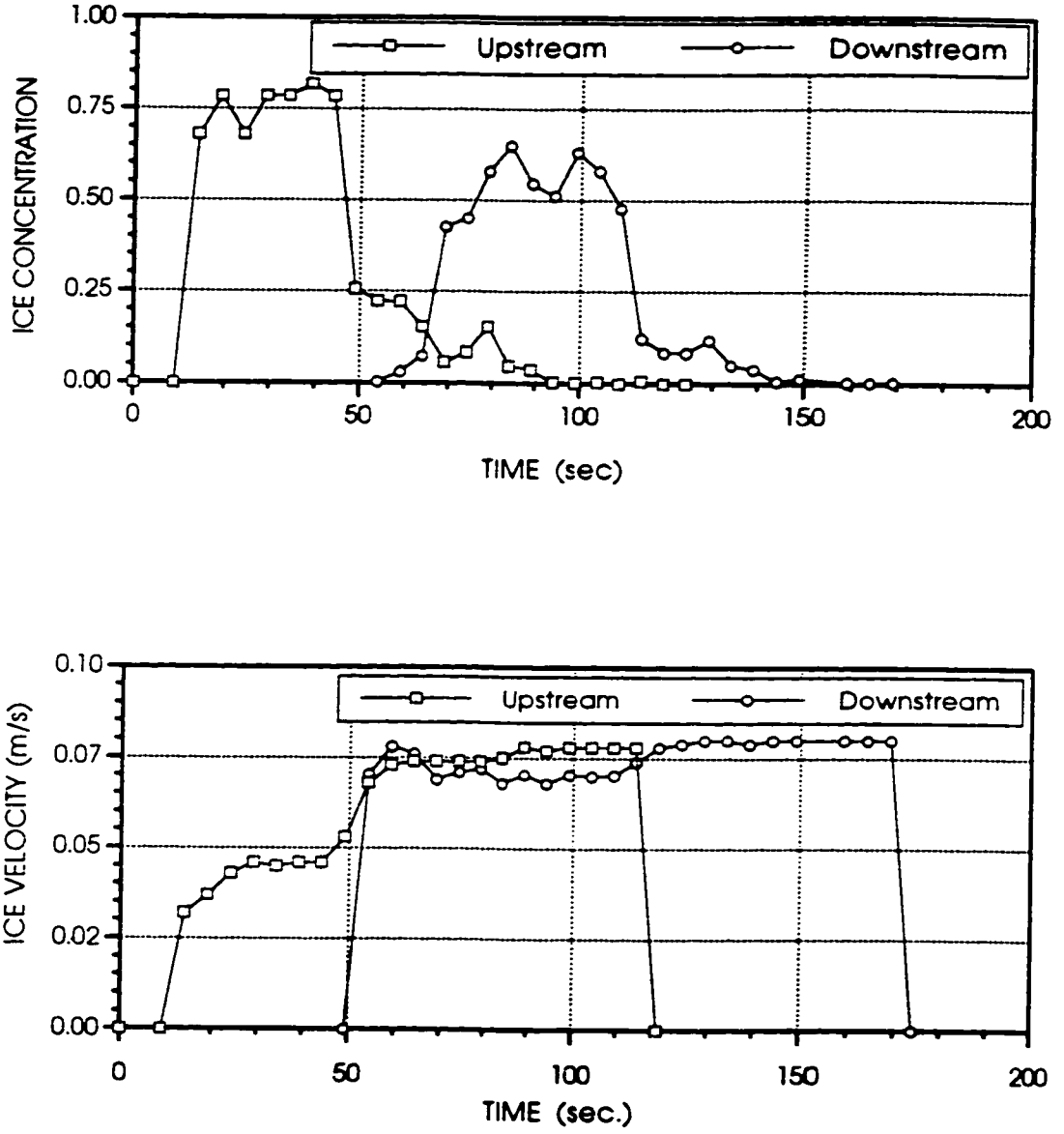

Figure 5.8: Observations of ice transport characteristics for test run 2.

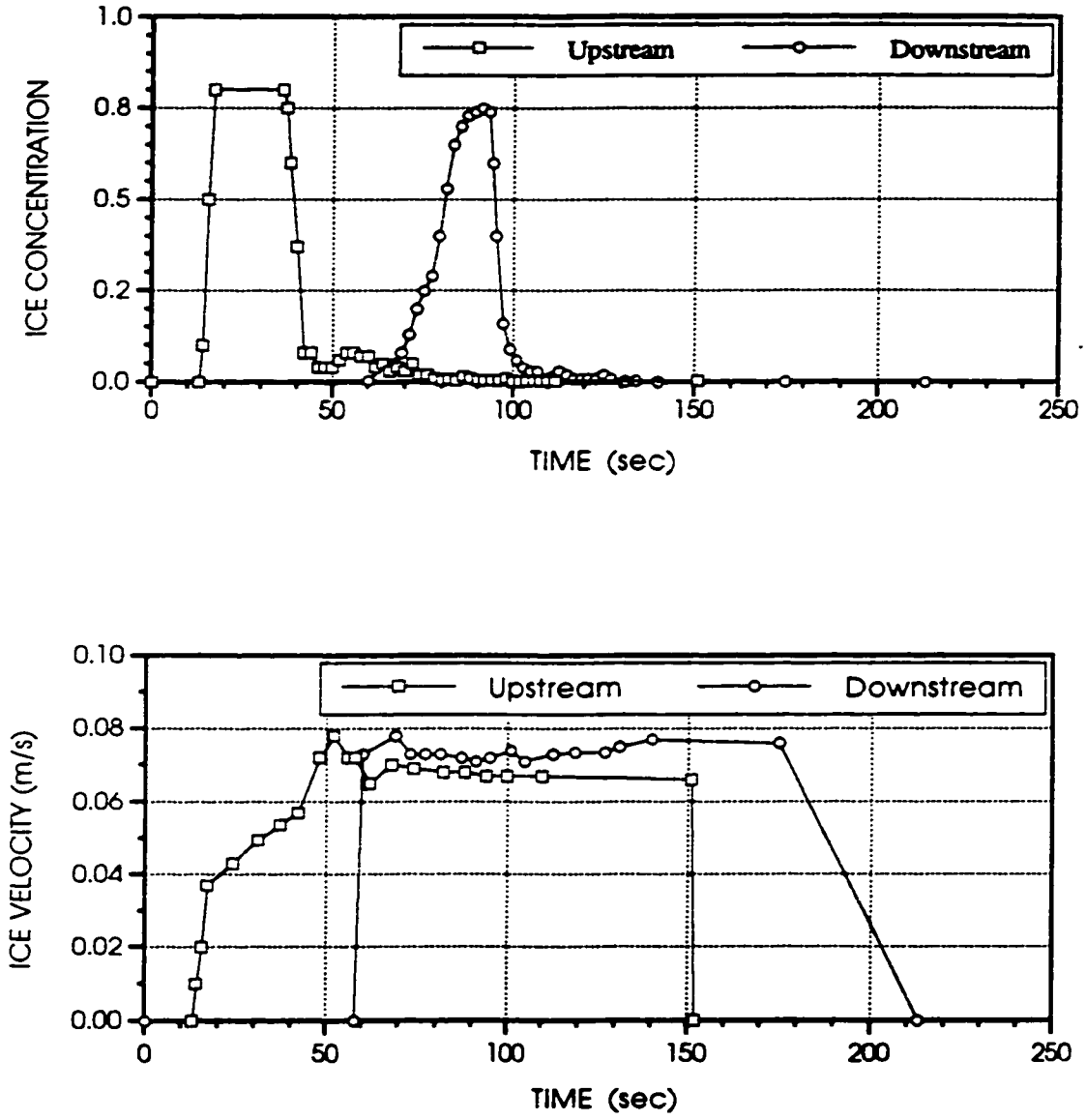

Figure 5.9: Observations of ice transport characteristics for test run 3.

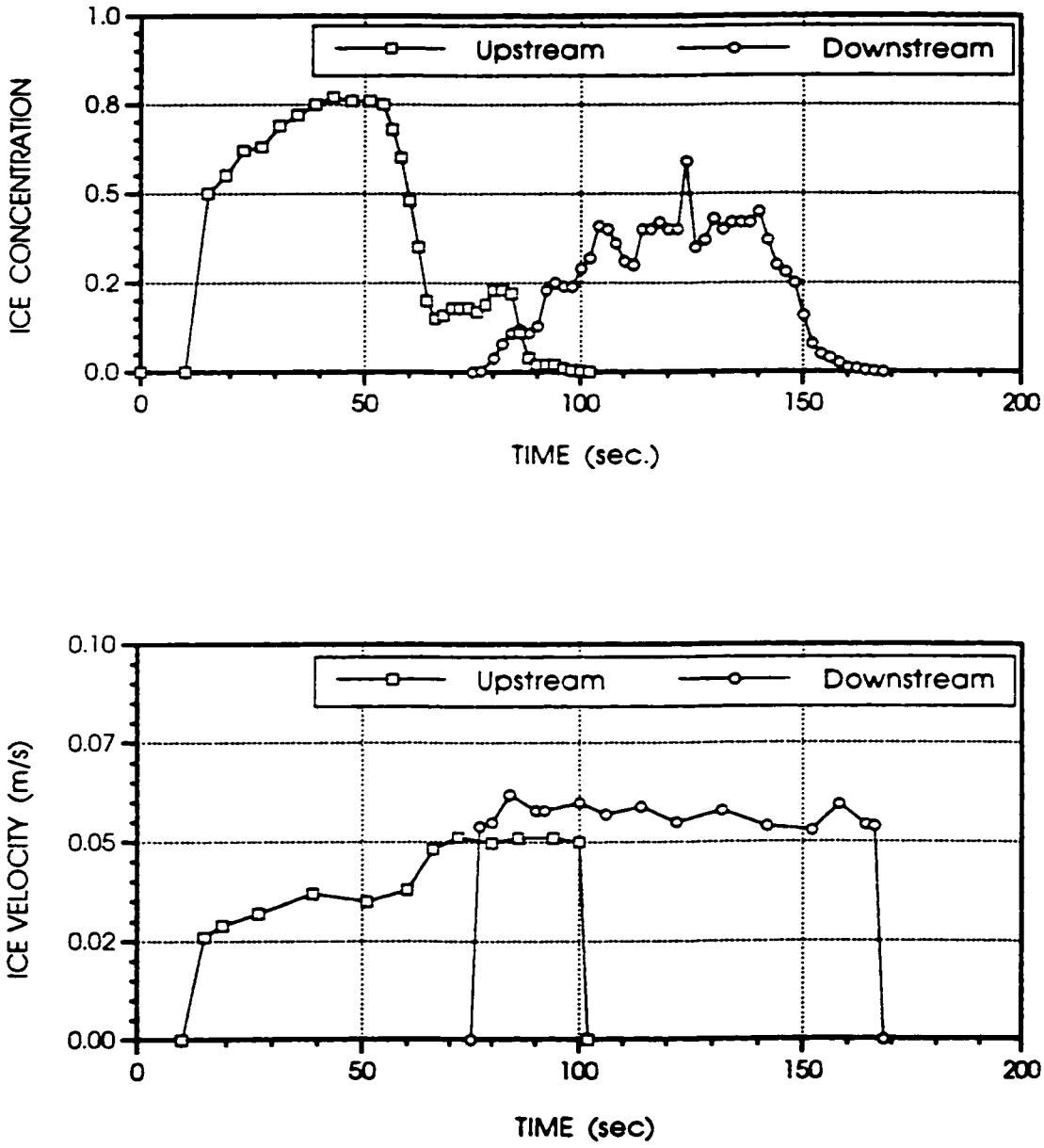

Figure 5.10: Observations of ice transport characteristics for test run 4.

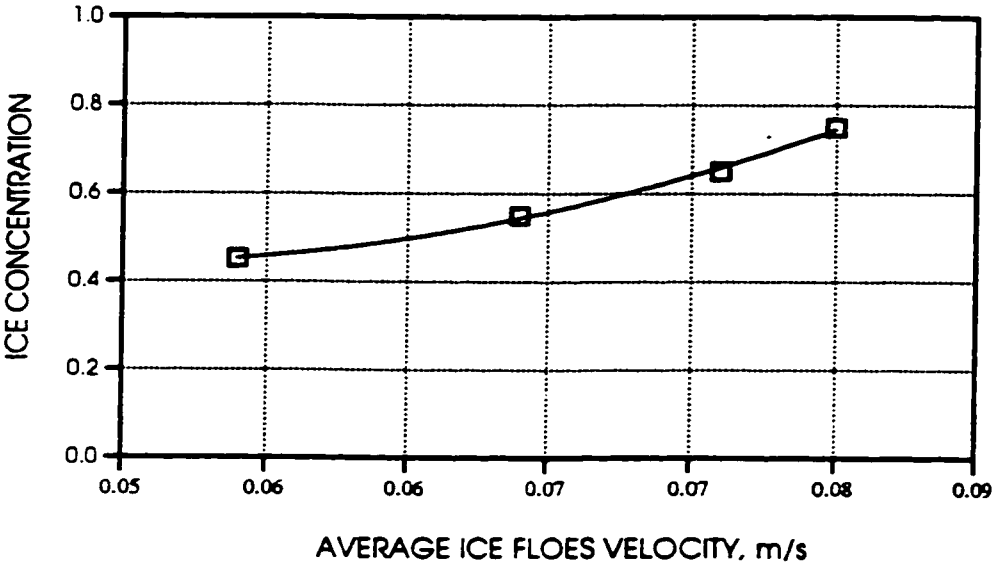

Figure 5.11: Variation of peak of surface area concentration with ice floes velocity

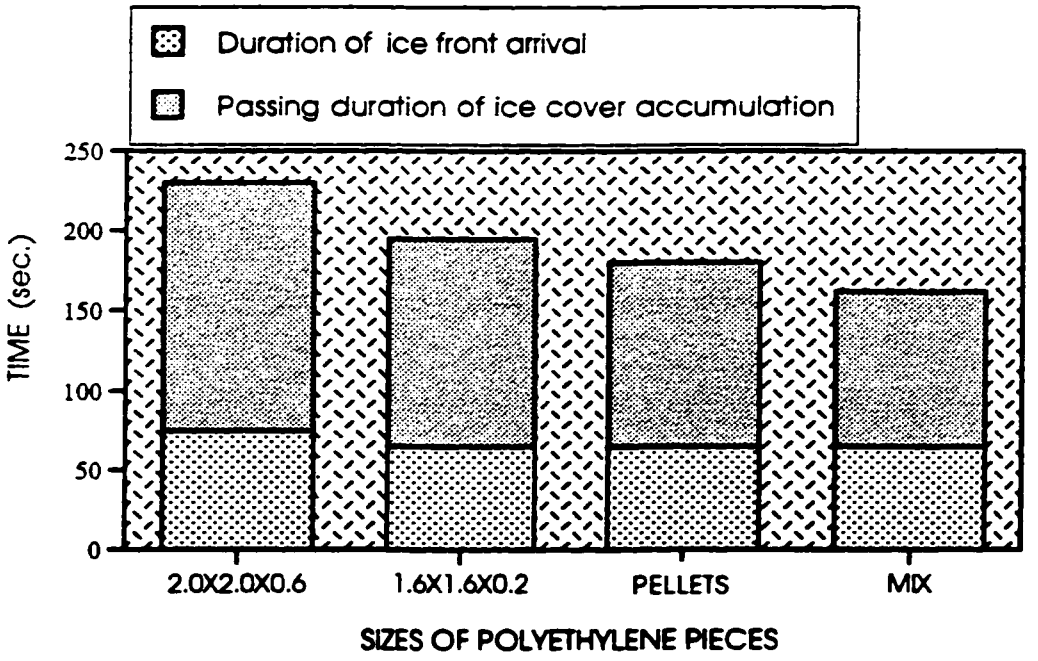

Figure 5.12: Characteristics of ice transport duration past downstream observation post.

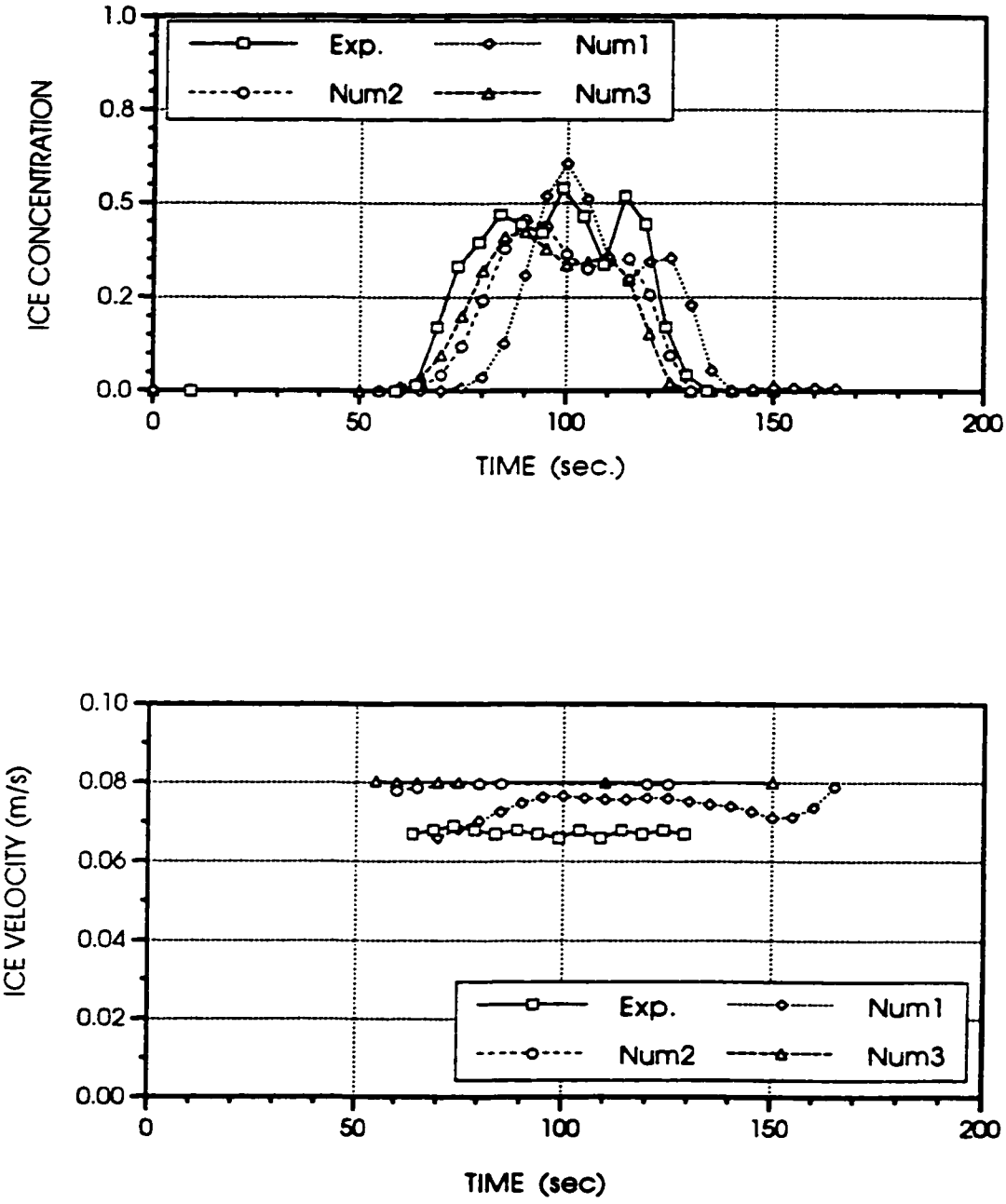

Figure 5.13: **Measured and computed ice concentration and velocities for test run 1.**

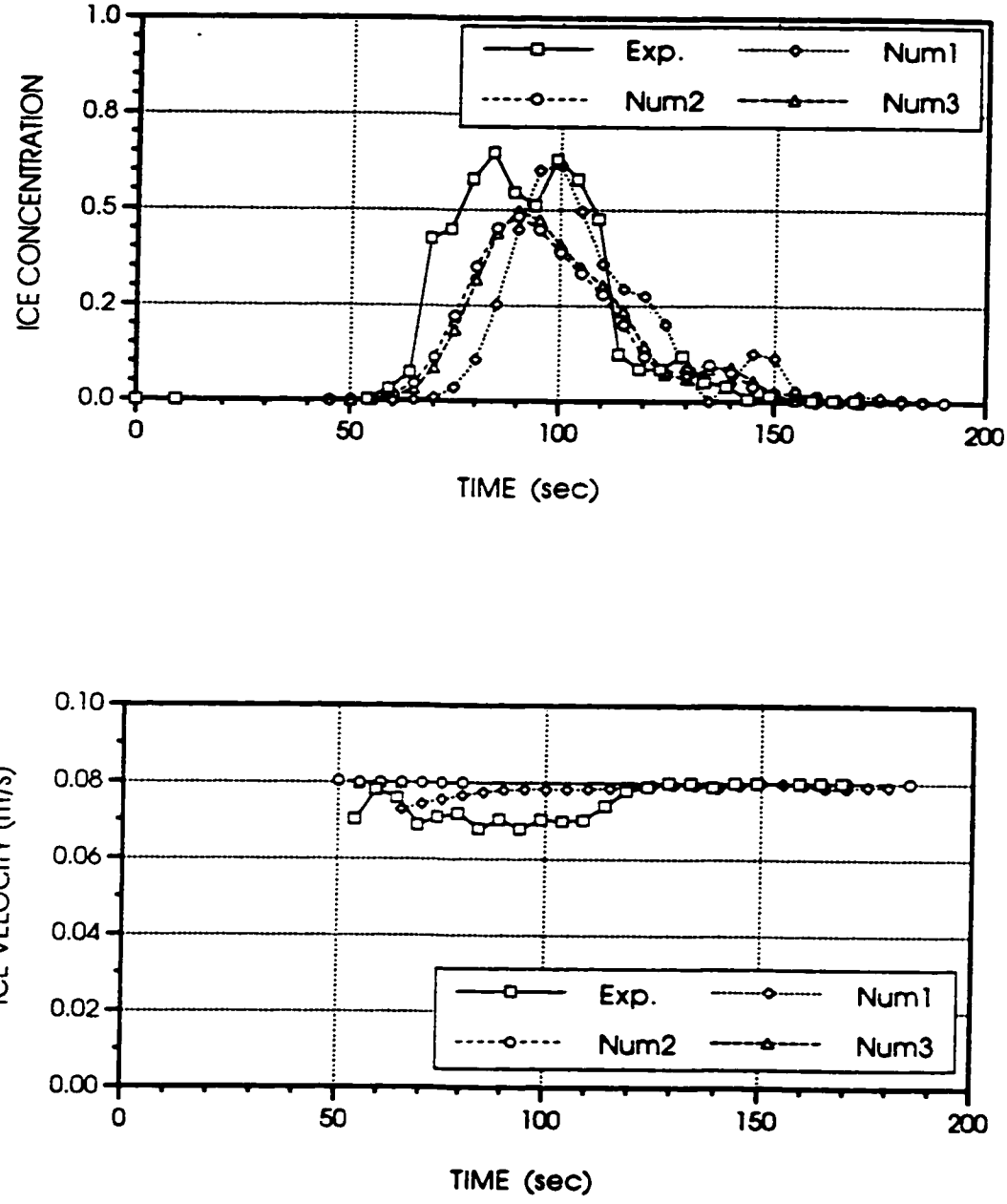

Figure 5.14: Measured and computed ice concentration and velocities for test run 2.

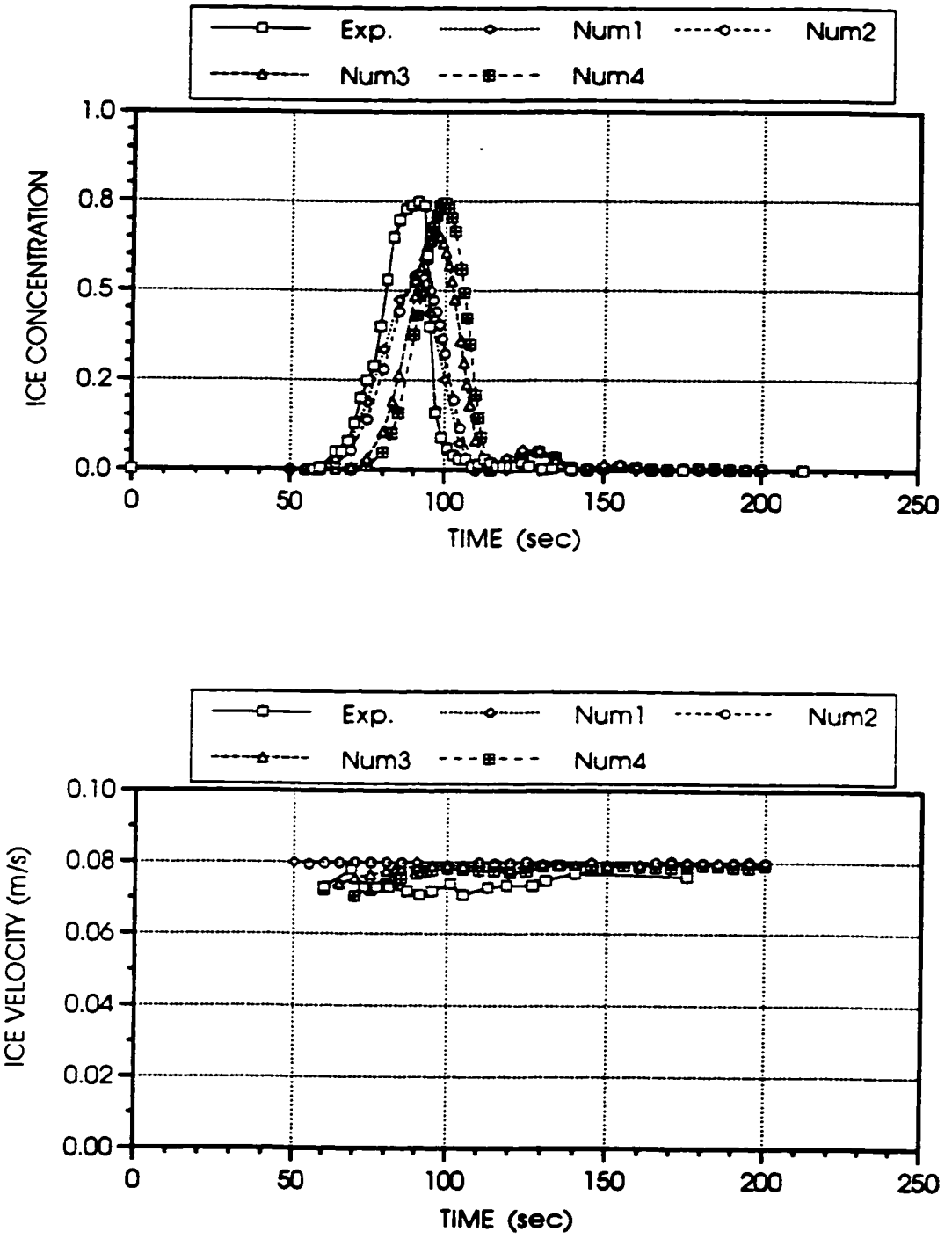

Figure 5.15: Measured and computed ice concentration and velocities for test run 3.

CHAPTER 6.0

ICE JAM INFLUENCE ON FLOW

The experimental investigation of breakup ice jams immediately before release is crucial for the understanding of the ice jam behavior and hydrodynamic characteristics after the release. This is true because the conditions prevailing at the instant before the release event constitute the initial conditions for the release of the ice jam which in turn dictates the dominant character of the development and propagation of the resulting surges and corresponding ice runs. Therefore, an experimental study was carried out to investigate the water surface levels throughout a rectangular channel just before the release of an ice jam (Raafat et al. 1994). The conditions prevailing before the release of ice jams were caused by the obstruction of the jam to the flow. This chapter deals with the experimental and numerical studies carried out to investigate the influence of the ice jam on the main channel flow. Measurements as well as the analysis of data are presented.

6.1 Development of water surface profile along ice jam (An experimental study)

The experimental investigation of the phreatic water surface levels along an ice jam as well as across its leading and trailing edges requires identifying dimensionless variables, which have physical significance, to be used for the analysis of results. In this section, the measurements taken and the analysis performed on the data are presented. Phreatic water surface levels, ice jam profiles, discharge and velocity measurements are used: (1) to evaluate and quantify the local effects of the ice jam thickness on local water levels for both polyethylene and wood ice jams, (2) to assess the stability of an ice jam as a whole and (3) to determine the global resistance of an ice jam to the main channel flow. Analysis of the data was carried out in order to obtain relations between the phreatic water levels and the ice jam thicknesses.

The parameters that are considered to be pertinent for the description of the flow and ice conditions (figure 6.1) are the water depths upstream and downstream of the ice jam's leading and trailing edges $h_{u/s}$ and $h_{d/s}$ respectively; the local ice jam thickness θ_i as a function of position i from the leading edge; the main channel water discharge per unit channel width, q; the type of material used to simulate ice floes; the total length of the ice jam L_j identified by the horizontal distance from the leading to the trailing edges; the distance along the ice jams length x_i measured from the leading edge; and the ice jam thicknesses at the leading θ_{le} and trailing θ_{te} edges respectively.

Considering the mass M, length L and time T as the basic dimensions for the analysis of the eight main variables and after the construction of the dimensional matrix and the grouping of related variables, five primary π-terms describing: the penetration of the phreatic water level into the ice jam thickness

from underneath of the jam as a function of the distance along the ice jam's length and normalized by its total length; the total stability of the ice jam; and the total resistance of the ice jam to the main channel flow are identified as non-dimensional variables which can be used for the analysis of ice jam influence on the main channel flow.

The first π-term given by equation 6.1 represents the local penetration of the phreatic water level into the ice jam from its underside at point 'i' along the ice jam length.The π-term x_i/L_j is evaluated as a function of the position along the ice jam normalized by its total length given by equation 6.2. The use of equation 6.1 provides some evidence as to the development of the phreatic water level and ice jam thickness as a function of its position along the ice jams length. The influence of the ice jam on the main channel flow characteristics at various points 'i' along the ice jam can also be estimated using equation 6.1.

$$\pi_{1i} = \frac{z_i^{wsel} - z_i^{bi}}{\theta_i} \qquad (6.1)$$

$$\pi_{2i} = \frac{x_i}{L_j} \qquad (6.2)$$

where, i is the spatial index along the length of the ice jam evaluated with respect to the position of the leading edge; z_i^{wsel} and z_i^{bi} are the elevations of the phreatic water surface and that of the bottom of the ice jam respectively; x_i is the distance along the downstream direction of the ice jam measured from the leading edge; and L_j is the total length of the ice jam.

The stability of an ice jam can be viewed as the average total attained thickness of the ice jam corresponding to specific steady hydrodynamic conditions, by which any additional inflow of ice floes from the upstream end may

result in the change of the ice jam thickness profile but not in the total average ice jam thickness. The total stability of the ice jam can be expressed by equation 6.3 as follows:

$$\pi_3 = \frac{\theta_{ave}}{L_j} \tag{6.3}$$

where, θ_{ave} is the average ice jam thickness estimated using the ice jam thickness profile measured in the laboratory experiments. The total resistance of the ice jam on the main channel flow can be estimated by considering the variation of the water surface as well as that of hydrodynamic conditions as a function of space. The total resistance of the ice jam to the main channel flow can be expressed with the help of equation 6.4 and 6.5 as follows:

$$\pi_4 = \frac{\Delta H}{h_{u/s}} \tag{6.4}$$

$$\pi_5 = \frac{F_{te} - F_{le}}{F_{te}} \tag{6.5}$$

where, ΔH is the total drop in the water level across the leading and trailing edges of the ice jam; and F_{te} and F_{le} are the Froude numbers at the trailing and leading edges of the ice jam respectively.

6.1.1 Description of experiments

A series of experiments were designed and executed in order to obtain data. The data were used first to analyse the conditions just before release and then to test some components of the numerical model. Ice jam thickness profiles and corresponding phreatic water surface levels for twelve experiments are

presented in figure 6.2. The fact that the ice jams in this study were formed under normal conditions made the ice jam formation process in this study a difficult one to follow. The difficulty arises from the constraint that the rate at which each experiment should progress is relatively small such that one experiment may consume an entire day before it could be considered successful. Basically, the vibration from the pump, transients in the flow, and small perturbations resulting from the movement of individual ice floes, contribute to the instability of the ice jam and its premature collapse.

Five experiments were carried out with polyethylene pieces while the other seven were carried out with wood pieces. Also, the flume characteristics were varied for the three sets of experiments. Table 6.1 presents the flow conditions and the ice floe types. Table 6.2 gives the channel and global ice jam characteristics that were used in each of the experiments.

Table 6.1: Flow conditions of experimental test cases.

Test Case	Q(m^3/s)	$h_{u/s}$ (m)	$h_{d/s}$ (m)	Δh (m)	Material
1	0.0028	0.074	0.056	0.018	Polyethylene mix
2	0.0054	0.101	0.05	0.051	Rectangular wood mix
3	0.0046	0.071	0.049	0.022	Triangular wood mix
4	0.0031	0.099	0.033	0.066	Triangular wood mix
5	0.0039	0.104	0.037	0.067	Wood mix
6	0.0067	0.160	0.041	0.119	Wood mix
7	0.0020	0.109	0.031	0.078	Polyethylene mix
8	0.0024	0.109	0.031	0.078	Polyethylene mix
9	0.0084	0.170	0.061	0.109	Wood mix
10	0.0094	0.180	0.07	0.110	Wood mix
11	0.0021	0.128	0.0425	0.085	Polyethylene mix
12	0.0035	0.118	0.050	0.068	Polyethylene mix

Table 6.2: Channel characteristics of experimental test cases.

Test Case	Slope at Inlet Region (Degrees)	Roughness at Inlet Region	Length of Ice Jam (cm)	Average Thickness (cm)
1	0	Low	150	2.1
2	0	Low	240	2.3
3	0	Low	185	3.1
4	1.5	High	260	3.5
5	1.5	High	270	4.5
6	2.6	High	260	5.8
7	2.6	High	220	4.6
8	2.6	High	225	4.5
9	2.6	High	260	4.5
10	2.6	High	250	4.7
11	2.6	High	220	5.5
12	2.6	High	170	5.3

Out of the twelve ice jams illustrated in figure 6.2, the first three ice jams were formed under channel conditions different than those formed during the nine others. A horizontal channel with constant roughness throughout its length was used for the first three experiments and without any variations in the channel characteristics throughout its length. For the other seven experiments, the channel characteristics were altered for a distance of 270cm from the inlet. Specifically, the Manning n value was increased by sticking polyethylene pellets at the channel bottom and walls randomly. Also, for a distance of 175cm from the inlet, a mild slope was imposed, such that beyond that stretch the channel slope returned to its original horizontal state.

6.1.2 Preliminary observations

The experiments revealed that a breakup ice jam giving a significant drop in water depth across its leading and trailing edges could be formed in the laboratory under normal unforced conditions. The formation of the ice jams in the laboratory under normal unforced conditions implies that neither the screen nor the gates have been used in one way or another for the formation of an ice jam. In this context, a floating polyethylene plate simulating a stationary ice cover was used in this study to stop the downstream flow of the ice pieces. An ice cover could then extend upstream thereby allowing for the formation of an ice jam.

Four different parameters, namely the type of ice floe pieces (polyethylene or wood), channel bed variation (horizontal or sloped), distribution of ice pieces and roughness of the flume (smooth or rough), were varied in order to investigate the favorable conditions for the formation of the required ice jam. The formation of ice jams using wood pieces occurred under higher water discharge as compared to ice jam that were formed using polyethylene pieces. Consequently, more severe conditions were dominant using the wood pieces such that higher water surface levels were obtained upstream of the ice jam. The more severe water surface level conditions resulting from the use of wood pieces to form an ice jam can be attributed to the fact that the wood surface is much rougher than that of polyethylene. This makes the friction factor between the wood pieces much higher and as a result more massive ice jams are obtained. Consequently, more resistance to the flow was noticeable. Also, the relatively larger sizes and the use of triangularly shaped wood for the formation of ice jams provide better interlocking between the individual pieces through wedging, thereby better transmission of forces from the ice to the walls of the flume and again increased resistance to the main flow as a consequence.

In the early stages of the first part of the experiments, different polyethylene and wood pieces of the same size were used for the formation of the ice jams. The experiments revealed that the required ice jams are obtained using a mix of all the sizes and shapes rather than one size alone. Other experiments were carried out with the flume bed constructed non-uniformly such that a slope was imposed for a stretch of 175cm from the inlet while the remainder portion of the bed was kept horizontal. Also between the inlet of the flume and approximately 300cm downstream of it, the roughness was increased by sticking polyethylene pellets on the bed and walls of the flume. This increase in the roughness even more favored conditions for the formation of ice jams as required.

In summary to the preliminary exploration, the first part of the experiments revealed that the formation of the required ice jams in the laboratory are possible and the favorable conditions to ensure the formation of these ice jams are: ice floes of mixed sizes and geometries; increased roughness for a certain stretch of the flume upstream of the trailing edge of the ice jam; and a sloped bed just before the location where an ice jam is expected to form.

6.1.3 Analysis and discussion of results

After exploring the many parameters affecting the formation of breakup ice jams and fixing those variables that provide the ideal setup for the ice jams required for analysis, a series of experiments were designed in order to obtain qualitative data for analysis and comparison purposes. Table 6.1 and 6.2 identify the hydrodynamic and flume geometry conditions for the twelve experiments respectively.

The five dimensionless terms given by equations 6.1 to 6.5 are used to analyze the influence of the ice jam on the water levels throughout the channel including the areas before, along and after the ice jam. The analysis of the results was carried out in two parts. The first part consisted of investigating the variation of the local phreatic water levels along the downstream direction of the ice jams. The second part was devoted to study the influence of the ice jam as a whole on the main channel water depths.

The first part of the analysis is limited to the region along the ice jam bound by its leading and trailing edges while the second part of the analysis involved the variation in the water levels before and after the ice jam. The importance of analyzing the results from both global and local point of views is due to the weakness in the current state of technology concerning the influence of stationary ice jams on the flow regime in channels as a whole and on the phreatic water surface profile along ice jams.

The twelve experimental test cases that were retained for analysis consist of a complete set of data which permits the analysis of the observations, measurements and results. The twelve experiments were subdivided into three groups, such that each group is identified by the channel configuration. The use of three different channel setup configurations was performed in order to generalize the results of the phreatic water surface levels by eliminating the effects of the channel conditions. The first group consisted of three experiments such that polyethylene pieces were used in the first experiment and wood pieces for the second. As shown in figure 6.2, for test case 1, two ice jams were formed. The first ice jam (ice jam 1) is lodged in place while the second (ice jam 2) is floating. As found in most of the other experiments, the trailing edge of ice jam 1 extends approximately to the bottom of the flume. Also common to all the other

experiments, the water level immediately downstream of the trailing edge of the ice jam is higher than the bottom elevation of the ice jam. This may imply that there is seepage at the downstream transition of the ice jam, which is not really the case as has been observed and measured in the present experiments.

Typical vertical velocity profiles measured at various locations in the flume and along the ice jams that were obtained in the first two experiments are presented in figure 6.5. This figure also shows the locations where the vertical velocity profiles have been measured. Velocity profiles have also been measured in the second experiment immediately upstream of the leading edge at two locations along the ice jams length (@240cm and @320cm from the leading edge), and after the trailing edge as shown in figure 6.3 (test case 2). As expected, the development of the vertical velocity profiles show that both the average and maximum velocities increase along the downstream direction of the ice jams. Immediately downstream of the trailing edge of the ice jams given in figure 6.3, the vertical velocity profile extends well above the bottom elevation of the ice jam. This is due to the ice jam extending at the sides to the bottom in the trailing edge region leaving a region in the middle with large cavities. It should be pointed out here that the velocity profile immediately downstream of the trailing edge of the wooden ice jam shows a negative value for the velocity close to the surface. During the experimental investigation, a vertical recirculation region was observed immediately downstream of the trailing edges of the ice jams.

The twelve experimental test cases given in figure 6.2 illustrate the twelve ice jams that were formed in the flume. Ice jams that resulted in approximately 75% drop in water depth were obtained regardless of the type of ice floes used (wood or polyethylene), size of ice floes, and channel discharge (9.4 l/s in one

case and 3.5 l/s in another). Figure 6.4 presents the longitudinal variation in the phreatic water levels along the length of the polyethylene ice jams. In this figure, the local penetration of the phreatic water level into the ice jam thickness is shown on a semi-log scale as a function of the distance x_i along the downstream direction of the ice jams. This itself was measured from the leading edge and normalized by the total ice jam length. The water level shown in figure 6.5 includes measurements from the leading edge to 0.91 L_j, where L_j is the total ice jam length.

Figure 6.4 shows that the phreatic water level drops linearly from the leading edge to approximately 0.91 L_j. The slope of this line is estimated at -1/9.8 and is given by equation 6.6:

$$\pi_{1i} = f(\pi_{2i}) = -\frac{1}{9.8}\pi_{2i} + 0.93 \qquad (6.6)$$

This characteristic of the phreatic water surface profile is general and does not depend on the channel geometry and characteristics. It is also not influenced by the main channel hydrodynamic conditions such as the discharge rate or velocity. Figure 6.4 shows that at 0.91 L_j, the value of is equal to 0.842, thereby indicating that the ice jam was not freely floating and that the water level at approximately 0.91 L_j has dropped nearly 7.8% from what is expected. It can be deduced from the foregoing that the resistance of the ice jam on the main channel flow is constant along much of its length, resulting in a linear drop in the phreatic water surface level.

The variation in the phreatic water surface levels for the polyethylene ice jams between 0.91L_j and 1.0 L_j is illustrated in figure 6.5. Downstream of 0.91 L_j, the water level drops sharply along a third order profile. From the figure, it can be shown that the maximum shift of the measured values from the fitted curve given

by equation 6.7 is approximately 6%.

$$\pi_{1i} = f(\pi_{2i}) = a\pi_{2i}^3 + b\pi_{2i}^2 + c\pi_{2i} + d \qquad (6.7)$$

where a = -1129; b = 3134; c = -2901; and d = 896.2. Figure 6.5 also reveals the development of the phreatic water surface profile at the downstream transition of the ice jam where the main channel flow passes the trailing edge region of the ice jam extending upstream a distance of approximately 10% of the ice jams length. The variation in the phreatic water surface along the downstream transition region of an ice jam as shown in figure 6.5 occurs when the ice jam is lodged in place and is stationary or when it is partially grounded as was experienced in the laboratory experiments.

Figure 6.6 presents the variation in the measured phreatic water levels along the ice jam length. However, for those ice jams obtained using wooden pieces to simulate ice floes. It is evident from the figure that the measured water levels are highly non-uniform and the water level downstream is nearly horizontal. The scatter in the local water levels is due to the fact that the wooden ice pieces are much larger than the polyethylene pieces and that the wood has a higher friction coefficient than that of polyethylene. In this case, local backwater effects were observed throughout the ice jam's length such that flooding within the ice jam and above the expected drop of the water surface level occurs. The effects of the local increase in the water levels accumulate in the upstream direction thereby increasing the water levels upstream of the ice jam and decreasing the slope of the phreatic water surface as it drops in the downstream direction and along the ice jam length.

The slope of the phreatic water surface profile along the ice jam is approximately - 0.04. The equation of the straight line which represents that profile is given as:

$$\pi_{1i} = f(\pi_{2i}) = (-\frac{1}{25})\,\pi_{2i} + 0.67 \qquad (6.8)$$

The intercept indicates the penetration of the phreatic water surface level from the ice cover underside. Since its slope is nearly zero, this penetration is uniform along the entire length of the ice jam. In the downstream transition region, the phreatic water surface drops suddenly in a stepwise fashion, contrary to what has been observed in ice jams using polyethylene pieces.

Figure 6.7 shows the variation in the average thickness of the ice jam obtained using polyethylene pieces as a function of the difference in the Froude number across its leading and trailing edges. This difference in the Froude number taken across the leading and trailing edges of the ice jam represents the change in momentum across the ice jam thereby giving an indication of the total force exerted by the ice jam against the main channel flow. This force is applied nonuniformely along the stretch of the ice jam. Figure 6.7 shows that the average thickness of an ice jam has the tendency to increase with increasing difference in the Froude number which is evaluated across the ice jam's leading and trailing edges.

Figure 6.7 also represents the global stability of an ice jam that identifies the maximum average thickness by which an ice jam can attain for a certain difference in the Froude number. Once an ice jam has attained its stable average thickness, additional ice floes from the upstream direction may change the ice jam profile, however they retain the same global average thickness.

The term π_3 can be considered as an indicator to the extent of obstruction that the ice jam imposes on the flow. In view of that, figure 6.7 reveals that for an obstruction of 0.025, a maximum change in the Froude number across the ice jam

is approximately 92%, beyond which any increase in the ice jam average thickness or decrease in the length of the ice jam would result in larger ice jams for smaller change in the Froude number. This is due to the fact that as a result of the increase in the obstruction to the flow beyond that maximum, the ice jam thickness profile would change and this would be accompanied by changes in the water surface levels, and corresponding Froude numbers upstream and downstream of the ice jam, such that smaller values of π_5 can be obtained for larger ice jams.

The global stability of the ice jams formed by using wooden pieces is depicted in figure 6.8. Similar to figure 6.7, this figure shows the variation of the average ice jam thickness (normalized by the ice jam's length) as a function of the difference in the Froude number measured across the ice jam's leading and trailing edges. In this case, the ice jam resistance to the flow as a function of the obstruction indicator (π_3) follows a linear profile. In comparison with figure 6.7, ice jams formed using wood pieces impose, in general, a higher resistance to the flow for smaller values of the obstruction indicator.

The total resistance of the main channel flow expressed as a function of the drop in the water surface level across the ice jam's leading and tailing edges is presented in figure 6.9. This figure includes the results of both wood and polyethylene ice jams. The total resistance of the ice jam on the flow increases with increasing obstruction index. A total drop in the water level across the ice jam attains a maximum value of approximately 72% for an obstruction indicator of 0.022, beyond which the resistance of the ice jam may decrease for an increasing obstruction created by the ice jam on the main channel flow.

6.2 Ice jam resistance to flow (Numerical simulations)

The relation describing the penetration of the water surface into the ice jam from underneath was incorporated into the numerical model by introducing the term π_{1i} as a function of π_{2i} into the momentum equations for water. Six experimental test cases were selected for the numerical simulations, three of which were performed by Wong et al. 1985 and the other three are from the twelve experiments carried out in this study (Raafat et al. 1994).

6.2.1 Description of simulation test cases

Table 6.3 presents the conditions describing the test cases used for the numerical simulations that were carried out for the reproduction of the ice jam effect on the main channel flow. These experiments consist of two series. The first series includes three experiments that were selected from Wong et al. 1985, and the second series entails three other experiments chosen from the present twelve experiments (described in section 6.1).

The six experiments were chosen to include a reasonable selection of different conditions by which the relation could be verified. The three numerical test cases 4, 5, and 6 correspond to the experimental test cases 6, 7, and 12 as presented in table 6.3. Test case 6 is an ice jam composed of wooden piece mix of rectangular and triangular dimensions. Test cases 7 and 12 are ice jams formed by using polyethylene mix of different sizes and dimension. In all the three test cases, the channel bed sloped for the first 175cm and continued horizontal for the remainder part of the channel section.

In order to verify the relation obtained from the present experimental study and consequently the ice jam resistance model, three experiments carried out by other researchers were selected. Wong et al. 1985 are the only investigators, to the knowledge of the author, who performed experiments of ice jam release where an ice jam was grown and the water levels were documented. The numerical test cases 1, 2 and 3 correspond to the experimental runs 1, 3 and 5. These experiments were performed in a 1.2 m wide, 20 m long rectangular flume. The ice jams were formed by feeding polyethylene blocks (5 X 5 X 0.6 cm) at the upstream section of the flume and by obstructing their passage with a retaining gate located about 3 m downstream. A photograph of a typical jam (test run 1) is shown in photo 6.1.

Table 6.3: Simulation test cases for ice jam resistance to flow.

Numerical Test Case	Expt. Test Case	Flow Rate (m^3/s)	Upstream water level (m)	Downstream water level (m)	Drop in water level (%)
1	Run no.1	0.026	0.31	0.18	42.0
2	Run no. 3	0.020	0.23	0.16	30.0
3	Run no. 5	0.025	0.21	0.19	9.5
4	6	0.0067	0.169	0.031	82.0
5	7	0.002	0.109	0.041	62
6	12*	0.0032	0.125	0.050	60

6.2.2 Numerical reproduction

Equations 6.1 and 6.2 were incorporated into the numerical model in order to investigate the resistance of ice jams on the main flow. The physical domain in all the simulation test runs was fitted into a uniform grid system. However, the entire channel length was not discretized. The channels used by Wong et al. and

in the present study were discretized into 128 by 5 cells, and 64 by 5 cells respectively. Each cell is 0.0625 m in the x-direction and 0.40 m and 0.297 m in the y-direction for the first and second test series respectively. Hence, channels 8 m and 4 m in length were reproduced for test series 1 and 2, respectively. Shorter channels were used for the simulation runs in order to reduce computations time. This could be justified by the fact that at this point in the investigation, only the upstream water level is of concern and only at steady state conditions.

The input to the numerical model includes the specification of two types of variables, namely those that should be measured in the laboratory and others which could be adjusted to obtain reasonable results. On the one hand, the main channel discharge and the water level at the far downstream are imposed exactly as measured. The Manning n value of the channel was set at 0.025, since the flume bed is made of polished stainless steel plates.

On the other hand, the ice jam profile for the first three test runs and the Manning n value for the ice jam underside were slightly adjusted to obtain the measured effects of the ice jam on the main flow. This was possible since the measured ice jam profiles for the first three experiments were not available. The estimation of the Manning n value for the ice jam underside is still a weak point in the state-of-the-art and is used as a calibration parameter in practice.

Simulation test runs with different drag coefficient for the ice cover underside revealed that its effect is small compared to other variables. Other simulation using different initial upstream water levels showed that the results at steady state remain the same. This confirms that initial conditions do not influence the ice jam resistance to the flow. The time step for computations was selected based on the CFL criteria (Courant-Freidrich-Levy) and was small enough to ensure stability in the calculations.

6.2.3 Discussion of results

The primary objective of the numerical simulations is to compute the rise in the water level upstream of the jam. The numerical model is run until steady state conditions are attained. The water level at the most upstream location of the flume is then noted down and compared with measurements.

Figure 6.10 illustrates the hydrodynamic and ice conditions used for the simulation test case 1. The ice jam thickness profile was estimated, since measurements were not available. The only available information is the trailing edge of the ice jam (at the same location as the grill), and the approximate length of the jam (Beltaos 1994). Figure 6.10 also shows the computed and estimated (Wong et al. 1985) water levels along the length of the channel. The estimated water surface profile is the one used for the numerical modeling carried out by Wong et al. in their study of ice jam releases. This profile is not measured or observed, but is based on an assumption that was used.

Figure 6.10 shows that the computed and assumed water surface profiles are in close agreement. This is not exactly what is expected, however by looking at the problem from a fundamental point of view, a clearer interpretation of the figure could be deduced. Two aspects should be considered namely, the model calculations, and the formation of the ice jam. By definition, the computed flow depth using the present model is defined as the vertical distance limited by the channel bed from the bottom and the underside of the ice cover from the top. Therefore, it is expected that the computed water surface profile follow the underside ice jam profile. In all of the first three simulation test cases, the water surface profile does not adhere to what is expected. This can be reasoned by considering the conditions by which the ice jams have been formed in the studies performed by Wong et al. 1985.

The jamming of the polyethylene blocks was achieved by feeding the blocks at the upstream section of the channel in a uniform flow and by obstructing the passage of the blocks with the help of a porous gate located about 3 m downstream and placed along the full depth of flow. The porous gate consisted of closely spaced vertical rods that were held together by two horizontal beams. The blocks accumulated at the gate and produced jams that generally resembled natural ones, with steep hydraulic gradient at the toe and increased stage upstream.

It is evident that the submerging ice pieces were not able to escape the ice jam with the flow and erosion of ice floes was not possible. In addition, the ice jam was supported (lodged or being held back) by the gate along its entire trailing edge frontal area, perpendicular to the flow. This was contrary to what occurs in nature where ice jams are supported by a strong downstream ice cover whose relative thickness is small compared to the ice jam thickness at the trailing edge, and at most where the ice jams are either totally or partially grounded.

Based on the above discussion, it is not surprising that the profile of the ice jam underside is linear and smoothly varying. Also, based on the computational results and observations from the experiments carried out in this study, the part of the ice jam below the water level shown in figure 6.10 should probably be eroded under normal conditions. The latter deductions and discussion are complemented by the results of simulation test case 7 which are presented in figure 6.11.

This figure gives the ice jam top and bottom surface profiles, the channel conditions, and the computed water surface profile. In this case, the computed longitudinal flow depth profile follow closely the ice jam bottom surface profile as well as the channel bed. Adding the penetration of the water surface into the ice

jam from underneath to the flow depth gives the phreatic water surface profile as measured in the laboratory experiments. The difference between the measured and computed phreatic water surface profile would be in the same order of magnitude as that between the flow depth and ice jam bottom surface profiles, as shown in figure 6.11.

In all the six simulation test cases, the variation of the velocity in the longitudinal direction as a function of the flow depth and ice jam thickness is consistent with observation. As the ice jam thickness increases, the flow depth decreases and the flow velocity increases as shown in figure 6.12. The transition of flow is smooth at the leading edge and abrupt at the trailing edge, where a sharp increase in the water depth occurs accompanied by an equally sharp drop in the flow velocity immediately after.

Table 6.4 presents the results of the six simulation test runs. It is evident that measured and computed ice jam resistance to the main flow, evaluated as a function of the rise in the water level at the farthest upstream location compare well with a maximum percentage difference of 4.8% occurring in test case 5.

Table 6.4: Measured and computed upstream water levels.

Test Case	Upstream water level measured (m)	Upstream water level computed (m)	Difference (%)
1	0.31	0.304	1.9
2	0.23	0.225	2.1
3	0.21	0.209	0.5
4	0.169	0.167	1.2
5	0.109	0.114	4.6
6	0.125	0.131	4.8

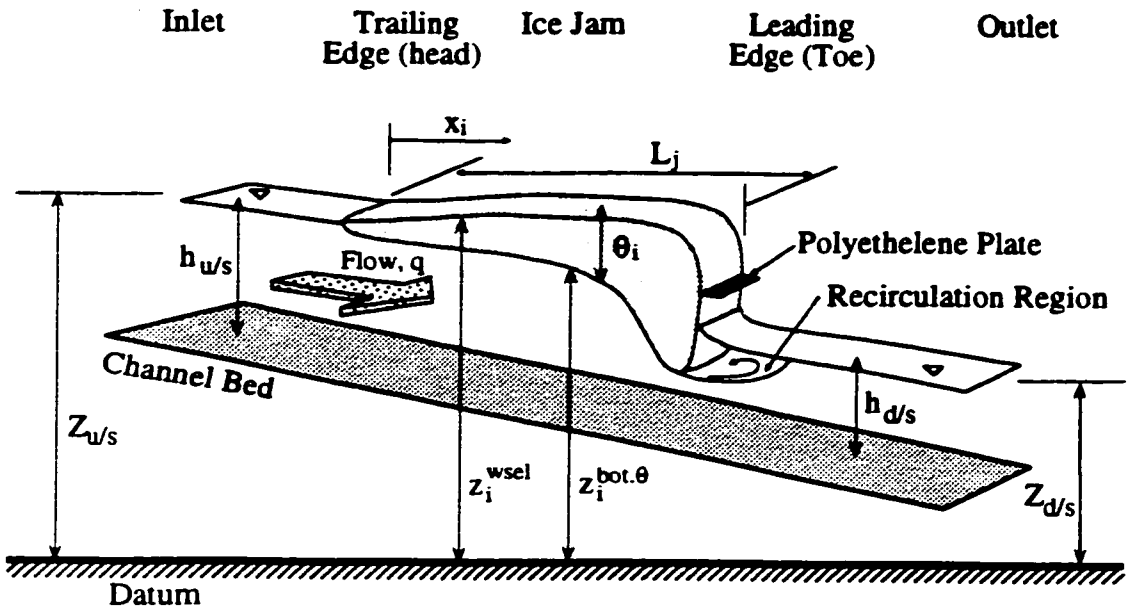

Figure 6.1:Typical breakup ice jam.

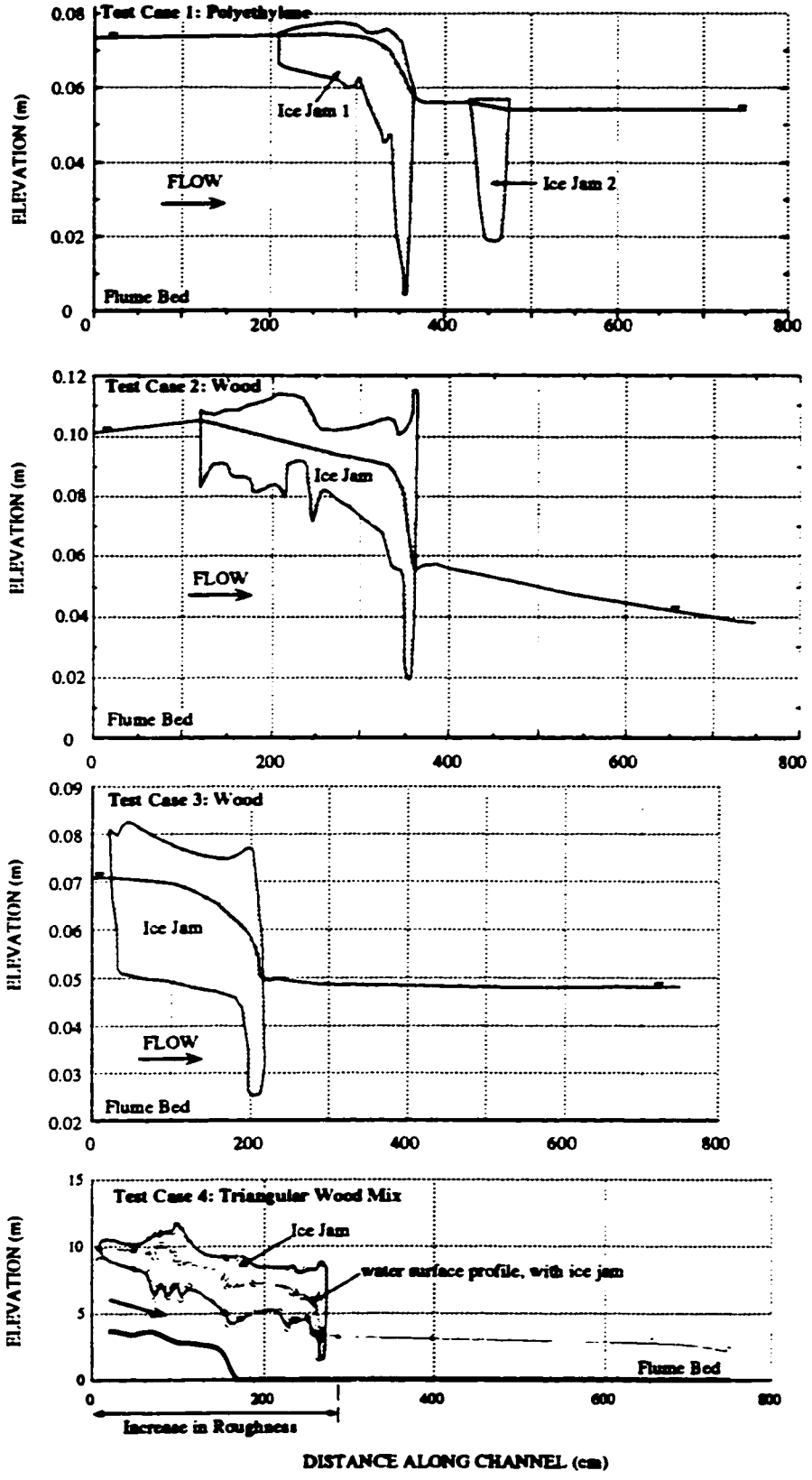

Figure 6.2: Measured ice jam thickness and water surface profiles.

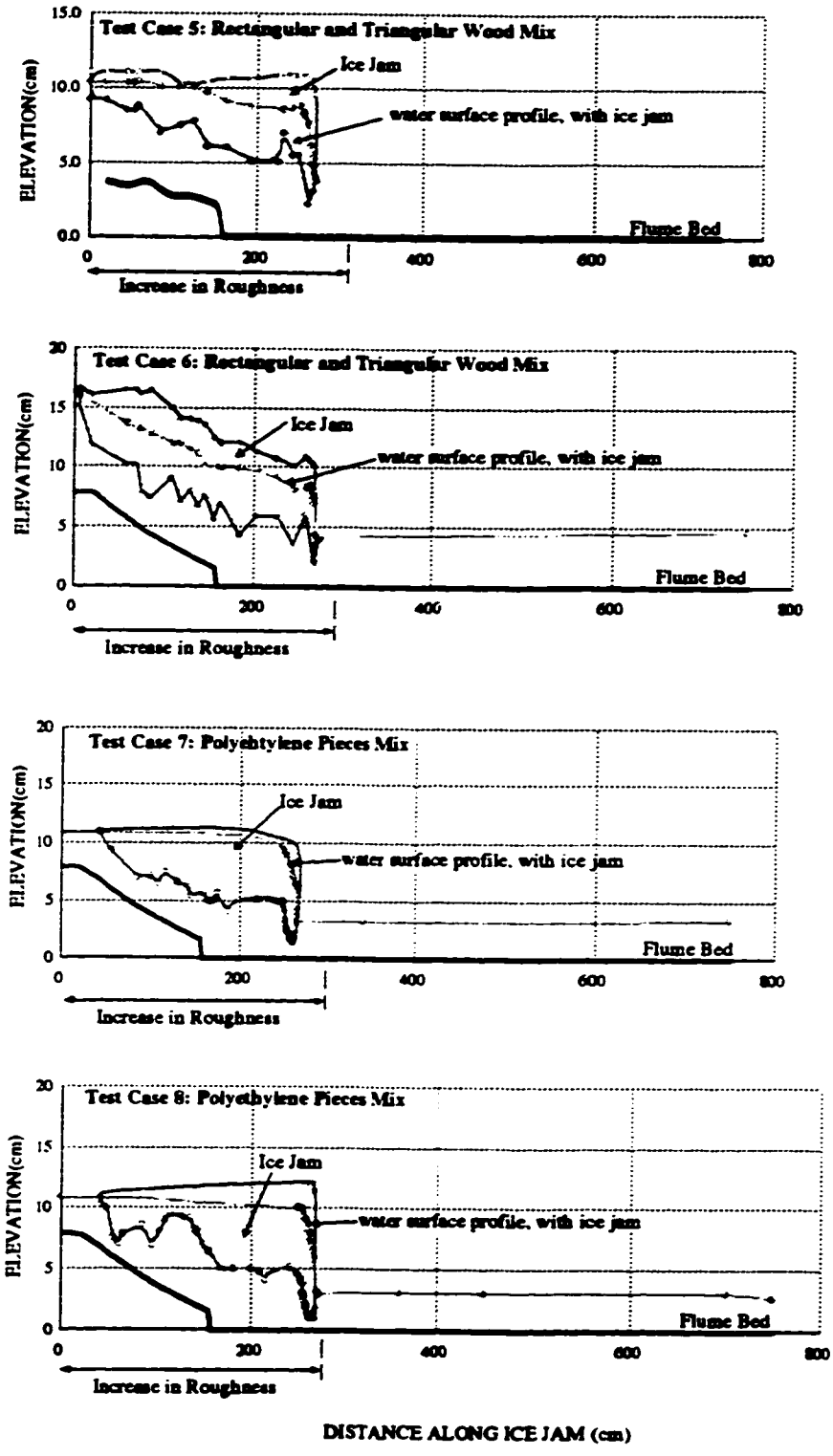

Figure 6.2: Measured ice jam thickness and water surface profiles (continued).

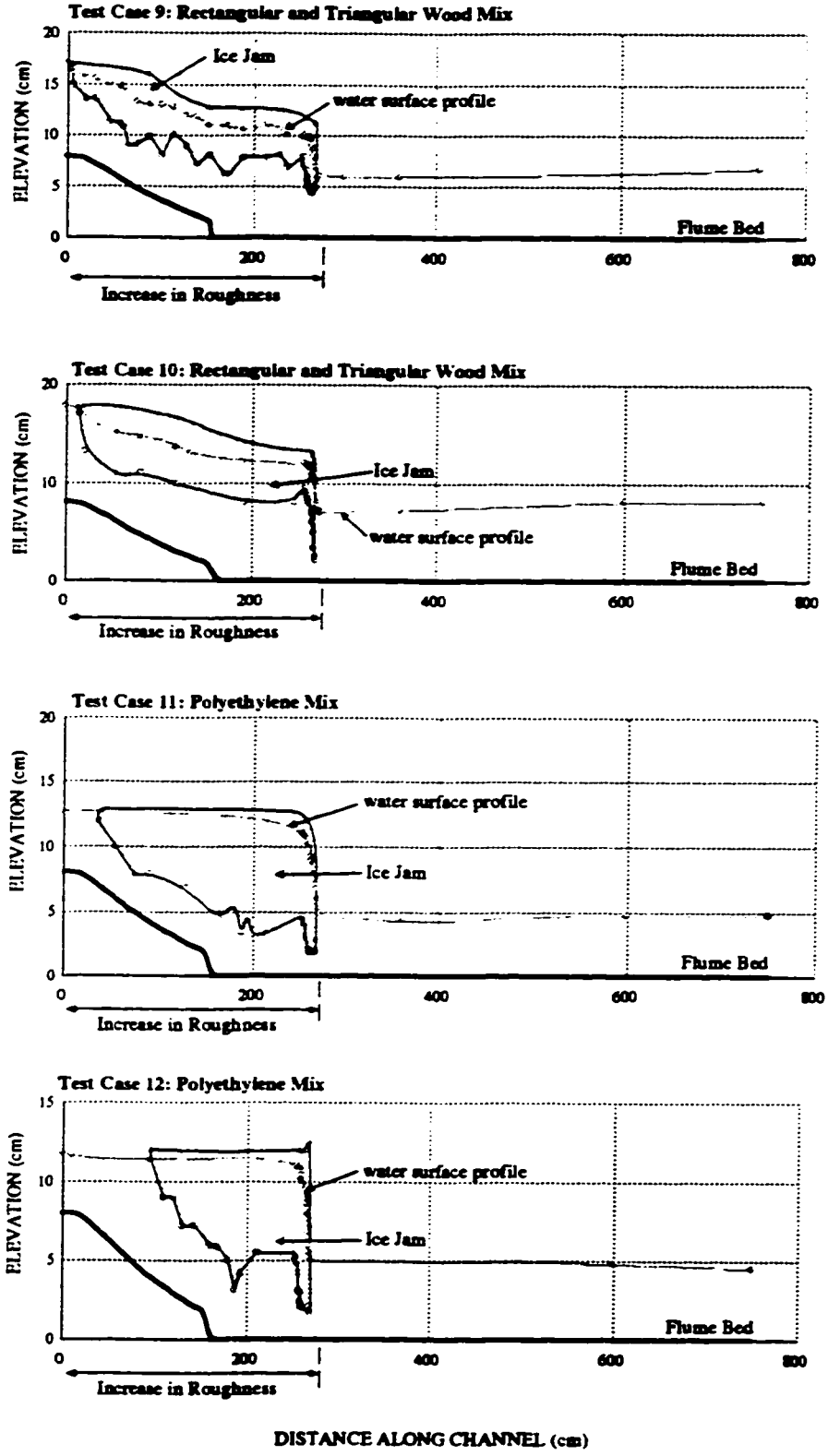

Figure 6.2: Measured ice jam thickness and water surface profiles (continued).

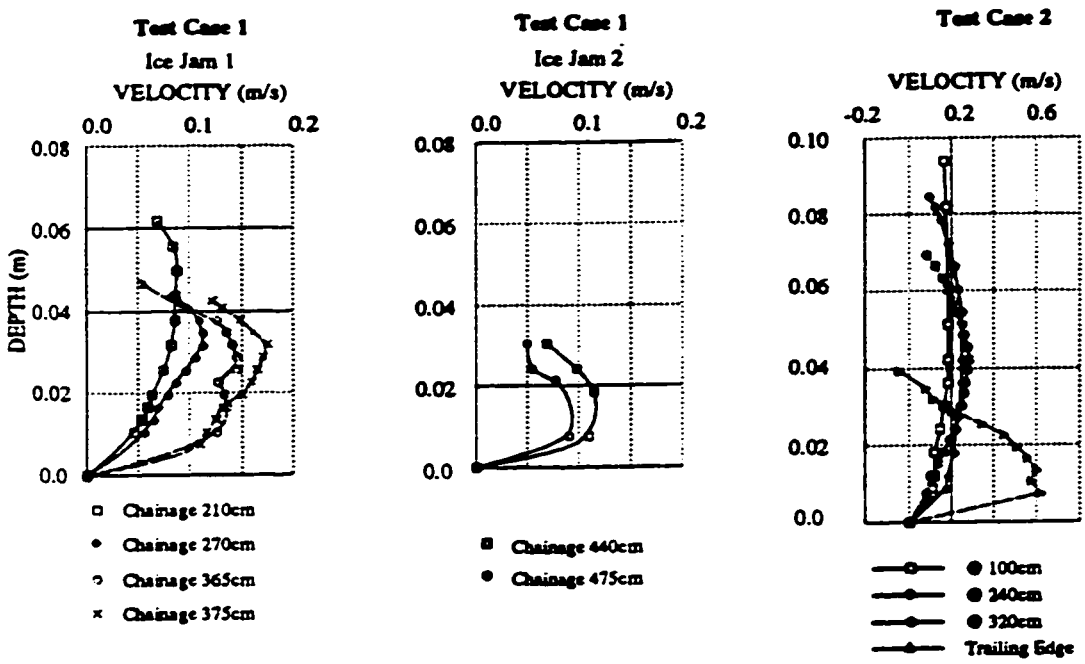

Figure 6.3: Typical measured vertical velocity profiles.

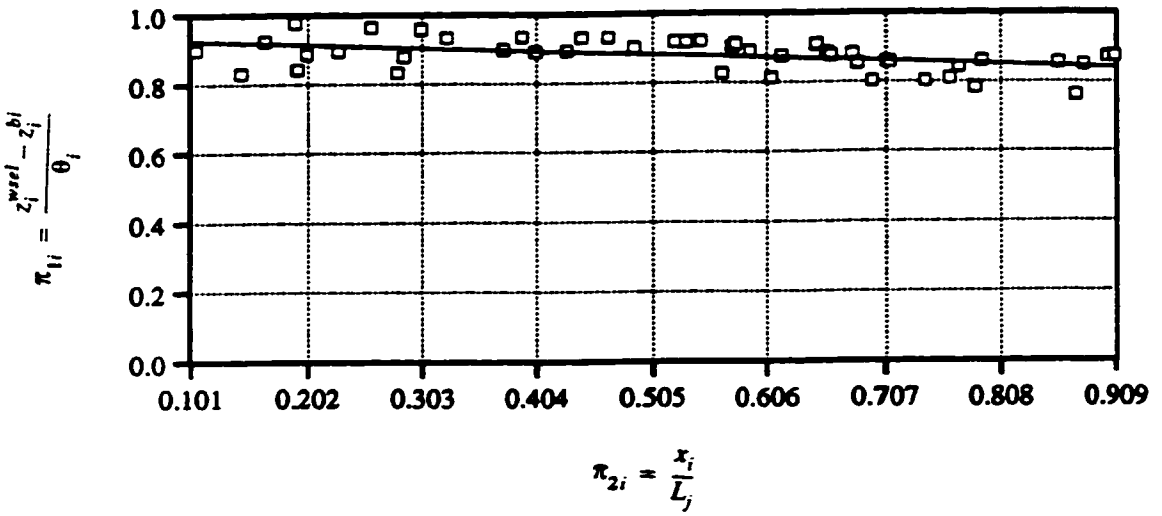

Figure 6.4: Penetration of water surface profile in polyethylene ice jams, from 0.0 L_j to 0.91 L_j.

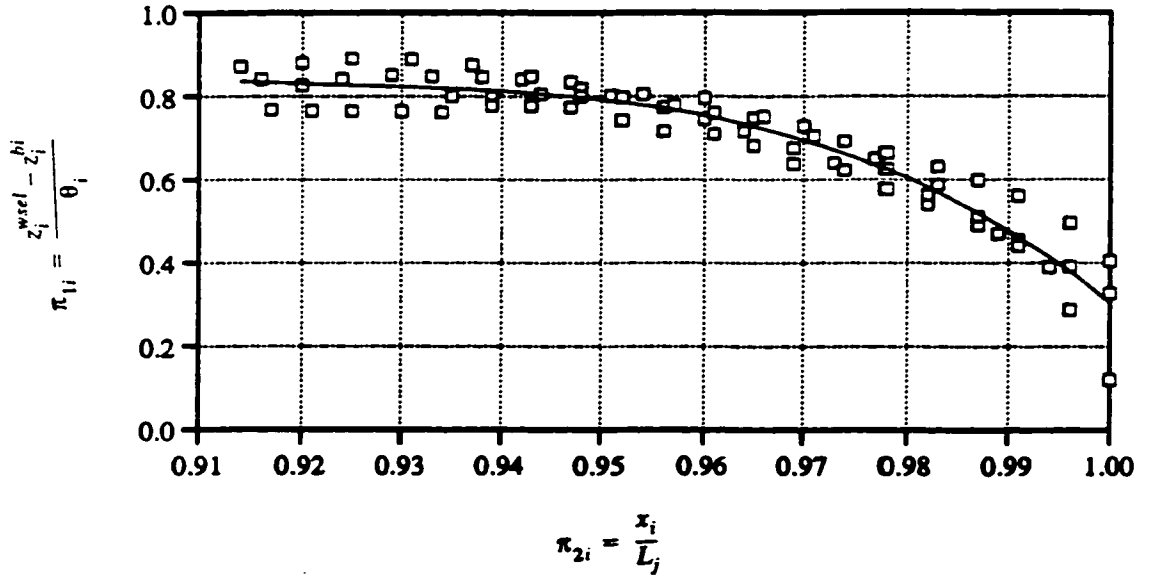

Figure 6.5: Penetration of water surface profile in polyethylene ice jams, from 0.91 L_j to1.0 L_j.

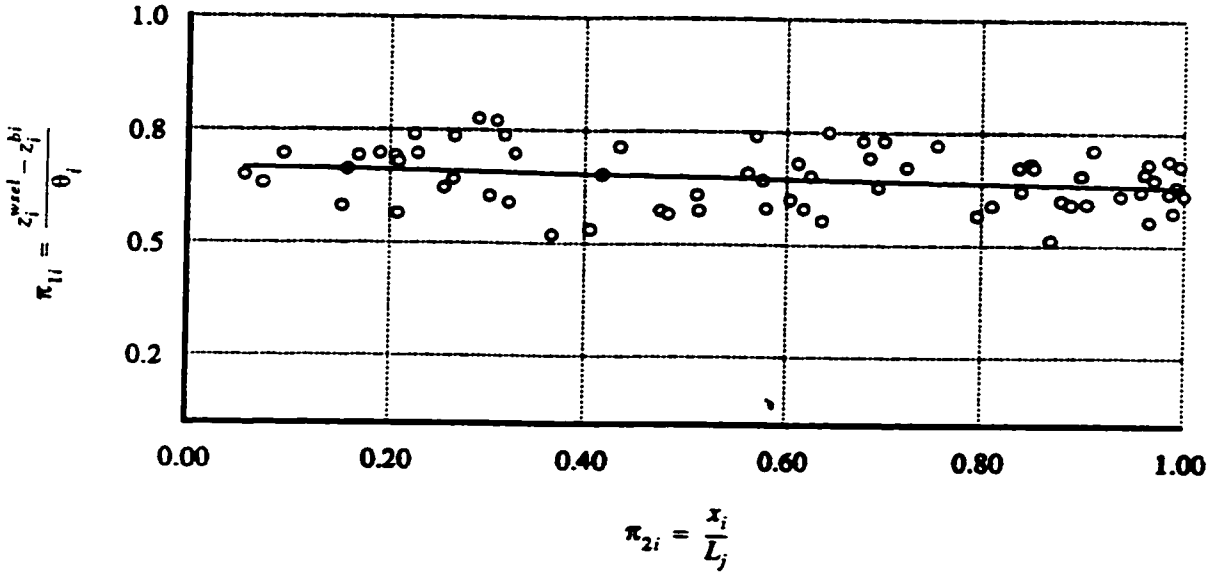

Figure 6.6: Penetration of water surface profile inwooden ice jams, from 0.0 Lj to 0.91 Lj

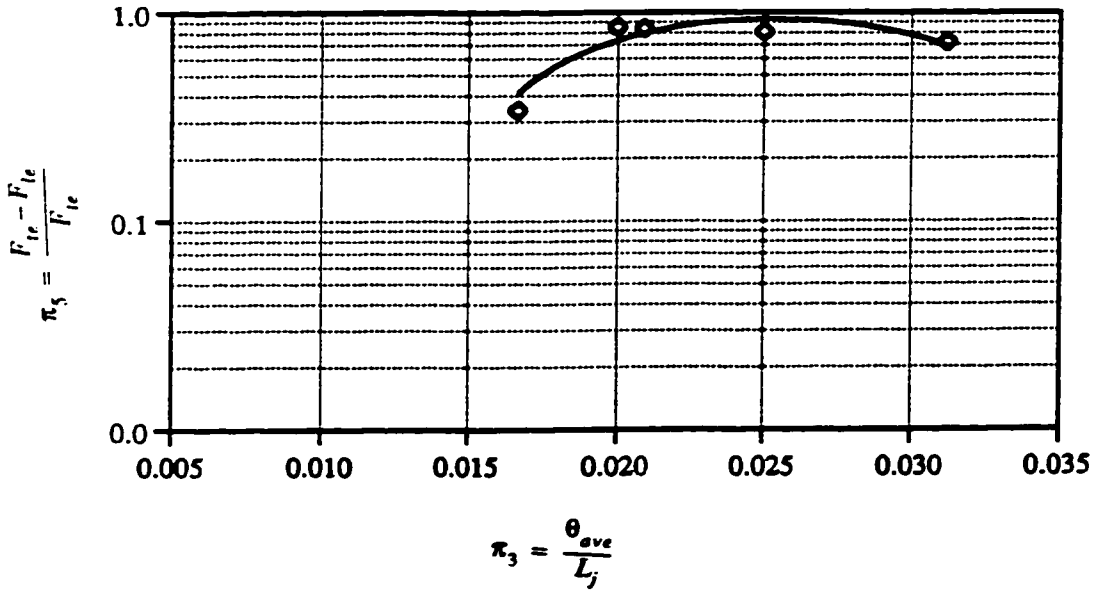

Figure 6.7: Global stability of ice jams (Polyethylene).

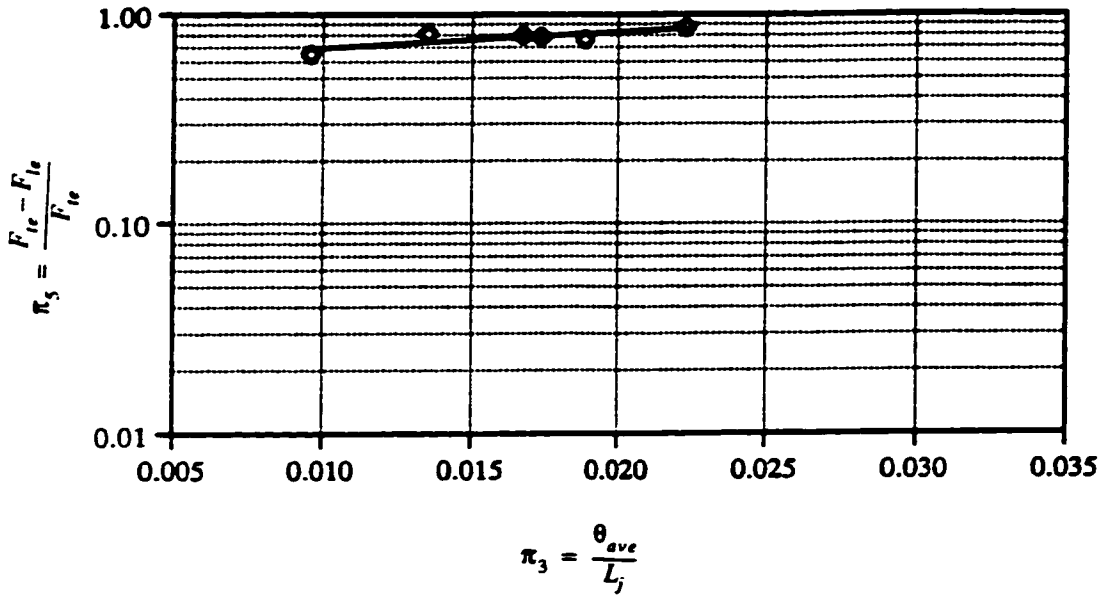

Figure 6.8: Global stability of ice jams (Wood).

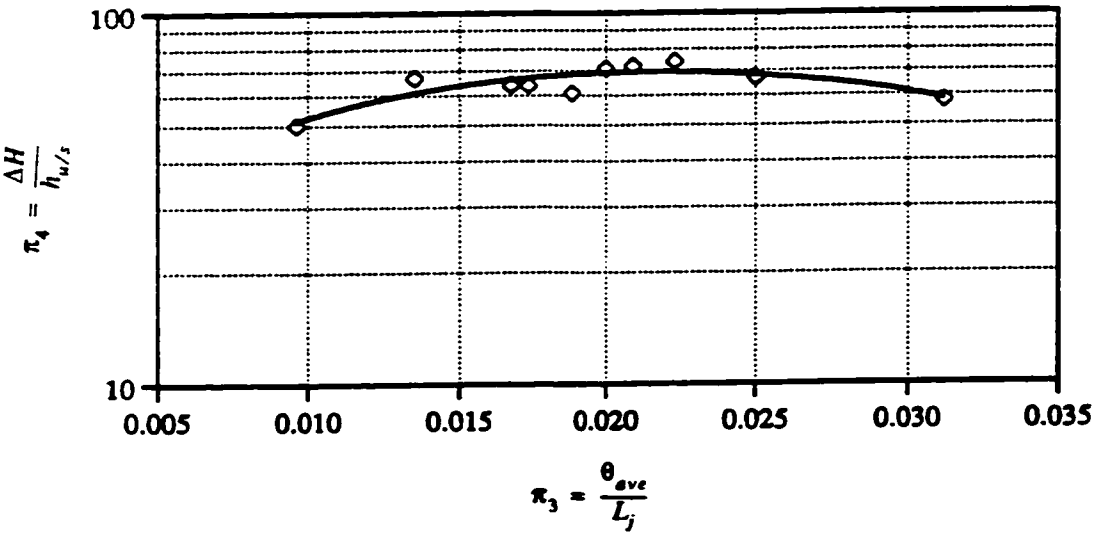

Figure 6.9: Total resistance of ice jams on main channel flow.

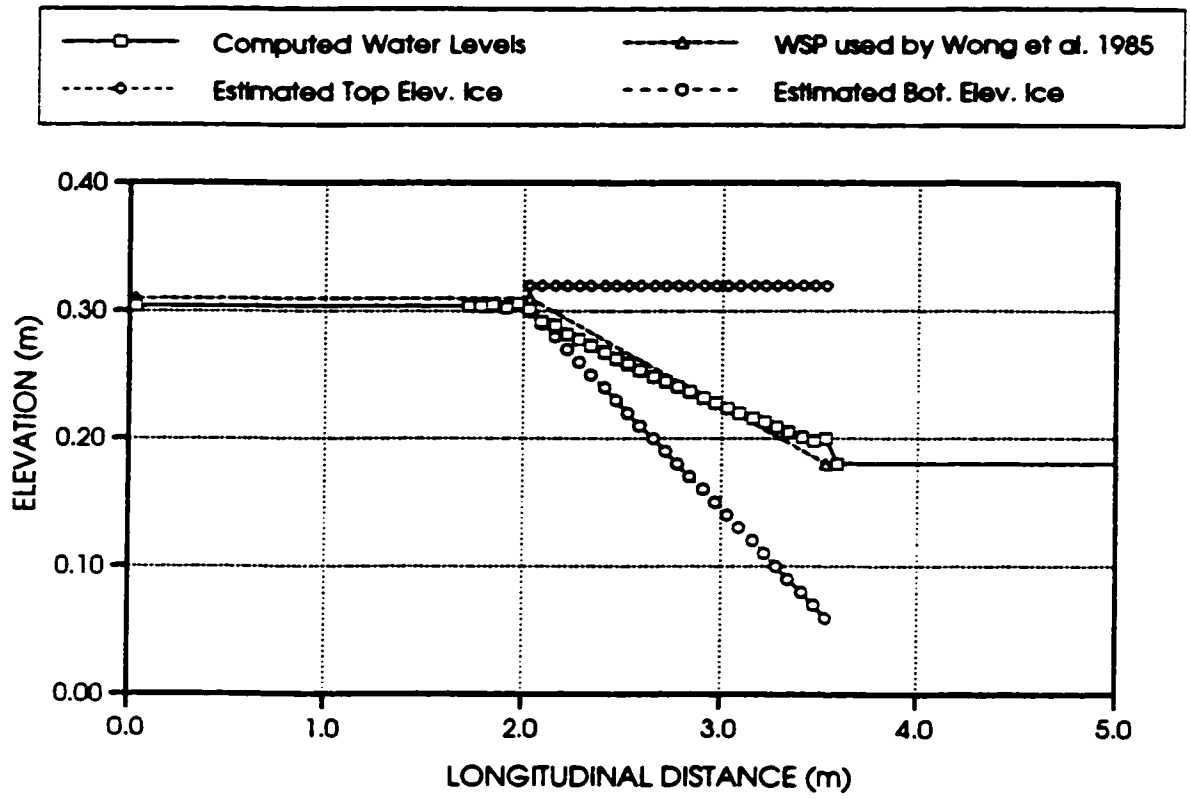

Figure 6.10: Computed and assumed water surface profile for test case 1.

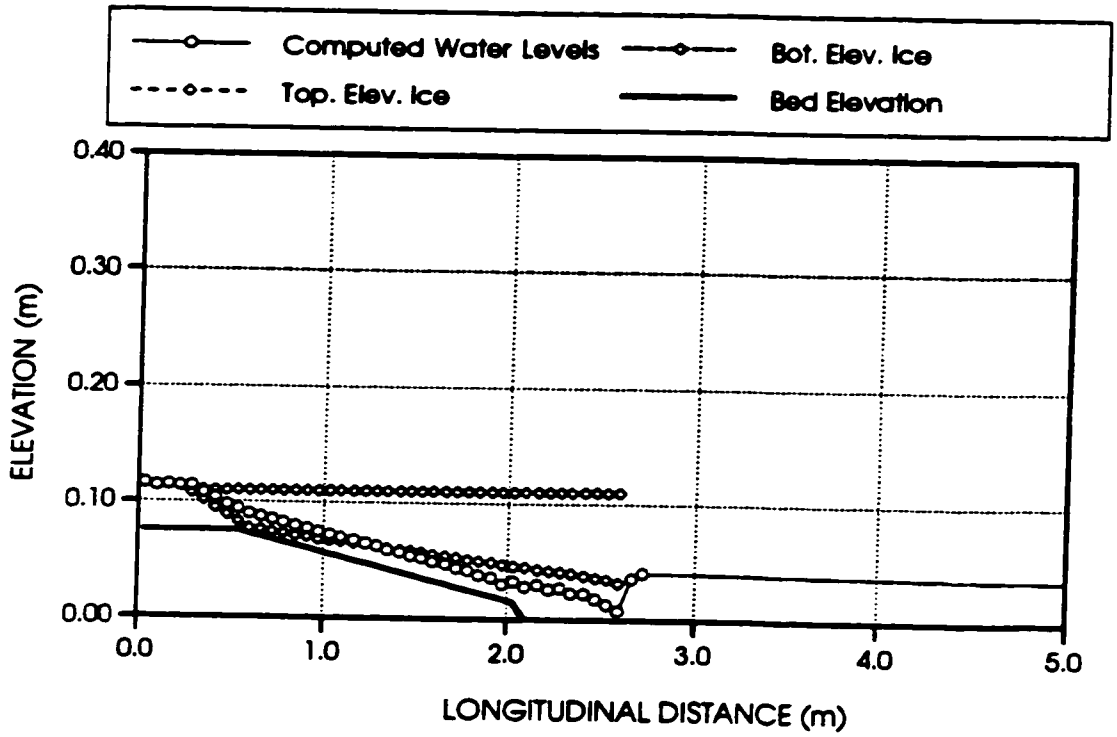

Figure 6.11: Computed water surface profile for test case 7.

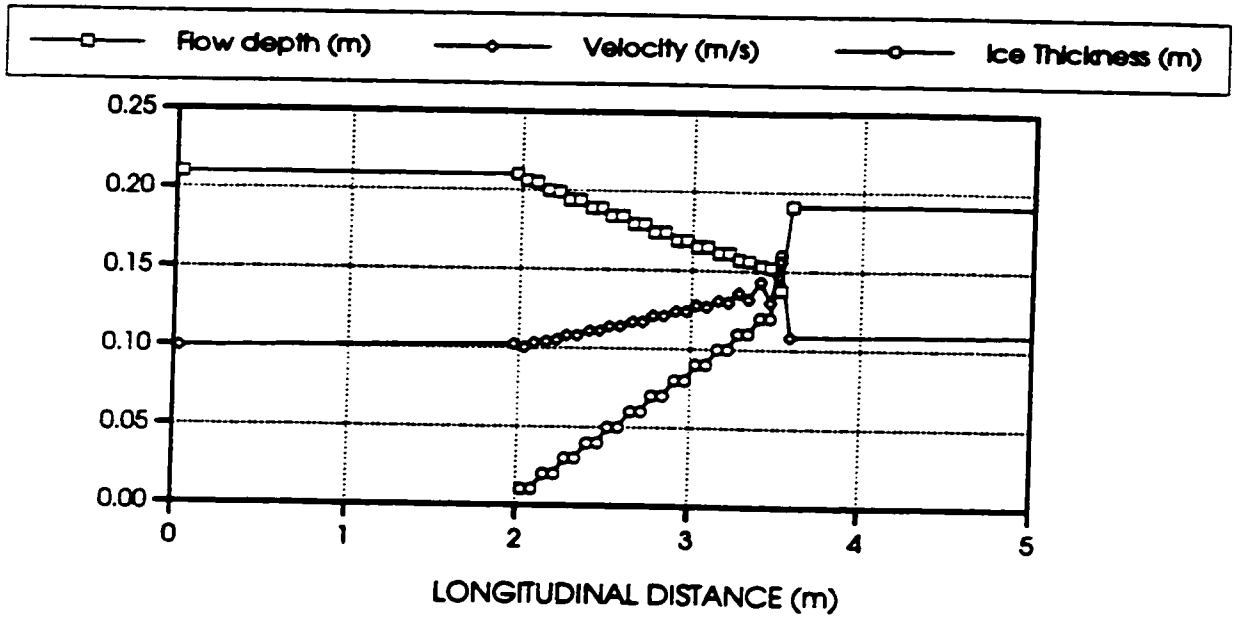

Figure 6.12: Computed hydrodynamic conditions for typical ice jam

CHAPTER 7.0

RELEASE OF ICE JAMS

In this chapter, the outcome of the work performed earlier in this study is used as the basis for modeling ice jam release events. Specifically, the results from chapter six are used to describe the initial conditions just before the release event, while those from chapter five are analyzed to verify the model computation results for ice mass transport.

The investigation of a release event is decomposed into two parts namely, the development of the ice run and surge immediately after release for a short duration of time and also the propagation and transport of the surge and ice run in the downstream direction.

7.1 Description of Ice Jam Release Tests (Experiments)

Immediately after release, and for a relatively short period of time, the ice mass, initially at rest, accelerates up to the point where its motion becomes constant. During the same period of time, a surge develops, accelerates and then propagate downstream at a constant speed. The instant of dislodgment of the ice jam marks the start of the release event. This event can be separated into two main parts namely, the transient part occurring during a short period of time after release and the ensuing steady part.

The results in this chapter are viewed and analyzed with respect to the changes in the water flow and ice conditions which occur during the above mentioned parts of the release event. In the first part and for a short period of time immediately after the release, four different processes occur in sequence as follows: (1) The ice mass suddenly dislodges (ice jam collapse); (2) A surge begins to form during the same time the jam is collapsing; (3) Both the ice mass and the surge transient character develops along the downstream direction and for a relatively short period of time; and (4) The steady transport of the surge and ice mass along the remainder part of the flume. The sudden dislodgment of the ice jam may occur under different release mechanisms which play the major role in defining the formation of the resulting surge as well as the ice run characteristics. The surge and the ice run during this initial transient part of the release event in turn, affect the character of the downstream propagation of the surge and of the ice mass transport.

Ice release mechanisms by which an ice jam gets dislodged are identified. The latter processes describing an ice jam release event was acquired from preliminary experimental observations. Although the transient part of the release event occurred in less than a second or two, the use of a video camera taping 30

frames per second provided considerable information and understanding through the observation of the processes involved. Therefore, in this section of the study, the analysis was carried out with respect to the two parts of a release event mentioned above (transient and steady). In section 7.2, the experimental observation are analyzed with one objective in mind, namely the understanding of the characteristics and behavior of ice jams during a release event. The observations are then quantified, the corresponding data are presented and finally, analysis of this data is carried out. As mentioned earlier, the observations and analysis are carried out in two parts namely the surge and ice run development (Section 7.2.2) and the d/s surge propagation and ice mass transport (Section 7.2.3)

Following the analysis of the observations, numerical simulations using the mathematical model are carried out for different test cases as shown in Table 7.1.

Table 7.1: General simulation test runs.

Test Case	Primary Objective(s)	Experimental Work
1	*Set a platform for comparisons* (Initial uniform conditions) (Water surface profile is linear)	Wong et al. 1985
2	Effect of non-linear water surface profile	Wong et al. 1985
3	Investigate differences between uniform and steady state conditions used for the initial conditions	Wong et. al 1985
4-tc1 4-tc2 4-tc3	- Influence of ice on surge calculations. - Numerical reproduction.	Wong et al. 1985
4-tc4	- Numerical reproduction	Present Study

The numerical simulations described in table 7.1 were performed to investigate the following:

1. Effect of the variation in the water surface profile before release on the surge characteristics (Test cases 1 and 2).

2. The difference between using steady state rather than uniform flow conditions immediately before release (Test cases 2 and 3).

3. The influence of ice mass on surge formation development and propagaton (Test cases 3 and 4).

It should be noted that test cases 1, 2 and 3 do not simulate the transport of ice mass after release, but consider the ice mass as a water body whose profile is identified as linearly varying from the upstream to the downstream levels or as non-linearly varying according to the results discussed in chapter 6.0. Test cases 4-tc1 to 4-tc4 include the numerical reproduction of different experimental text runs. The first three of them are of those carried out by Wong et al. 1985 and consist of a partial set of measured data namely hydrographs at 4 locations downstream of the ice jam and average ice from velocities. The last test case (4-tc4) is the numerical reproduction of a single experimental test case performed in the present study.

7.2 Present Experimental Observations

Prior to the numerical reproduction of surges and corresponding ice runs caused by the release of ice jams, a set of observations to that regard were compiled and analyzed in order to improve upon the understanding of the mechanisms under which an ice jam collapses during a release event. Observations were noted immediately after the release, at the toe of the ice jam and at a downstream location approximately 10 widths from the ice jam toe.

7.2.1 Description of experiments

Twelve experimental test cases were used for the analysis of ice jam release as shown in Table 7.2. A review of the hydrodynamic conditions immediately before release for these experimental test cases is also given in table 7.3. Nine of these experiments (experimental test cases 4 to 12) were already used for the analysis of the water surface profiles presented in Chapter 6. Out of the 12 experimental test cases, 5 were carried out using wood pieces (test cases 4, 5, 6, 9, and 10) while the remaining 7 were done using polyethylene pieces. Also, all of the 12 experiments were used to analyze the ice run and surge formation and development characteristics immediately after release, however only the last 6 experiments were used for the analysis of the downstream propagation of the surge and transport of the ice mass, since for those last six experiments another video camera became available and was used to record the downstream conditions following an ice jam release event.

Table 7.2: Laboratory test cases used for the analysis of surges.

Test Case	Development	Propagation	Type of Material Used
4	X		Wood Mix
5	X		Wood Mix
6	X		Wood Mix
7	X		Polyethylene Mix
8	X		Polyethylene Mix
9	X		Wood Mix
10	X	X	Wood Mix
11	X	X	Polyethylene Mix
12	X	X	Polyethylene Mix
13	X	X	Polyethylene Mix
14	X	X	Polyethylene Mix

Table 7.3: Initial conditions for release tests.

Test Case	Q(m^3/s) $X10^{-3}$	$h_{u/s}$ (m)	$h_{d/s}$ (m)	% Drop in Elevation
4 (W)	3.10	0.099	0.033	66.7
5 (w)	3.90	0.104	0.037	64.4
6 (w)	6.70	0.160	0.041	74.4
7 (P)	2.00	0.109	0.031	71.6
8 (P)	2.40	0.109	0.031	71.6
9 (W)	8.40	0.170	0.061	64.1
10 (W)	9.40	0.180	0.070	61.0
11 (P)	2.10	0.128	0.0425	66.8
12 (P)	3.50	0.118	0.050	57.6
13 (P)	1.10	0.049	0.030	38.8
14 (P)	1.40	0.0387	0.0321	17.1

Once an ice jam was formed and a significant drop in the water level was obtained, the polyethylene plate was lifted suddenly and a surge was allowed to form and develop followed by the ice run. The entire release event was recorded on two 8mm video cameras.

7.2.2 Surge formation and ice run development

Experimental observations of the conditions dominant immediately after the sudden release of an ice jam revealed that the trailing edge region of the jam dislodges under a specific mechanism. The characteristics of the ice run and the surge(s) were observed to be a function of this failure mechanisms. The region where the ice mass release mechanism occurs is identified along the stretch where the water level along the jam drops sharply and non-linearly.

Analysis of video recordings of the 11 experimental test cases have identified five release mechanism by which an ice jam collapses. This mechanism occurs under one of the following conditions:

Condition 1: Horizontal movement of front

Condition 2: Ice mass slide (similar to landslide)

Condition 3: Ice mass surfacing

Condition 4: Gradual leveling

Condition 5: Combinations of the above conditions

The latter five conditions under which ice jams in the laboratory were observed to collapse are dictated by the following parameters: extent at which the ice jam is lodged along the flume walls; the ice jam thickness profile at the trailing edge of the jam; the amount of blockage that the jam is imposing on the main flow; the drop in the water level across the jams leading and trailing edges; the ice floes properties; and the ice jam internal stress condition at the trailing edge region. Unfortunately most of these parameters are very difficult to evaluate if not practically impossible. However, certain assumptions could be taken to reduce the complexity of the problem. At present, the best that could be done is try to understand how these parameters could play a major role in identifying an ice jam release mechanism. Many more experiments are necessary before even an attempt is made to quantify these parameters. Considering the relatively limited number of experiments performed, a brief description of each of the release mechanisms are presented below:

Condition 1: Horizontal movement of front (Figure 7.1)

At release, the ice mass begins to accelerate from zero, and moves horizontally. Very little erosion of individual ice floes occurs at the leading edge region underneath the ice jam. This release mechanism is characterized by the

horizontal movement of the ice mass at the trailing edge region. The surge forms gradually as the ice mass accelerates and propagates ahead of the ice jam front.

Condition 2: Ice-mass slide (Figure 7.2)

Observations have shown that in the trailing edge region the ice mass above the water level slides along the water surface profile into the flowing water immediately after the trailing edge of the jam. This is analogous to a landslide event and can form surges significantly larger than those formed under the mechanism identified by condition 1. This condition is usually characterized by the formation of multiple surges developing according to the mode by which the ice mass falls into water.

Condition 3: Ice Mass Surfacing (Figure 7.3)

In this case, a significant portion of the ice jam is sheared along a failure plane. The sheared ice mass moves in front of the trailing edge and generates a local wave. This surfacing occurs very fast due to the buoyancy of the ice floes and the high water flow velocities. This type of release mechanism is characterized by the formation of one surge. This surge acquires a shape of a bell curve.

Condition 4: Gradual Leveling

The release mechanism by which the ice jam would collapse was observed to gradually drop upstream and rise downstream. A wave would form and develop simultaneously. The wave formed under such a release mechanism is identified by the gradual rise in the water level and not by a bell shape or sharp transition of the water surface.

Condition 5: Compund Failure (combination of conditions, Figure 7.4)

Observations have indicated that in most cases, two release mechanisms would occur simultaneously. The combination of two release mechanisms adds to the severity of the problem and results in more adverse conditions.

Table 7.4 identifies the release mechanism for each ice jam. Observations showed that ice jams made of polyethylene pieces have dislodged under a combined release mechanism, namely, condition 1 and 3. However, ice jams made of wood pieces dislodged under one release mechanism. Although ice jams made of wood pieces caused a greater drop in the water level across its leading and trailing edges, more severe conditions were obtained from ice jams made of polyethylene pieces. It is evident that the release mechanism is the primary factor affecting the severity of ice runs and surges caused by the sudden dislodgment of ice jams.

Table 7.4: Identification of release conditions.

Test Case	Condition	Combination ?
4 (Wood)	2	-
5 (Wood)	2	-
6 (Wood)	3	-
7 (Poly.)	5	1+2
8 (Poly.)	5	1+2
9 (Wood)	4	-
10 (Wood)	4	-
11 (Poly.)	5	1+2
12 (Poly.)	5	1+2
13 (Poly.)	5	1+3
14 (Poly.)	5	1+3

A general analysis of the 11 release events carried out in the laboratory have shown that in the initial stages immediately after release, a large portion of the ice jam in the trailing edge region is eroded in a relatively short period of time. Erosion of the ice jam at the trailing edge region may occur either from the top (above the water level) or from the bottom (below downstream water level), as shown in figure 7.4. After this initial erosion stage, the ice floes constituting the entire ice jam are transported downstream by the main channel flow in a single layer scenario. Their transport is characterized by little variation in the overall ice cover thickness profile and occurs in a relatively close pack accumulation with uniform variation in the surface area concentration. One would expect a more chaotic behavior due to multiple surges traveling in both upstream and downstream directions. However, the ice jam after release, which is more appropriately referred to as an ice cover accumulation, acts to attenuate almost all waves and surges and promotes uniform flow. Therefore, the only significant surge is the initial one.

Figures 7.5 and 7.6 give the position of the ice jam front as a function of time during the first second immediately after release for polyethylene and wood ice jams, respectively. It is evident from the two figures that the ice run accelerated, decelerated and became steady. The acceleration/deceleration occurred as a function of the release mechanism described earlier. For example, in test case 7, the ice jam accelerated during the first 0.2 sec., then decelerated and accelerated in sequence for a period of approximately 0.4 sec., and then proceeded again at a steady rate at a constant speed.

The time variation of the ice jam front position is typical for all test cases with little variation in the acceleration/deceleration/steady motion processes. Also, it has been observed and confirmed by figures 7.5 and 7.6 that this transient

character of ice mass motion immediately after release in general occurs in a relatively very short period of time. In this study, this period was of the order of 1.0 sec., or less. This behavior is also supported by field observations. For example, in one case on the Nashwaak River in 1902, according to an eye witness account, it was observed that "The ice run seemed to gain in power and velocity as it advanced. The force of ice and water carried away three large mill dams before the ice jammed near Stanley...Grounded on gravel deposits, this jam caused the Nashwaak River to rise to an unprecedented height and subsequently inundated numerous homes and farms...When this immense jam released, it carried away the 53m long Stanley Bridge..." (from Beltaos, S., 1988, Monograph on River Ice Jams). Also, no quantitative field observations of ice run and surge formation immediately after release are available since they occur very fast (Beltaos 1994). Instruments to obtain such data are not available. As a matter of fact, NWRI is presently in the process of designing instruments to measure in the field various ice and hydrodynamic conditions.

The development of the surge immediately after release for five (5) test cases is presented in figure 7.7. Similar to the ice run, the surge accelerated, decelerated, or moved in a steady motion. It should be pointed out that at time zero, the position of the surge front was at 270 cm from the inlet of the flume, and immediately after release, the surge could only be observed after approximately 10 cm and 0.15 sec. from release. This is indicative of the time frame in which the formation of the surge occurs. Beyond that time, the surge in general accelerated and propagated downstream at a constant speed. Compared to the ice run development shown in figure 7.5, the surge develops and propagates downstream at a faster rate as shown in figure 7.8. From a general point of view, for all test cases where polyethylene pieces were used, the speed of the surge as it developed was twice that of the ice run, and was estimated to be 0.75 m/s and

0.37 m/s, respectively. The ice run and surge development as a function of time for test cases 7, 8, 10, 11 and 12 are presented in figure 7.8. This figure shows the difference in the velocity of the surges and ice runs as well as their behavior immediately after release. In figure 7.8, the speed of the surge being approximately double the speed of the ice run is better shown. For example, in test case 8, the ice front takes approximately 0.9 seconds to reach position 300 cm along the flume while the surge arrives at this point in approximately 0.4 seconds. The conditions are relatively similar for the other test cases. Photo 7.1 gives snapshots of a typical ice jam release event at intervals of 1/30 of a second.

7.2.3 Downstream ice run transport and surge propagation

The characteristics of the ice mass transport and surge propagation in the downstream direction are evident in figures 7.9 to 7.12 and table 7.6. The variation of the average ice front velocity to the uniform flow downstream velocity ratio ($u_i/u_{d/s}$) as a function of the change in the uniform velocity across the edges of the ice jam (ΔU) is given in figures 7.9 and 7.10 for the polyethylene and wood ice jams, respectively.

Table 7.6: Observed downstream surge characteristics.

Test Case	$T_{arr.\ ice\ front}$ (sec.)	$T_{arr.\ surge}$ (sec.)	$V_{ice\ front}$ (m/s)	V_{surge} (m/s)	Max. Elevation (m)	$h_{u/s}$ (m)	$h_{d/s}$ (m)
10 (W)	6.00**	2.07**	0.353	0.90	0.100	0.180	0.070
11 (P)	5.47**	2.88**	0.429	1.00	0.082	0.128	0.042
12 (P)	4.53**	2.60**	0.545	1.05	0.083	0.118	0.050
13 (P)	6.60***	3.47***	0.39/0.63*	0.75/0.92*	0.040	0.049	0.030
14 (P)			0.11/0.16*			0.0387	0.032

* First value is the average value based on distance from trailing edge of stationary ice jam to 4.6m downstream of the inlet, just before the obstruction.
Second value is the average value based on distance across the edges of the obstruction which is 0.40m.

** Measured at approximately 5.80m from the inlet.

*** Measured at approximately 4.6m from the inlet.

These figures show the influence of the total force applied on the ice jam before release, on the downstream velocity of the jam front after release. It is evident from the figures that ice jams made of polyethylene pieces behave differently from those made of wood pieces. Figure 7.9 shows that when the force on the ice jam immediately before release increases, the ice front velocity after release relative to the downstream velocity before release decrease parabolically. Increasing the force on the ice jam immediately before release is due to an increase in the drop of the water surface elevation across the ice jam's leading and trailing edges. Consequently, the velocity downstream of the ice jam increases. This alone decreases the ratio $u_i/u_{d/s}$. However, one would expect that the variation of the downstream water velocity as a function of the drop in the water surface level across the ice jam's leading and trailing edges to be linear. Therefore, the variation of $(u_i/u_{d/s})$ would be expected to be linear as well. This is not true since the variation of the downstream ice front velocity as a function of the uniform flow velocity before release is not linear as shown in figure 7.11, and therefore the ratio $(u_i/u_{d/s})$ is not linear.

After the collapse of an ice jam, the ice run follows the surge as stated earlier. The downstream character of the surge or wave is depicted in figure 7.12. This figure presents the variation in the wave height at the crest location relative to the downstream flow depth as a function of the percentage of drop in the water surface level for test cases 11, 12, and 13. These three test cases provide a good range in the drop of water level basically from approximately 40% to 67%.

This figure gives an indication of the maximum water level which is to be expected downstream of the jam, for a given percent drop in the water level across an ice jam's leading and trailing edges.

Figure 7.12 shows that the maximum wave height h_{max} that could be caused by the release of an ice jam increases linearly with the increasing drop in the water surface elevation Δh across an ice jam's leading and trailing edges. This variation can be expressed by the following relation:

$$h_{max} = 0.021\Delta h - 0.495 \qquad (7.1)$$

For example, figure 7.12 shows that an ice jam giving a 50% drop in the water level across its leading and trailing edges can cause a wave height 0.7 the depth of the downstream flow or a downstream flow depth 1.7 the depth before release.

7.3 Numerical reproduction of experiments carried out by Wong et Al. 1985

The observation from the 11 ice jam release experiments provided a significant amount of insight concerning the behavior of the ice run, surge formation, downstream transport of the ice run and downstream propagation of surges after release. So far chapter 5.0 applied the numerical model to simple cases of ice mass transport in a release scenario. It is important to note that the ice floes in these tests were transported in a single layer where the thickness does not change in time and space, much similar to what was observed during the actual ice jam release events. In chapter 6.0, measurements of water surface profiles were taken for a set of experiments. In chapters 5.0 and 6.0,

computational results were compared with observations and measurements and showed good agreement.

The final and most difficult part of the numerical simulation process is the execution of the numerical model in a complete ice jam release test case. This includes the following computational stages which should be carried out in the exact sequence presented as follows:

A. *Obtaining initial conditions:*

Set the ice jam stationary, and impose the ice jam profile and run the model until hydrodynamic steady state conditions are attained.

Three parameters could be used to adjust for the upstream water level, namely the coefficients found in equations 6.7 and 6.8 and the ice jam profile. Some simulations were carried out to investigate the influence of Manning n for the ice cover underside on the upstream water level which indicated that the effect of n is small and its choice is not a dominant factor.

B. *Simulation of ice thickness redistribution and downstream transport:*

After setting up the input file consisting of all the parameters describing the flow conditions obtained from the previous run as the initial conditions, a second simulation run was carried out. This simulation included a user specified time at which the ice jam was dislodged and the option which allowed for calculating the transport of ice after the release.

When the time of release was attained, the conservation of ice thickness, the conservation of surface area ice concentration and ice transport equations were solved. The conservation of ice thickness equation is solved for the first second of the simulation time immediately after release. Beyond this one second

of simulation time, the conservation of ice mass was then solved instead. This technique of switching in the solution of different equations was based on observation. While analyzing the laboratory experiments, it was found that during the first second immediately after release, the ice mass thickness in the trailing edge region was redistributed due to hydrodynamic and gravity forces, and beyond that initial thickness redistribution phase, the ice jam was observed to float downstream with little change in its ice thickness profile. In order to numerically reproduce this behavior that was observed in the laboratory experiments, the conservation of ice thickness equation was solved at every iteration for the first second after release, thereby numerically reproducing the initial ice thickness redistribution through the simulation of the dispersion of the ice mass. The maximum dispersion occurred at the trailing edge region where high velocity gradients existed. After the first second and until the end of the simulation process, the ice mass conservation equation was instead of the ice thickness conservation, thereby numerically reproducing the transport of ice jam in a relatively single layer situation, again as observed in the experimental phase of the study.

7.3.1 Description of numerical test cases

The test cases carried out for the simulation of surges caused by the release of ice jams are presented in table 7.6. Basically eight simulation test cases were carried out. These simulation test cases were performed in a sequence which allows the investigation of the following different conditions on the surge characteristics: (1) Non-linear initial water surface profile versus a linear profile; (2) Steady state conditions used for the initial conditions or uniform flow conditions; and (3) This influence of ice run by computing the ice transport conditions versus

the assumption that the ice jams turns into a body of water. Simulation test case 4 is actually a series of test cases where five laboratory experiments are numerically reproduced and the analysis and comparison of the results are presented.

Table 7.6: Description of simulation test cases.

Test Case	Initial WSP Conditions	Initial Flow Conditions	Ice Flow After Release	Corresponding Experimental Test Case
1	Linear	Not S. S.	No	Wong et al. 1985 - Run 1
2	Non-Linear	Not S. S.	No	Wong et al. 1985 - Run 1
3	Non-Linear	S. S.	No	Wong et al. 1985 - Run 1
4 - tc1	Non-Linear	S. S.	Yes	Wong et al. 1985 - Run 1
4 - tc2	Non-Linear	S. S.	Yes	Wong et al. 1985 - Run 3
4 - tc3	Non-Linear	S. S.	Yes	Wong et al. 1985 - Run 5
4 - tc4	Non-Linear	S. S.	Yes	Test Case 13

S.S.: Steady State.
tc1: Test case number 1.

7.3.2 Numerical reproduction

The numerical reproduction of the simulation test cases 1, 2, 3, 4-tc1, 4-tc2, 4-tc3 was performed by first discretizing the physical domain into a uniform grid system composed of three cells in the y- direction and 80 cells in the x-direction. Each cell was therefore 0.25 m length and 0.10 m in width. An ice jam was imposed at a certain distance downstream of the flume inlet. Figure 7.13 shows the set-up used in test cases 1, 2, 3, 4-tc1. The same basic flume set up was used for test cases 4-tc2 and 4-tc3 with only the ice jam profile being different due to different hydrodynamic conditions, as shown in figures 7.14 and 7.15 repectively.

The ice jam thickness profiles that were imposed for the simulation test cases 1, 2, 3, 4-tc1, 4-tc2 and 4-tc3 are shown in figures 7.13, 7.14 and 7.15 respectively. Photographs other than the one presented in the paper by Wong et

al.1985 (see photo 7.1) were not available. The measurements of the ice jam thickness profiles were not taken and therefore were also not available. The approximate positions of the leading edge of the ice jams in test cases 4-tc1 and 4-tc3 were anywhere from 2 to 3 meters downstream of the inlet (Beltaos 1994). For test case 4-tc2, the leading edge was approximately 2 meters from the inlet (Beltaos 1994). The trailing edge of the ice jams for the latter three test cases were at the retaining porous gate. For all practical purposes, the leading edge of all the ice jams obtained from Wong et al. 1985 was taken at 2 meters downstream from the inlet as shown in figures 7.13 to 7.15. For the test cases 4-tc4 and 4-tc5, the uniform grid that was used to dicretize the physical domain was composed of 60 cells in the x-direction and 3 cells in the y-direction where the cell size was 0.125 m and 0.01 in the x and y directions repectively.

The ice jam thickness profile was imposed as per the information available. Specifically, for the ice jam that Wong et al. 1985 obtained in the laboratory, the ice thickness profile was obtained from one photo. When reproducing the experiments carried out in this study, the ice jam thickness profile was measured and imposed as such. The initial water surface profile was imposed according to the relation obtained in chapter 6.0. An inlet velocity of Q/A and the water depth at the tailgate were set constant throughout the simulation period for all the test cases.

7.3.3 Analysis and discussion of results

The results of the simulation test cases were analyzed and discussed with respect to two objectives, such that each objective was considered from two points of view, as follows:

Objective 1: Influence of initial water surface profile and hydrodynamic and ice conditions on surge propagation after release (test cases 1, 2, 3, and 4-tc1)

viewpoint a: Variation with time at different fixed positions.

viewpoint b: Longitudinal profiles as a function of time.

Objective 2: Numerical reproduction of laboratory experiments

Viewpoint a: Surge and ice front development immediately after release.

Viewpoint b: Downstream ice transport and surge propagation characteristics.

Figures 7.16 to 7.19 present the depth hydrographs for test cases 1, 2, 3 and 4-tc1 respectively, obtained at 10 m, 14m and 18m from the inlet. Starting with the results shown in figure 7.16, the initial water surface profile in this test case was assumed to vary linearly from the leading edge to the trailing edge of the ice jam. The hydrographs show the time of arrival of the surge and the peak flow depth at the three special locations along the flume. In this test case the surge maximum height did not attenuate along the flume and remained constant at approximately 25.5 cm. Figure 7.16 also indicate that the speed of the surge is nearly constant. Approximately 6.5m downstream of the retaining porous gate, the passing of two waves is simulated. Reflected waves (negative surges) traveling in the upstream direction at approximately a constant speed are also simulated. It should be pointed out that the initial velocity of the flow through the flume for test case 1 is estimated by dividing the flume discharge by the area of flow.

Test case 2 was carried out exactly as test case 1, however with a different water surface profile. In this test, the water surface profile was imposed according

to equations 6.7 and 6.8. The depth hydrographs are give in figure 7.17 which show that the wave traveled downstream at a higher speed as compared to that simulated in test case 1 and four waves were simulated rather than three. Re-executing test case 2, with different initial hydrodynamic conditions defined test case 3. The numerical model was run with a stationary ice jam imposed in place until hydrodynamic steady state conditions were attained. This case gave more realistic conditions since this is what is expected to occur in nature. Higher downstream and lower upstream velocities were computed. The depth hydrograph for test case 3 is given in figure 7.18. In this test case, waves that look more like surges with sharp discontinuity in the water surface profile were simulated. The peak of the downstream traveling surges were less than those computed in test cases 1 and 2. This was due to the higher downstream velocities which imposed less resistance to the surge as it propagated in the downstream direction over the main channel flow depth.

Up to now, the simulation of the ice jam release in test cases 1, 2, and 3 was carried out by neglecting the effect of the ice mass on the main flow in general and on the surge in particular. Therefore, the ice transport after release was not simulated. In order to investigate the influence of the ice mass on the surge characteristics, test case 4-tc1 was carried out for that purpose. The depth hydrograph for this test case is given in figure 7.19. It could be quickly established that the ice mass did have considerable effect on the waves propagating in the downstream direction as well as the reflected wave characteristics. The differences in the surge characteristics and conditions between test case 4-tc1 and the previous three test cases could be summed up in terms of the following factors: (1) downstream propagation of surge; (2) number of waves generated by the release; (3) height development of generated waves; and (4) reflected wave characteristics. The following are clearly evident from the figure: (1) some

generated waves get damped out along the downstream direction; (2) the reflected wave dissipates as it travels in the upstream direction and; (3) the peak of the wave slightly attenuates in the downstream direction.

The differences in the flow depth hydrographs of test cases 1, 2, 3 and 4-tc1 are shown in figures 7.20 to 7.23. These figures present a comparison between test cases 1, 2 and 3 (figure 7.20), test cases 1 and 4-tc1 (figure 7.21), test cases 2 and 4-tc1 (figures 7.22), and test cases 3 and 4-tc1 (figure 7.23). It could be deduced from figure 7.20 that differences increase along the downstream end of the flume. Specifically, the difference in the peak wave height between test cases 1 and 2 at 10 m and 18m from the inlet is significant and estimated at approximately 3.5% and 5%. As discussed earlier, the influence of the ice mass on the downstream as well as upstream propagation of the surge is clearly shown in figures 7.21, 7.22 and 7.23 where the hydrographs for test case 4-tc1 are compared to those of test cases 1, 2 and 3 at 10m, 14m and 18m from the inlet respectively. A few major differences are listed as follows:

a) In figure 7.21, two waves followed by a smooth drop in the water level is simulated in test case 1, while five waves followed by a sharp drop in the water level is simulated in test case 4-tc1.

b) At all three locations along the flume, the wave in test case 4-tc1 is simulated to travel faster than that in the other test cases.

c) Higher peak values of water levels are obtained in test case 4-tc1 (figure 7.21, all three graphs; figure 7.22 third graph; and figure 7.23, third graph).

Longitudinal water surface profiles for test cases 1, 2, 3 and 4-tc1 are given in figures 7.24 to 7.27 repectively. Similar to the flow depth hydrographs, the water surface profiles for the four above mentioned test cases at different times are

compared to each other in figures 7.28 to 7.32. In the first series of figures (figure 7.24 - figure 7.27) the water surface profiles at about 0, 1, 2, 3, 4, 5, 6, 10, 20 and 30 seconds are illustrated. These figures show the pattern of the upstream water level drop as well as the rate at which this fall occurs. These figures also represent the instantaneous water surface level profile at one section in time. For example, the average rate at which the upstream water level drops is 2.47 cm/s, 2.1 cm/s, 2.2 cm/s and 2.5 cm/s for test cases 1, 2, 3, and 4-tc1 respectively. After the release of the ice jam, the water level upstream drops at the rate indicated above and levels out towards the downstream water level. In test case 4-tc1 however, the upstream water level continues to drop up to another 20% below that of the downstream depth. This is a clear indication that a negative surge traveling in the upstream direction is being simulated at the same time as that of the surge propagating downstream. It should be pointed out here that the drop of the water surface level upstream of the ice jam occurs at a non-linear rate such that this rate increases to a maximum and then decreases back to zero, where the water surface levels out to that of the downstream water level.

Figures 7.28 to 7.32 present a graphical comparison between the four test cases at five different points in time namely, 0, 1, 2, 5, and 30 seconds. The initial water surface profile across the ice jam's length is shown in figure 7.28. It should be noted that the profile at time 0 seconds for test case 4-tc1 is the same as that of test case 3. Immediately after release and at approximately 1 sec., the negative and positive surges formed in test case 4-tc1 are evident in figure 7.29. Test cases 1, 2 and 3 do not produce any negative surges. Also, the surge formed in test case 4-tc1 travels faster in the downstream direction, as compared to those simulated in the first three test runs. From then on figures 7.30 to 7.32 confirm that the difference in the surge characteristics between the four test runs remain unchanged.

Having analyzed the major parameters and conditions that affect the propagation of a surge caused by the sudden release of breakup ice jams, test cases 4-tc1, 4-tc2, and 4-tc3 were carried out to reproduce numerically three experimental test cases carried out by Wong et al. 1985 and compare the computational results with the measured values. Figures 7.33, 7.34 and 7.35 present the results obtained from the model computations as well as those measured in the laboratory (Wong et al. 1985), analytical model (Henderson and Gerard 1981) and another one-dimensional model (Beltaos and Krishnappan 1982). It can be seen that the agreement between the measured levels and predicted ones using the present numerical model is good for all the test cases. There is a discrepancy in the results between the present model computations and measurements which occurs for a certain period of time.

In the studies of Wong et al. 1985, a similar discrepancy was noticed and it was attributed to the fact that during the time at which the discrepancy occurred, the ice blocks were traveling across the measuring instrument. Therefore, during the passage of the blocks, the float gauge which was used to measure the water surface levels, rides over the ice blocks and produces a trace that is irregular and higher than the actual water level. In order to investigate the model performance in terms of the flow depth and ice velocities and with respect to other analytical and other numerical modeling studies, observed and predicted maximum water levels and times of travel of the ice jam front are summarized in tables 7.7 and 7.8. The present numerical model gives good overall predictions for both maximum water levels and the ice jam front velocity. Actually, the present numerical model provides an improvement to practically all three test cases and for both maximum water levels and times of travel of ice jam front. Tables 7.7 and 7.8 also present the percentage improvement to the analytical and other model. These percentages are given in brackets where the

first and second percentages give the improvement of the present numerical model with respect to the analytical and other numerical model predictions, respectively. For example, the maximum improvement was shown to be 10.7% with respect to the analytical solution of the maximum water level and 58.5% with respect to the analytical solution of the ice jam front travel time.

Table 7.7: Computed and measured maximum water levels (cm).

Test Case	Q(m^3/s) X 10^2	Δh (cm)	Measured (cm)	Analytical (cm)	Other model (cm)	Present model (cm)
1	2.6	15.0	26.5	23.5	24.5	25.3 (6.7%, 3%)
2	2.0	7.0	21.9	19.2	18.0	19.0 (0%, 4.5%)
3	2.5	3.0	23.2	20.5	23.6	23.0 (10.7%, 0.85)

Table 7.8: Time of arrival of ice jam front (seconds).

Test Case	Measured	Analytical	Other model	Present model
1 @ch.8	7.0	8.0	9.0	6.5 (7%, 21.4%)
1 @ch.18	46.0	24.0	53.0	51.0 (58.5%, 4.4%)
2 @ch.8	11.0	11.0	14.0	14.0 (0%, 0%)
2 @ch.18	55.0	36.0	79.0	49.0 (23.6%, 32.7%)
3 @ch.8	12.0	18.0	16.0	14.0 (33%, 16.7%)
3 @ch.18	65.0	56.0	72.0	70.0 (6.1%, 3%)

Another very important consequence of ice jam release is the ice run that develops. The latest study related to the investigation of ice runs is that of Wong et

al. 1985. However, their analysis included only a brief statement of their observations and there is no quantitative data concerning the processes involved during an ice run occurring after an ice jam release (Beltaos 1994). Visual evidence during the experiments carried out by Wong et al. 1985 has shown that the thickness of the moving jam changes with distance traveled and time elapsed, after release. The change in ice thickness as a function of time and space was assumed to be caused by dispersive and flotation effects. They finally stated that this phenomena is important when ice jam reformation is considered, because it would influence the incoming ice discharge. Similar phenomena have been observed during the laboratory experiments carried out in the present study. However, by carefully reviewing the video tapes of over 12 ice jam release test cases and by directly observing in excess of 25 experiments, it was found that the change in thickness of the ice jam after its release is caused by mechanical processes rather than dispersive and flotation effects. Observations based on this study revealed that after the release of an ice jam, a major portion of the ice mass in the trailing edge region is eroded by shearing along a certain failure plain, and that this occurs in a very short period of time. After this initial dislodgment stage, the ice jam becomes an ice cover accumulation which moves downstream at a high speed. As the ice cover accumulation travels downstream, it expands by the process of dispersion of the ice mass alone. This means that the local thicknesses of the ice cover accumulation does not change, and only the surface area ice concentration decreases. Assuming that there is no obstruction along the ice run passage, two cases are identified from observations, by which the ice cover accumulation could change in thickness: 1) a local velocity gradient sufficiently strong to erode one or more layers of the ice mass, such that when this layer is eroded, it will rise into an open area through the process of buoyancy; 2) a local obstruction from the sides or bottom of the

channel which has the same effect as in (1) and results in the retardation of one or more ice floe layers and consequently floatation of the ice pieces from the ice cover accumulation underside and therefore change in thickness. In either two cases, the local surface area ice concentration increases as the local ice cover thickness in the same location decreases.

In order to investigate the conditions occurring during an ice run event, test case 4-tc3 is selected for further detailed analysis. Figures 7.36 to 7.40 illustrate the profiles as a function of time for the flow depth, flow velocity, ice velocity, surface area ice concentration, and ice cover accumulation thickness, respectively. This set of figures constitutes the five primary parameters describing the evolution and progression of an ice cover accumulation after an ice jam release event. The computed ice run characteristics represented in these five figures correspond very closely to the observations by Wong et al. 1985 as well as the observation made in the present study. Considering figure 7.38 which presents the velocity profiles of the ice cover accumulation at time t=1 sec., the ice jam is subjected to a positive as well as a negative surge (figure 7.36) such that in the leading edge region, the ice accumulation acquires a velocity in the same direction as that of the negative surge. The inverse occurs in the trailing edge region. As the ice cover accumulation moves downstream with the flow, the local ice velocities gradually decrease and at a certain point in time attain the velocity of the main flow. In this case, the maximum velocity of the ice run exceeds that of water by approximately 60%, and this occurs around 1 second after the time of release. After approximately 40 sec., the velocity of the ice cover accumulation becomes uniform and attains the same velocity of the flow, which in this case is approximately 0.1 m/s.

Surface area ice concentration and ice cover accumulation thickness profiles presented in figures 7.39 and 7.40 show the dispersive effects evaluated by the present numerical model. The surface area ice concentration is maximum at time t = 0 and decreases as a function of space and time. An interesting aspect is shown in figure 7.39. The surface area ice concentration profile develops two peaks, after two seconds from release, such that the upstream peak is always larger than the downstream one as the ice cover accumulation moves downstream. However, the difference in these peaks decreases in time from 74% at time t = 2 sec. to approximately 55% at time t = 60 seconds. The upstream peak itself decreases non-linearly by approximately 77% in 60 seconds. In accordance with the behavior of the surface area ice concentration, the ice cover accumulation profiles, figure 7.40 also show the dispersion of the ice mass as well as its downstream transport in a single layer formation. By cross-examining the flow velocity profiles and the ice cover accumulation thickness profiles, it could be shown that at the point where very little water velocity gradient exists, little dispersion of the ice cover thickness occurs and only the surface area ice concentration decreases due to the dispersion of the ice mass.

The characteristics of the ice jam front downstream progression and the water surge propagation are investigated from a global point of view in order to note general patterns and tendencies. This is done by analyzing the downstream movement of the ice jam front and surge for the three test cases 4-tc1, 4-tc2 and 4-tc3. Figures 7.41 and 7.42 illustrate the position along the flume as a function of time of the ice jam front and surge, respectively, for the three test cases. It is evident from figure 7.41 that in all test cases, the downstream travel of the ice jam front as a function of time is non-linear and implies that the ice jam front undergoes acceleration/deceleration/uniform motion processes, as has been observed in the laboratory. However, the downstream propagation of the surge is

linear, as shown in figure 7.42. The ice jam front and surge downstream movement are also viewed with respect to each other for each of the three test cases as illustrated in figure 7.43. This figure shows that for all of the three test cases the ice jam front begins its travel in the downstream direction at speeds as high as the surge and then decelerates in a parabolic fashion until it reaches the speed of the main channel flow. However, the surge continues to propagate downstream at a constant speed.

One final simulation test case, r4tc4, was carried out by reproducing experimental test case 12 performed in the present study. Figures 7.44 and 7.45 present the measured and computed ice jam front and surge front development respectively. Table 7.9 however gives the measured and computed downstream travel times and average velocities of the ice jam front and surge. Both figures show that the computed results do not reproduce the acceleration and deceleration effects as has been observed. However, the propagation of the ice jam front as well as the surge front immediately after release are well simulated. In any case, the computed results are overestimated, thereby simulating the ice jam front and surge to travel faster than that observed. The average difference between the computed and measured ice jam front and surge travel as a function of time is in the order of 10% and 15% respectively.

The difference between the measured and computed results can be attributed to the fact that the mechanism of failure of the ice jam during release is not accounted for in the model. It is obvious that the ice jam retards the formation and development of the surge by approximately 100%. This means that immediately after release, the surge, measured, developed in twice the time of that computed, again evidence of the effect of the ice jam on the surge formation and propagation.

Table 7.9: Ice jam front and surge characteristics for test case r4tc4.

	$T_{arr.\ ice\ front}$ (sec.)	$T_{arr.\ surge}$ (sec.)	$V_{ice\ front}$ (m/s)	V_{surge} (m/s)	Max. Elevation (m)
Measured	4.53	2.63	0.545	1.05	0.083
Computed	5.01	3.06	0.475	1.19	0.071
Difference (%)	9.5	16	13	13	14

The measured and computed travel time of the ice jam and surge fronts as well as the average velocities in the downstream region approximately 5.8 m from the inlet are presented in table 7.9. The percentage difference between the measured and computed results are slightly higher than 10%. This difference is rather significant and can be attributed to the fact that the effect of ice jam on the surge development immediately after release is not totally accounted for.

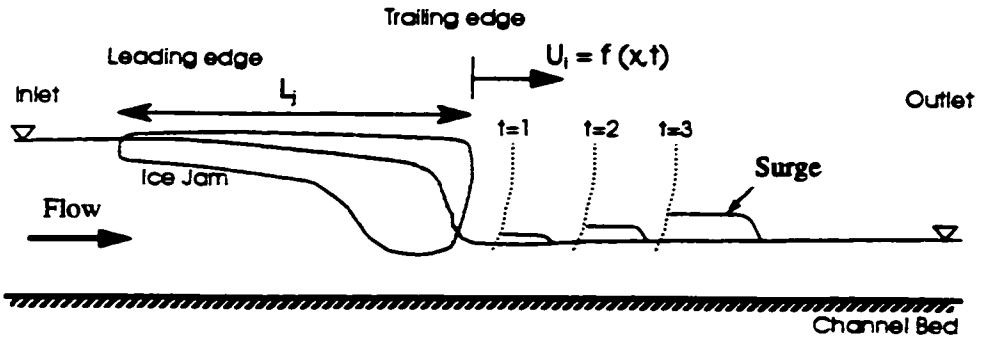

Figure 7.1: Horizontal movement of ice jam from (Scenario 1).

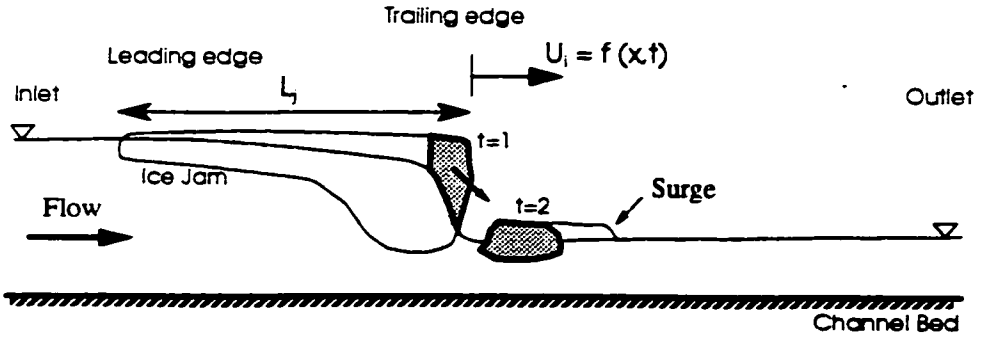

Figure 7.2: Ice mass slide (Scenario 2).

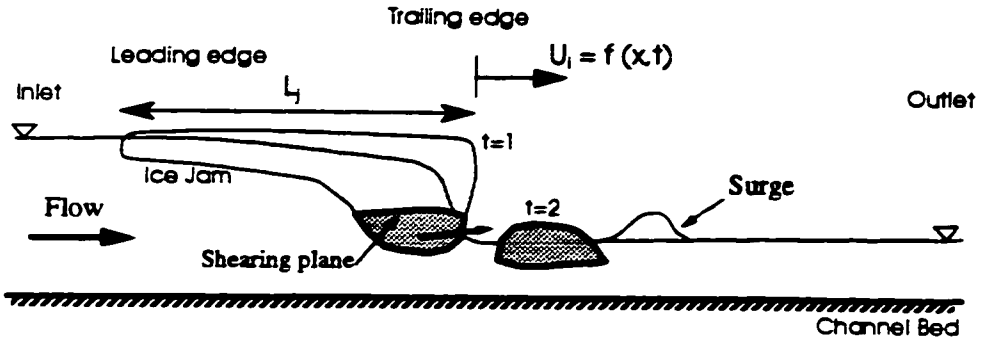

Figure 7.3: Ice mass surfacing (Scenario 3).

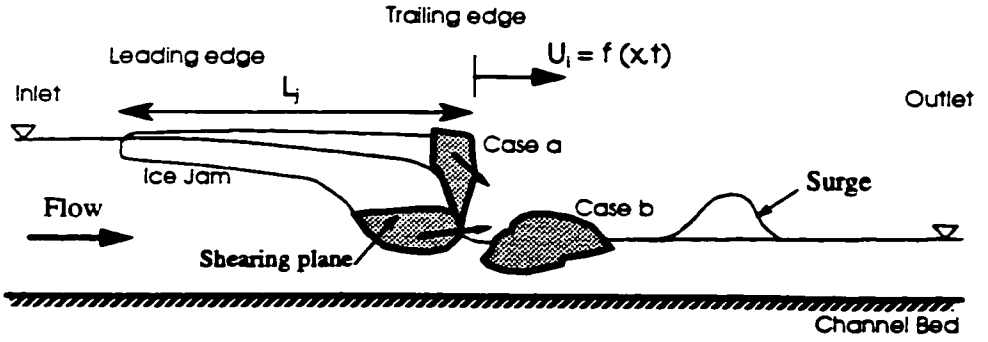

Figure 7.4: Combination of two scenarios (Scenario 5).

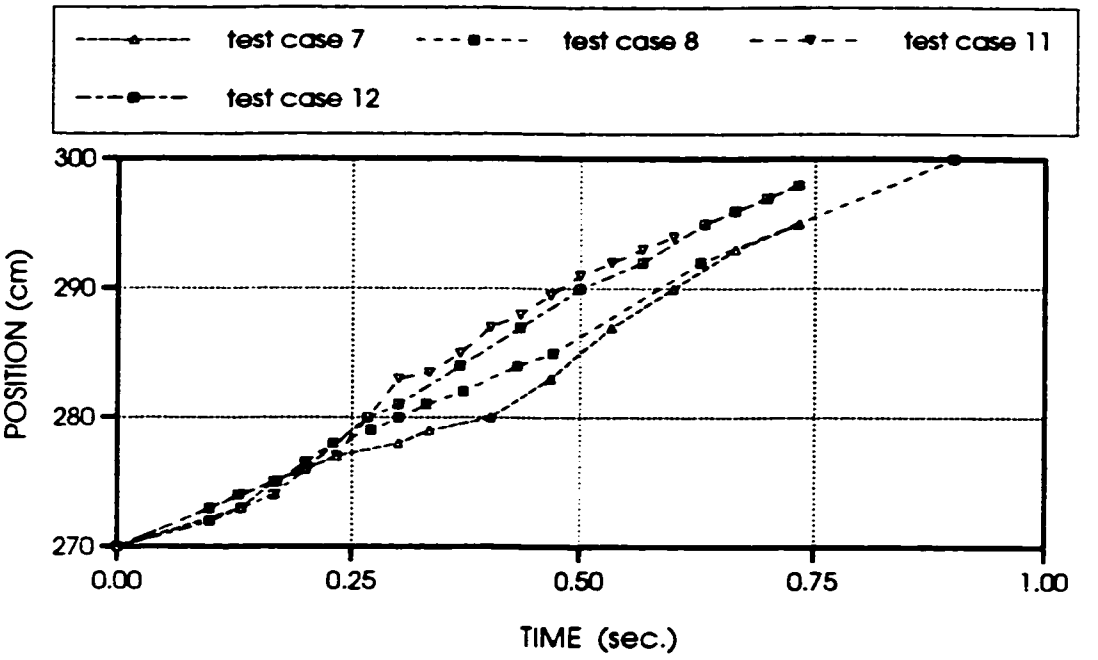

Figure 7.5: Observed ice run development (Polyethylene)

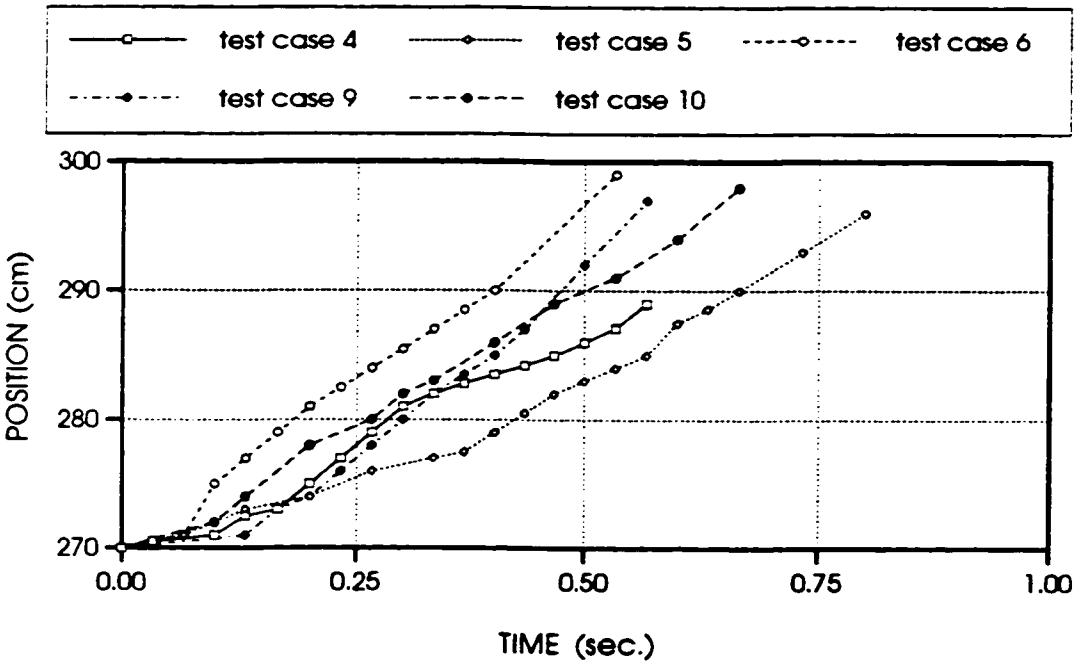

Figure 7.6: Observed ice run development (Wood)

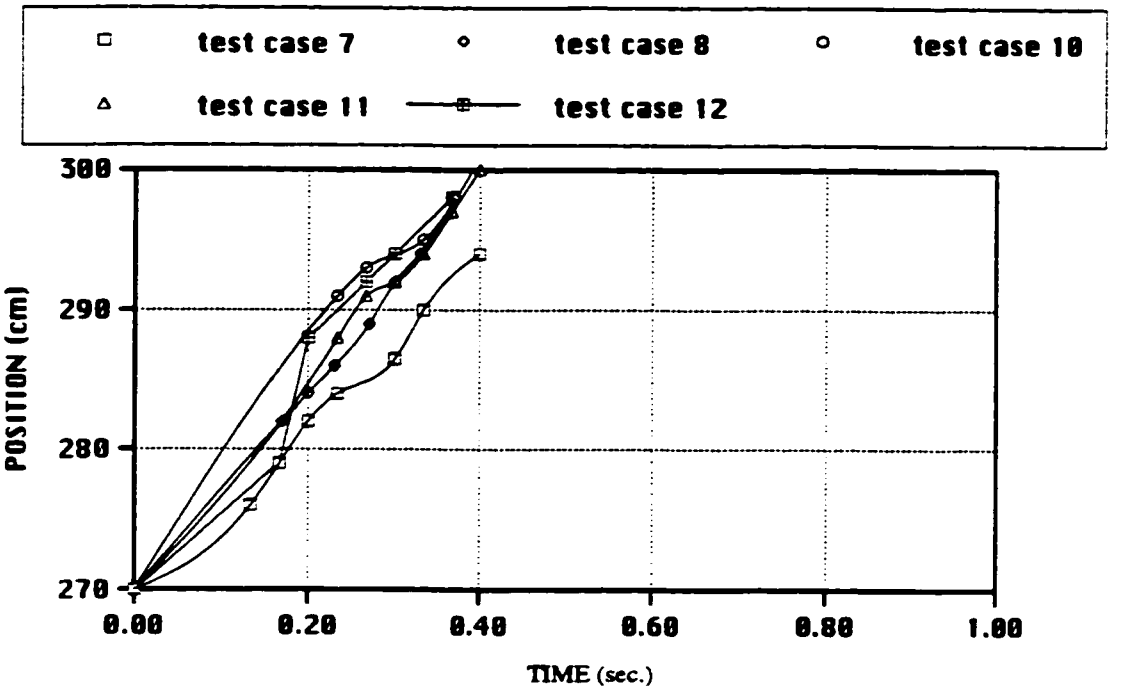

Figure 7.7: Observed surge development

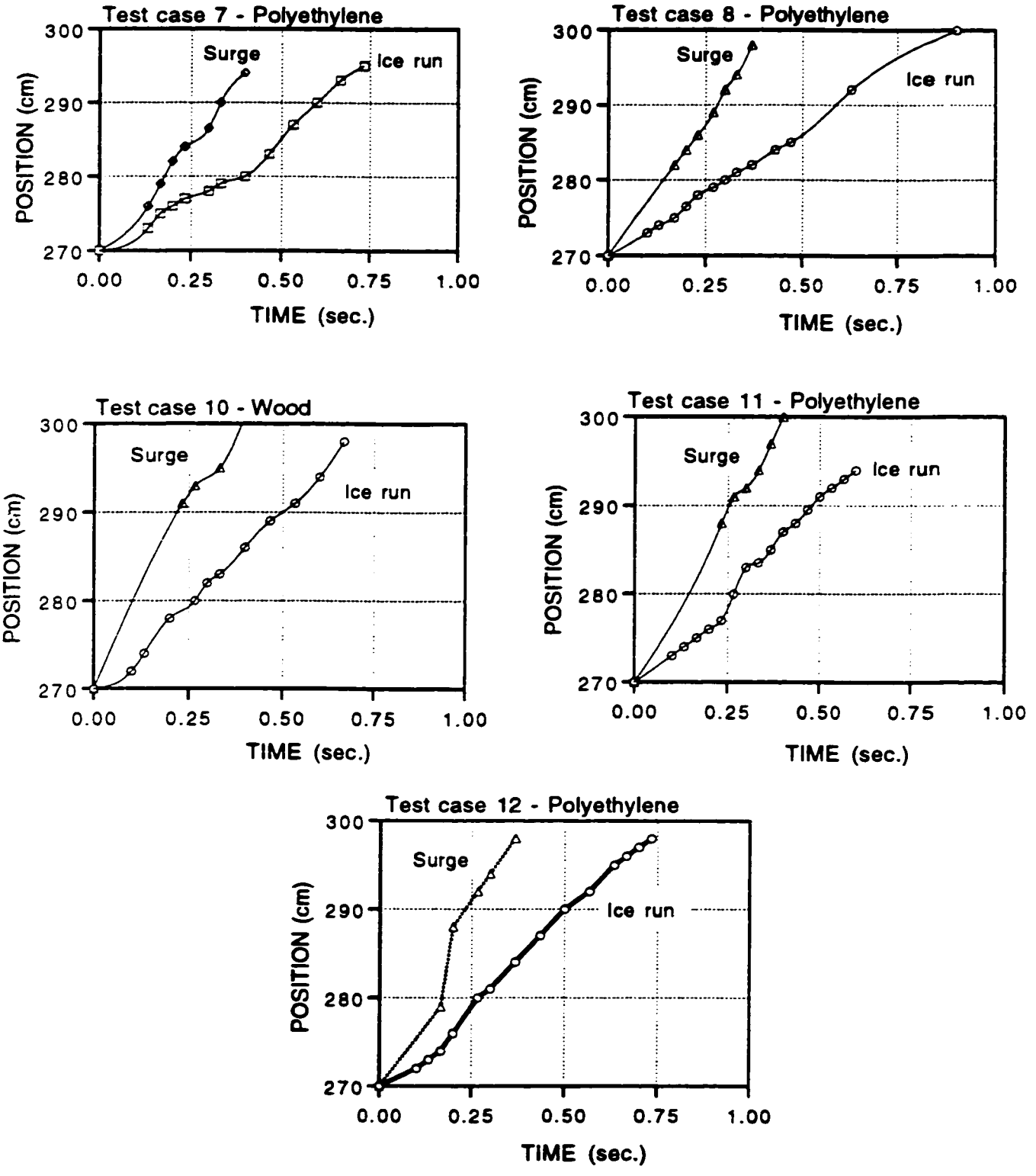

Figure 7.8: Observed ice run and surge development

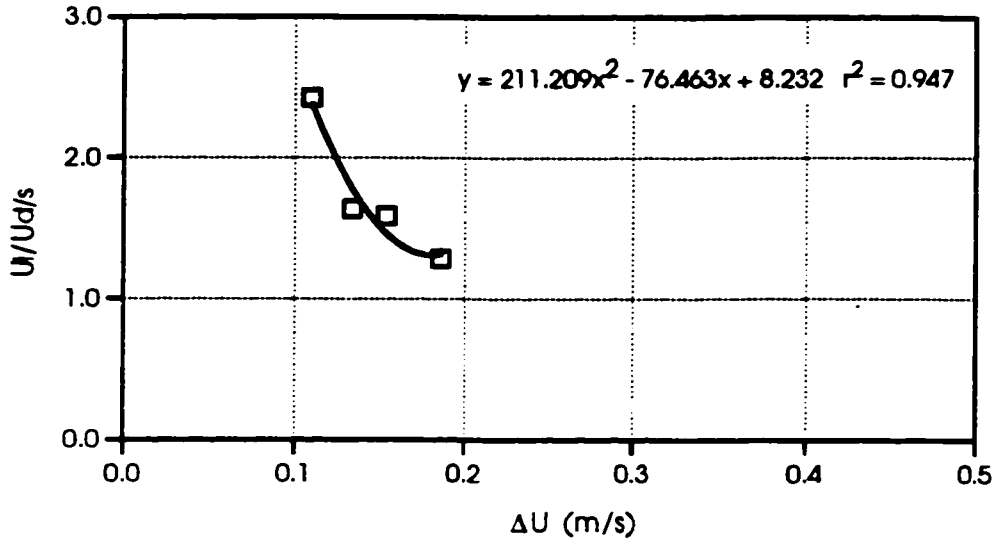

Figure 7.9: Donwstream travel of ice front (Polyethylene)

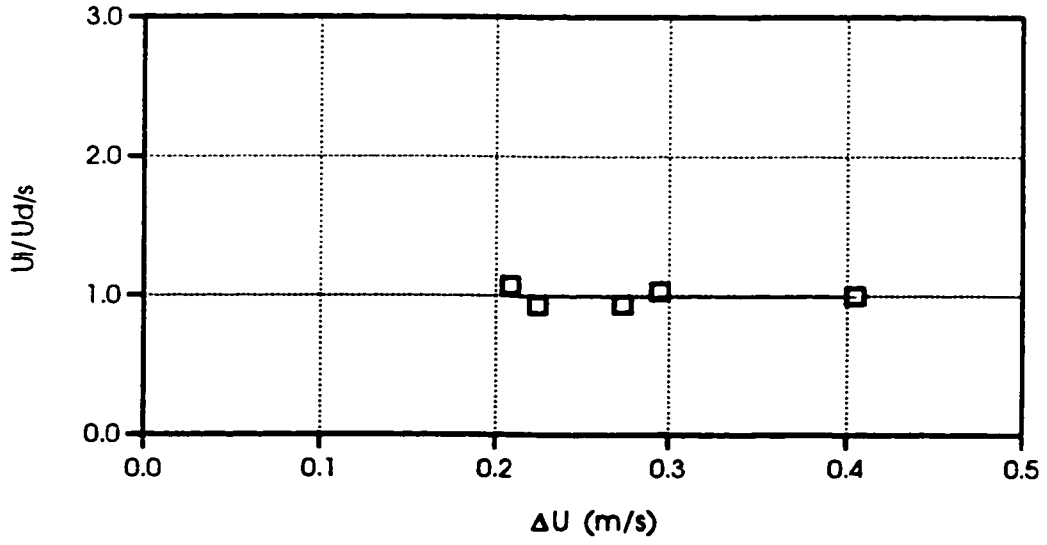

Figure 7.10: Downstream travel of ice front (Wood)

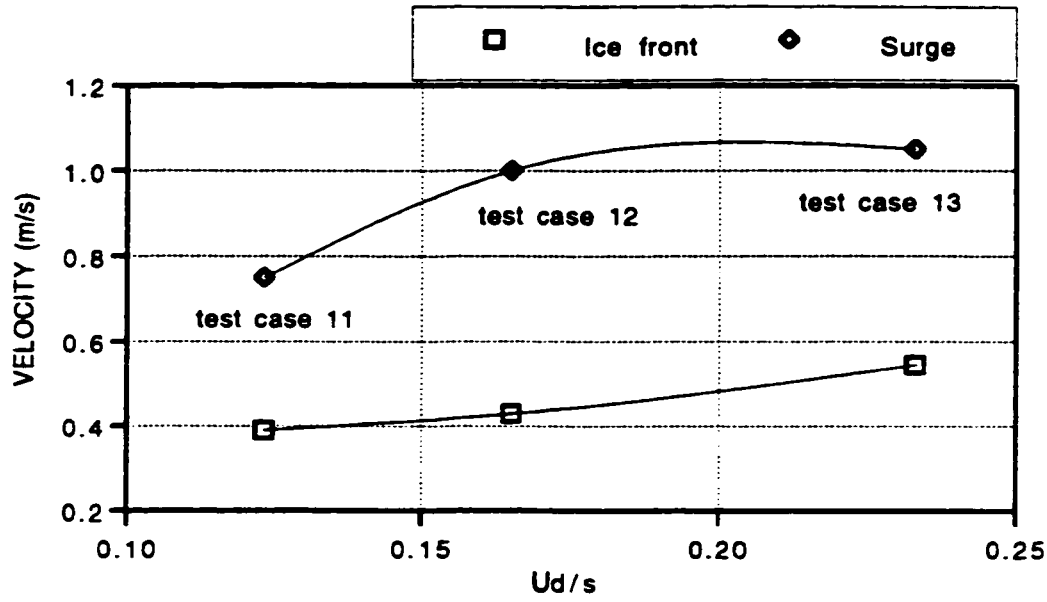

Figure 7.11: Donwstream propagation of ice front and surge

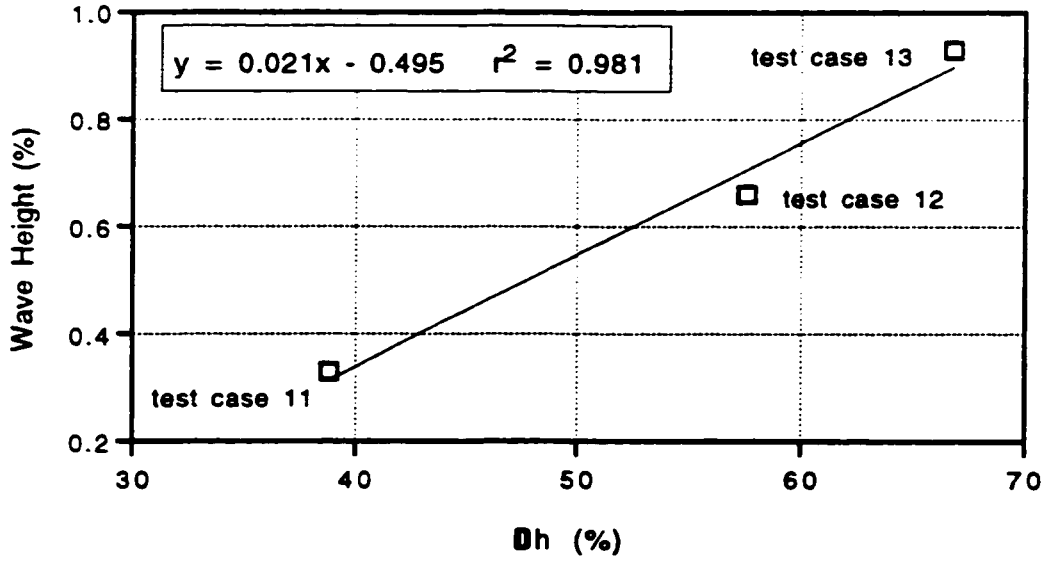

Figure 7.12: Maximum downstream wave height

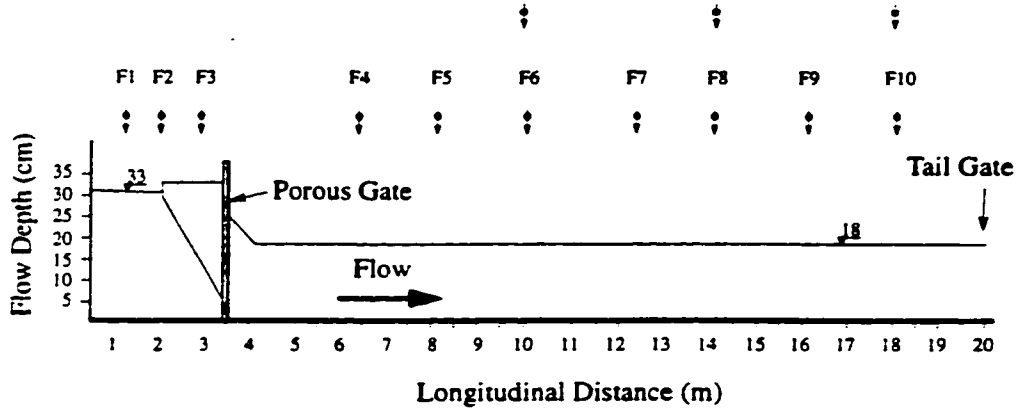

Figure 7.13: Flume set-up for experiment test case 4-tc1 (Wong et al. 1985)

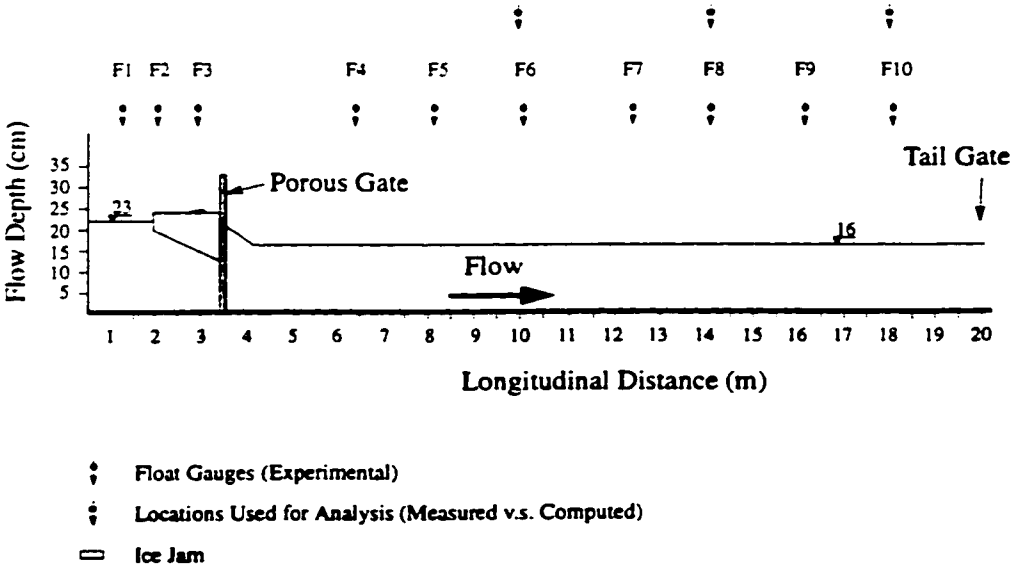

Figure 7.14: Flume set-up for experiment test case 4-tc2 (Wong et al. 1985)

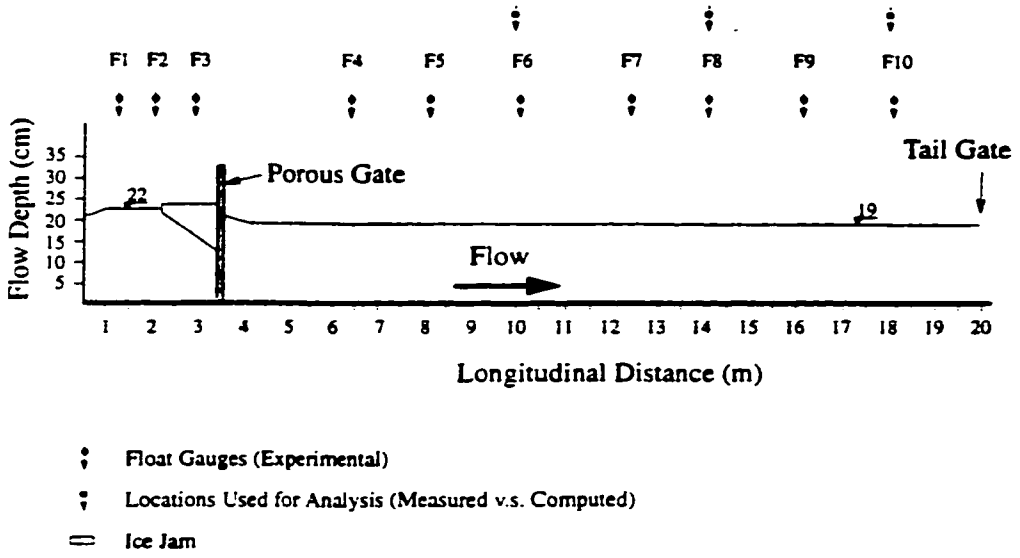

Figure 7.15: Flume set-up for experiment test case 4-tc3 (Wong et al. 1985)

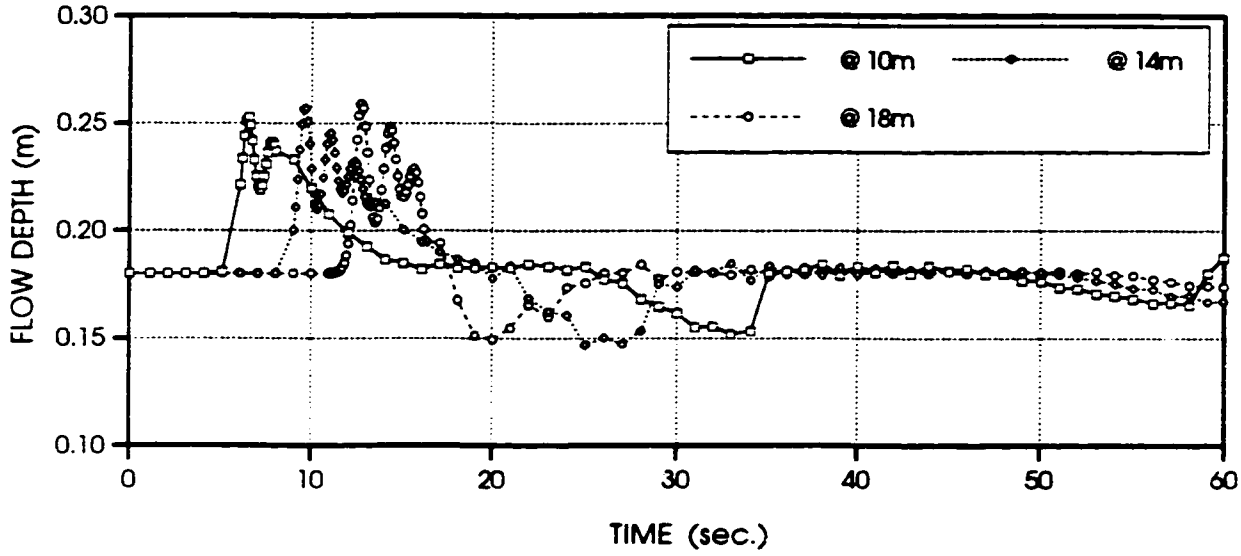

Figure 7.16: Depth flow hydrograph for test case 1

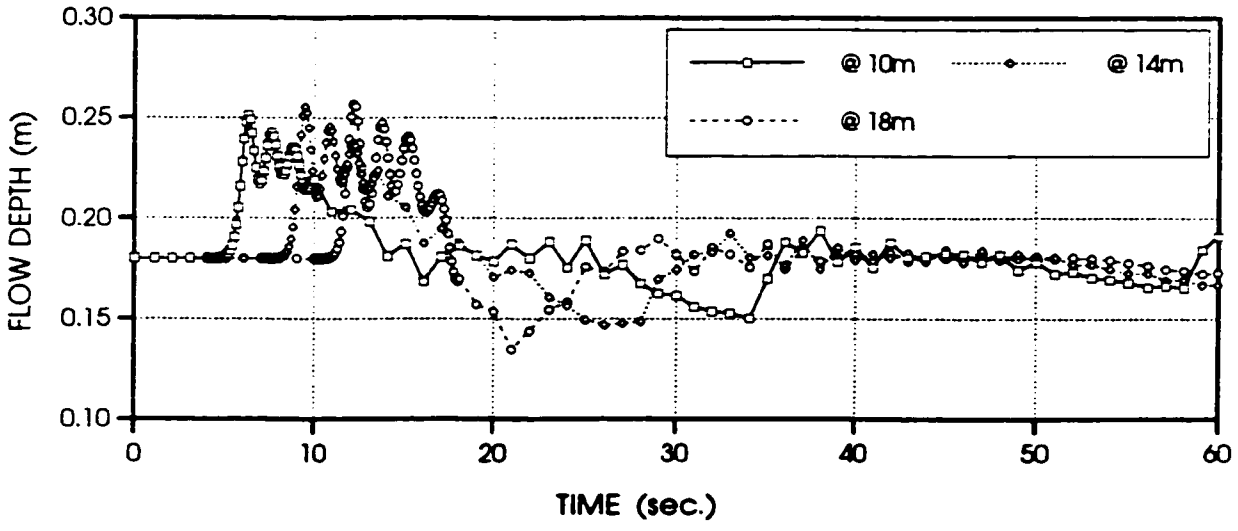

Figure 7.17: Depth flow hydrograph for test case 2

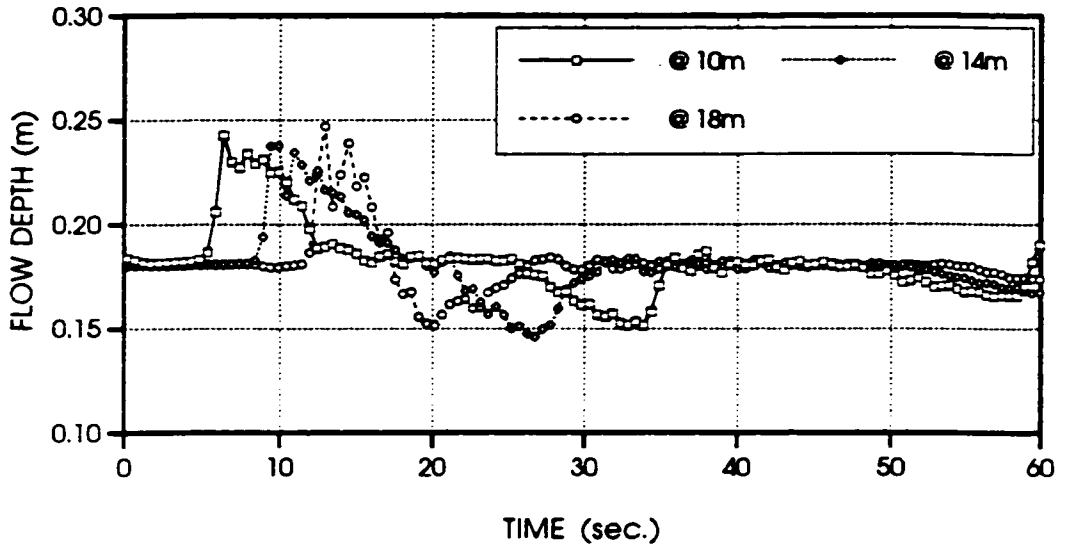

Figure 7.18: Depth flow hydrograph for test case 3

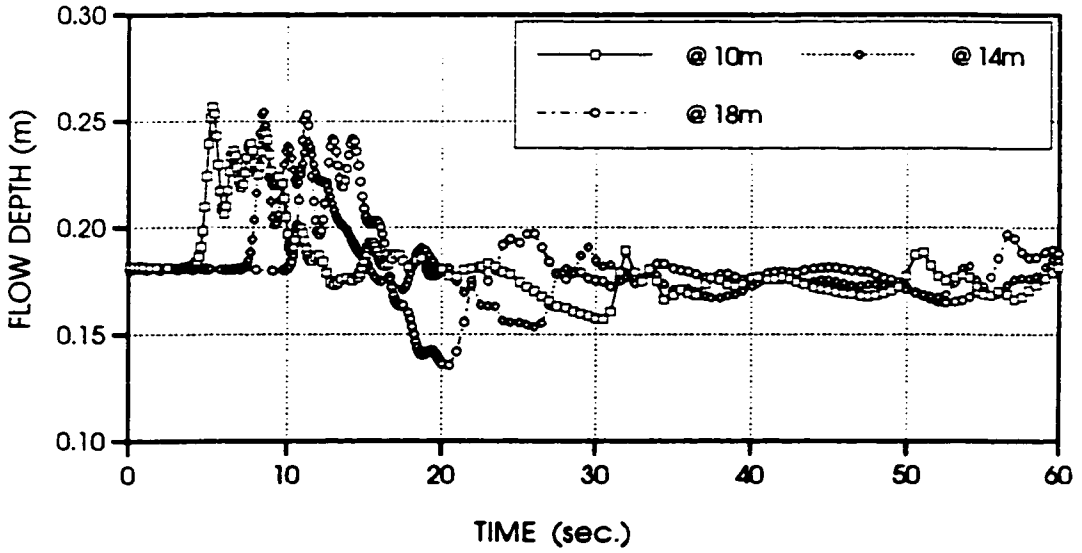

Figure 7.19: Depth flow hydrograph for test case 4-tc1

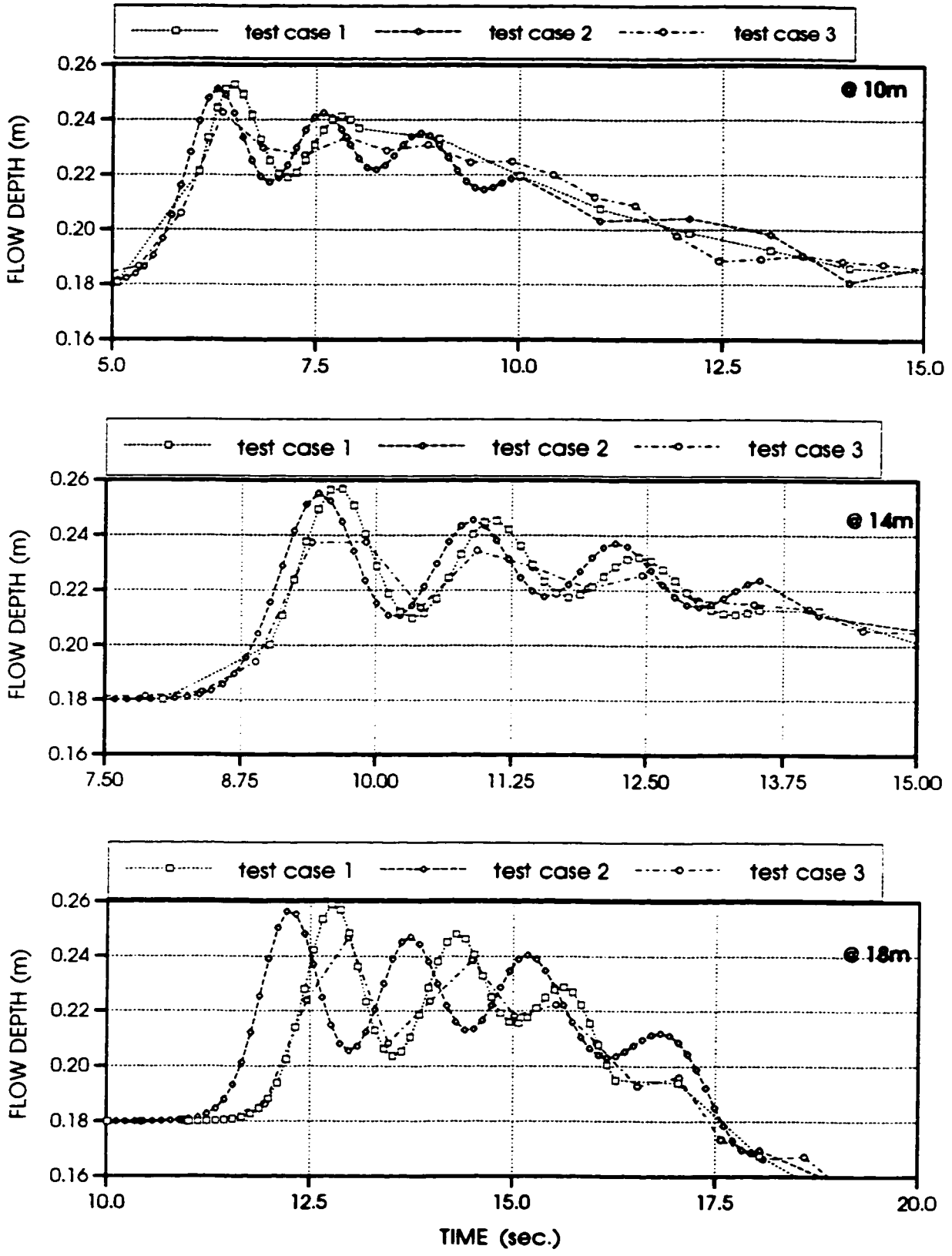

Figure 7.20: Flow depth hydrographs for test cases 1, 2, and 3

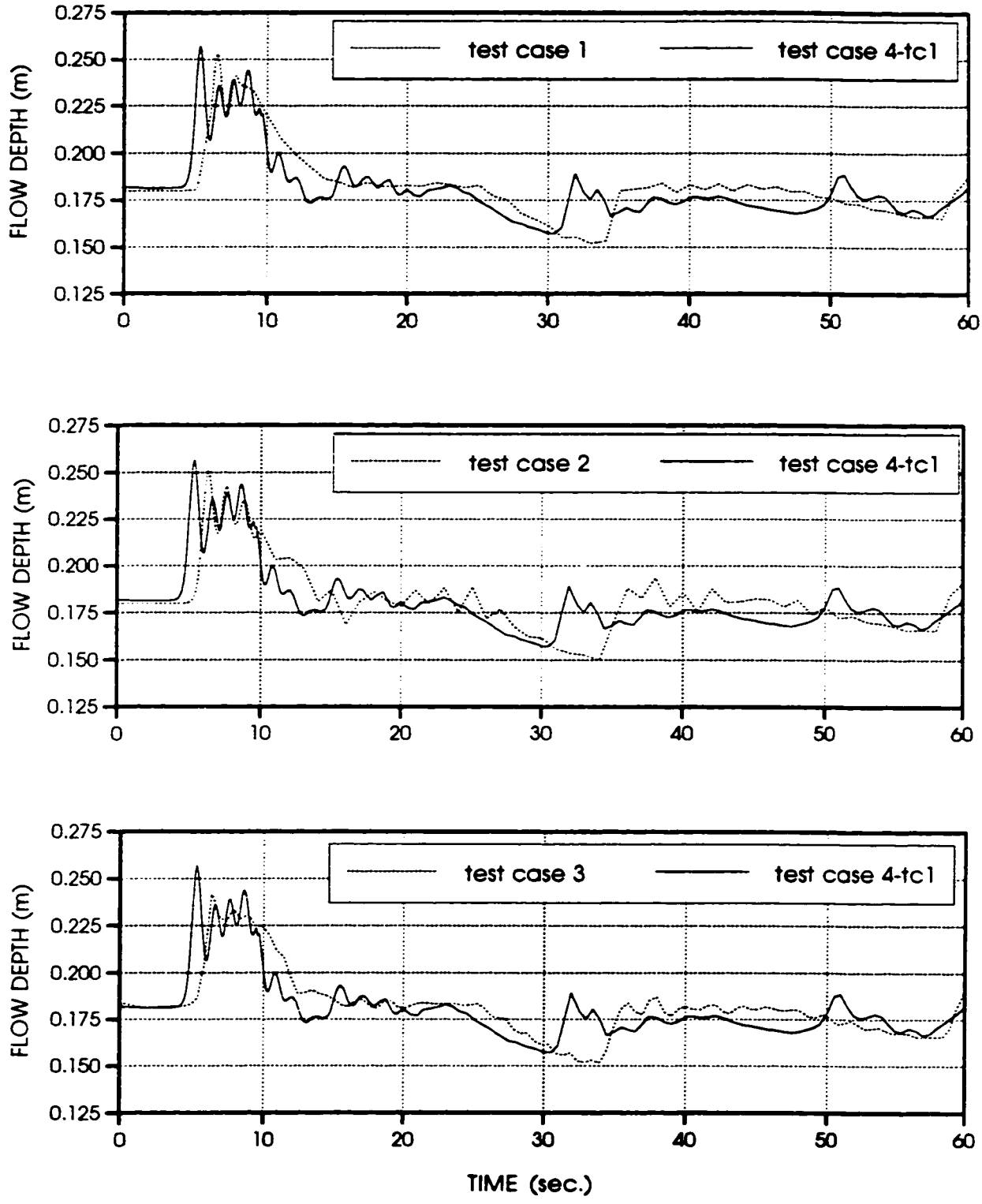

Figure 7.21: Ice mass effects on surge, @ 10m

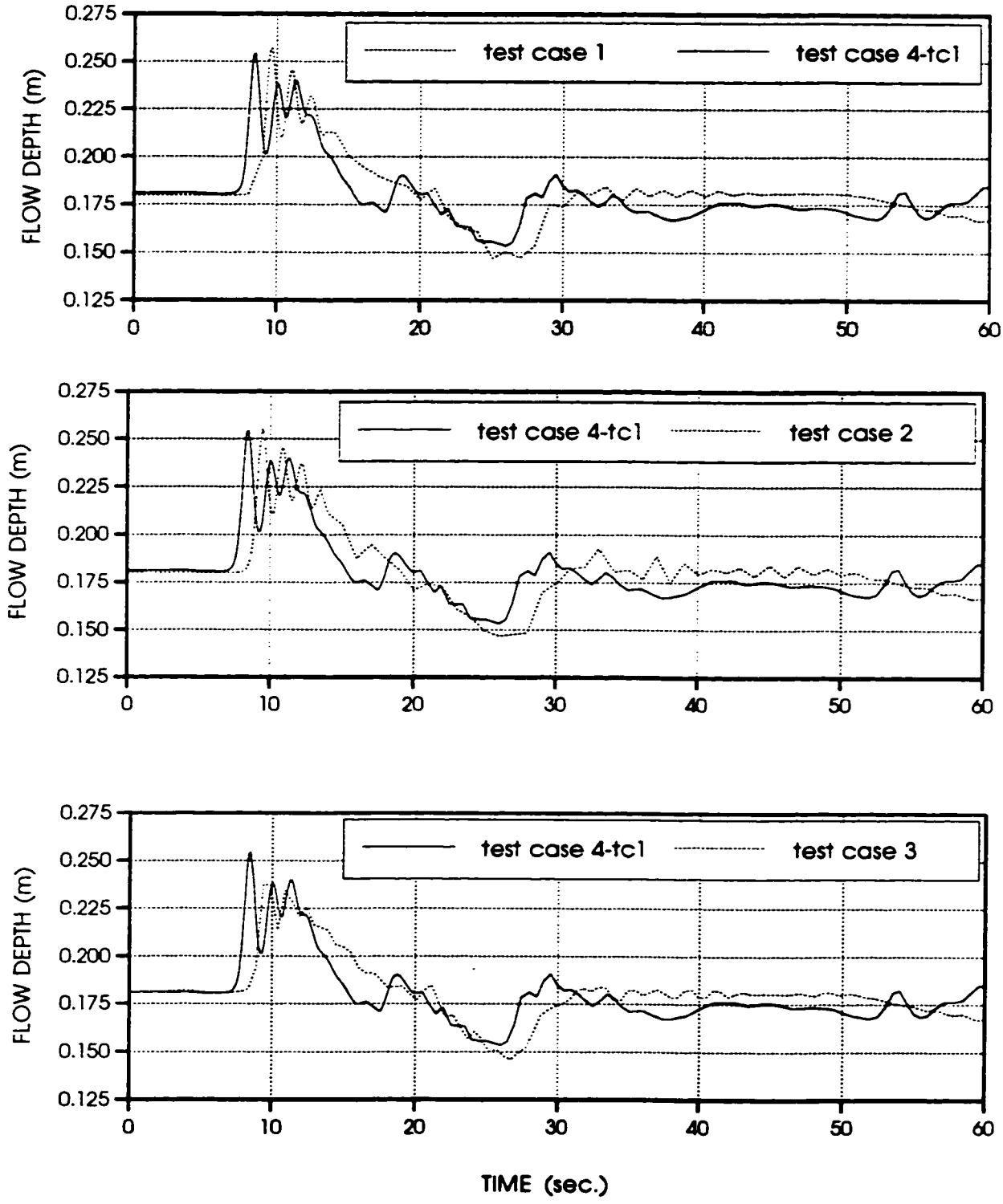

Figure 7.22: Ice mass effects on surge, @ 14m

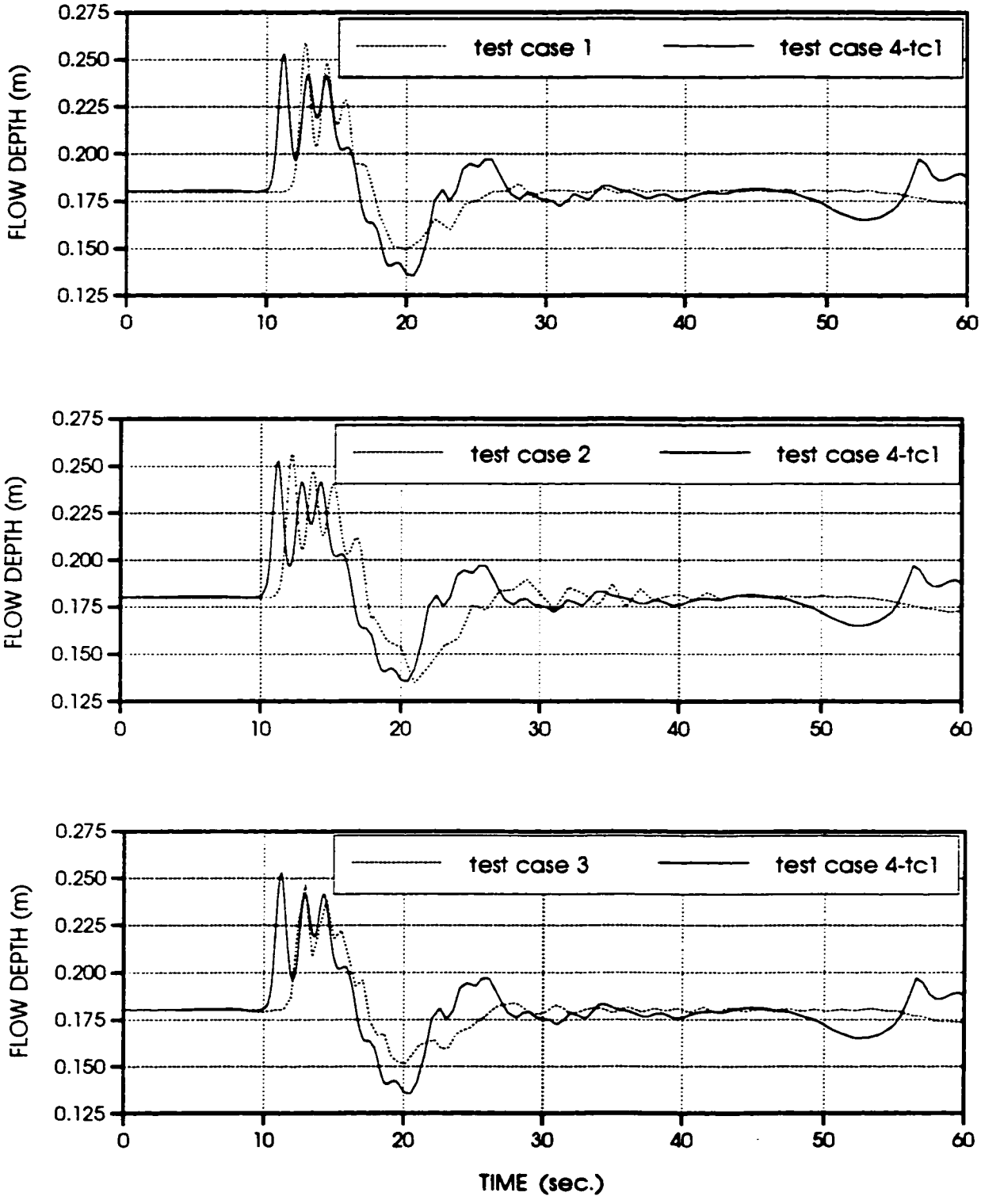

Figure 7.23: Ice mass effects on surge, @ 18m

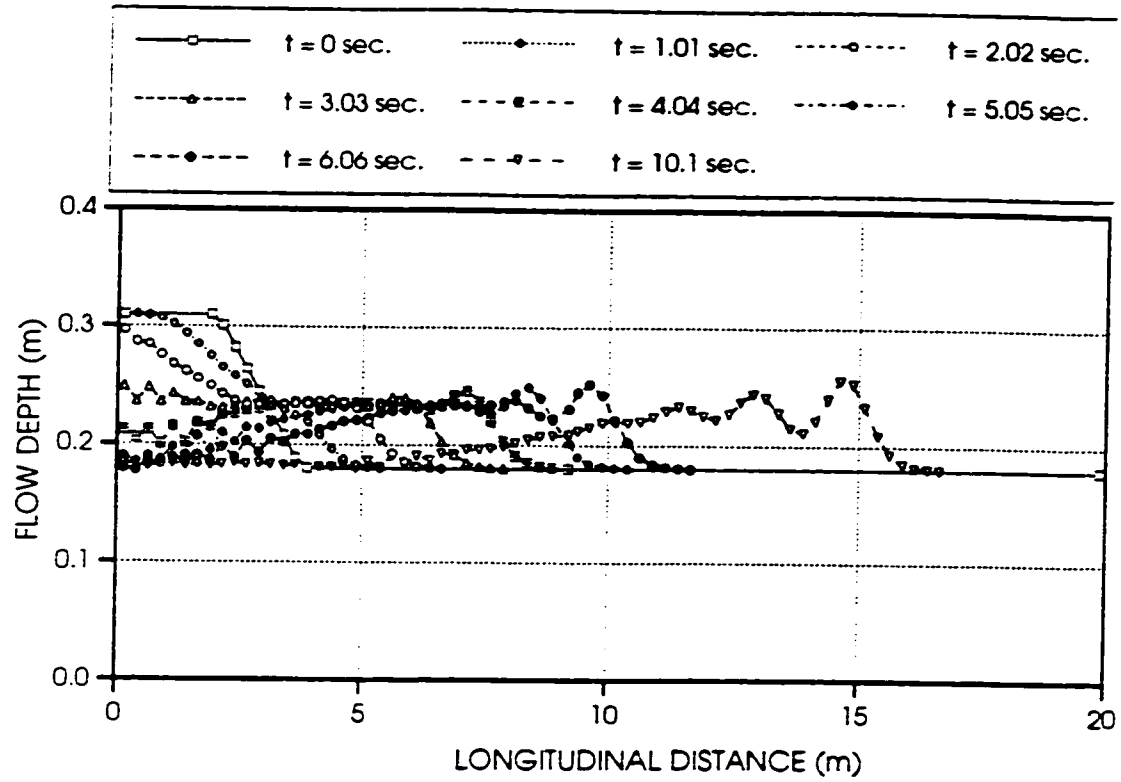

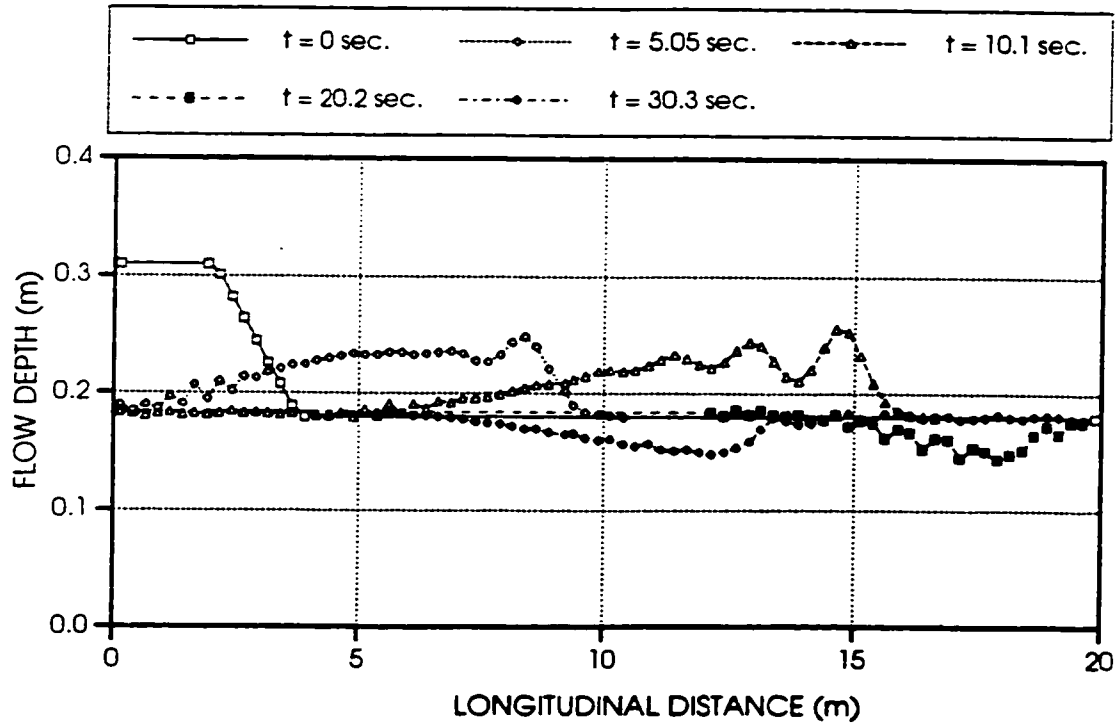

Figure 7.24: Longitudinal flow depth profiles for test case 1

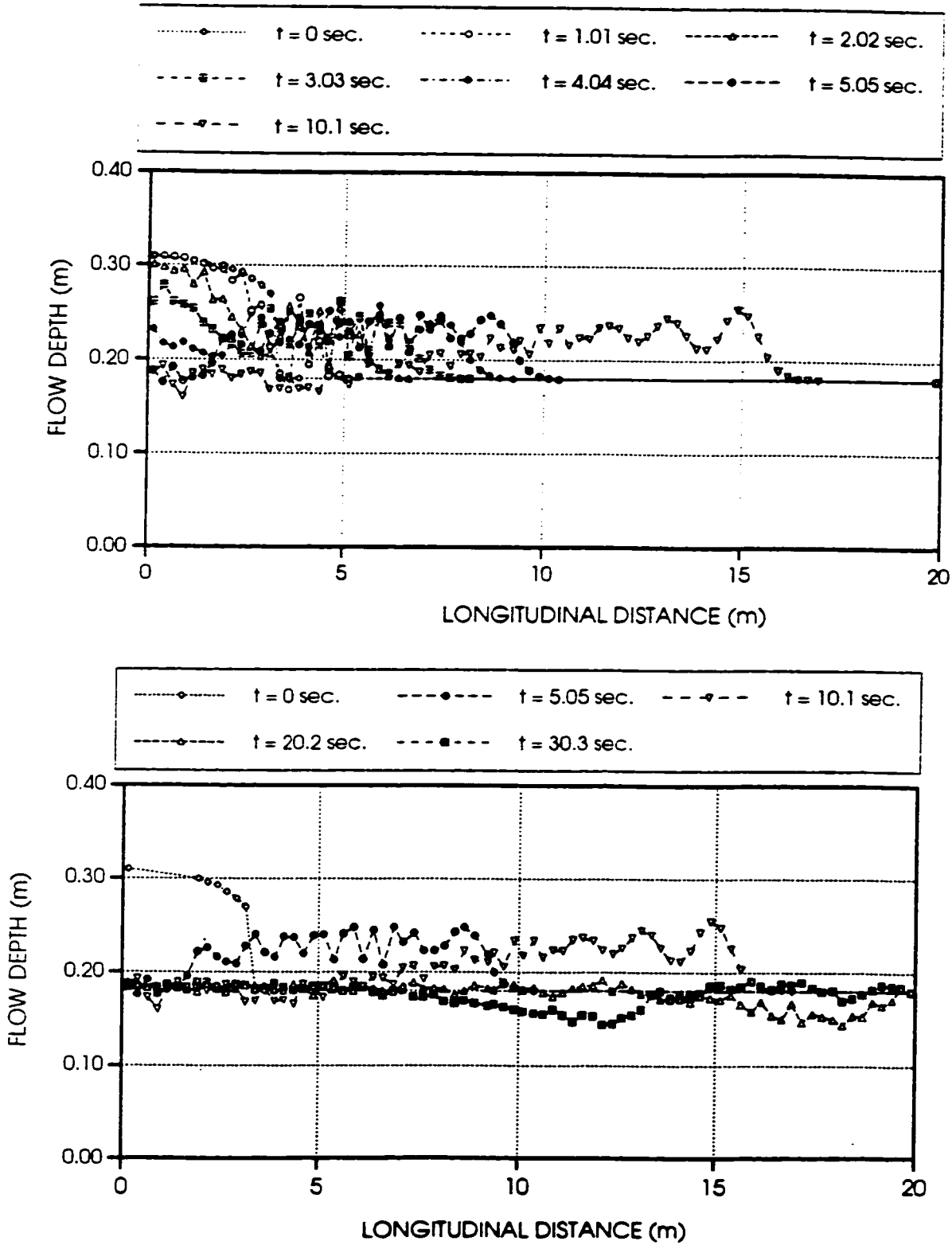

Figure 7.25: Longitudinal flow depth profiles for test case 2

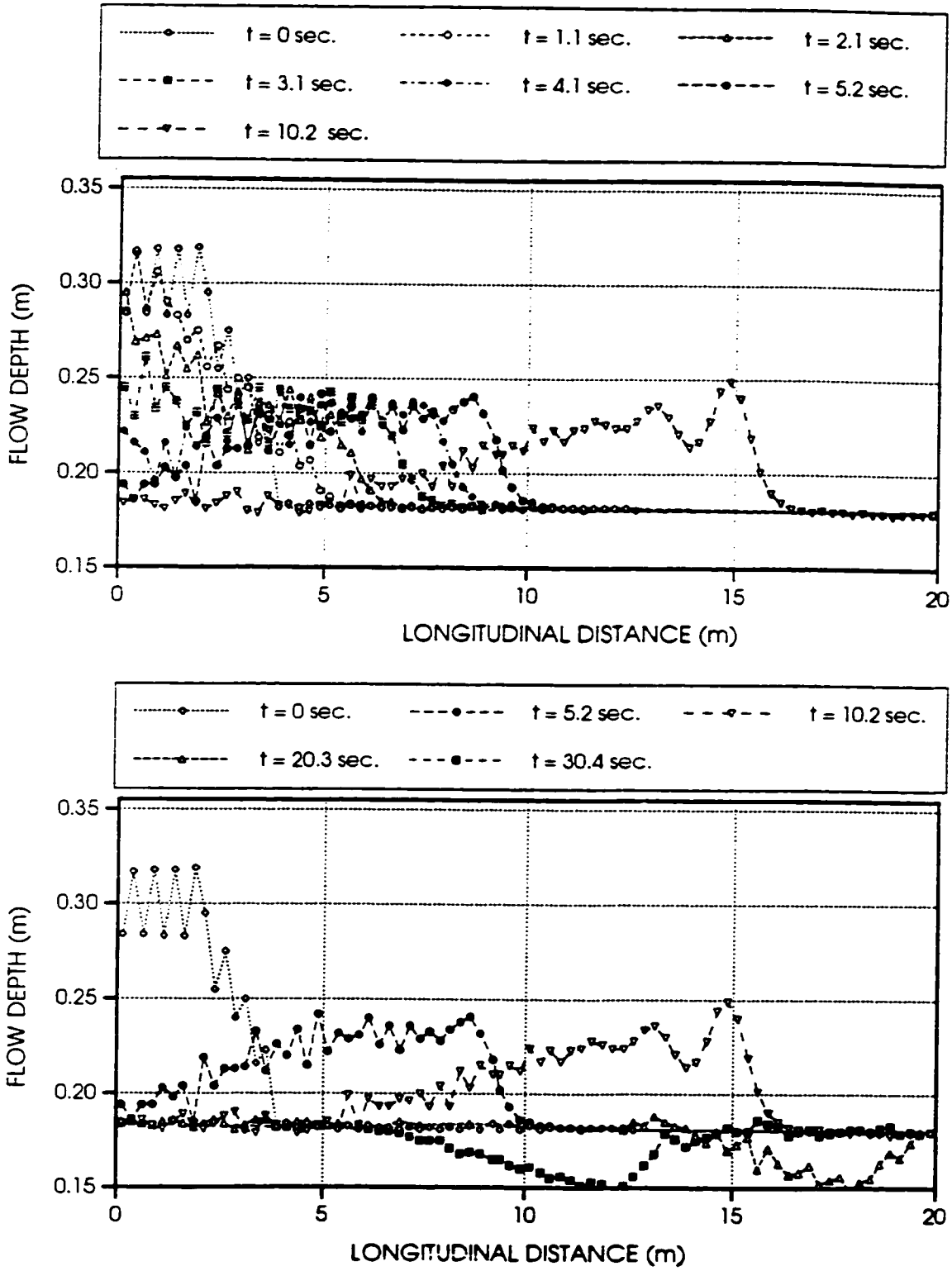

Figure 7.26: Longitudinal flow depth profiles for test case 3

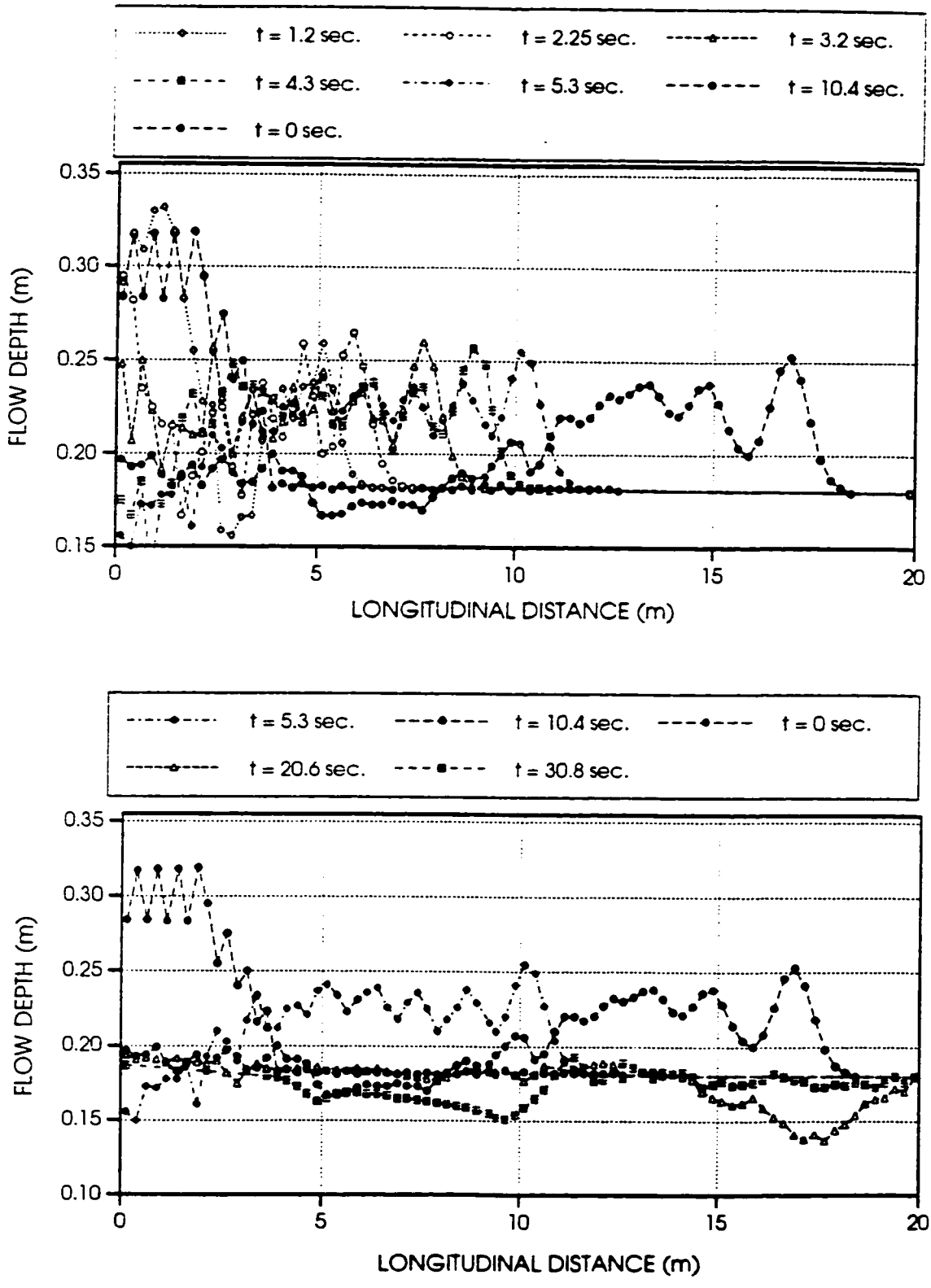

Figure 7.27: Longitudinal flow depth profiles for test case 4-tc1

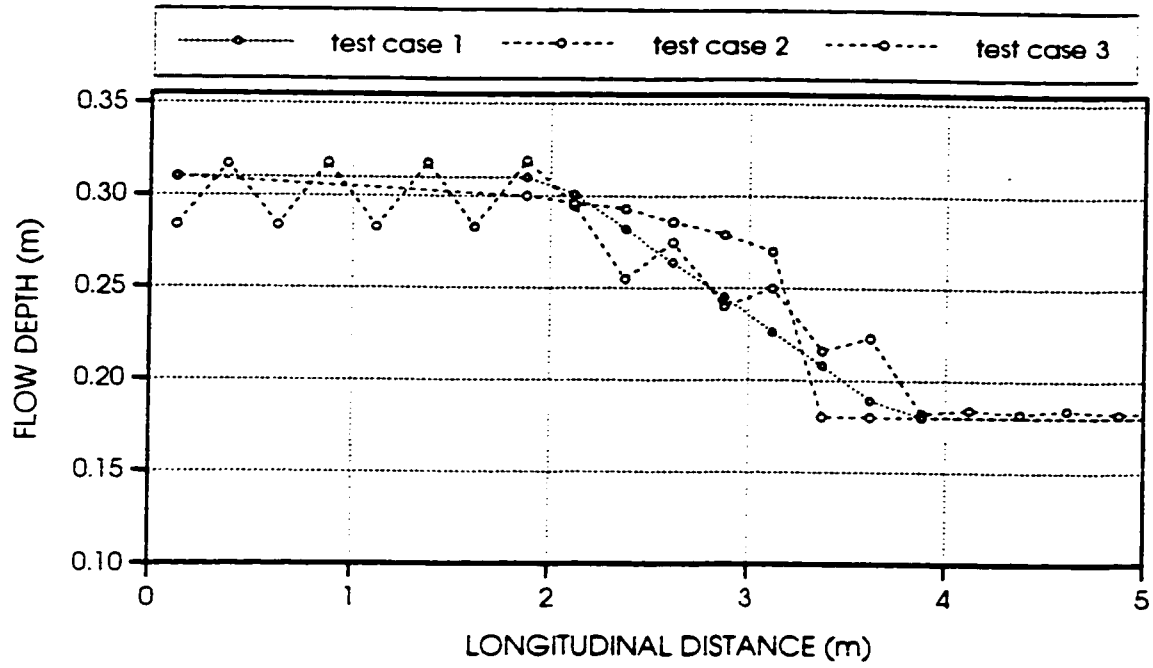

Figure 7.28: Water surface profile at time t=0 seconds

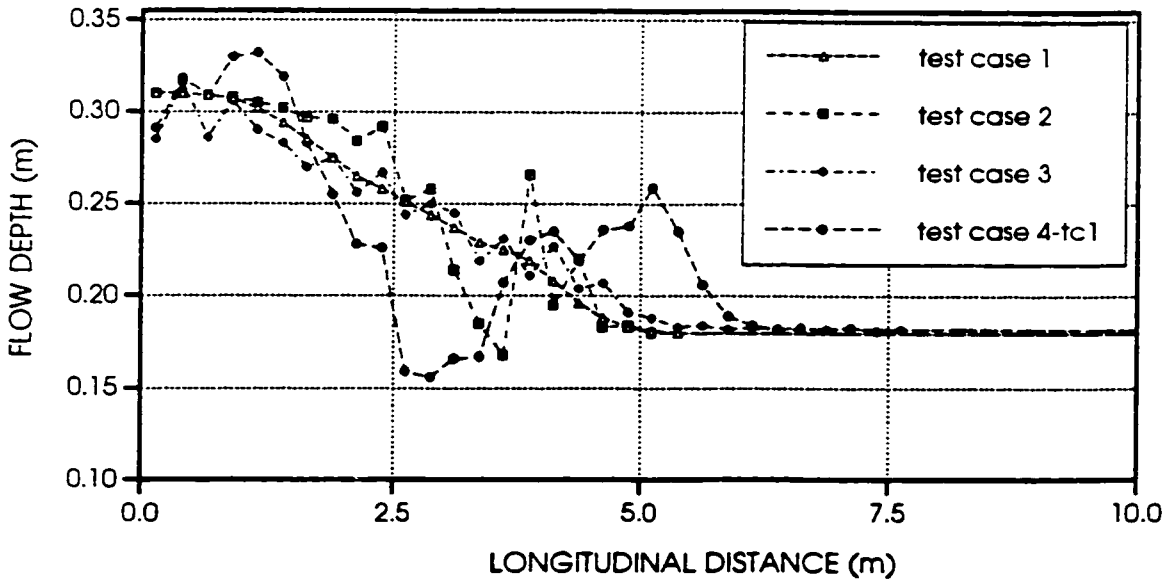

Figure 7.29: Water surface profiles at time t = 1 seconds

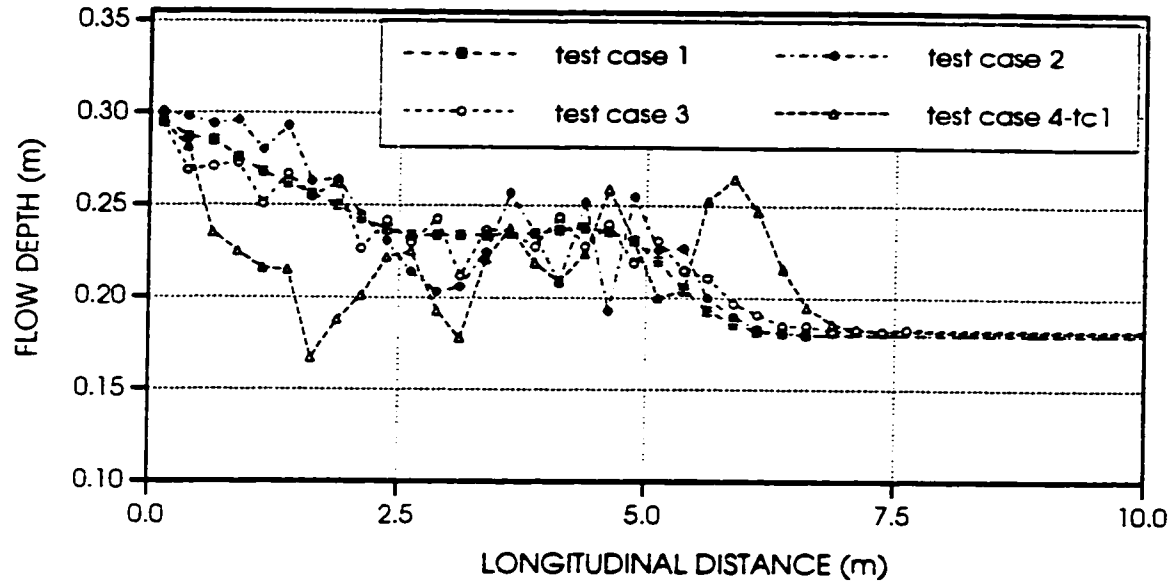

Figure 7.30: Water surface profiles at time t = 2 seconds

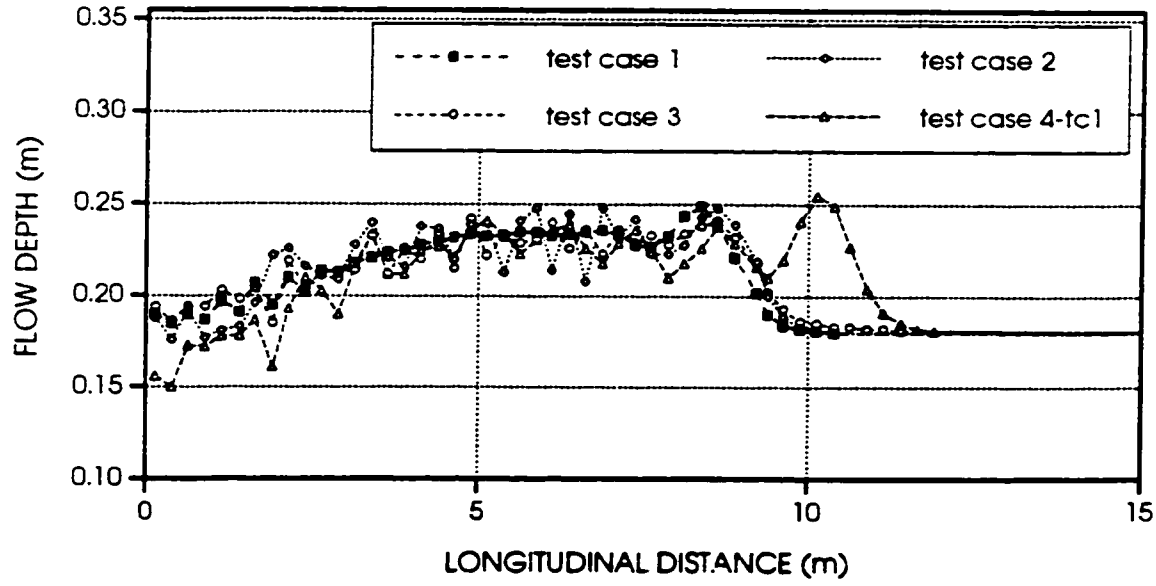

Figure 7.31: Water surface profiles at time t = 5 seconds

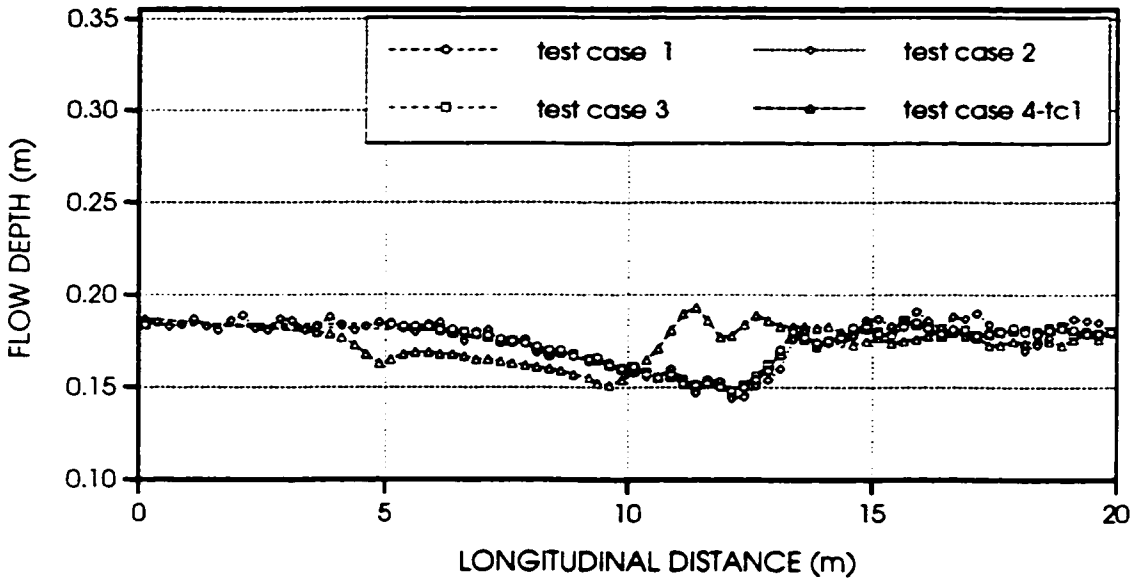

Figure 7.32: Water surface profiles at time t = 30 seconds

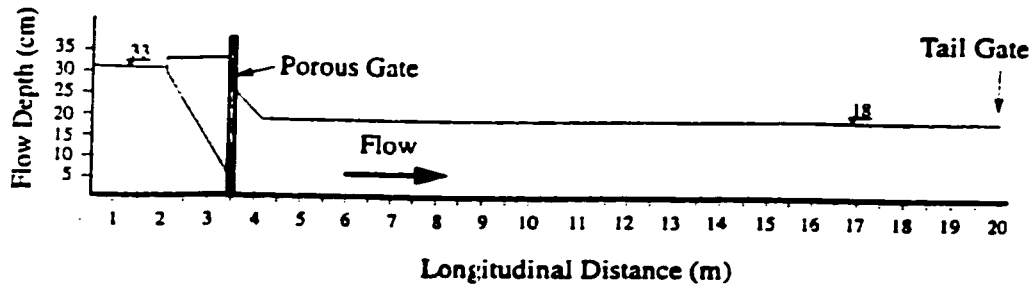

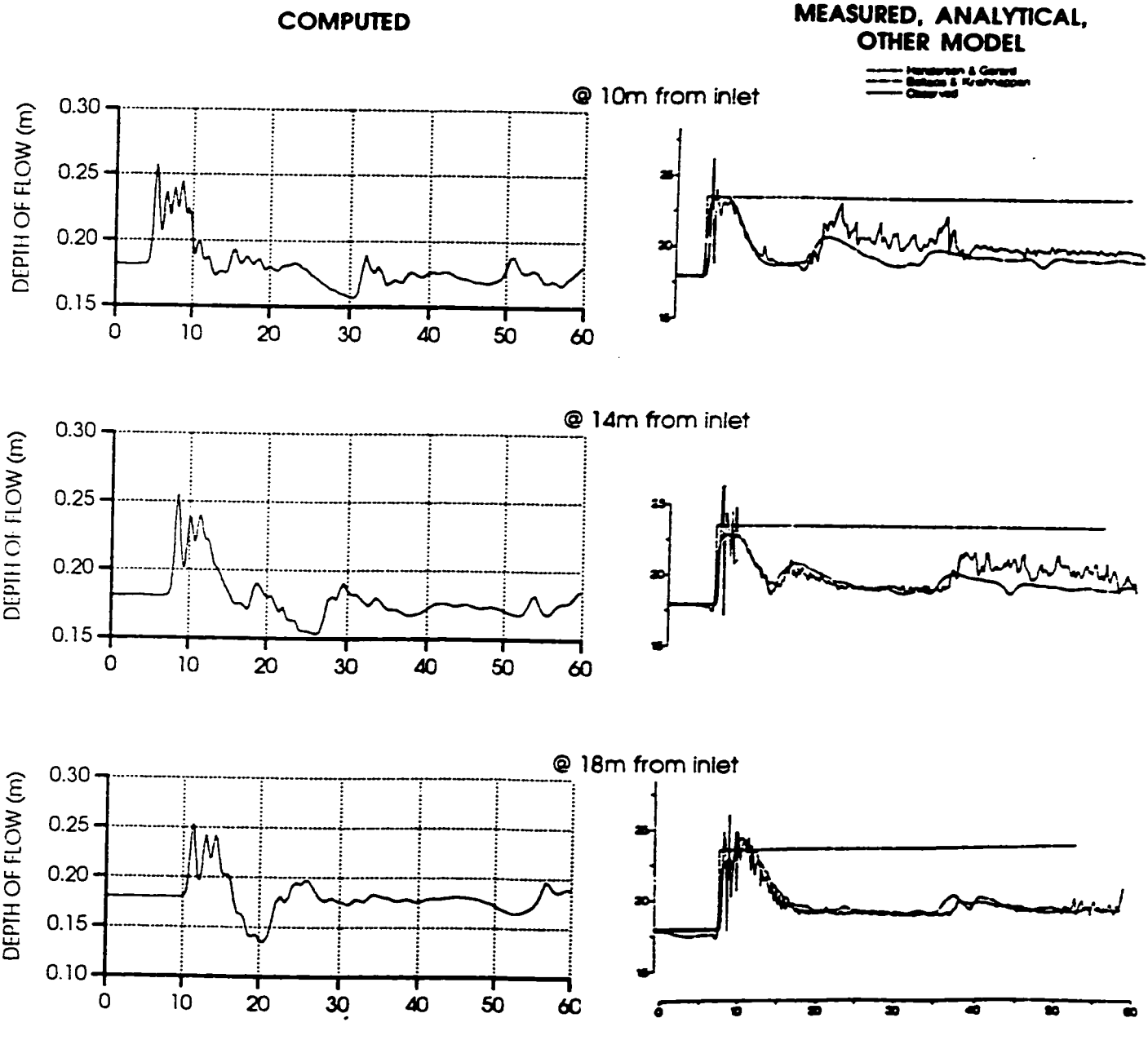

Figure 7.33: Measured and computed water level variation as as a function of time, test case 4-tc1

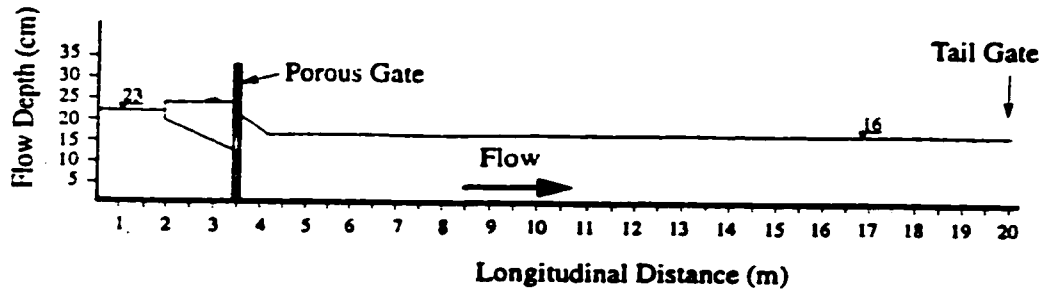

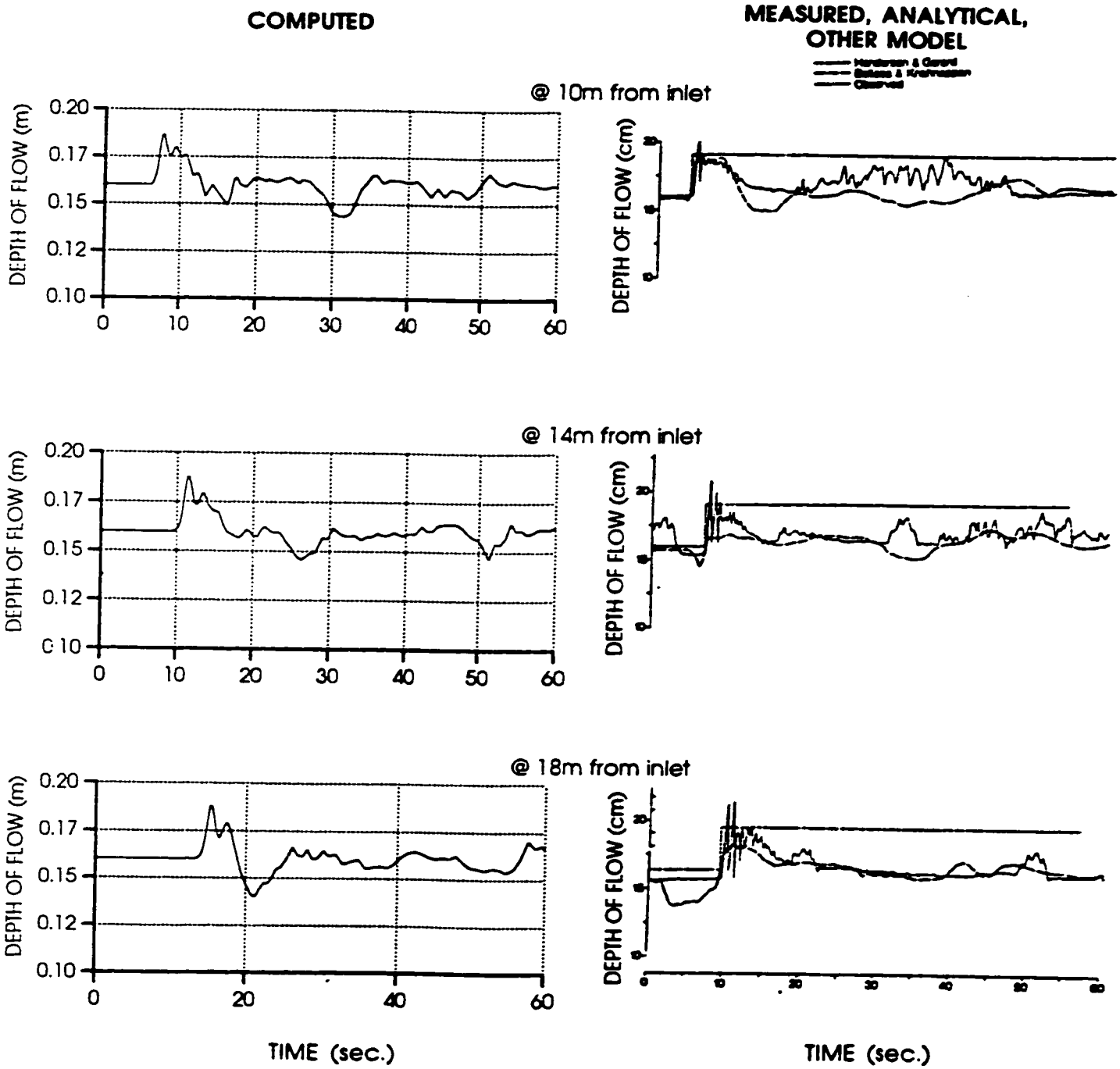

Figure 7.34: Measured and computed water level variation as as a function of time, test case 4-tc2

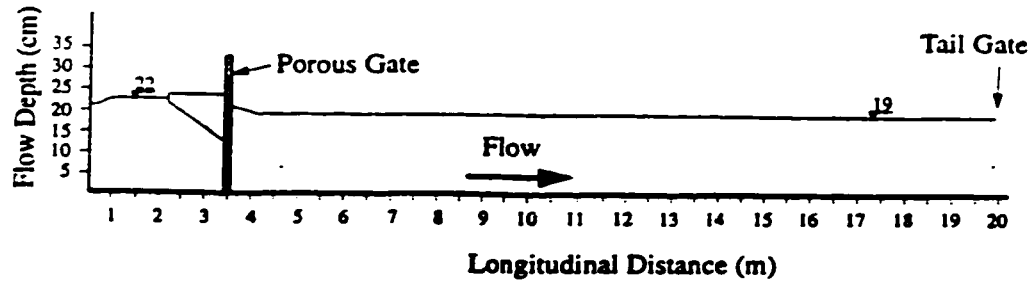

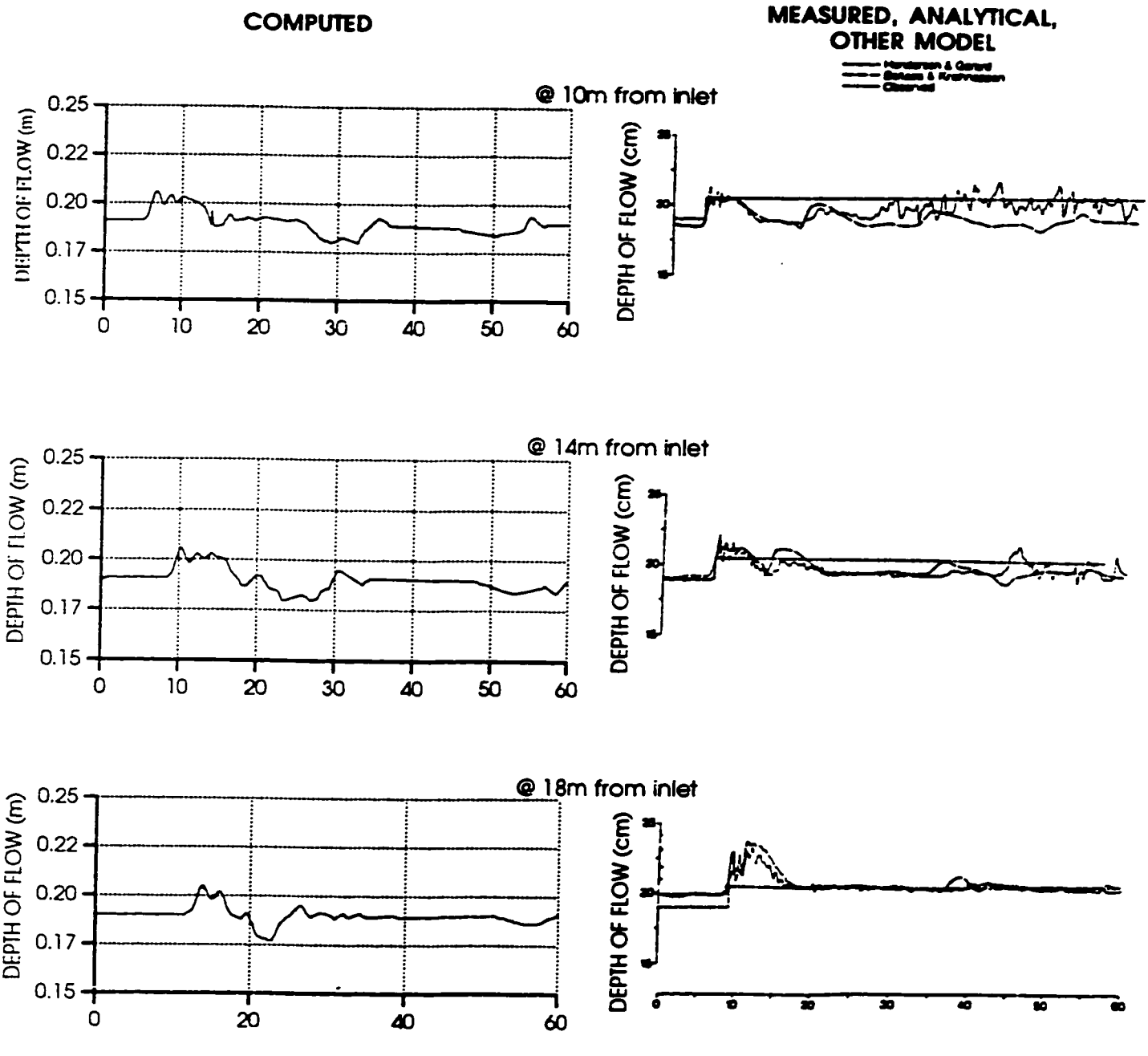

Figure 7.35: Measured and computed water level variation as as a function of time, test case 4-tc3

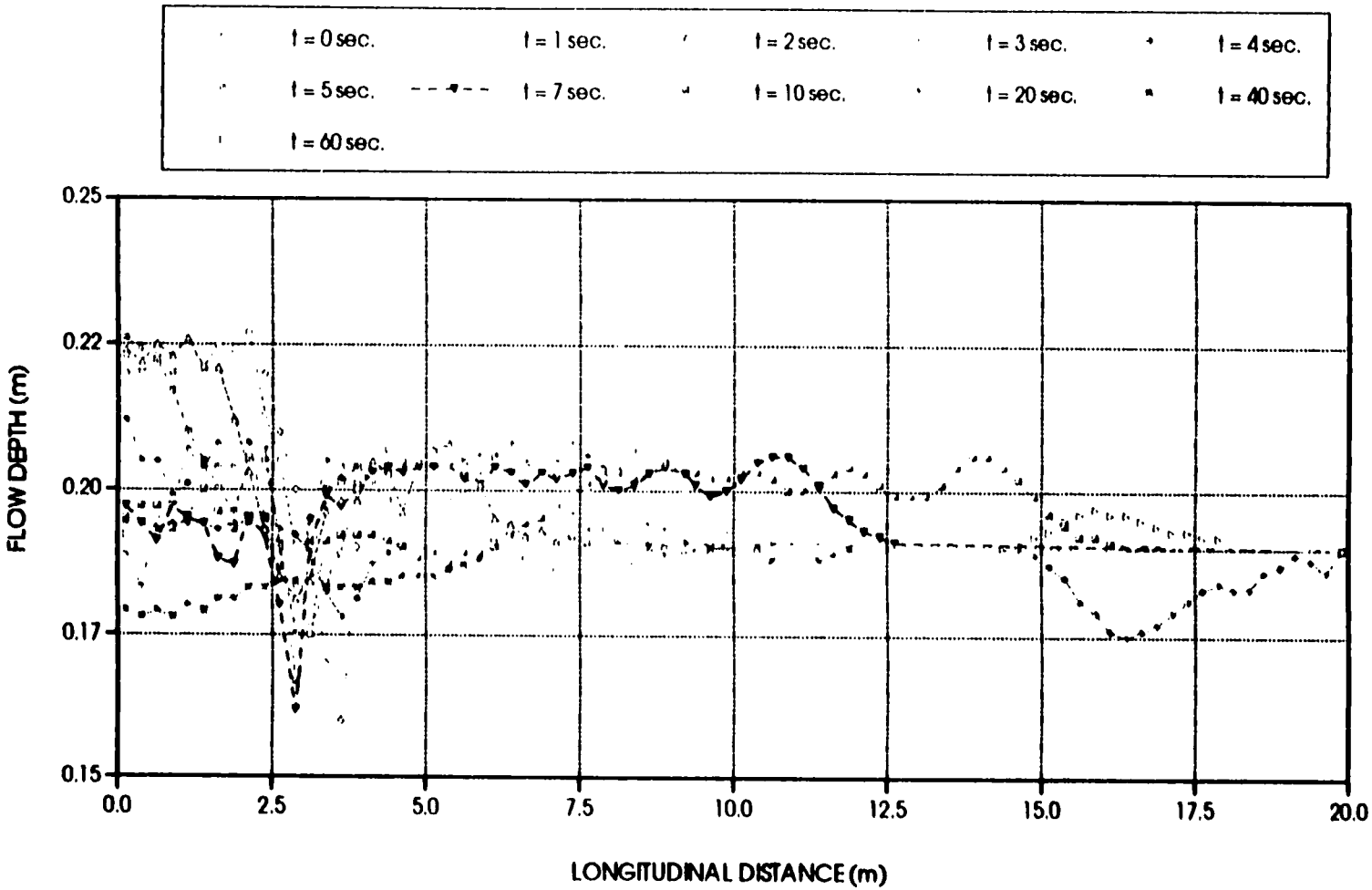

Figure 7.36: Flow depth profiles as a function of time for test case 4-tc3

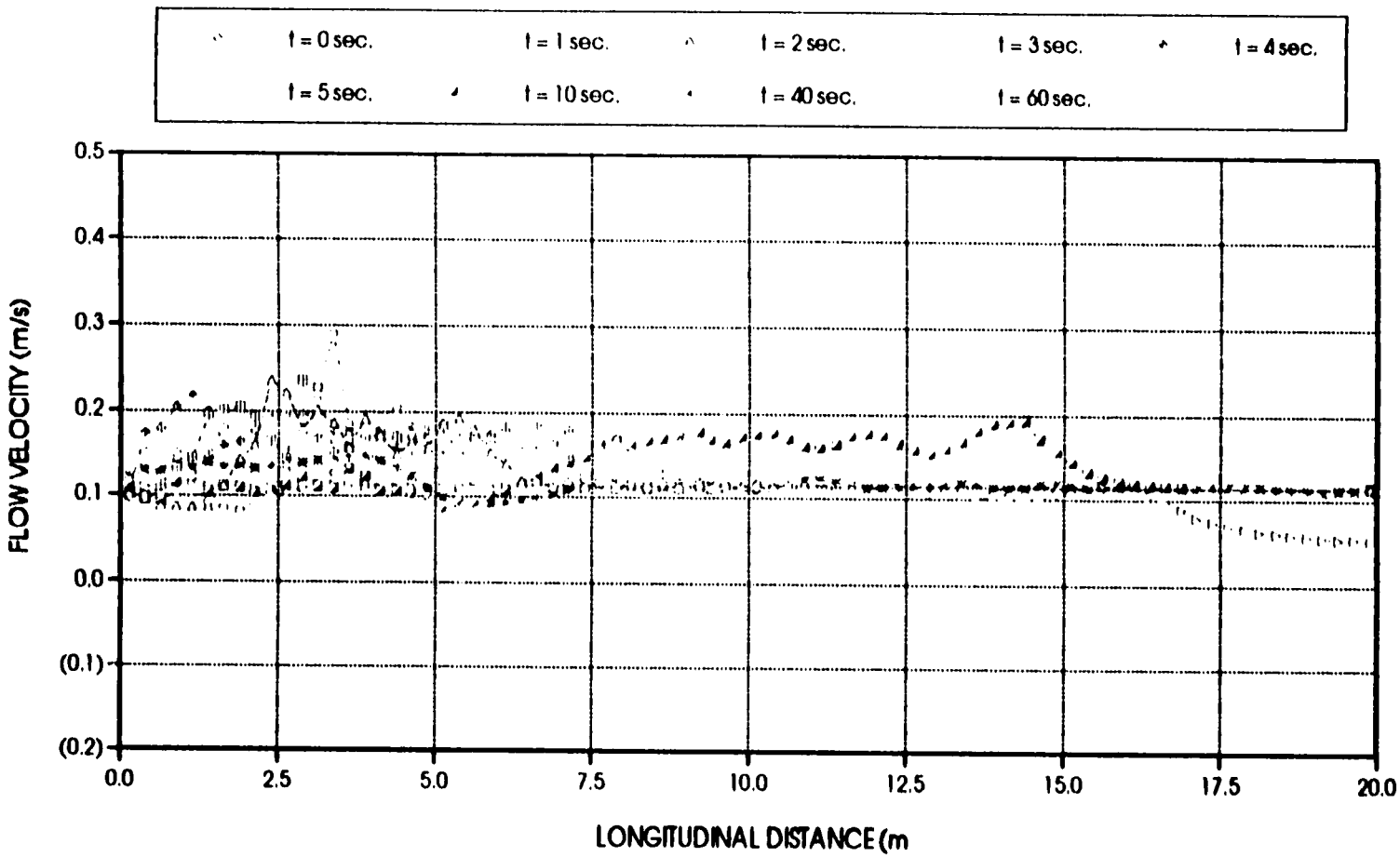

Figure 7.37: Flow velocity profiles as a function of time for test case 4-tc3

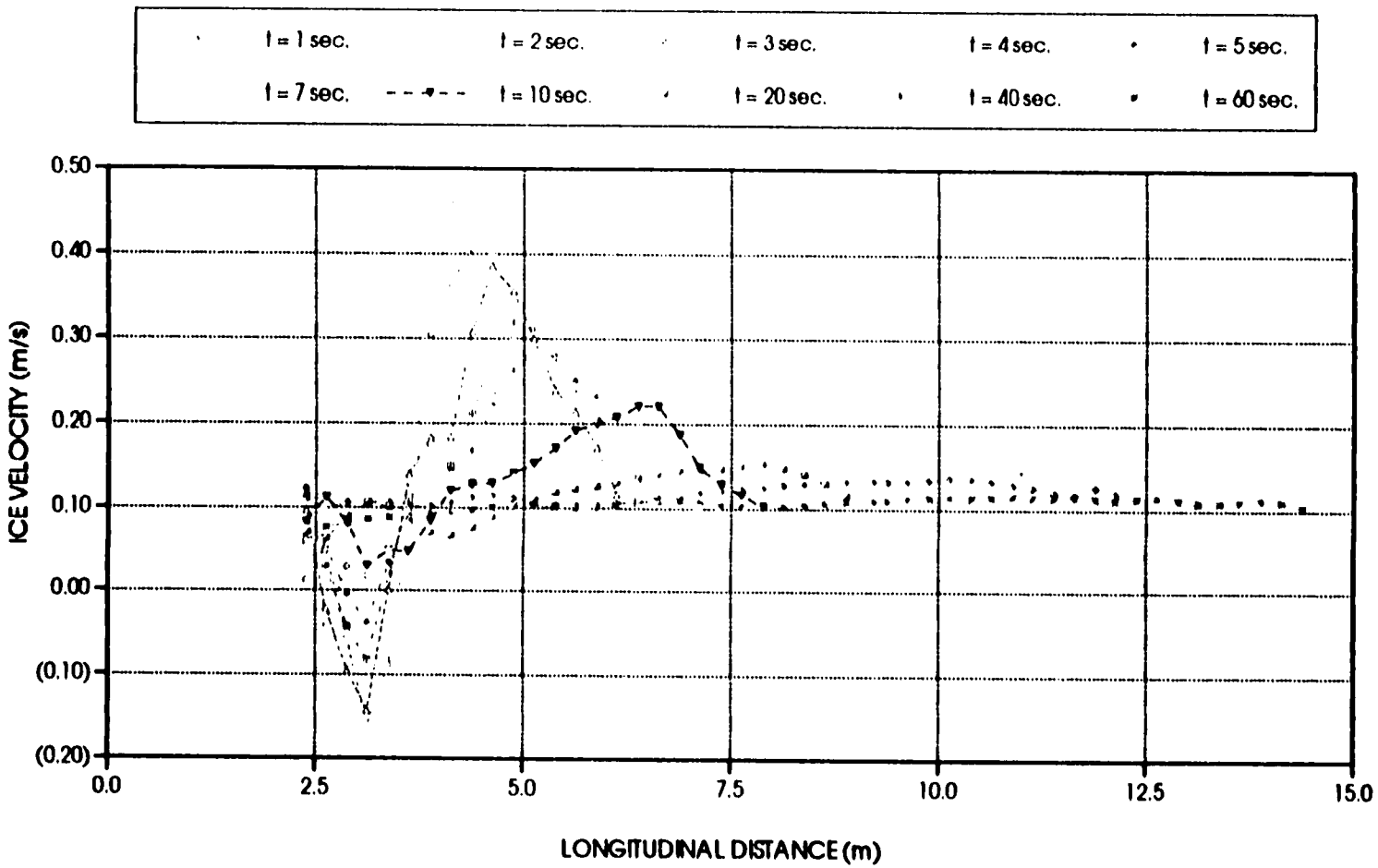

Figure 7.38: Ice velocity profiles as a function of time for test case 4-tc3

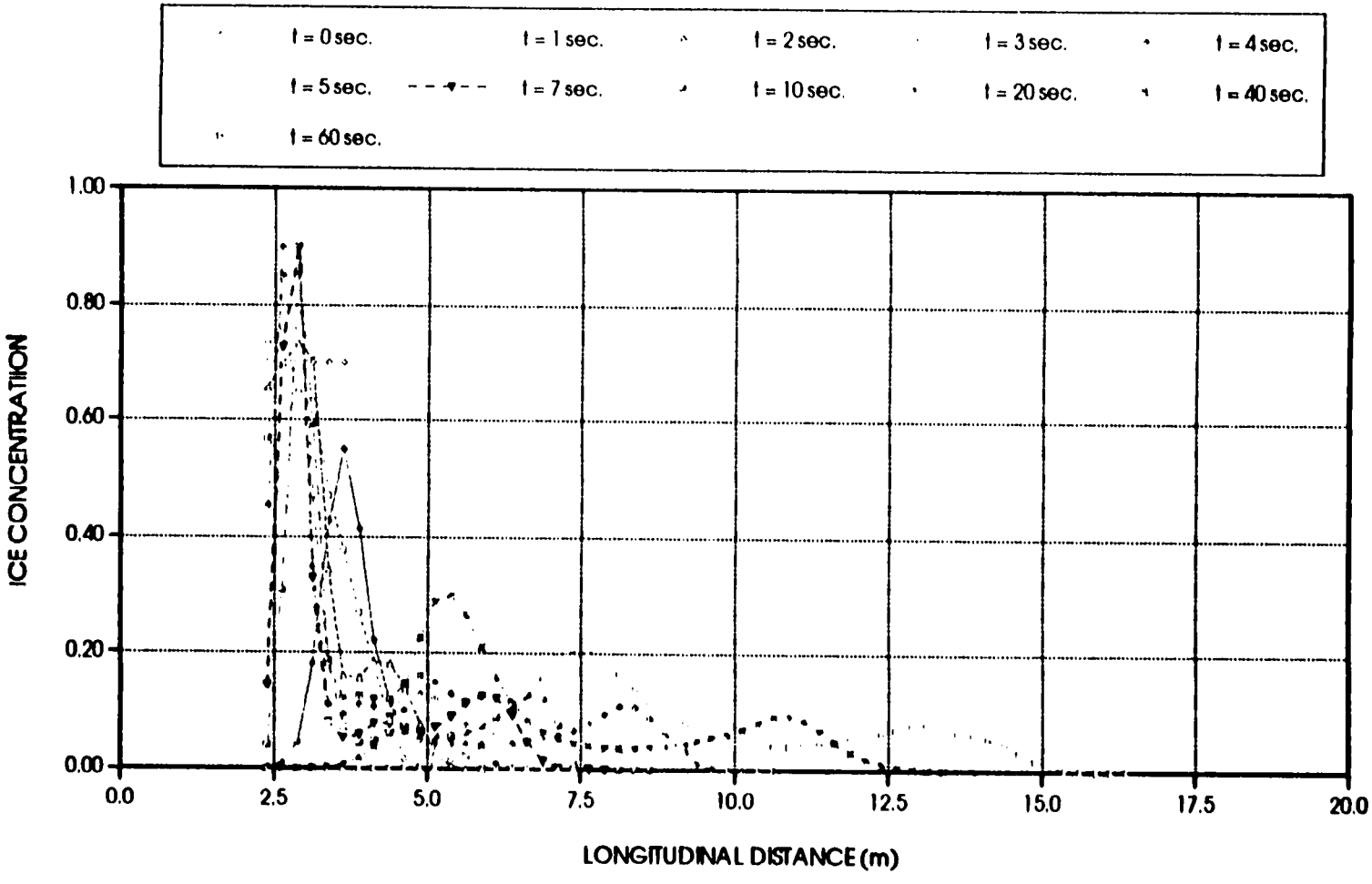

Figure 7.39: Surface area ice concentration profiles as a function of time for test a case 4-tc3

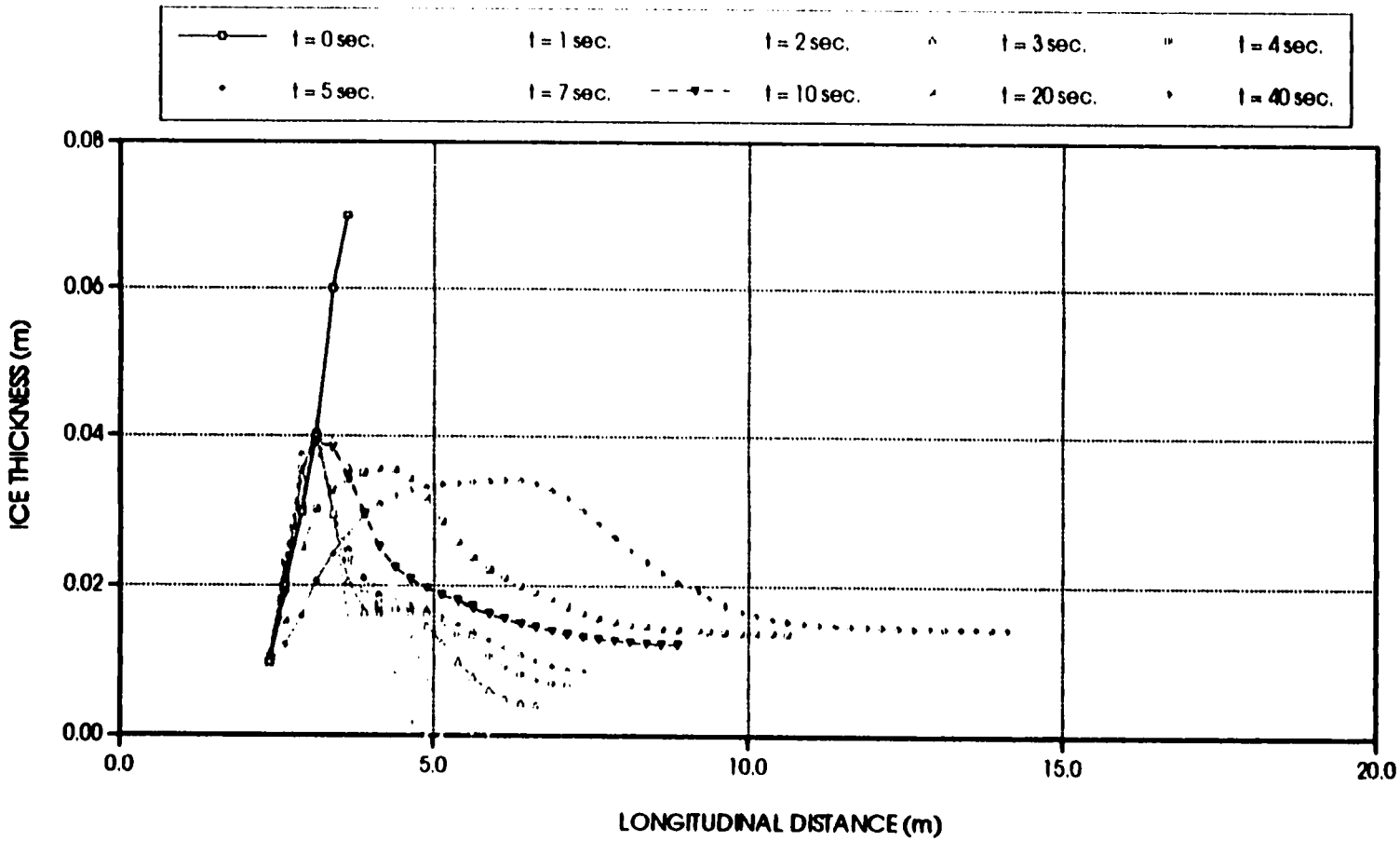

Figure 7.40: Ice thickness profiles as a function of time for test case 4-tc3

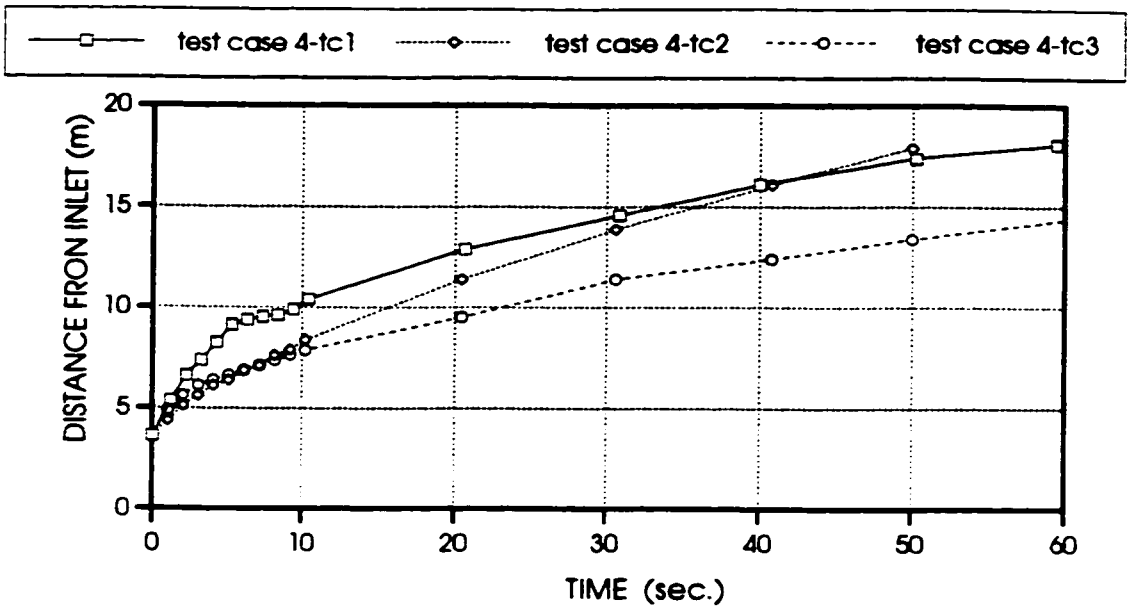

Figure 7.41: Downstream travel of ice jam front

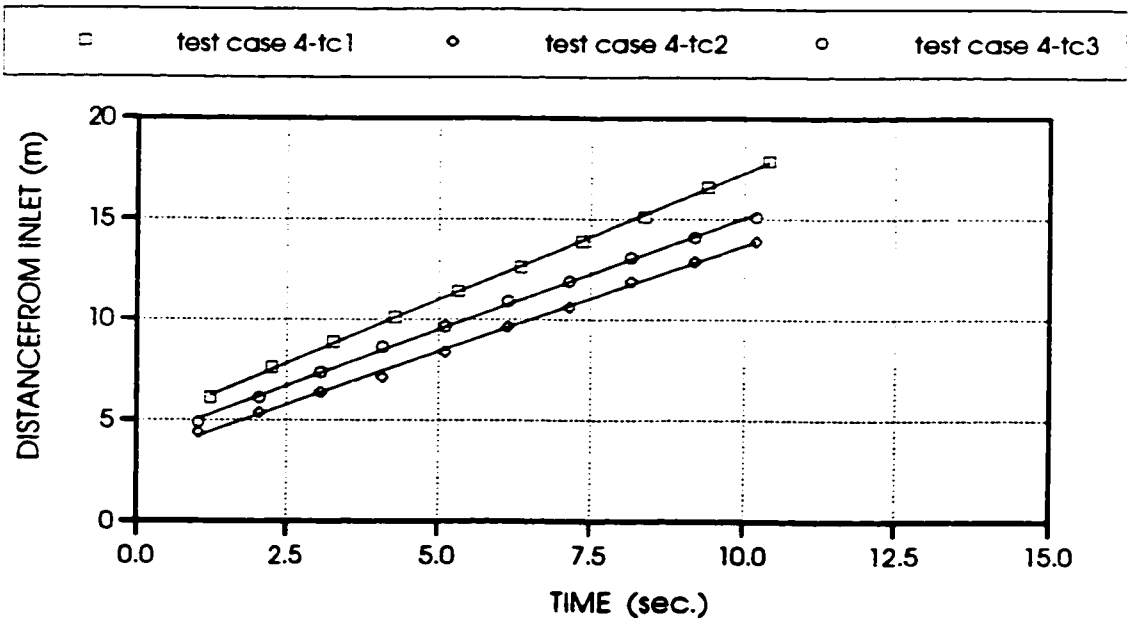

Figure 7.42: Downstream propagation of surge

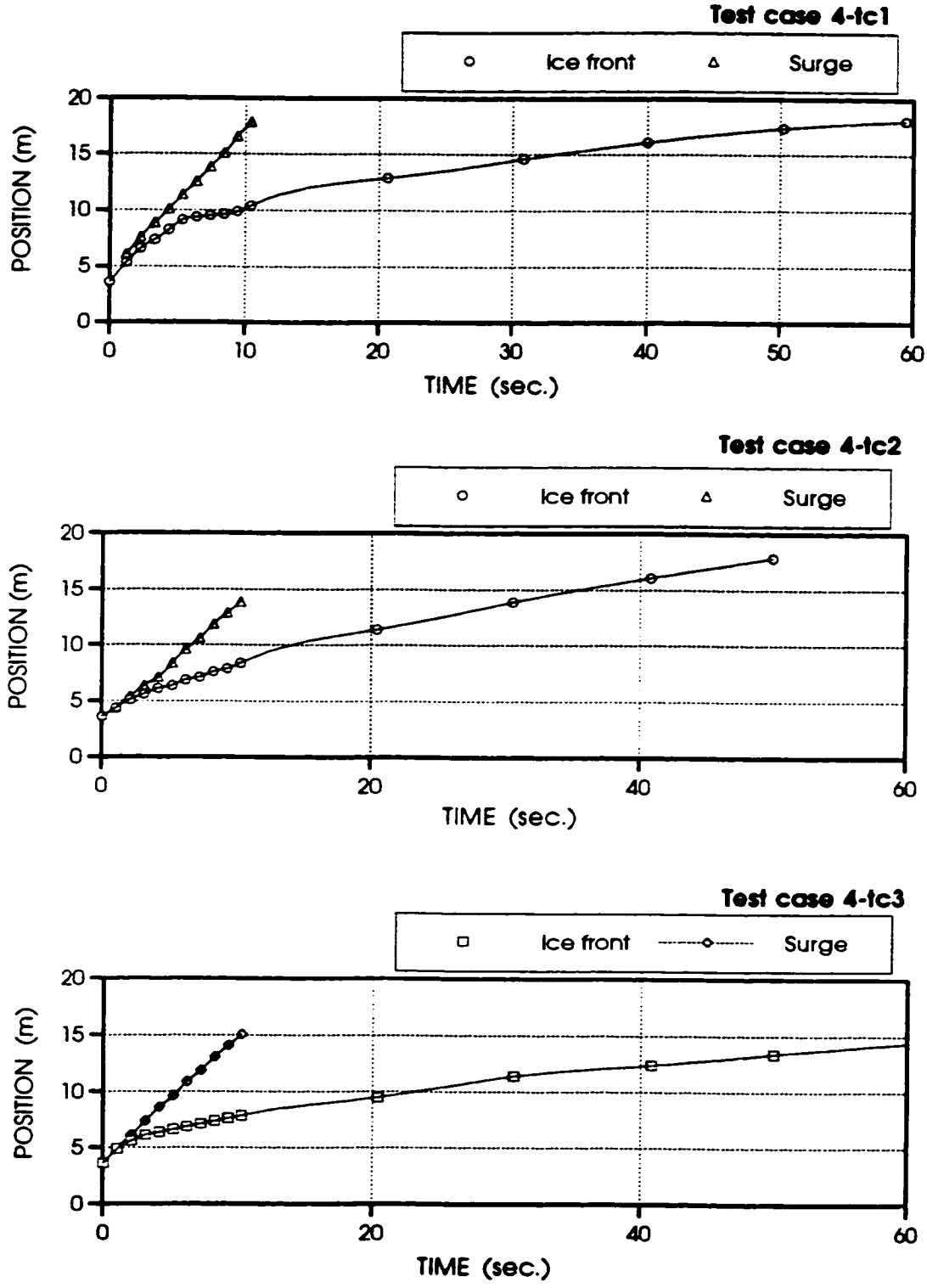

Figure 7.43: Downstream propagation of ice jam front and surge

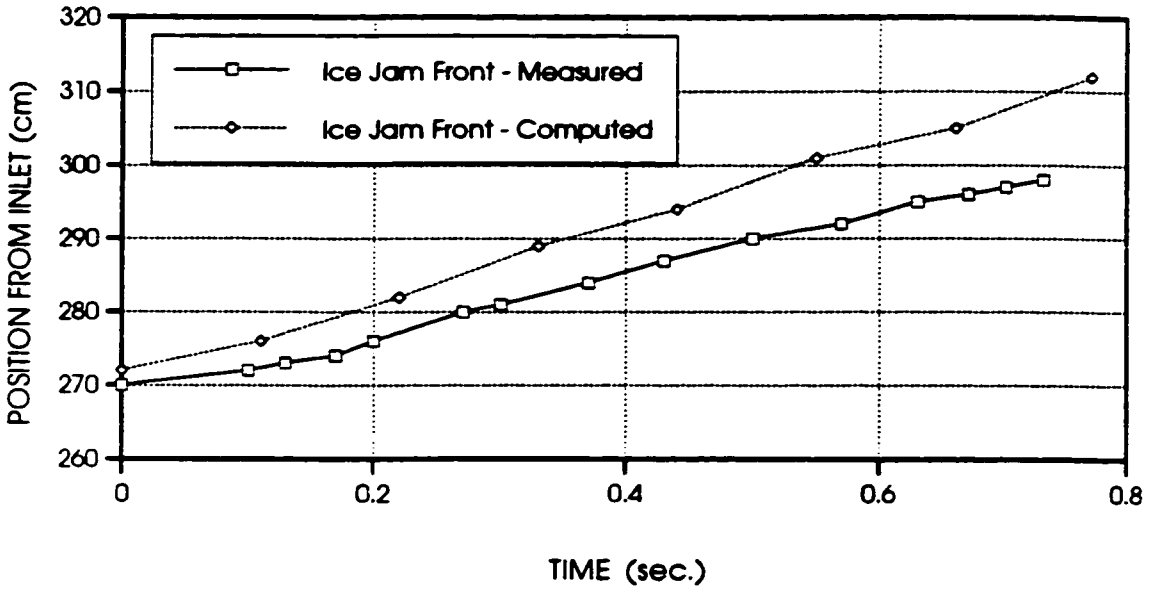

Figure 7.44: Measured and computed ice jam front development for test case r4tc4

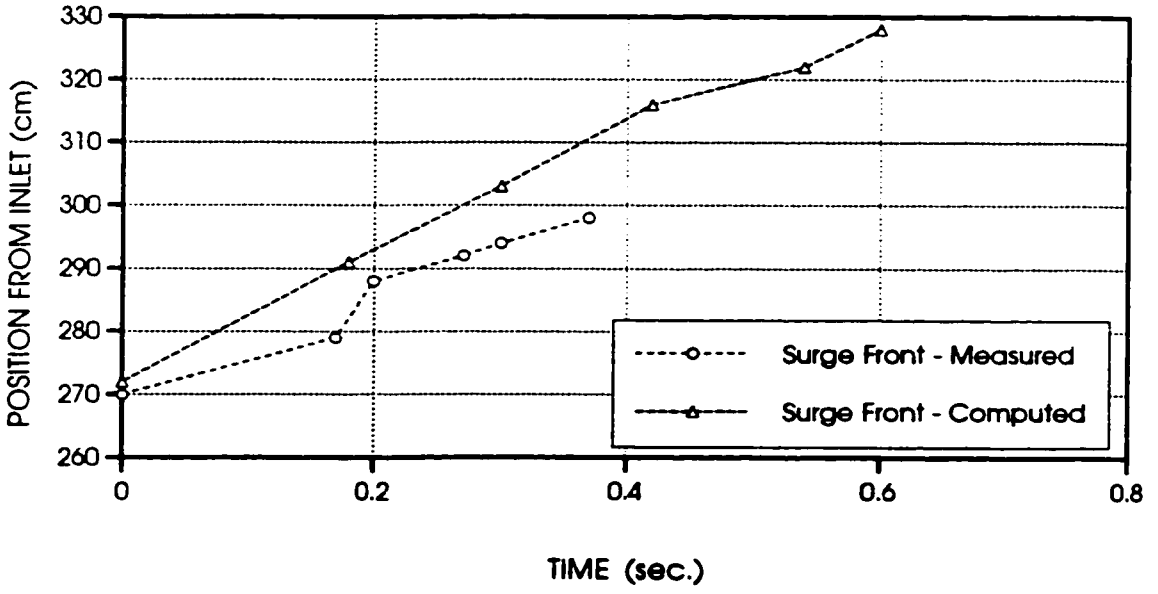

Figure 7.45: Measured and computed surge development for test case r4tc4

CHAPTER 8.0

CONCLUSIONS AND SUGGESTIONS FOR FUTURE RESEARCH

8.1 Conclusions

The following conclusions can be drawn on the basis of the present study. The surges and ice runs caused by the release of breakup ice jams are greatly influenced by: (a) the initial water surface and ice jam thickness profiles; (b) the ice floes characteristics; and (c) the conditions under which the jam collapses.

the tests related to surges and ice runs revealed that surges formed after the ice run was almost fully developed. The characteristics of the ice runs immediately after release were identified to occur under five different mechanisms. These mechanisms are: horizontal movement of front; ice mass slide; ice mass surfacing; gradual leveling; and combination of the above. The surge characteristics depend highly on the type of the release mechanism. Observations have shown that immediately after release and for a very short period of time, the ice jam thickness in the trailing edge region changes in thickness. After that time, the ice jam which becomes more of an ice cover accumulation after release, moves in the downstream direction with little change in its thickness profile. The downstream propagation of the surge as well as the ice jam front occurs at a constant speed. The ice jam front velocity was observed to be much higher than that of the flow immediately after release, and appeared to gradually decrease to the flow velocity. In certain cases, the surge traveling above the main channel flow in the downstream region was observed to attain a peak depth as high as the flow depth.

The numerical models simulation of the tests related to the ice jam release event showed that the assumption of a linear water surface profile between the leading and trailing edges of the ice jam underestimate the maximum water level expected downstream.

The numerical model is capable of reproducing the features of the laboratory experiments. The model correctly simulates the dispersion of the ice mass in the trailing edge region immediately after release. Computed and measured maximum water levels, and ice jam front speeds compare well. Overall, the numerical model presented in this study provides an improvement over the analytical, and existing numerical models.

8.2 Recommendations for further research

A working group on river ice jams consisting of Beltaos, Gerard, Petryk and Prows prepared a science report on field studies of ice jams and research needs. This report was published by the National Hydrology Research Institute, Environment Canada in 1990. Part of this report was to define research needs in relation to ice jams, in Canada. In view of their recommendations, the present study was conducted in order to improve upon the understanding of the surge generation and propagation as well as the accompanying ice run which results after the release of breakup ice jams, as well as to advance the state-of-the-art to that respect. Recommendations for further research are given below:

8.2.1 Experimental work

1. The characteristics of the negative surge traveling in the upstream direction.

2. Seepage across partially grounded ice jams especially in the trailing edge region.

3. Measurements of forces on the plate as well as on the walls of the flume would provide a much better understanding of the initial conditions immediately prior to release.

4. Further experiments on surges propagating in the downstream direction under ice covered conditions should be performed.

5. Experiments to investigate the ice transport characteristics of an accumulation ice cover in two-dimensions and in a release scenario.

8.2.2 Numerical modeling work

1. Better treatment of boundary conditions for surges.

2. The model should be improved to account for the redistribution of thicknesses not through dispersion but rather by erosion, deposition, and shoving.

3. Development of a two-dimensional model along the depth of the flume.

LIST OF REFERENCES

1. Abbot, M.B. (1979), "Computational Hydraulics - Elements of Theory of Free Surface Flows", International Institute for Hydraulic and Environmental Engineering, Delft and Danish Hydraulic Institute, Horsholm.

2. Anderson, D. A., Tannehill, J. C. and Pletcher, R. H. (1984), "Computational Fluid Mechanics and Heat Transfer", Hemisphere Publishing Corporation.

3. Beltaos, S., (1993), Personal communications.

4. Beltaos, S., (1994), Written communications.

5. Beltaos, S. (1988), "Configuration Properties of a Breakup Jam", CJCE, Vol.15, No.4, pp.685-697.

6. Beltaos, S. and B.G.Krishnappan (1982), "Surges from Ice Jam Releases: A Case Study", CJCE, 9(2), pp.276-284.

7. Beltaos, S., Gerard, R., Petryk, S. and Prowse, T.D. (1991), "Working Group on River Ice Jams - Field Studies and Research Needs", NHRI, Science Report Series, Environment Canada.

8. Beltaos S. and Wong, J. (1986), "Downstream Transition of River Ice Jams," ASCE, Journal of Hydraulic Engineering, Vol. 112, No.2, pp 91-110.

9. Beltaos S. and Krishnappan, B. G. (1990), "Frature and Break of River Ice Cover," Canadian Journal of Civil Engineering, Vol. 17, pp 173-183.

10. Beltaos, S., and Dean M. A., "Field Investigation of a Hanging Dam", NWRI, Alberta Research Council, Published in the CSCE.

11. Beltaos, S. and Wong, J. (1986), "Preliminary Studies of Grounded Ice Jams", IAHR Ice Symposium, IOWA City, IOWA.

12. Bjedov, G. (1991), "Ice Transport and Jamming in River Bends", Ph.D. Thesis, Department of Civil and Environmental Engineering, Clarkson University, Potsdam, New York.

13. Budgen, L. G. (1979), " The Deformation of Pack Ice by Ridging", Journal of Geophysical Research, Vol. 84, No.C4, April 20.

14. Doyle, P. F. (1977), " 1977 Breakup and Subsequent Ice Jam at Fort McMurray," Alberta Research Council - Transportation and Surface Water Engineering Division.

15. Doyle, P. F. and Andres, D. D. (1979), " 1979 Spring Breakup and Ice Jamming on the Athabasca River near Fort McMurry", Alberta Research Council, Edmonton, Alberta.

16. Ettema, R. (1990), "Jam Initiation in Unobstructed Channels: Laboratory Observations", Journal of Hydraulic Research, Vol.28, No.6, pp.573-684.

17. Ettema, R., and Schaefer, J., (1986), "Experiments on Freeze-Bonding Between Ice Blocks", Journal of Glaciology, Vol. 32, No. 112, pp.397-403.

18. Ettema, R., Matsuishi, M. and Kitazawa, T., (1986), "Model Tests on Ice-Rubble Size and Ship Resistance in Ice Rubble", Cold Regions Science and Technology, Vol. 12, pp.229-243, Elsevier, Netherlands.

19. Ettema, R., and Urroz, G., (1987), "Simple-Shear-Box Experiments on Ice Rubble", Cold Regions Science and Technology, Vol. 14, pp.185-199, Elsevier, Netherlands.

20. Ettema, R., and Huang, H. P., (1988), "Ice-Rubble Accumulation Beneath Barges Moving Through Ice-Covered Waters", IAHR, Journal of Hydraulic Research, Vol. 26, No. 4, Elsevier, Netherlands.

21. Fennema, R. J. and Chaudhry, M. H., (1990), "Explicit Methods for 2-D Transport Free-Surface Flows", ASCE, Journal of Hydraulic Engineering, Vol. 116, No. 8, pp. 1013-1033.

22. Ferrick, M.G., Mulherin N.D. (1989), "Framework for Control of Dynamic Ice Breakup by River Regulation", CRREL Report CR 89-12.

23. Ferrick, M.G., P.B.Weyrick and S.T.Hunnewell (1991), "Analysis of River Ice Motion Near a Breaking Front", CJCE, to be submitted.

24. Ferrick, M.G. (1985), "Analysis of River Wave Types", Water Resources Research, Vol. 21, pp.209-220.

25. Ferrick, M.G., Bilmes, and S.E. Long (1984), "Modelling Rapidly Varied Flow in Tailwaters", Water Resources Research, Vol.20, pp.271-289.

26. Garcia, F.R. (1983), "Mathematical Modelling of Two-Dimensional Hydraulic Problems Using a Fully Dense Finite Difference Scheme," M.Sc.A. Thesis, Ecole Polytechnique de Montreal, Montreal, Quebec, Canada.

27. Garcia, R., and Kahawita, R.A. (1986), "Numerical Solution of the St.Venant Equations with the McCormack Finite Difference Scheme", Int. Journal for Numerical Methods in Fluids, Vol. 6, pp. 259-274.

28. Garcia-Navarro and Saviron J.M. (1992), "MacCormack Method for the Numerical Simulation of One-Dimensional Discontinuous Unstready Open Channel Flow", IAHR, Vol.30, No.1.

29. Gerard, R. (1984), "Ice Jam Research", Proceeding of Workshop, Fredericton, N.Brunswick, Canada, pp 181-196.

30. Gogus M., and Tatinclaux, J.C. (1981), "Mean Characteristics of Asymmetric Flows: Application to Flow Below Ice Jams", CJCE, Vol.8, pp.342-350.

31. Henderson, F.M. and Gerard, R. (1981), "Flood Wave Caused by Ice Jam Formation and Failure," Proceedings, IAHR, International Symposium on Ice, Quebec City, pp 209-219.

32. Hibler III, W. D. (1979), "A Dynamic Thermodynamic Sea Ice Model", Journal of Geophysical Oceonography, Vol.9, No.4, pp.815-846.

33. Hibler III, W. D. (1986), "Ice Dynamics", Ch. 9, The Geophysics of Sea Ice, N. Untersteiner (ed.), NATO ASI Series, Plenum Press, 577-639.

34. Hibler III, D.H. and Tucker III, B.W. (1979), "Some Results from a Linear-viscous Model of the Arctic Ice Cover", Journal of Glaciology, Vol.22, No.87.

35. Joliffe, I. and Gerard, R. (1982), "Surges Released by Ice Jams", Proceedings of Workshop on Hydraulics of Ice-Covered Rivers, Edmonton, Alta., pp.253-259.

36. Kennedy, F. J. (1975), "Ice-Jam Mechanics", IAHR Third Inernational Symposium on Ice Problems, Hanover, New Hampshire.

37. Lal, W. and Shen, H. T., (1990), "Mathematical Model for River Ice Process", ASCE, Journal of Hydraulic Engineering, Vol. 117, No. 7, pp.851-867.

38. Pariset, E., and Hausser, R. (1961), "Formation and Evolution of Ice Covers on Rivers", ASME-EIC, Vol.5, No.1.

39. Pariset, E, Hausser, R, and Gagnon, M. (1961), "Formation of Ice Covers and Ice Jams Rivers," ASCE, Journal of Hydraulic Engineers, HY 6, November, pp 1-24.

40. Pariset, E, Hausser, R, and Gagnon, M. (1966), "Formation and Evolution of Ice Covers on Rivers", Engineering Institute of Canada, Transactions, Vol. 5, No.1, pp.41-49.

41. Parkinson, F.E. (1981), "Field Observations of Ice Conditions on the Liard/Mackenzie River System", IAHR International Symposium on Ice, Quebec, Vol.1, pp.252-259.

42. Parkinson, F., and Holder, G. (1982), "Liard-Macknezie Winter Regime Study", LHL-830, Vol. 1 - 4.

43. Parkinson, F. (1982), "Liard-Macknezie Winter Regime Study - Observations of 1982 Break-up", LHL-868, Vol. 1 - 4.

44. Parkinson, F.E. and Holder, G.K. (1988), "Ice Jam Development, Release and Surge Wave Propagation, Mackenzie River at Norman Wells," Fifth Workshop on Hydraulics of River Ice/Ice Jams, Winnipeg, Canada, pp 209-223.

45. Parmeter, R.R. and Coon, D.M. (1972), "Model of Pressure Ridge Formation in Sea Ice", Journal of Geophysical Research, Vol.77, No.3, November 20.

46. Peyret, R. and Taylor T.D. (1983), "Computational Methods for Fluid Flow," Springer-Verlag New York Inc.

47. Rivard, G., Kemp, T. and Gerard, R. (1984), " Documentation and Analysis of the Water Level Profile Through an Ice Jam, Mackenzie River", Workshop on the Hydraulics of River Ice, Fredericton, New Brunswick.

48. Rothrock, A.D. (1975), "The Energetics of the Plastic Deformation of Pack Ice by Ridging", Journal of Geophysical Research, Vol.80, No.33, November 20.

49. Saade, R., and Sarraf, S. (1994), "Phreatic Water Surface Profiles Along Ice Jams - An Experimental Study", Accepted in Nordic Hydrology, Revised and Resubmitted.

50. Saade, R., Tsai, W. F. and Chen, H. L. (1994), "Laboratory and Numerical Studies of Ice Transport in Channels", Accepted in ASCE, Journal of Engineering Mechanics, Revised and Resubmitted.

51. Saade, R., Tsai, W. F., and Sarraf, S., (1994), "Development of MacCormack Method and Stability Analysis for Ice Release in Rivers", Submitted to ASCE, Jounal of Hydraulic Engineering, Accepted with Revision.

52. Saade, R., Troitsky, M., and Ramamurthy, A., (1994), "Modeling of Ice Jam Resistance to Main Channel Flow", Submitted to International Journal of Numerical Methods in Fluid Flow.

53. Saade, R.G. (1990), "Numerical Modelling of Ice Cover Melting under Turbulent Flow Conditions," Master Thesis, Department of Civil engineering, Concordia University, Montreal, Quebec, Canada.

54. Saade, R., and Sarraf, S. (1993), "Analysis of Surges Resulting from Ice Jam Releases", 14th Canadian Congress of Applied Mechanics, Kingston, Ontario, Canada, May.

55. Saade, R., Sarraf, S., and El Jabi, N. (1993), "Numerical Modeling of Surges Resulting from Ice Jam Release", 11th Canadian Hydrotechnical Conference, CSCE, Fredericton, New Brunswick, Canada, June.

56. Sayed I. and Davis, J.L. (1992), "Ice Jam Thickness Profiling on the Saint John River, New Brunswick", IAHR Ice Symposium, Banff, Alberta.

57. Shen, H. and Ackermann, N. (1982), "Constitutive Relationships for Fluid-Solid Mixtures", Americal Society of Civil Engineering, Journal of Engineering Mechanics Division, Vol. 108, No. EM5, October.

58. Shen, H. T., Shen, H., and Tsai, S. M. (1990), "Dynamic Transport of River Ice," Journal of Hydraulic Research, Vol. 28, No.6, pp 659-671.

59. Shen, H.T., Chen, Y.C. (1992)," Lagrangian Discrete Parcel Simulation of Two Dimensional River Ice Dynamics," Report No. 92-9, Department of Civil and Environmental Engineering, Clarkson University, Potsdam, NY.

60. Shen, H.T., Chen, Y.C., Wake, A., and Crissman, R.R. (1991)," A Two-Dimensional Surface Drift Model for River Ice," ASCE Conference, Cold Regions Engineering, pp 355-362.

61. Shen, H.H., Hibler, W. D., and Shen, H. T., (1987)," A Role of Floe Collisions in Sea Ice Rheology", Journal of Geophysical Research, Vol. 92, No. C7, pp.7085-7096.

62. Shen, H. T., and Yapa, P. D., (1984), "Computer Simulation on Ice Cover Formation in the Upper St. Lawrence River", Workshop on the Hydraulics of River Ice, Fredericton, New Brunswick, pp.247-275.

63. Tatinclaux, J.C. (1977), "Equilibrium Thickness of Ice Jams, " ASCE, Journal of Hydraulic Engineers, HY9, September, pp 959-974.

64. Tatinclaux, J.C. and Gogus M. (1983), "Asymmetric Plane Flow with Application to Ice Jams, " ASCE, Journal of the Hydraulic Division, Vol.109, No. 11.

65. Thorndike, S.A., Rothrock, A.D., Maykut, A.G., and Colony, R. (1975), "The Thickness Distribution of Sea Ice", Journal of Geophysical Research, Vol. 80, NO. 33, November 20.

66. Tsai, S.-M., Shen, H.T., and Shen, H. (1988), "Dynamic Transport of River Ice and Jam Initiation," Report No. 88-2, Department of Civil and Environmental Engineering, Clarkson University, Potsdam, NY.

67. Uzuner, M.S. and Kennedy, J.F. (1976), "Theoretical Model of River Ice Jams," Journal of Hydraulic Division, ASCE, Vol. 102, HY9, pp 1365-1383.

68. Wong, J., S. Beltaos, and Krishnappan, B. G. (1985), "Laboratory Tests on Surges Created by Ice Jam Releases, " Canadian Journal of Civil Engineering, Vol. 12, pp. 930-933.

LIST OF SYMBOLS

A	=	Jacobian of E;
C_d^{aw}	=	wind stress coefficient at air-water interface;
C_i	=	ice concentration;
C_{imax}	=	maximum packing ice concentration;
C_r	=	Courant number of water;
C_{ri}	=	Courant number of ice;
C_{rx}, C_{ry}	=	Courant number of water in the x and y directions, respectively;
e	=	principal axes ration of an elliptical yield curve of ice;
F_{ax}, F_{ay}	=	components of wind drag on ice in the x and y directions, respectively;
F_C	=	ice cohesive force;
F_N	=	the normal force of ice against the boundary;
$(F_f)_x$, $(F_f)_y$	=	components of friction forces on the wall in the x and y directions, respectively;
F_{px}, F_{py}	=	components of pressure force on ice in the x and y directions, respectively;
F_{Rd}	=	Froude number of water;
F_{Rdy}, F_{Rdy}	=	Froude number of water in the x and y directions, respectively;
F_{wx}, F_{wy}	=	components of water drag on ice in the x and y directions, respectively;
G	=	amplification matrix;
g	=	gravitational acceleration;
h	=	Flow depth;
J	=	an empirical constant;
L	=	wave length of particular wave;

L_x, L_y = finite difference operators in the x and y directions, respectively;

M_i = ice mass;

n_b = Manning's coefficient of the bed;

P_{wx}, P_{wy} = pressure in the x and y directions, respectively;

R = hydraulic radius;

R_x, R_y = components of internal ice resistance in the x and y directions, respectively;

S_{fx}, S_{fy} = the friction slopes in the x and y directions, respectively;

s_i = specific weight of ice;

T = period of particular wave;

t = time;

u, v = depth-averaged velocities in the x and y directions, respectively;

u_i, v_i = ice velocities in the x and y directions, respectively;

W = wind velocity at 10 m above the water surface;

x, y = spatial coordinates;

Z_b = bottom elevation of bed;

α = wave number of particular wave;

α_w = angle between the wind direction and the x axis;

β = angular frequency of particular wave;

ϕ = angle of internal friction of surface ice;

ϕ_B = dynamic internal friction angle;

Δt = computational time step;

Δx, Δy = computational grid spacing in the x and y directions, respectively;

i = $\sqrt{-1}$;

λ = the eigenvalue of A;

λ_{max} = the largest eigenvalue of A;

θ = ice thickness;

ρ = density of water;

ρ_a = density of air;

ρ_i = density of ice;

σ_{max} = the largest eigenvalue of G;

σ_{xx}, σ_{yy} = ice internal normal stress components;

σ_{xy}, σ_{yx} = ice internal shear stress components.

τ_x^{aw}, τ_y^{aw} = wind drags on air-water interface in the x and y directions, respectively;

τ_x^{wi}, τ_y^{wi} = water drags on ice-water interface in the x and y directions, respectively;

τ_{bx},τ_{by} = the bottom shear stresses in the x and y directions, respectively;

APPENDIX A
DESCRETIZATION OF THE GOVERNING HYDRODYNAMIC AND ICE DYNAMIC EQUATIONS

Lx OPERATOR (calculation of derivatives in the x direction)

Terms computed by the operator

HYDRODYNAMIC EQUATIONS

• continuity

$$\frac{\partial h}{\partial t} + \frac{\partial[uh - (u-u_i)C_i s_i \theta]}{\partial x} = 0 \qquad \text{(A.1)}$$

• momentum x-direction

$$\frac{\partial u(h - C_i s_i \theta)}{\partial t} + \frac{\partial u^2(h - C_i s_i \theta)}{\partial x} = \frac{1}{\rho}(1 - C_i)\tau_x^{aw} - \frac{1}{\rho}(C_i \tau_x^{wi} + \tau_{bx}) - gh\frac{\partial(h + Z_b)}{\partial x} \qquad \text{(A.2)}$$

• momentum y-direction

$$\frac{\partial v(h - C_i s_i \theta)}{\partial t} + \frac{\partial uv(h - C_i s_i \theta)}{\partial x} = 0 \qquad \text{(A.3)}$$

ICE DYNAMIC EQUATIONS

• momentum x-direction

$$\frac{\partial u_i}{\partial t} + \frac{1}{2}\frac{\partial u_i^2}{\partial x} = \left[\frac{\partial(C_i \theta \sigma_{xx})}{\partial x} + C_i \tau_x^{ai} + C_i \tau_x^{wi} - C_i \rho g s_i \theta \frac{\partial(h + Z_b)}{\partial x}\right]\frac{1}{M_i} \qquad \text{(A.4)}$$

• momentum y-direction

$$\frac{\partial v_i}{\partial t} + u_i\frac{\partial v_i}{\partial x} = \frac{\partial(C_i \theta \sigma_{xy})}{\partial x}\frac{1}{M_i} \qquad \text{(A.5)}$$

• conservation of ice mass

$$\frac{\partial(M_i)}{\partial t} + \frac{\partial(u_i M_i)}{\partial x} = 0 \qquad \text{(A.6)}$$

• conservation of surface area ice concentration

$$\frac{\partial C_i}{\partial t} + \frac{\partial(u_i C_i)}{\partial x} = 0 \qquad \text{(A.7)}$$

Discretization of the L_x operator

Predictor Sequence: Backward Difference

$$hl^p_{i,j} = hl^o_{i,j} - \frac{\Delta t_x}{\Delta x}\left[ul^o_{i,j}\, hl^o_{i,j} - ul^o_{i-1,j}\, hl^o_{i-1,j} + s_i[(ul^o_{i,j} - u_i l^o_{i,j})C_i l^o_{i,j}\theta l^o_{i,j} - (ul^o_{i-1,j} - u_i l^o_{i-1,j})C_i l^o_{i-1,j}\theta l^o_{i-1,j}]\right] \qquad \text{(A.8)}$$

$$Ul^{p}_{i,j} = Ul^{o}_{i,j} - \frac{\Delta t_x}{\Delta x}\left[(ul^{o}_{i,j}\,Ul^{o}_{i,j} - ul^{o}_{i-1,j}\,Ul^{o}_{i-1,j})\right]$$
$$- \Delta t_x\left[\frac{1}{\rho}(1 - C_i l^{o}_{i,j})\tau^{aw}_{x} l^{o}_{i,j} - \frac{1}{\rho}(C_i l^{o}_{i,j}\,\tau^{wi}_{x} l^{o}_{i,j} + \tau_{bx} l^{o}_{i,j})\right]$$
$$- g h l^{o}_{i,j}\,\frac{\Delta t_x}{\Delta x}\left[(h l^{o}_{i,j} + Z_b l^{o}_{i,j}) - (h l^{o}_{i-1,j} + Z_b l^{o}_{i-1,j})\right] \qquad \text{(A.9)}$$

in which $Ul_{i,j} = ul_{i,j}(h l_{i,j} - C_i l_{i,j} s_i \theta l_{i,j})$

$$Vl^{p}_{i,j} = Vl^{o}_{i,j} - \frac{\Delta t_x}{\Delta x}\left[(ul^{o}_{i,j}\,Vl^{o}_{i,j} - ul^{o}_{i-1,j}\,Vl^{o}_{i-1,j})\right]$$

in which $Vl_{i,j} = vl_{i,j}(h l_{i,j} - C_i l_{i,j} s_i \theta l_{i,j})$ (A.10)

$$u_i l^{p}_{i,j} = u_i l^{o}_{i,j} - \frac{\Delta t_x}{\Delta x}\left[\frac{1}{2}(ul^{o\,2}_{i,j} - ul^{o\,2}_{i-1,j}) - (C_i l^{o}_{i,j}\theta l^{o}_{i,j}\sigma_{xx} l^{o}_{i,j} - C_i l^{o}_{i-1,j}\theta l^{o}_{i-1,j}\sigma_{xx} l^{o}_{i-1,j})\right]$$
$$+ \Delta t_x\left[C_i l^{o}_{i,j}\tau^{ai}_{x} l^{o}_{i,j} + C_i l^{o}_{i,j}\,\tau^{wi}_{x} l^{o}_{i,j})\right]$$
$$- \rho g s_i \theta l^{o}_{i,j}\,\frac{\Delta t_x}{\Delta x}\left[(h l^{o}_{i,j} + Z_b l^{o}_{i,j}) - (h l^{o}_{i-1,j} + Z_b l^{o}_{i-1,j})\right]\frac{1}{(\rho g s_i \theta l^{o}_{i,j})} \qquad \text{(A.11)}$$

$$v_i l^{p}_{i,j} = v_i l^{o}_{i,j} - \frac{\Delta t_x}{\Delta x}\left[ul^{o}_{i,j}\,(vl^{o}_{i,j} - vl^{o}_{i-1,j})\right.$$
$$\left. - (C_i l^{o}_{i,j}\theta l^{o}_{i,j}\sigma_{xy} l^{o}_{i,j} - C_i l^{o}_{i-1,j}\theta l^{o}_{i-1,j}\sigma_{xy} l^{o}_{i-1,j})\right]\frac{1}{(\rho g s_i \theta l^{o}_{i,j})} \qquad \text{(A.12)}$$

$$Ml^{p}_{i,j} = Ml^{o}_{i,j} - \frac{\Delta t_x}{\Delta x}\left[(ul^{o}_{i,j}\,Ml^{o}_{i,j} - ul^{o}_{i-1,j}\,Ml^{o}_{i-1,j})\right] \qquad \text{(A.13)}$$

$$Cl^{p}_{i,j} = Cl^{o}_{i,j} - \frac{\Delta t_x}{\Delta x}\left[(ul^{o}_{i,j}\,Cl^{o}_{i,j} - ul^{o}_{i-1,j}\,Cl^{o}_{i-1,j})\right] \qquad \text{(A.14)}$$

in which $Ml_{i,j} = C_i l_{i,j} \rho_i \theta l_{i,j}$

*Corrector Sequence: **Forward Difference***

$$hl^{c}_{i,j} = hl^{p}_{i,j} - \frac{\Delta t_x}{\Delta x}\left[ul^{p}_{i+1,j}\,hl^{p}_{i+1,j} - ul^{p}_{i,j}\,hl^{p}_{i,j} + \right.$$
$$\left. s_i[(ul^{p}_{i+1,j} - u_i l^{p}_{i+1,j})C_i l^{p}_{i+1,j}\theta l^{p}_{i+1,j} - (ul^{p}_{i,j} - u_i l^{p}_{i,j})C_i l^{p}_{i,j}\theta l^{p}_{i,j}\right] \qquad \text{(A.15)}$$

$$Ul^{c}_{i,j} = Ul^{p}_{i,j} - \frac{\Delta t_x}{\Delta x}\left[(ul^{p}_{i+1,j}\,Ul^{p}_{i+1,j} - ul^{p}_{i,j}\,Ul^{p}_{i,j})\right]$$
$$- \Delta t_x\left[\frac{1}{\rho}(1 - C_i l^{p}_{i,j})\tau^{aw}_{x} l^{p}_{i,j} - \frac{1}{\rho}(C_i l^{p}_{i,j}\,\tau^{wi}_{x} l^{p}_{i,j} + \tau_{bx} l^{p}_{i,j})\right]$$
$$- g h l^{p}_{i,j}\,\frac{\Delta t_x}{\Delta x}\left[(hl^{p}_{i+1,j} + Z_b l^{p}_{i+1,j}) - (hl^{p}_{i,j} + Z_b l^{p}_{i,j})\right] \qquad \text{(A.16)}$$

$$Vl^{c}_{i,j} = Vl^{p}_{i,j} - \frac{\Delta t_x}{\Delta x}\left[(ul^{p}_{i+1,j}\,Vl^{p}_{i+1,j} - ul^{p}_{i,j}\,Vl^{p}_{i,j})\right] \qquad \text{(A.17)}$$

$$u_i l^{c}_{i,j} = u_i l^{p}_{i,j} + \frac{\Delta t_x}{\Delta x}\left[-\frac{1}{2}(ul^{p}_{i+1,j}{}^{2} - ul^{p}_{i,j}{}^{2}) + (C_i l^{p}_{i+1,j}\theta l^{p}_{i+1,j}\sigma_{xx} l^{p}_{i+1,j} - C_i l^{p}_{i,j}\theta l^{p}_{i,j}\sigma_{xx} l^{p}_{i,j})\right]$$
$$+ \Delta t_x\left[C_i l^{p}_{i,j}\tau^{ai}_{x} l^{p}_{i,j} + C_i l^{p}_{i,j}\,\tau^{wi}_{x} l^{p}_{i,j} + \tau_{bx} l^{p}_{i,j}\right]$$
$$- \rho g s_i \theta l^{p}_{i,j}\,\frac{\Delta t_x}{\Delta x}\left[(hl^{p}_{i+1,j} + Z_b l^{p}_{i+1,j}) - (hl^{p}_{i,j} + Z_b l^{p}_{i,j})\right] \qquad \text{(A.18)}$$

$$v_i l^{c}_{i,j} = v_i l^{p}_{i,j} + \frac{\Delta t_x}{\Delta x}\left[-u_i l^{p}_{i,j}\,(v_i l^{p}_{i+1,j} - v_i l^{p}_{i,j}) + (C_i l^{p}_{i+1,j}\theta l^{p}_{i+1,j}\sigma_{xy} l^{p}_{i+1,j} - C_i l^{p}_{i,j}\theta l^{p}_{i,j}\sigma_{xy} l^{p}_{i,j})\right] \qquad \text{(A.19)}$$

$$M_i l^{c}_{i,j} = M_i l^{p}_{i,j} - \frac{\Delta t_x}{\Delta x}\left[(u_i l^{p}_{i+1,j} M_i l^{p}_{i+1,j} - u_i l^{p}_{i,j}\,M_i l^{p}_{i,j})\right] \qquad \text{(A.20)}$$

$$C_i l^{c}_{i,j} = C_i l^{p}_{i,j} - \frac{\Delta t_x}{\Delta x}\left[(ul^{p}_{i+1,j} C_i l^{p}_{i+1,j} - u_i l^{p}_{i,j}\,C_i l^{p}_{i,j})\right] \qquad \text{(A.21)}$$

The values of variables for continuing next operator **Ly** should be updated as:

$$(hl^{o}_{i,j})_{Ly} = \frac{1}{2}(hl^{c}_{i,j} + hl^{o}_{i,j})_{Lx} \qquad \text{(A.22)}$$

$$(Ul^{o}_{i,j})_{Ly} = \frac{1}{2}(Ul^{c}_{i,j} + Ul^{o}_{i,j})_{Lx} \qquad \text{(A.23)}$$

$$(Vl^{o}_{i,j})_{Ly} = \frac{1}{2}(Vl^{c}_{i,j} + Vl^{o}_{i,j})_{Lx} \qquad \text{(A.24)}$$

$$(u_i l^{o}_{i,j})_{Ly} = \frac{1}{2}(u_i l^{c}_{i,j} + u_i l^{o}_{i,j})_{Lx} \qquad \text{(A.25)}$$

$$(v_i l^{o}_{i,j})_{Ly} = \frac{1}{2}(v_i l^{c}_{i,j} + v_i l^{o}_{i,j})_{Lx} \qquad \text{(A.26)}$$

$$(M_i l^{o}_{i,j})_{Ly} = \frac{1}{2}(M_i l^{c}_{i,j} + M_i l^{o}_{i,j})_{Lx} \qquad \text{(A.27)}$$

$$(C_i l^{o}_{i,j})_{Ly} = \frac{1}{2}(C_i l^{c}_{i,j} + C_i l^{o}_{i,j})_{Lx} \qquad \text{(A.28)}$$

Because the variables U, V, and M_i used in carrying out the MacCormack scheme each include more than one variables: for example, U includes h, u_i, θ, and C_i; V includes h, v_i, θ, and C_i; and M_i includes θ and C_i. Therefore, the variables h, u_i, v_i, and C_i can be

solved first. After U, V, and M_i are solved, then u, v, and θ can be recovered from U, V, and M_i by the following manipulation:

$$(\theta l^{\circ}_{i,j})_{Ly} = (M_i l^{\circ}_{i,j})_{Ly} / s_i \rho (C_i l^{\circ}_{i,j})_{Ly} \quad \text{(A.29)}$$

$$(u l^{\circ}_{i,j})_{Ly} = (U l^{\circ}_{i,j})_{Ly} / (h l^{\circ}_{i,j} - s_i \theta l^{\circ}_{i,j} C_i l^{\circ}_{i,j})_{Ly} \quad \text{(A.30)}$$

and

$$(v l^{\circ}_{i,j})_{Ly} = (V l^{\circ}_{i,j})_{Ly} / (h l^{\circ}_{i,j} - s_i \theta l^{\circ}_{i,j} C_i l^{\circ}_{i,j})_{Ly} \quad \text{(A.31)}$$

Ly OPERATOR (calculation of derivatives in the y direction)

Terms computed by the operator

HYDRODYNAMIC EQUATIONS

• continuity

$$\frac{\partial h}{\partial t} + \frac{\partial [vh - (v - v_i) C_i s_i \theta]}{\partial y} = 0 \quad \text{(A.32)}$$

• momentum x-direction

$$\frac{\partial u(h - C_i s_i \theta)}{\partial t} + \frac{\partial uv(h - C_i s_i \theta)}{\partial y} = 0 \quad \text{(A.33)}$$

• momentum y-direction

$$\frac{\partial v(h - C_i s_i \theta)}{\partial t} + \frac{\partial v^2(h - C_i s_i \theta)}{\partial y} = \frac{1}{\rho}(1 - C_i)\tau_y^{aw} - \frac{1}{\rho}(C_i \tau_y^{wi} + \tau_{by}) - gh \frac{\partial (h + Z_b)}{\partial y} \quad \text{(A.34)}$$

ICE DYNAMIC EQUATIONS

• momentum x-direction

$$\frac{\partial u_i}{\partial t} + v_i \frac{\partial u_i}{\partial y} = \frac{\partial (C_i \theta \sigma_{yx})}{\partial y} \frac{1}{M_i} \quad \text{(A.35)}$$

• momentum y-direction

$$\frac{\partial v_i}{\partial t} + \frac{1 \partial v_i^2}{2 \partial y} = [\frac{\partial (C_i \theta \sigma_{yy})}{\partial y} + C_i \tau_y^{ai} + C_i \rho g s_i \theta \frac{\partial (h + Z_b)}{\partial y} + C_i \tau_y^{wi}] \frac{1}{M_i} \quad \text{(A.36)}$$

• conservation of ice mass

$$\frac{\partial (M_i)}{\partial t} + \frac{\partial (v_i M_i)}{\partial y} = 0 \quad \text{(A.37)}$$

• conservation of surface area ice conventration

$$\frac{\partial C_i}{\partial t} + \frac{\partial (v_i C_i)}{\partial y} = 0 \quad \text{(A.38)}$$

Discretization of the L_y operator

Predictor Sequence: Backward Difference

$$hl^{p}_{i,j} = hl^{o}_{i,j} - \frac{\Delta t_y}{\Delta y}\left[vf^{o}_{i,j}\, hl^{o}_{i,j} - vl^{o}_{i,j-1}\, hl^{o}_{i,j-1} + s_i[(vf^{o}_{i,j} - v_i l^{o}_{i,j})C_i l^{o}_{i,j}\theta l^{o}_{i,j} - (vf^{o}_{i,j-1} - v_i l^{o}_{i,j-1})C_i l^{o}_{i,j-1}\theta l^{o}_{i,j-1}\right] \quad \text{(A.39)}$$

$$Ul^{p}_{i,j} = Ul^{o}_{i,j} - \frac{\Delta t_y}{\Delta y}\left[(vf^{o}_{i,j}\, Ul^{o}_{i,j} - vl^{o}_{i,j-1}\, Ul^{o}_{i,j-1})\right] \quad \text{(A.40)}$$

$$Vl^{p}_{i,j} = Vl^{o}_{i,j} - \frac{\Delta t_y}{\Delta y}\left[(vf^{o}_{i,j} Vl^{o}_{i,j} - vl^{o}_{i,j-1}\, Vl^{o}_{i,j-1})\right] - \Delta t_y\left[\frac{1}{\rho}(1 - C_i l^{o}_{i,j})\tau^{aw}_{y} l^{o}_{i,j} - \frac{1}{\rho}(C_i l^{o}_{i,j}\, \tau^{wi}_{y} l^{o}_{i,j} + \tau_{by} l^{o}_{i,j})\right] - g hl^{o}_{i,j}\frac{\Delta t_y}{\Delta y}\left[(hl^{o}_{i,j} + Z_b l^{o}_{i,j}) - (hl^{o}_{i,j-1} + Z_b l^{o}_{i,j-1})\right] \quad \text{(A.41)}$$

$$u_i l^{p}_{i,j} = u_i l^{o}_{i,j} - \frac{\Delta t_y}{\Delta y}\left[vl^{o}_{i,j}\,(ul^{o}_{i,j} - ul^{o}_{i,j-1}) - (C_i l^{o}_{i,j}\theta l^{o}_{i,j}\sigma_{yx} l^{o}_{i,j} - C_i l^{o}_{i,j-1}\theta l^{o}_{i,j-1}\sigma_{yx} l^{o}_{i,j-1})\right]\frac{1}{(\rho g s_i \theta l^{o}_{i,j})} \quad \text{(A.42)}$$

$$v_i l^{p}_{i,j} = v_i l^{o}_{i,j} - \left\{\frac{\Delta t_y}{\Delta y}\left[\frac{1}{2}(vl^{o\,2}_{i,j} - vl^{o\,2}_{i,j-1}) - (C_i l^{o}_{i,j}\theta l^{o}_{i,j}\sigma_{yy} l^{o}_{i,j} - C_i l^{o}_{1,j-1}\theta l^{o}_{1,j-1}\sigma_{yy} l^{o}_{1,j-1})\right] + \Delta t_y\left[C_i l^{o}_{i,j}\tau^{ai}_{y} l^{o}_{i,j} + C_i l^{o}_{i,j}\tau^{wi}_{y} l^{o}_{i,j})\right] - \rho g s_i \theta l^{o}_{i,j}\frac{\Delta t_y}{\Delta y}\left[(hl^{o}_{i,j} + Z_b l^{o}_{i,j}) - (hl^{o}_{i,j-1} + Z_b l^{o}_{i,j-1})\right]\right\}\frac{1}{(\rho g s_i \theta l^{o}_{i,j})} \quad \text{(A.43)}$$

$$M_i l^{p}_{i,j} = M_i l^{o}_{i,j} - \frac{\Delta t_y}{\Delta y}\left[(vf^{o}_{i,j} M_i l^{o}_{i,j} - v_i l^{o}_{i,j-1}\, M_i l^{o}_{i,j-1})\right] \quad \text{(A.44)}$$

$$C_i l^{p}_{i,j} = C_i l^{o}_{i,j} - \frac{\Delta t_y}{\Delta y}\left[(vf^{o}_{i,j} C_i l^{o}_{i,j} - v_i l^{o}_{i,j-1}\, C_i l^{o}_{i,j-1})\right] \quad \text{(A.45)}$$

Corrector Sequence: Forward Difference

$$hl^{c}_{i,j} = hl^{p}_{i,j} - \frac{\Delta t_y}{\Delta y}\left[vl^{p}_{i,j+1}\, hl^{p}_{i,j+1} - vl^{p}_{i,j}\, hl^{p}_{i,j} + s_i[(vl^{p}_{i,j+1} - v_i l^{p}_{i,j+1})C_i l^{p}_{i,j+1}\theta l^{p}_{i,j+1} - (vl^{p}_{i,j} - v_i l^{p}_{i,j})C_i l^{p}_{i,j}\theta l^{p}_{i,j}]\right] \quad \text{(A.46)}$$

$$Ul^{c}_{i,j} = Ul^{p}_{i,j} - \frac{\Delta t_y}{\Delta y}\left[(vl^{p}_{i,j+1}\, Ul^{p}_{i,j+1} - vl^{p}_{i,j}\, Ul^{p}_{i,j})\right] \quad \text{(A.47)}$$

$$Vl^{c}_{i,j} = Vl^{p}_{i,j} - \frac{\Delta t_y}{\Delta y}\left[(vl^{p}_{i,j+1} Vl^{p}_{i,j+1} - vl^{p}_{i,j}\, Vl^{p}_{i,j})\right] - \Delta t_y\left[\frac{1}{\rho}(1 - C_i l^{p}_{i,j})\tau^{aw}_{y} l^{p}_{i,j} - \frac{1}{\rho}(C_i l^{p}_{i,j}\, \tau^{wi}_{y} l^{p}_{i,j} + \tau_{by} l^{p}_{i,j})\right] - g hl^{p}_{i,j}\frac{\Delta t_y}{\Delta y}\left[(hl^{p}_{i,J+1} + Z_b l^{p}_{i,J+1}) - (hl^{p}_{i,j} + Z_b l^{p}_{i,j})\right] \quad \text{(A.48)}$$

$$u_i l^{c}_{i,j} = u_i l^{p}_{i,j} + \frac{\Delta t_y}{\Delta y}\left[-vl^{p}_{i,j}(ul^{p}_{i,j+1} - ul^{p}_{i,j}) + (C_i l^{p}_{i,j+1}\theta l^{p}_{i,j+1}\sigma_{yx} l^{p}_{i,j+1} - C_i l^{p}_{i,j}\theta l^{p}_{i,j}\sigma_{yx} l^{p}_{i,j})\right] \quad \text{(4.44)}$$

$$v_i l^{c}_{i,j} = v_i l^{p}_{i,j} + \frac{\Delta t_y}{\Delta y}\left[-\frac{1}{2}(vl^{p\,2}_{i,j+1} - vl^{p\,2}_{i,j}) + (C_i l^{p}_{i,j+1}\theta l^{p}_{i,j+1}\sigma_{yy} l^{p}_{i,j+1} - C_i l^{p}_{i,j}\theta l^{p}_{i,j}\sigma_{yy} l^{p}_{i,j})\right] + \Delta t_y\left[C_i l^{p}_{i,j+1}\tau^{ai}_{y} l^{p}_{i,j+1} + C_i l^{p}_{i,j}\tau^{wi}_{y} l^{p}_{i,j})\right] - \rho g s_i \theta l^{p}_{i,j}\frac{\Delta t_y}{\Delta y}\left[(hl^{p}_{i,j+1} + Z_b l^{p}_{i,j+1}) - (hl^{p}_{i,j} + Z_b l^{p}_{i,j})\right] \quad \text{(A.49)}$$

$$Ml^{c}_{i,j} = Ml^{p}_{i,j} - \frac{\Delta t_y}{\Delta y}\left[(vl^{p}_{i,j+1} Ml^{p}_{i,j+1} - vl^{p}_{i,j}\, Ml^{p}_{i,j})\right] \quad \text{(A.50)}$$

$$C_i l^{c}_{i,j} = C_i l^{p}_{i,j} - \frac{\Delta t_y}{\Delta y}\left[(vl^{p}_{i,j+1} C_i l^{p}_{i,j+1} - vl^{p}_{i,j}\, C_i l^{p}_{i,j})\right] \quad \text{(A.51)}$$

The values of variables for continuing next operator **Ly'** should be updated as

$$(hl^{o}_{i,j})_{Ly'} = \frac{1}{2}(hl^{c}_{i,j} + hl^{o}_{i,j})_{Ly} \quad \text{(A.52)}$$

$$(Ul^{o}_{i,j})_{Ly'} = \frac{1}{2}(Ul^{c}_{i,j} + Ul^{o}_{i,j})_{Ly} \quad \text{(A.53)}$$

$$(Vl^{o}_{i,j})_{Ly'} = \frac{1}{2}(Vl^{c}_{i,j} + Vl^{o}_{i,j})_{Ly} \quad \text{(A.54)}$$

$$(u_i l^{o}_{i,j})_{Ly'} = \frac{1}{2}(u_i l^{c}_{i,j} + u_i l^{o}_{i,j})_{Ly} \quad \text{(A.55)}$$

$$(v_i l^{o}_{i,j})_{Ly'} = \frac{1}{2}(v_i l^{c}_{i,j} + v_i l^{o}_{i,j})_{Ly} \quad \text{(A.56)}$$

$$(M_i l^{o}_{i,j})_{Ly'} = \frac{1}{2}(M_i l^{c}_{i,j} + M_i l^{o}_{i,j})_{Ly} \quad (A.57)$$

$$(C_i l^{o}_{i,j})_{Ly'} = \frac{1}{2}(C_i l^{c}_{i,j} + C_i l^{o}_{i,j})_{Ly} \quad (A.58)$$

and $(\theta l^{o}_{i,j})_{Ly'}$, $(ul^{o}_{i,j})_{Ly'}$, and $(vl^{o}_{i,j})_{Ly'}$ can be determined from the following manipulation:

$$(\theta l^{o}_{i,j})_{Ly'} = (M_i l^{o}_{i,j})_{Ly'} / s_i \rho (C_i l^{o}_{i,j})_{Ly'} \quad (A.59)$$

$$(ul^{o}_{i,j})_{Ly'} = (Ul^{o}_{i,j})_{Ly'} / (hl^{o}_{i,j} - s_i \theta l^{o}_{i,j} C_i l^{o}_{i,j})_{Ly'} \quad (A.60)$$

and

$$(vl^{o}_{i,j})_{Ly'} = (Vl^{o}_{i,j})_{Ly'} / (hl^{o}_{i,j} - s_i \theta l^{o}_{i,j} C_i l^{o}_{i,j})_{Ly'} \quad (A.61)$$

DISCRETIZATION OF STRESSES IN THE CONSTITUTIVE EQUATIONS

The compressive and shear stresses are also needed to discretize in the finite difference solution. The derivative terms included in Δ (or η and ς), for simplicity, can be first linearized at node (i,j). This means no matter in backward or forward operators, these first derivative terms can be discretized using central difference at node (i,j), and are taken as constant during predictor-corrector procedure. To evaluate the terms \f($\partial\sigma_{xx}$,∂x), $\frac{\partial\sigma_{xx}}{\partial y}$, $\frac{\partial\sigma_{yy}}{\partial x}$, $\frac{\partial\sigma_{yy}}{\partial y}$, $\frac{\partial\sigma_{xy}}{\partial x}$, and $\frac{\partial\sigma_{xy}}{\partial y}$, during backward procedure, all first derivative terms included in the σ_{xx}, σ_{yy}, and σ_{xy} are discretized by forward difference. This discretization treating the mixed/cross derivatives was proposed by LeBalleur et al. (1980).

$$\sigma_{xx}|_{i,j} = 2\eta|_{i,j} \frac{(u_i|_{i+1,j} - u_i|_{i,j})}{\Delta x} + (\varsigma|_{i,j} - \eta|_{i,j}) \left[\frac{(u_i|_{i+1,j} - u_i|_{i,j})}{\Delta x} + \frac{(v_i|_{i,j+1} - v_i|_{i,j})}{\Delta y} \right] - \frac{(P|_{i,j})}{2} \quad (A.62)$$

$$\sigma_{yy}|_{i,j} = 2\eta|_{i,j} \frac{(v_i|_{i,j+1} - v_i|_{i,j})}{\Delta y} + (\varsigma|_{i,j} - \eta|_{i,j}) \left[\frac{(u_i|_{i+1,j} - u_i|_{i,j})}{\Delta x} + \frac{(v_i|_{i,j+1} - v_i|_{i,j})}{\Delta y} \right] - \frac{(P|_{i,j})}{2} \quad (A.63)$$

$$\sigma_{xy}|_{i,j} = \eta|_{i,j} \left[\frac{(v_i|_{i+1,j} - v_i|_{i,j})}{\Delta x} + \frac{(u_i|_{i,j+1} - u_i|_{i,j})}{\Delta y} \right] \quad (A.64)$$

$$\varsigma|_{i,j} = \frac{(P|_{i,j})}{2(\Delta|_{i,j})} \text{ and } \eta|_{i,j} = \frac{(\varsigma|_{i,j})}{e^2}, \tag{A.65}$$

$$\Delta|_{i,j} = \left\{\left[\frac{(u_i|_{i+1,j} - u_i|_{i,j})}{\Delta x} + \frac{(v_i|_{i,j+1} - v_i|_{i,j})}{\Delta y}\right]^2 + \left[\frac{(u_i|_{i+1,j} - u_i|_{i,j})}{\Delta x} - \frac{(v_i|_{i,j+1} - v_i|_{i,j})}{\Delta y}\right]^2 + \left[\frac{(v_i|_{i+1,j} - v_i|_{i,j})}{\Delta x} + \frac{(u_i|_{i,j+1} - u_i|_{i,j})}{\Delta y}\right]^2/2e\right\}^{1/2}$$

$$P|_{i,j} = \tan^2\left(\frac{\pi}{4} - \frac{\phi}{2}\right)\left(1 - \frac{\rho_i}{\rho}\right)\frac{(\rho_i g \theta|_{i,j})}{2}\left(\frac{C_i|_{jj}}{C_{imax}}\right)^j \tag{A.66}$$

During forward procedure, all first derivatives included in the σ_{xx}, σ_{yy}, and σ_{xy} are discretized by backward difference such as in the following

$$\sigma_{xx}|_{i,j} = 2\eta|_{i,j}\frac{(u_i|_{i,j} - u_i|_{i-1,j})}{\Delta x} + (\varsigma|_{i,j} - \eta|_{i,j})\left[\frac{(u_i|_{i,j} - u_i|_{i-1,j})}{\Delta x} + \frac{(v_i|_{i,j} - v_i|_{i,j-1})}{\Delta y}\right] - \frac{(P|_{i,j})}{2} \tag{A.67}$$

$$\sigma_{yy}|_{i,j} = 2\eta|_{i,j}\frac{(v_i|_{i,j} - v_i|_{i,j-1})}{\Delta y} + (\varsigma|_{i,j} - \eta|_{i,j})\left[\frac{(u_i|_{i,j} - u_i|_{i-1,j})}{\Delta x} + \frac{(v_i|_{i,j} - v_i|_{i,j-1})}{\Delta y}\right] - \frac{(P|_{i,j})}{2} \tag{A.68}$$

$$\sigma_{xy}|_{i,j} = \eta|_{i,j}\left[\frac{(v_i|_{i,j} - v_i|_{i-1,j})}{\Delta x} + \frac{(u_i|_{i,j} - u_i|_{i,j-1})}{\Delta y}\right] \tag{A.69}$$

$$\Delta|_{i,j} = \left\{\left[\frac{(u_i|_{i,j} - u_i|_{i-1,j})}{\Delta x} + \frac{(v_i|_{i,j} - v_i|_{i,j-1})}{\Delta y}\right]^2 + \left[\frac{(u_i|_{i,j} - u_i|_{i-1,j})}{\Delta x} - \frac{(v_i|_{i,j} - v_i|_{i,j-1})}{\Delta y}\right]^2 + \left[\frac{(v_i|_{i,j} - v_i|_{i-1,j})}{\Delta x} + \frac{(u_i|_{i,j} - u_i|_{i,j-1})}{\Delta y}\right]^2/2e\right\}^{1/2} \tag{A.70}$$

APPENDIX B
THE VON NEWMANN ANALYSIS FOR THE HYDRODYNAMIC AND ICE DYNAMIC EQUATIONS

In this study the von Neumann analysis was used to investigate the stability of the governing hydrodynmic and ice dynamic equations constituting the mathematical model presented earlier. The stability analysis was carried out for two cases: (1) a single equation and (2) for a system of equations, which can be written in the conservative form as

$$\frac{\partial \mathbf{E}}{\partial t} + \frac{\partial \mathbf{F}}{\partial x} = 0 \qquad \text{(B.1)}$$

where **E** and **F** are vectors and **F = F(E)**. In general this system of equations is nonlinear. To perform a linear stability analysis, we rewrite the system as

$$\frac{\partial \mathbf{E}}{\partial t} + \frac{\partial \mathbf{F}}{\partial \mathbf{E}} \frac{\partial \mathbf{E}}{\partial x} = 0 \qquad \text{(B.2)}$$

or

$$\frac{\partial \mathbf{E}}{\partial t} + [A] \frac{\partial \mathbf{E}}{\partial x} = 0 \qquad \text{(B.3)}$$

where [A] is the Jacobian matrix (=∂F/∂E). We locally linearize the system by holding [A] constant while the E vector is advanced through a single time step. A similar linearization is frequently used for a single nonlinear equation permitting the application of the von Neumann method.

Note that Eq. (B.3) is not in conservative form. It has been shown that the eigenvalue matrixes for hydrodynamic equations in conservative form and non conservative form are identical (Fennema and Chaudhry 1990). Now with the coupling of the ice dynamic equations, the eigenvalue matrixes may not be the same for the conservative and non conservative forms. However, for an approximate solution, this stability criterion can be taken to be a necessary condition when utilizing the non conservative form of linearized system of equations for stability analysis.

System of Linearized Equations (L_x operator)

The system of linearized equations in the L_x operator can be simplified by neglecting friction terms (or source terms) and rewritten as

$$\frac{\partial h}{\partial t} + \frac{\partial U}{\partial x} + \frac{\partial M_{ui}}{\partial x} = 0 \qquad \text{(B.4)}$$

$$\frac{\partial U}{\partial t} + 2u\frac{\partial U}{\partial x} + u^2\frac{\partial N_i}{\partial x} + (gh - u^2)\frac{\partial h}{\partial x} = 0 \qquad \text{(B.5)}$$

$$\frac{\partial V}{\partial t} + v\frac{\partial U}{\partial x} + u\frac{\partial V}{\partial x} + uv\frac{\partial N_i}{\partial x} - uv\frac{\partial h}{\partial x} = 0 \qquad \text{(B.6)}$$

$$\frac{\partial M_{ui}}{\partial t} - u_i^2\frac{\partial N_i}{\partial x} + 2u_i\frac{\partial M_{ui}}{\partial x} + N_i g\frac{\partial h}{\partial x} = 0 \qquad \text{(B.7)}$$

$$\frac{\partial M_{vi}}{\partial t} - u_i v_i\frac{\partial N_i}{\partial x} + v_i\frac{\partial M_{ui}}{\partial x} + u_i\frac{\partial M_{vi}}{\partial x} = 0 \qquad \text{(B.8)}$$

$$\frac{\partial N_i}{\partial t} + \frac{\partial M_{ui}}{\partial x} = 0 \qquad \text{(B.9)}$$

$$\frac{\partial C_i}{\partial t} - \frac{u_i C_i}{N_i}\frac{\partial N_i}{\partial x} + \frac{C_i}{N_i}\frac{\partial M_{ui}}{\partial x} + u_i\frac{\partial C_i}{\partial x} = 0 \qquad \text{(B.10)}$$

According to Eqs. (B.4) to (B.10), the matrix E and [A] are

$$\mathbf{E} = \begin{bmatrix} h \\ U \\ V \\ M_{ui} \\ M_{vi} \\ N_i \\ C_i \end{bmatrix} \tag{B.11}$$

and

$$[A] = \begin{bmatrix} 0 & 1 & 0 & 1 & 0 & 0 & 0 \\ gh-u^2 & 2u & 0 & 0 & 0 & u^2 & 0 \\ -uv & v & u & 0 & 0 & uv & 0 \\ N_i g & 0 & 0 & 2u_i & 0 & -u_i^2 & 0 \\ 0 & 0 & 0 & v_i & u_i & -u_i v_i & 0 \\ 0 & 0 & 0 & 1 & 0 & 0 & 0 \\ 0 & 0 & 0 & C_i/N_i & 0 & 0 & -u_i C_i/N_i \end{bmatrix} \tag{B.12}$$

When the MacCormack Method is applied to linear system of equations like Eq. (B.3), the explicit, predictor-corrector method written in matrix form becomes

$$\overline{\mathbf{E}_i^{n+1}} = \mathbf{E}_i^n - [A]^n \frac{\Delta t}{\Delta x} (\mathbf{E}_i^n - \mathbf{E}_{i-1}^n) \tag{B.13}$$

$$\mathbf{E}_i^{n+1} = \frac{1}{2}(\mathbf{E}_i^n + \overline{\mathbf{E}_i^{n+1}} - [A]^n \frac{\Delta t}{\Delta x} (\overline{\mathbf{E}_{i+1}^{n+1}} - \overline{\mathbf{E}_i^{n+1}}) \tag{B.14}$$

The term $\overline{\mathbf{E}_i^{n+1}}$ is a temporary "predicted" matrix of **E** at the time level n+1. The corrector equation, Eq. (76), provides the final value of **E** at the time level n+1. Note that in the predictor equation a backward difference is used for $\partial E/\partial x$, while in the corrector equation a forward difference is used. This differencing can be reversed by forward-backward procedure. For single partial differential equation in Eq. (65), both backward-forward and forward-backward procedures of MacCormack scheme are equivalent to the original Lax-Wendroff scheme, which is second-order accurate with a truncation error of $O[(\Delta x)^2,(\Delta t)^2]$ and is stable whenever Courant number is less than or equal to one. Combination of Eq. (B.13) and (B.14) leads to:

$$\mathbf{E}_i^{n+1} = \mathbf{E}_i^n - \frac{[A]^n}{2} \frac{\Delta t}{\Delta x} (\mathbf{E}_{i+1}^n - \mathbf{E}_{i-1}^n) + \frac{\{[A]^n\}^2}{2} \frac{(\Delta t)^2}{(\Delta x)^2} (\mathbf{E}_{i+1}^n - 2\mathbf{E}_i^n + \mathbf{E}_{i-1}^n) \tag{B.15}$$

Performing the von Neumann analysis on Eq. (B.15), attention is focused on one Fourier component of the following form:

$$E_i^n = e^{-i\beta t} e^{i\alpha x} = e^{-i\beta n\Delta t} e^{i\alpha i\Delta x} \tag{B.16}$$

where α (= $2\pi/L$, L is wave length) is wave number of particular wave component; β (= $2\pi/T$, T is period) is angular frequency of particular wave component; and $i = \sqrt{-1}$. Substitution of Eq. (78) into Eq. (77) leads to:

$$e^{-i\beta (n+1)\Delta t} = e^{-i\beta n\Delta t} [G] \tag{B.17}$$

and

$$[G] = [I] - \{[A]^n\}^2 \frac{(\Delta t)^2}{(\Delta x)^2}(1 - \cos \alpha\Delta x) \quad - i [A]^n \frac{\Delta t}{\Delta x} \sin \alpha\Delta x \tag{B.18}$$

where [G] is amplification matrix representing a Fourier component of unit amplitude that grows in one time step, and [I] is identity matrix. This amplification matrix [G] is now dependent upon step size and frequency or wave number, i.e., [G] = [G(Δt,α)]. For a stable finite-difference calculation, the largest eigenvalue of [G], σ_{max}, must obey (Anderson et al. 1984)

$$|\sigma_{max}| \leq 1 \tag{B.19}$$

This leads to the requirement that

$$\left|\lambda_{max}\frac{\Delta t}{\Delta x}\right| \leq 1 \tag{B.20}$$

where λ_{max} is the largest eigenvalue of the [A] matrix, i.e., the Jacobian matrix of the system. The eigenvalue of the [A] matrix can be arrived at by the following determinant.

$$|A-\lambda(I)| = \begin{bmatrix} -\lambda & 1 & 0 & 1 & 0 & 0 & 0 \\ gh-u^2 & 2u-\lambda & 0 & 0 & 0 & u^2 & 0 \\ -uv & v & u-\lambda & 0 & 0 & uv & 0 \\ N_i g & 0 & 0 & 2u_i-\lambda & 0 & -u_i^2 & 0 \\ 0 & 0 & 0 & v_i & u_i-\lambda & -u_i v_i & 0 \\ 0 & 0 & 0 & 1 & 0 & -\lambda & 0 \\ 0 & 0 & 0 & C_i/N_i & 0 & 0 & -u_i C_i/N_i-\lambda \end{bmatrix} = 0 \tag{B.21}$$

This leads to

$$(u-\lambda)(u_i-\lambda)^2\{[(\lambda-u+\sqrt{gh})(\lambda-u-\sqrt{gh})[(\lambda-u_i+\sqrt{N_ig})(\lambda-u_i-\sqrt{N_ig})]-g^2hN_i\}= \quad \text{(B.22)}$$

Eq. (B.22) shows that the eigenvalues are $\lambda_1 = u$, $\lambda_2 = u_i$, and λ_3, λ_4, λ_5, and λ_6 are roots of the following equation:

$$F(\lambda) = (\lambda-u+\sqrt{gh})(\lambda-u-\sqrt{gh})(\lambda-u_i+\sqrt{N_ig})(\lambda-u_i-\sqrt{N_ig}) - g^2hN_i = 0 \quad \text{(B.23)}$$

Since the roots cannot be obtained explicitly from Eq. (B.23), it requires further analysis to obtain the maximum eigenvalue λ_{max}.

Case 1: $u > u_i$

It is obvious that when $\lambda = u+\sqrt{gh}$, the function $F(\lambda)$ has a negative value, $-g^2hN_i$, if u is greater than u_i. As λ increases to $u+\sqrt{gh}+\sqrt{N_ig}$, the function $F(\lambda)$ becomes positive, that implies a root located between $\lambda = u+\sqrt{gh}$ and $\lambda = u+\sqrt{gh}+\sqrt{N_ig}$. Further increase of λ ($= u+\sqrt{gh}+\sqrt{N_ig}$) leads to all positive value of $F(\lambda)$. This is an indication that $\lambda = u+\sqrt{gh}+\sqrt{N_ig}$ can be safely taken as λ_{max} for approximation. Same phenomenon can be found for $\lambda = -u-\sqrt{gh}-\sqrt{N_ig}$. In this case

$$|\lambda_{max}| = |u|+\sqrt{gh}+\sqrt{N_ig} \quad \text{(B.24)}$$

Case 2: $u \le u_i$

Following the same procedure presented for case 1, the maximum eigenvalue for this case is:

$$|\lambda_{max}| = |u_i|+\sqrt{gh}+\sqrt{N_ig} \quad \text{(B.25)}$$

Combination of cases 1 and 2, therefore, the stability criterion for L_x operator is

$$\text{Max}\left[(|u|+\sqrt{gh}+\sqrt{N_ig}), |u_i|+\sqrt{gh}+\sqrt{N_ig}\right]\frac{\Delta t}{\Delta x} \le 1 \quad \text{(B.26)}$$

or

$$C_{rx} \le \frac{1}{1+\kappa F_{Rdx}+\sqrt{\frac{C_i s_i \theta}{h}}} \quad \text{(B.27)}$$

where C_{rx} is Courant number ($= u\Delta t/\Delta x$) in the x direction, κ is one or $|u_i/u|$ whichever is larger, and F_{Rdx} is Froude number in the x direction ($= u/\sqrt{gh}$).

In the absence of ice, Eq. (B.26) reduces to:

$$\lambda_{max} = |u|+\sqrt{gh} \quad \text{(B.28)}$$

and the stability criterion becomes:

$$C_{rx} \leq \frac{1}{1+F_{Rdx}} \tag{B.29}$$

System of Linearized Equations (L_y operator)

Similarly, the linearized system of equations in Ly operator without friction terms can be written as

$$\frac{\partial h}{\partial t} + \frac{\partial V}{\partial y} + \frac{\partial M_{vi}}{\partial y} = 0 \tag{B.30}$$

$$\frac{\partial U}{\partial t} + v\frac{\partial U}{\partial y} + u\frac{\partial V}{\partial y} + uv\frac{\partial N_i}{\partial y} - uv\frac{\partial h}{\partial y} = 0 \tag{B.31}$$

$$\frac{\partial V}{\partial t} + 2v\frac{\partial V}{\partial y} + v^2\frac{\partial N_i}{\partial y} + (gh - v^2)\frac{\partial h}{\partial y} = 0 \tag{B.32}$$

$$\frac{\partial M_{ui}}{\partial t} - u_i v_i \frac{\partial N_i}{\partial y} + u_i \frac{\partial M_{vi}}{\partial y} + v_i \frac{\partial M_{ui}}{\partial y} = 0 \tag{B.33}$$

$$\frac{\partial M_{vi}}{\partial t} - v_i^2 \frac{\partial N_i}{\partial y} + 2v_i \frac{\partial M_{vi}}{\partial y} + N_i g \frac{\partial h}{\partial y} = 0 \tag{B.34}$$

$$\frac{\partial N_i}{\partial t} + \frac{\partial M_{vi}}{\partial y} = 0 \tag{B.35}$$

$$\frac{\partial C_i}{\partial t} - \frac{v_i C_i}{N_i}\frac{\partial N_i}{\partial y} + \frac{C_i}{N_i}\frac{\partial M_{ui}}{\partial y} + v_i \frac{\partial C_i}{\partial y} = 0 \tag{B.36}$$

Following the same procedure of stability analysis as presented in L_x operator, the stability criterion for Ly operator is:

$$\text{Max}\left[(|u| + \sqrt{gh} + \sqrt{N_i g}), |u_i| + \sqrt{gh} + \sqrt{N_i g}\right]\frac{\Delta t}{\Delta y} \leq 1 \tag{B.37}$$

or

$$C_{ry} \leq \frac{1}{1 + \kappa F_{Rdy} + \sqrt{\frac{C_i s_i \theta}{h}}} \tag{B.38}$$

where C_{ry} is Courant number ($= v\Delta t/\Delta y$) in the y direction, β is one or $|v_i/v|$ whichever is larger, and F_{Rdy} is Froude number in the y direction ($v/\sqrt{gh}$).

In the absence of ice, the stability criterion reduces to:

$$C_{ry} \leq \frac{1}{1+F_{Rdy}} \tag{B.39}$$

Eqs. (B.27) and (B.38) conclude that larger Froude number, higher ice concentration and ice velocity, and higher ratio of ice thickness to flow depth would reduce the maximum allowable computational Courant number for time splitting MacCormack scheme. It should be noted that the stability analysis presented above does not include the effect of boundary conditions, and friction term also are neglected.

Stability for Uncoupled Hydrodynamic and Ice Equations

In some application of MacCormack method the hydrodynamic and ice equations are not coupled (e.g. Bjedov 1991), then the stability criterion for hydrodynamic equations are Eqs. (B.28) and (B.39), and the stability criterion for ice equations is as follows:

$$C_{ri} \leq 1 \tag{B.40}$$

where C_{ri} is ice Courant number, $u_i\Delta t/\Delta x$ or $v_i\Delta t/\Delta y$. Eqs. (90), (99), and (100) indicate higher Courant number can be used under sacrifice of more accurate presentation of the coupled two-phase flow.